THE UNIVERSITY *of* EDINBURGH

Modelling submarine melting at tidewater glaciers in Greenland

Donald Alexander Slater

Thesis submitted in fulfilment of the requirements for the degree of

Doctor of Philosophy

to the

University of Edinburgh

2017

Declaration

The work presented in this thesis is original and my own, except where work which has formed part of jointly-authored publications has been included. The contribution of the candidate and the other authors to this work has been explicitly indicated below. The candidate confirms that appropriate credit has been given within the thesis where reference has been made to the work of others. No part of the thesis has been submitted for any other award or professional qualification.

Chapter 4

Citation: Slater, D. A., P. W. Nienow, T. R. Cowton, D. N. Goldberg, and A. J. Sole (2015), Effect of near-terminus subglacial hydrology on tidewater glacier submarine melt rates, *Geophysical Research Letters, 42*(8), 2861-2868, doi: 10.1002/2014GL062494.

Author contributions: D.A.S., P.W.N., T.R.C. and A.J.S designed the research. D.A.S. set up the MITgcm runs with help from T.R.C., D.N.G. and A.J.S. D.A.S. ran the simulations and analysed the results. D.A.S. wrote the paper, with input from all other authors.

Chapter 5

Citation: Slater, D. A., D. N. Goldberg, P. W. Nienow, and T. R. Cowton (2016), Scalings for submarine melting at tidewater glaciers from buoyant plume theory, *Journal of Physical Oceanography, 46*(6), 1839-1855, doi: 10.1175/JPO-D-15-0132.1.

Author contributions: All authors guided the research. D.A.S. performed the calculations with guidance from D.N.G. D.A.S. wrote the paper, with input from all other authors.

Chapter 6

Citation: Slater, D. A., P. W. Nienow, D. N. Goldberg, T. R. Cowton, and A. J. Sole (2017), A model for tidewater glacier undercutting by submarine melting, *Geophysical Research Letters, 44*(5), 2360-2368, doi: 10.1002/2016GL072374.

Author contributions: D.A.S. designed the research and developed the model under guidance from all other authors. D.A.S wrote the paper with input from all other authors.

Chapter 7

Citation: Slater, D. A., P. W. Nienow, A. J. Sole, T. R. Cowton, R. H. Mottram, P. L. Langen and D. W. F. Mair (2017), Spatially distributed runoff at the grounding line of a large Greenlandic tidewater glacier inferred from plume modelling, *Journal of Glaciology, 63*(238), 309-323, doi: 10.1017/jog.2016.139.

Author contributions: D.A.S., P.W.N., A.J.S. and T.R.C. designed the research. P.W.N., A.J.S., T.R.C. and D.W.F.M. collected field observations. A.J.S. processed field observations. R.H.M. and P.L.L. contributed runoff estimates. D.A.S. performed the analysis and D.A.S., P.W.N., A.J.S. and T.R.C. developed the interpretation. D.A.S wrote the paper with input from all other authors.

Donald Slater

May 2017

Abstract

The recent thinning, acceleration and retreat of tidewater glaciers around Greenland suggests that these systems are highly sensitive to a change in climate. Tidewater glacier dynamics have already had a significant impact on global sea level, and, given projected future climate warming, will likely continue to do so over the coming century. Understanding of the processes connecting climatic change to tidewater glacier response is, however, at an early stage. Current leading thinking links tidewater glacier change to ocean warming by submarine melting of glacier calving fronts, yet the process of submarine melting remains poorly understood. This thesis combines modelling and field data to investigate submarine melting at tidewater glaciers, ultimately seeking to constrain the sensitivity of the Greenland Ice Sheet to climate change.

Submarine melting is thought to be enhanced where subglacial runoff enters the ocean and drives energetic ice-marginal plumes. In this thesis, two contrasting models are used to examine the dynamics of these plumes; the Massachusetts Institute of Technology general circulation model (MITgcm) and the simpler buoyant plume theory (BPT).

The first result of this thesis, obtained with the MITgcm, is that the spatial distribution of subglacial runoff at the grounding line of a tidewater glacier is a key control on the rate and spatial distribution of submarine melting. Focussed subglacial runoff induces rapid but localised melting, while diffuse runoff induces slower but spatially homogeneous melting. Furthermore, for the same subglacial runoff, total ablation by submarine melting from diffuse runoff exceeds that from focussed runoff by at least a factor of five.

BPT is then used to examine the relationship between plume-induced submarine melting and key physical parameters, such as plume geometry, fjord stratification, and the magnitude of subglacial runoff. It is shown that submarine melt rate is proportional to the magnitude of subglacial runoff raised to the exponent of 1/3, regardless of plume geometry, provided runoff lies below a critical threshold and the fjord is weakly stratified. Above the runoff threshold and for strongly stratified fjords, the exponent respectively decreases and increases. The obtained relationships are combined into a single parameterisation thereby providing a useful first-order estimate of submarine melt rate with potential for incorporation into predictive ice flow models.

Having investigated many of the factors affecting submarine melt rate, this thesis turns to the effect of melting on tidewater glacier dynamics and calving processes. Specifically, feedbacks between submarine melting and calving front shape are evaluated by coupling BPT to a dynamic ice-ocean boundary which evolves according to modelled submarine melt rates. In agreement with observations, the model shows calving fronts becoming undercut by submarine melting, but hints at a critical role for subglacial channels in this process. The total ablation by submarine melting increases with the degree of undercutting due to increased ice-ocean surface area. It is suggested that the relative pace of undercutting versus ice velocity may define the dominant calving style at a tidewater glacier.

Finally, comparison of plumes modelled in both MITgcm and BPT with those observed at Kangiata Nunata Sermia (KNS), a large tidewater glacier in south-west Greenland, suggests that subglacial runoff at KNS is often diffuse in nature. In addition to the above implications for submarine melting, diffuse drainage may enhance basal sliding during warmer summers, thereby providing a potential link between increasing atmospheric temperature and tidewater glacier acceleration which does not invoke the role of the ocean.

This thesis provides a comprehensive investigation and quantification of the factors affecting submarine melting at tidewater glaciers, a complex process that is believed to be one of the key influences on the current and future stability of the Greenland Ice

Sheet. Based on the magnitude of modelled melt rates, and their effect on calving front shape, the process of submarine melting is a likely driver of retreat at slower-flowing tidewater glaciers in Greenland. For melting to influence the largest and fastest-flowing glaciers requires invoking a sensitive coupling between melting and calving which is as yet obscure. It should however be noted that modelled melt rates depend critically on parameters which are poorly constrained. The results and parameterisations developed in this thesis should now be taken forward through testing against field observations - which are currently rare - and, from a modelling perspective, coupling with ice flow models to provide a more complete picture of the interaction of the Greenland Ice Sheet with the ocean.

Lay Summary

The Greenland Ice Sheet is a vast mass of ice located in the North Atlantic. The ice sheet contains sufficient ice to raise global sea level by 7 m, should it all melt. Over the past few decades, both air and ocean temperatures around Greenland have risen, and the ice sheet has been losing mass at an increasing rate, contributing significantly to sea level rise.

Ice loss from the Greenland Ice Sheet occurs through two mechanisms. First, during summer, warm air temperatures melt the ice sheet surface. Second, parts of the ice sheet (called tidewater glaciers) flow directly into the ocean where ice is lost due to melting by the ocean (called submarine melting) and due to the production of icebergs. The recent increase in ice loss from Greenland is due to both increased ice sheet surface melting and increased flow speed of tidewater glaciers; the latter meaning that more ice is lost from the ice sheet into the ocean.

These changes are clearly climate-driven, and given that over the coming century the atmosphere and ocean around Greenland are projected to warm further, there is clear potential for further ice mass loss. Accurate predictions of the future sea level contribution from Greenland require a good understanding of the link between mass loss and climate, yet the processes driving increased flow of tidewater glaciers are particularly poorly understood. It is thought that increased submarine melting due to increased ocean temperature may play an important role, yet we currently understand little of this process. This thesis therefore aims to contribute by studying the interaction of tidewater glaciers with the ocean.

During summer, meltwater from the ice sheet surface penetrates through the ice sheet and emerges into the ocean from beneath tidewater glaciers, several hundred metres below the ocean surface. The emerging surface meltwater (called subglacial discharge) rises towards the ocean surface as a buoyant plume after entering the ocean, driving high rates of submarine melting. Plumes are therefore a key link between the ocean and ice, and in this thesis, numerical modelling is used to examine the dynamics of these plumes and the submarine melting induced.

Many of the important factors affecting plume dynamics are investigated, and the relationships between these factors and the rate of submarine melting are quantified. Submarine melting is found to increase linearly with the ocean temperature, and sublinearly with the magnitude of subglacial discharge. Since subglacial discharge originates from melting of the ice sheet surface, submarine melting will vary with both ocean and air temperature.

The spatial pattern of submarine melting at a tidewater glacier is found to depend strongly on how the subglacial discharge emerges from beneath the glacier. Rapid but localised melting of the calving front occurs if all of the subglacial discharge emerges from a single subglacial channel, while more widespread but weaker melting occurs if the subglacial discharge is spread across the width of the tidewater glacier. Using observations of plumes from a time-lapse camera, it is suggested that the latter situation prevails at a tidewater glacier in south-west Greenland.

This thesis finally considers how spatial variability in submarine melting at a tidewater glacier may shape the front of the glacier, creating chimney-like incisions in the ice, and resulting in glacier fronts which are undercut near their base. It is suggested that this undercutting increases total submarine melt volumes due to increased ice-ocean surface area, providing a positive feedback between submarine melting and glacier front shape. Undercutting of a calving front by submarine melting may increase the production of icebergs and is therefore integral to understanding the effect of the ocean on tidewater glaciers.

This work provides a comprehensive quantification of the factors affecting submarine

melting. Based on this understanding, it is suggested that submarine melt rates have increased by ∼50% in recent decades. This increase may have been sufficient to result in tidewater glacier acceleration at slower-flowing glaciers, where submarine melt rates are comparable to the ice flow velocity, but the role of submarine melting at Greenland's largest and fastest-flowing glaciers, where ice flow velocity substantially exceeds submarine melt rates, remains unclear. The drawing of more definitive conclusions on the importance of submarine melting is at present precluded by a lack of observations of submarine melting with which to verify the modelling undertaken in this thesis. Therefore, better observational constraints are much needed to improve understanding of the effect of the ocean on the Greenland Ice Sheet, and ultimately to reduce uncertainty on future sea level rise.

Acknowledgements

My first and biggest thanks go to my principal supervisor Pete, for his inexhaustible generosity of time, support, research freedom and beer, and for creating a research environment in Edinburgh which has been both productive and great fun from start to finish. Special mention must be made of his tolerance of my mathematical tendencies. Thanks also for a wonderful trip to Greenland which will live long in the memory.

I am extremely grateful to my second supervisor Dan, again for generosity of time, for always being there with mathematical support, for extending his expertise into the oceanographic realm, and for many memorable excursions from Edinburgh. Thank you to my final supervisor Andrew for numerical support, his very thorough feedback, great ideas, and good times whenever we met. Big thanks to Tom for setting an example to follow, for his invaluable research input, and for much amusement both in and out of the office.

From April to July 2016 I visited Woods Hole Oceanographic Institute in the US; I am very grateful to Fiamma Straneo and all the friends I made there for making it a great few months. This trip was funded by the Scottish Alliance for Geoscience, Environment and Society (SAGES), and on this theme, I have been lucky to benefit from a Natural Environmental Research Council (NERC) fully-funded PhD studentship.

The entertainment provided by fellow PhD students has been a particular highlight of my PhD. Notable mentions go to Damon for climbing adventures, to Lizzie for warding off normality, to Andrew for being a good sport, to Ed for all round strong chat, to Alexis for bringing the sass, to Frazer for lowering the tone, to Luca for putting up

with me, and to John, Fiona, Penny and the rest for making it a blast. Kudos also to Imogen, Gen and Luke for being the best flatmates anyone could wish for.

Last but not by any means least, thank you to Granny for much-needed quiet evenings and weekends at the Coltbridge sanctuary and to Rory for much fun whenever we see each other. To Alice, for always being there and for countless good times over the past two years. Final thanks to Mum and Dad for unwavering support, for great escapes all around Scotland and for patience with my decision-making - it was all right in the end!

Contents

List of Tables

List of Figures

Chapter 1

Introduction

The polar regions perhaps assume greater global significance today than ever before. These regions stand at the front line of climate change, with change in these regions now attaining sufficient magnitude as to be societally relevant on short timescales. The polar regions contain the two great ice sheets of Greenland and Antarctica, numerous ice caps, glaciers and seasonal sea ice. Excepting Antarctic sea ice, each of these cryospheric components are diminishing in volume and extent, and increasingly so in recent decades. Arctic sea ice annual extent decreased at ∼4% per decade over the period 1979-2012 (*Vaughan et al.*, 2013) while ice sheet mass loss contributed ∼14 mm to sea level in the period 1992-2012 (Fig. 1.1; *Vaughan et al.* (2013)). Globally, ice caps and glaciers (most of which lie in the polar regions) contributed ∼0.8 mm/yr to sea level in the period 1993-2009 (Fig. 1.1; *Vaughan et al.* (2013)). Collectively, loss of global ice accounted for ∼40% of the observed sea level rise of 3.2 mm/yr in the period 1993-2010 (*IPCC*, 2013).

These changes are certainly driven in part by atmospheric warming; global mean surface temperature increased by 0.85°C in the period 1880-2012, with the three decades preceding 2012 successively the warmest decades since at least 1850 (Fig. 1.2; *IPCC* (2013)). Ocean warming is also thought to play a role in ice mass loss, with evidence suggesting that the subsurface ocean surrounding the Greenland Ice Sheet warmed by

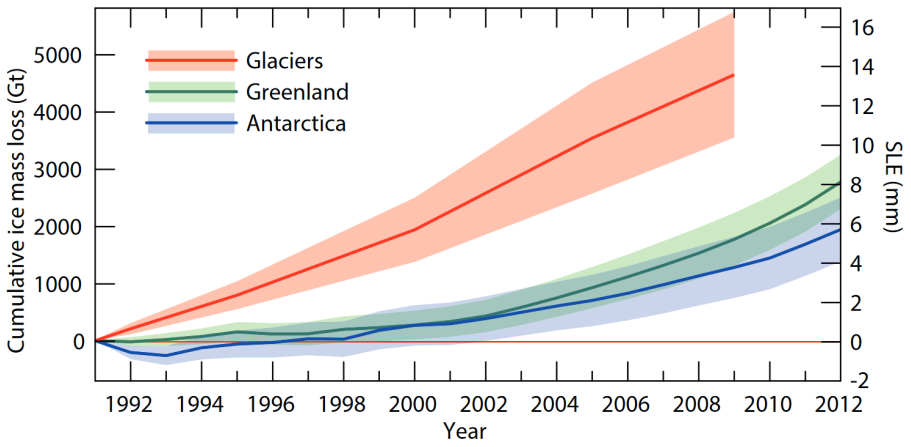

Figure 1.1: Cryospheric contributions to sea level change from 1991 to 2012, reproduced from *Vaughan et al.* (2013).

1.5-2°C between the mid-90s and mid-00s (*Rignot et al.*, 2012). Even supposing that international efforts to restrict atmospheric warming to 2°C above pre-industrial levels are successful, we will see further substantial change in the polar regions in coming decades (*IPCC*, 2013), not least due to the polar amplification which sees greater warming at high latitudes (e.g. *Hansen et al.*, 1997).

Given the rapid changes occurring in the high latitudes, there is a pressing need to understand the processes linking atmospheric and oceanic warming to ice mass response in the polar regions. Through this understanding we may constrain future evolution of the polar regions, and better inform policy decisions on climate change mitigation and adaptation. This thesis contributes by studying the interaction between glaciers and the ocean, thought to be a crucial link between climate, ice mass loss and sea level change.

1.1 Ice sheets and tidewater glaciers

The present-day world has two ice sheets located in Antarctica and Greenland. The Antarctic Ice Sheet extends from the south pole to 60°S and contains 27 million km^3 of ice, equivalent in water volume to approximately 60 m of sea level (*Fretwell et al.*, 2013). The Greenland Ice Sheet stretches from ∼60°N to 82°N in the north Atlantic

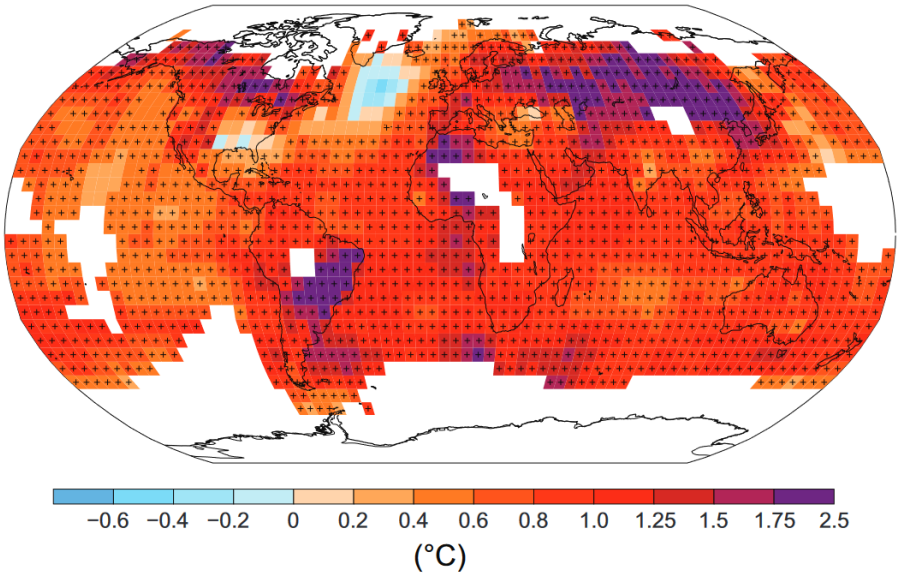

Figure 1.2: Observed surface air temperature change from 1901 to 2012, reproduced from *IPCC* (2013). White boxes indicate a lack of data while plus signs within boxes indicate significant trends.

and is about one tenth the volume of Antarctica, containing 7 m of potential sea level (*Bamber et al.*, 2013). Differing climatic settings lend the two ice sheets contrasting character. The Antarctic, with the exception of the peninsula, is extremely cold with only a small fraction of the ice sheet experiencing temperatures above zero during the summer (e.g. *Lenaerts et al.*, 2012). Over much of its periphery, the Antarctic Ice Sheet thus extends into the ocean and forms vast floating ice shelves. In contrast, the Greenland Ice Sheet experiences significant melting during the summer (e.g. *van den Broeke et al.*, 2016) and the ice sheet extends into the ocean only in topographically confined fjords, with a significant proportion of the ice sheet terminating on land.

Ice sheets gain mass predominantly through snowfall and lose mass by melting of ice and calving of icebergs (Fig. 1.3). Melting may take place on the ice sheet surface or where the ice sheet is in contact with the ocean, with the latter process referred to as submarine melting. Meltwater generated at the ice sheet surface may leave the ice sheet as liquid water or be retained on the ice sheet by refreezing in the snowpack (*Cuffey and Paterson*, 2010). In Antarctica, the balance of mass is mostly a competition between

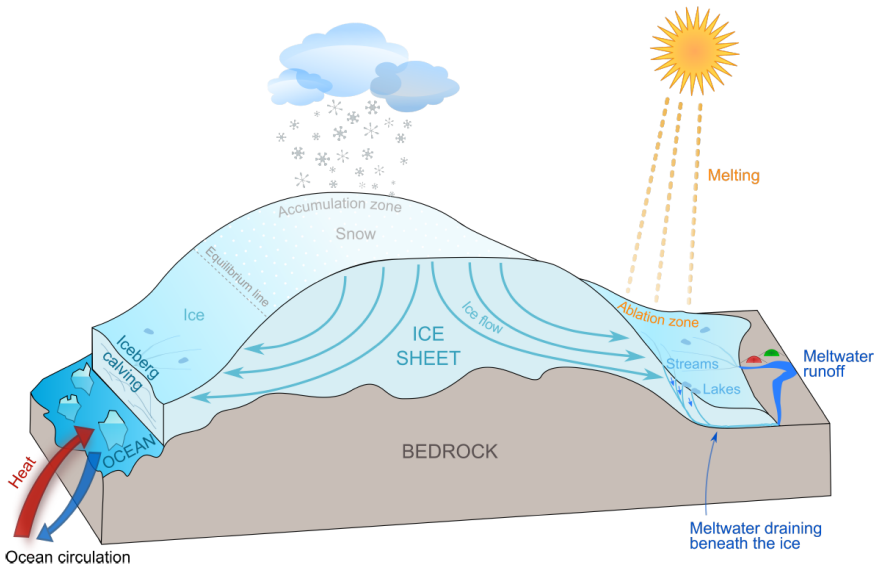

Figure 1.3: A schematic illustration of the processes determining ice sheet mass balance, reproduced from *Tedstone* (2015).

snowfall, iceberg calving and submarine melting (*Rignot et al.*, 2008). Mass balance of the warmer Greenland Ice Sheet is dominated by the processes of snowfall, surface melting, refreezing, iceberg calving and potentially submarine melting (*van den Broeke et al.*, 2016).

The motivation for this thesis comes from the changing mass balance of the Greenland Ice Sheet in recent decades. A time series of GrIS mass balance from 1958 to 2015 (Fig. 1.4) is suggestive of an ice sheet which was in approximate dynamic equilibrium before 1990 and which has lost mass at an increasing rate since 1990, with a peak sea level contribution of 1.2 mm/yr in 2012 (*van den Broeke et al.*, 2016). The negative mass balance since 1990 results partly from decreasing surface mass balance (Fig. 1.4), which accounts for snowfall, surface melting and refreezing, with the downward trend driven largely by increased surface melting (*van den Broeke et al.*, 2016). Increases in iceberg calving and submarine melting, collectively referred to as discharge (Fig. 1.4) also contribute significantly to mass loss (*Enderlin et al.*, 2014). From 2000 to 2008, the negative mass balance of the ice sheet can be equally attributed to decreased surface mass balance and increased ice discharge (*van den Broeke et al.*, 2009); while over the

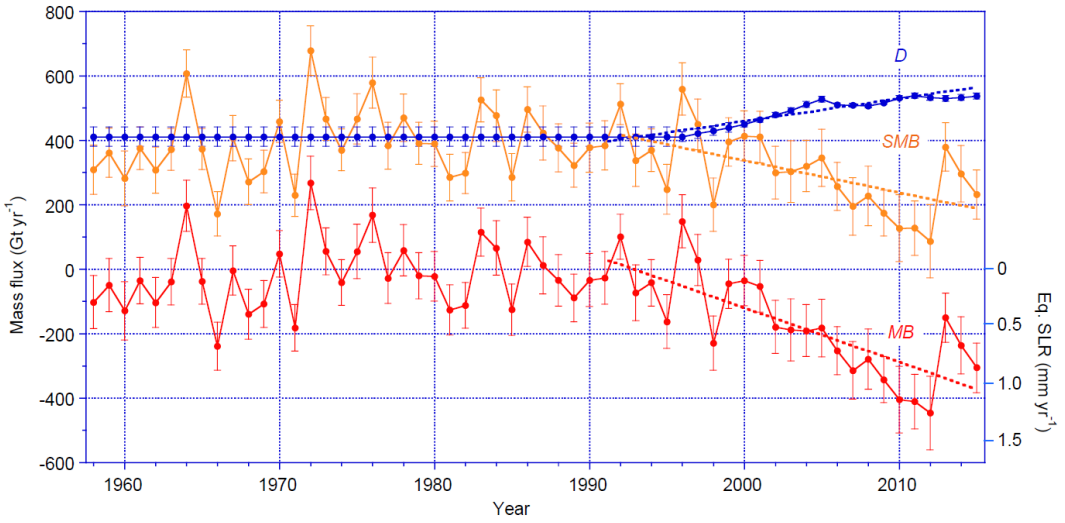

Figure 1.4: Contemporary Greenland Ice Sheet mass balance determined from regional climate modelling and satellite observations of ice motion, reproduced from *van den Broeke et al.* (2016). Surface mass balance (*SMB*) accounts for snowfall, surface melting and refreezing. Discharge (*D*) accounts for calving of icebergs and submarine melting. Overall mass balance (*MB*) is calculated as *SMB* - *D*. Note that due to lack of observations, discharge is assumed constant pre-1995.

longer period from 1991 to 2015, surface mass balance assumes a slightly greater role, accounting for ∼60% of ice loss (*van den Broeke et al.*, 2016). While the dominant driver of decreased surface mass balance is clear (increased atmospheric temperature drives increased surface melting), the processes responsible for increased ice discharge remain poorly understood.

Discharge of ice into the ocean from the Greenland Ice Sheet occurs through tidewater glaciers (Figs. 1.5 and 1.6). These are topographically-confined streams of ice which transport mass rapidly from the interior of the ice sheet into the ocean, where the ice is lost either by submarine melting or by calving of icebergs. Tidewater glaciers have a typical width of ∼1-10 km, thickness of ∼200-1000 m and flow at ∼1-50 m/d. There are over 200 tidewater glaciers distributed around Greenland, with high concentrations in the south-east and north-west of the ice sheet. Tidewater glaciers often flow into long and narrow fjords (Fig. 1.5) which can be choked with icebergs and sea ice (Fig. 1.6).

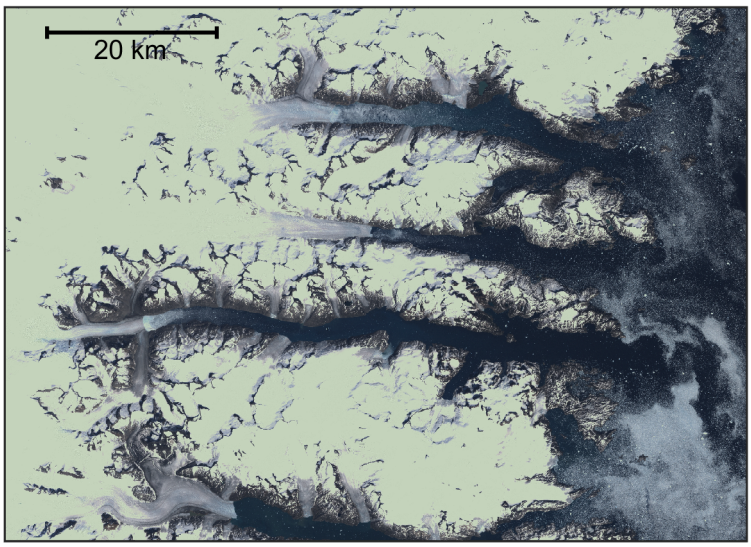

Figure 1.5: A typical section of Greenland coastline, in this case south-east Greenland. Topographically confined tidewater glaciers flow into deep and narrow fjords. Imagery from *Howat et al.* (2014) and *Howat* (2017).

Where tidewater glaciers meet the ocean, they either form an approximately vertical wall of ice (calving front) extending from above the ocean surface to the ocean bottom (Fig. 1.6) or, for a few large tidewater glaciers in northern Greenland, a floating ice tongue or shelf.

In recent decades, tidewater glaciers around Greenland have retreated, accelerated, and thinned (*Pritchard et al.*, 2009; *Moon et al.*, 2012; *Murray et al.*, 2015). In combination, these changes have increased ice discharge from the Greenland Ice Sheet by ∼35% since 1995 (Fig. 1.4) such that submarine melting and iceberg calving now drains ∼550 billion tonnes of ice from the ice sheet each year (*Enderlin et al.*, 2014; *van den Broeke et al.*, 2016). The widespread and synchronous response of tidewater glaciers (*Murray et al.*, 2015) suggests these changes have been driven by a climate forcing. Atmospheric warming could drive change by increasing surface melting which may in turn lubricate tidewater glacier flow, as postulated by *Sugiyama et al.* (2011) based on evidence from a glacier terminating in a freshwater lake. Ocean warming could drive change by increasing submarine melting and iceberg calving (*Straneo and Heimbach*, 2013). At

Figure 1.6: Kangiata Nunata Sermia is the largest tidewater glacier in south-west Greenland. The calving front is approximately 5 km across and extends hundreds of metres below the ocean surface, which is in this image covered by icebergs and bergy bits. Image from 27/9/2016.

present, ocean warming is the leading candidate as a driver of change (e.g. *Vaughan et al.*, 2013), although we understand little of the processes linking the ocean and the ice sheet or of the significance of these links. Given the potential importance for the future evolution of the ice sheet, this thesis focusses on the interaction of the ocean with the Greenland Ice Sheet, and in particular on the process of submarine melting.

1.2 Outline of thesis

This thesis aims to improve our understanding of the effect of the ocean on the Greenland Ice Sheet through investigation of the process of submarine melting. It uses numerical modelling to assess the likely magnitude of submarine melting and the variability in submarine melt rates driven by various physical processes. Both idealised and real systems are considered, seeking to reach conclusions which are relevant to tidewater glaciers both in Greenland and elsewhere. This thesis aims to assess the

importance of submarine melting to tidewater glacier dynamics, contributing to the identification of the drivers of recent Greenland Ice Sheet mass loss and building the understanding needed to constrain future evolution of the ice sheet. The work presented in this thesis can be divided into three broad themes.

I **Quantifying the magnitude of and variability in submarine melting**

This thesis seeks to use numerical methods to quantify rates of submarine melting which provide a first order estimate of the importance of submarine melting to tidewater glacier dynamics. Many of the factors potentially affecting submarine melt rate are explored, including the magnitude of subglacial discharge at the base of the calving front, fjord water temperature, fjord density profile, subglacial hydrology and calving front shape. This thesis also seeks to encompass key factors from the above list into a single parameterisation for submarine melting which is suitable for representation of submarine melting in coarse ice sheet and ocean models.

II **Quantification of spatial variability in submarine melting**

In this theme, the spatial distribution of submarine melting at a tidewater glacier calving front is explored using both simple theoretical models and more complex general circulation models. This thesis explores two drivers of spatial variability in submarine melt rate: (i) vertical variation due to the dynamics of buoyant plumes initiated by the drainage of subglacial discharge at the base of the calving front, and (ii) horizontal variation due to differing patterns of water drainage at the base of the calving front as a result of the subglacial hydrology. Recognising the importance of subglacial hydrology to the process of submarine melting, the subglacial hydrology at a tidewater glacier in south-west Greenland is constrained using time-lapse photography of the glacier terminus.

III **The effect of submarine melting on calving front shape**

The previous theme assessed spatial variability in submarine melt, while considering only static vertical calving fronts. Differential rates of submarine melting at

two points on a calving front will change the shape of the calving front, with vertical variability resulting in undercutting or overcutting of the calving front, and horizontal variability creating incised chimneys and protruding headlands. During the course of the work undertaken in this thesis, these calving front shapes have been observed for the first time (*Rignot et al.*, 2015; *Fried et al.*, 2015), as discussed in more detail in Chapter 2.

Building on the previous theme, this thesis therefore studies how calving front shape changes in response to differential submarine melting, and how changing calving front shape subsequently feeds back on and impacts submarine melt rate. This thesis couples a dynamic ice-ocean boundary to a simple model for vertical variability in submarine melt rate to study the process of calving front undercutting. This last theme is particularly important because calving front shape is thought to exert a significant control on the style and rate of iceberg calving, and therefore on discharge of ice from the ice sheet.

This thesis finally seeks to bring the above three themes together to assess the importance of submarine melting to tidewater glacier dynamics, particularly in relation to the observed changes in tidewater glacier behaviour in Greenland in recent decades. Implications for the future evolution of the ice sheet are discussed and methods for implementing submarine melting in models of future ice sheet evolution are considered.

While this thesis focusses on Greenland, for example through choice of ocean conditions for the models and in the discussion of the results, many of the conclusions will be more widely applicable to tidewater glaciers in for example Alaska, Svalbard, the Canadian Arctic and the West Antarctic Peninsula.

This thesis proceeds as follows. Chapter 2 provides a more detailed description of the motivation and background for the thesis, including observed changes in Greenlandic tidewater glaciers, the climatic setting of Greenland, a review of tidewater glacier dynamics and a summary of research on submarine melting. With respect particularly to the last two points, much research has been ongoing by numerous groups during the course of this thesis; a reflection of the fast-moving and exciting nature of the research

topic. Chapter 3 provides a brief overview of the methods employed in this thesis, with more detailed descriptions left to the individual results chapters and supporting information.

Chapters 4-7 describe the results of the thesis focussing on the three themes identified above, with some chapters relevant across more than one of the themes. Finally, Chapter 8 provides a synthesis of the results, identifying key conclusions, placing the findings in the context of the literature and identifying avenues and recommendations for future research.

1.3 Format of thesis

All of the results chapters have been written as standalone papers to make the results accessible to the research community, and all have already been published. The contributions of all of the authors on each of these publications are summarised at the start of each chapter. The work undertaken in this thesis has also made important contributions to two further publications on which I am a co-author. The published formats of all of these papers are included as appendices.

Chapter 2

Background

The great current interest in the interaction of the Greenland Ice Sheet with the ocean stems from the widespread and synchronous acceleration of tidewater glaciers around Greenland during a period of ocean warming (*Straneo and Heimbach*, 2013). This background chapter therefore begins by outlining tidewater glacier behaviour in recent decades, and the climatic conditions under which changes at Greenland's tidewater glaciers have occurred. Drivers of tidewater glacier dynamics are then discussed, with both ocean and other processes reviewed. This chapter then focusses on ice-ocean interaction, summarising the current state of knowledge of fjord circulation, proglacial plumes, and submarine melting and its possible links to glacier dynamics.

2.1 Tidewater glacier behaviour in Greenland

2.1.1 Regional behaviour during the satellite era

Satellite capabilities have revolutionised glaciology, facilitating the study of the remote and difficult to access regions embodied by the ice sheets. Satellite imagery has both high spatial resolution (<100 m), is available with good frequency (<1 month), and provides ice sheet-wide coverage. From these products ice surface elevation, glacier terminus position and ice flow speed may be extracted, permitting study of processes and mass balance of individual glaciers and crucially, at the whole ice

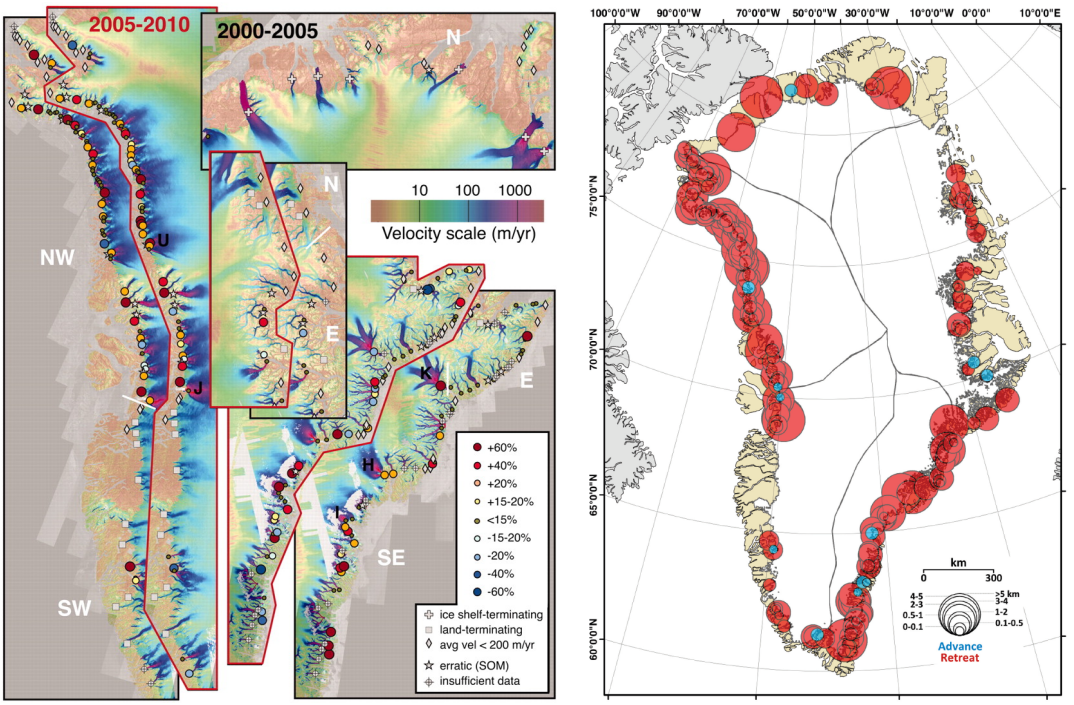

Figure 2.1: Behaviour of tidewater glaciers in Greenland over the past few decades. Left: trends in tidewater glacier velocity reproduced from *Moon et al.* (2012). Right: change in tidewater glacier terminus position between 2000 and 2010 reproduced from *Murray et al.* (2015).

sheet scale. These ice-sheet scale datasets reveal that over the past few decades marine-terminating glaciers have, in contrast to land-terminating glaciers, undergone rapid change (Fig. 2.1). Broadly speaking, these changes have been widespread and synchronous. However, significant regional, temporal and glacier-to-glacier variability is also seen, confounding attempts to understand marine-terminating glacier dynamics.

Within the period of study permitted to date by satellite data, significant change at tidewater glaciers is first seen in the mid- to late-90s, observed as a moderate but widespread increase in flow velocity and terminus retreat focussed in south-east Greenland (*Rignot and Kanagaratnam*, 2006; *Jiskoot et al.*, 2012). The same region underwent a pulse of very rapid change in the years 2000-2005, during which period ice discharge and terminus retreat rate approximately doubled (*Rignot and Kanagaratnam*, 2006; *Jiskoot et al.*, 2012). More recently, glaciers in the south-east appear to have

stabilised, such that at a regional scale, flow speeds in 2010 were similar to 2005 (*Moon et al.*, 2012) and approximately a quarter of terminus retreat during 2000-2005 was recovered by re-advance during 2005-2009. In contrast to those further south, tidewater glaciers north of 69°N on the east coast of Greenland showed little change in either terminus position or flow velocity between 2000 and 2009 (*Seale et al.*, 2011; *Moon et al.*, 2012). On Greenland's west coast, a high concentration of tidewater glaciers is found in the north-west, with only a few tidewater glaciers in south-west Greenland. The behaviour of these west coast glaciers is steadier, with gradual acceleration in ice velocity amounting to a 27% increase between 2000 and 2010 (*Moon et al.*, 2012). Around the north of Greenland, the major glaciers terminate in ice shelves, and showed little change between 1996 and 2010 (*Rignot and Kanagaratnam*, 2006; *Moon et al.*, 2012).

The major regional changes at tidewater glaciers in Greenland are therefore a short but rapid period of thinning, acceleration and retreat of tidewater glaciers in the south-east in the early 2000s and a slower but more sustained response in the north-west (Fig. 2.1). Together, glaciers in these two regions represent ∼80% of Greenland's discharge of solid ice to the ocean, and account for 86% of change in solid ice discharge between 2000 and 2012 (*Enderlin et al.*, 2014). The described regional changes are well illustrated by time series of solid ice discharge (Fig. 2.2). Overall, tidewater glacier acceleration has increased total Greenland ice discharge from ∼460 Gt/yr in 2000 to ∼550 Gt/yr in 2012 (Fig. 2.2; *Rignot et al.* (2011); *Enderlin et al.* (2014)), contributing an additional ∼3 mm to global sea level since 2000.

Despite clear regional trends, significant variability exists both between and within regions. The rapid pulse of retreat followed by stability in the south-east contrasts with slow and steady retreat in the north-west. Within the north-west, and despite increasing regional ice discharge, a third of tidewater glaciers showed no trend in velocity and a quarter slowed over the decade 2000-2010 (Fig. 2.1; *Moon et al.* (2012)). Large individual glaciers can also dominate trends in ice discharge from a region or indeed from the ice sheet. Of the increase in ice discharge from Greenland between 2000 and 2012, 77% is accounted for by 15 glaciers while just 4 glaciers (Jakobshavn Isbrae,

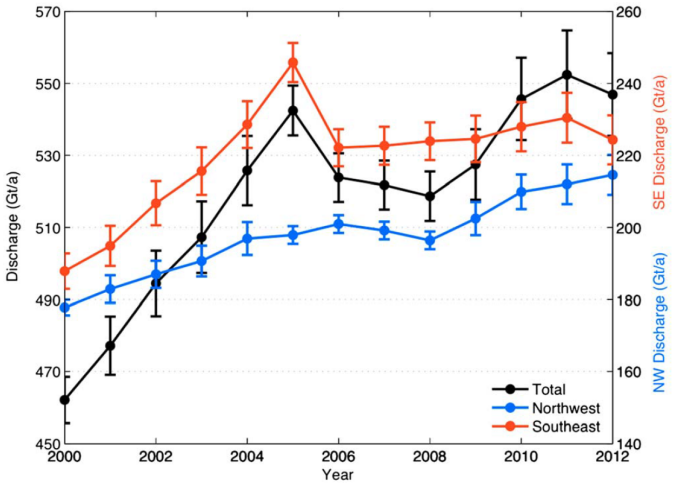

Figure 2.2: Ice discharge from the Greenland ice sheet from 2000 to 2012, reproduced from *Enderlin et al.* (2014).

Kangerdlugssuaq, Koge Bugt, and Ikertivaq South) account for half (*Enderlin et al.*, 2014). Therefore, while we seek an understanding of tidewater glacier dynamics at the ice sheet scale, it may be necessary to consider individual glaciers, particularly considering how important a handful of glaciers are to the mass balance of the ice sheet.

2.1.2 Behaviour of selected glaciers

A few well-studied large tidewater glaciers exemplify the described regional changes. Greenland's fastest-flowing and largest by ice discharge is Jakobshavn Isbrae, draining to the west coast. From 1997, the grounded part of the glacier began thinning at rates up to 15 m/yr and the 15 km floating ice tongue at rates of 80 m/yr, leading to the disintegration of the ice tongue in the early 2000s (*Thomas*, 2004). Ice velocity doubled between the mid-90s and 2003 (*Holland et al.*, 2008a), and accompanied by further thinning and grounding line retreat, continues to increase with velocities of 17 km/yr (nearly 50 m/d) recorded in 2012 (*Joughin and Smith*, 2013).

In the south-east, Kangerdlugssuaq and Helheim Glaciers typify the regional trend, accelerating slowly from the mid-90s, with rapid change from 2003, velocities peaking

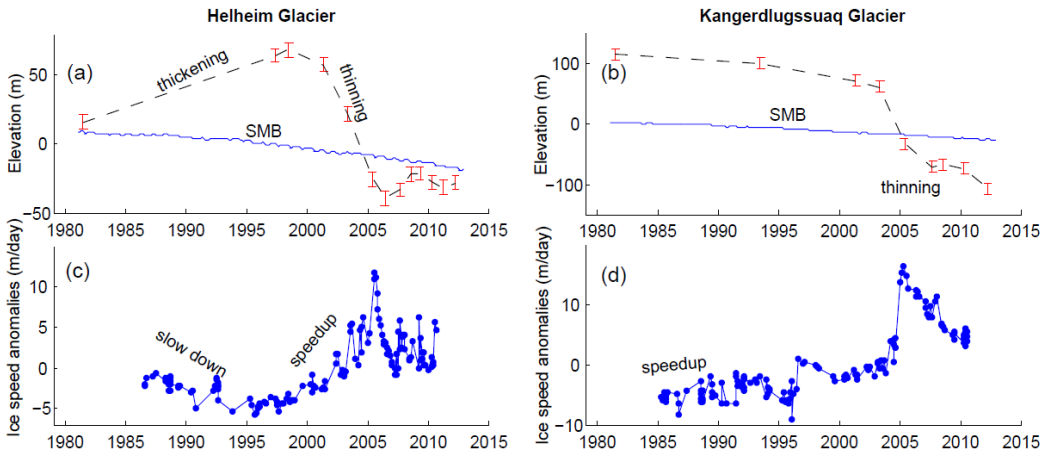

Figure 2.3: Surface elevation change and ice velocity at Helheim and Kangerdlugssuaq Glaciers since 1980, reproduced from *Khan et al.* (2014). Data are extracted from points approximately 5-10 km behind the 2010 calving fronts.

in 2005 and a more quiescent phase since (Fig. 2.3; *Christoffersen et al.* (2012); *Moon et al.* (2012); *Khan et al.* (2014)). Helheim and Kangerdlugssuaq thinned by 100 and 200 m respectively between 1998 and 2010, both undergoing velocity increases of 15-20 m/d (5-7 km/yr) by 2005 (Fig. 2.3; *Khan et al.* (2014)). Change at Kangerdlugssuaq was particularly rapid; this velocity increase coming almost exclusively between July 2004 and April 2005 during which period the glacier also retreated 7 km (*Luckman et al.*, 2006; *Joughin et al.*, 2008a). Helheim reached its furthest retreated position in 2005, a retreat of ∼7 km since the late 90s. Both glaciers have subsequently slowed and somewhat stabilised, although Kangerdlugssuaq continues to undergo slow thinning and retreat (*Khan et al.*, 2014).

Contrasting examples are provided by Rink and Store Glaciers on the west coast, which show anomalous stability relative to many glaciers in the region. Over the past few decades, both have undergone little change in terminus position and show no trend in ice velocity (*Howat et al.*, 2010; *Moon et al.*, 2014; *Bartholomaus et al.*, 2016).

2.1.3 Longer-term perspectives

It is important to place the behaviour of tidewater glaciers over the past few decades in a (slightly) longer term context. While the spatial and temporal precision of observations made before satellites is clearly poorer, a combination of archived photographs and maps, proxies and geomorphic evidence offer valuable insight.

Using a combination of geomorphological evidence and archived photographs, *Lea et al.* (2014) show that Kangiata Nunata Sermia (KNS), the largest tidewater glacier in south-west Greenland, had retreated ∼15 km from its Little Ice Age maximum by 1859. They further show that KNS retreated steadily at ∼100 m/yr between 1921 and 1968, interrupted by rapid retreat of 4 km in the late 1940s. There are periods of slow advance in the 1970s and early 90s, with otherwise moderate retreat at ∼100 m/yr up to the present day. At KNS then, retreat over the past few decades is not exceptional within the past 150 years.

On the east coast, records and reconstructions exist for Kangerdlugssuaq and Helheim glaciers. *Andresen et al.* (2012) reconstruct calving activity since 1890 at Helheim glacier from ice-rafted debris in fjord sediment cores. This record shows low calving activity pre-1930 and variable calving rate since, with particular spikes of activity in the late 1930s/early 1940s and early 2000s. The latter spike agrees well with the satellite-observed behaviour discussed above, while the former spike ties in well with historical aerial imagery showing that Helheim glacier was more retreated in the 1930s than in 2003 (*Khan et al.*, 2014). Between 1933 and 1981, Helheim recovered to its Little Ice Age maxima both in terms of terminus position and surface elevation (*Bjork et al.*, 2012; *Khan et al.*, 2014). In contrast, Kangerdlugssuaq glacier was close to its Little Ice Age maxima in the early 1930s before the collapse of its 7 km floating tongue in 1932-1933 initiated thinning of >200 m by 1981 (*Spender*, 1933; *Khan et al.*, 2014). These studies suggest that a period of rapid change, similar to that seen in the early 2000s may have occurred in the 1930s/1940s.

At the ice sheet scale, *Kjeldsen et al.* (2015) suggest that many of the glaciers undergoing dynamic change in recent decades underwent similar change in the early 20th century.

They further suggest that the dynamic contribution of the ice sheet to sea level (that is, the discharge of ice from tidewater glaciers) has remained relatively constant over the past 110 years, suggesting that in agreement with the above evidence, the observed changes over recent decades may not be unprecedented in the past century.

2.1.4 Drivers of change

While recognising variability from glacier to glacier, the synchronous and widespread nature of changes at tidewater glaciers around Greenland is indicative of a common climatic forcing. The challenge is to identify this forcing and understand exactly how it affects tidewater glacier dynamics. The forcing could be atmospheric or oceanic, and while atmospheric changes should not be dismissed (and indeed may help to amplify ocean forcing), the current leading hypothesis concerns primarily the ocean, and it is ice-ocean interaction which forms the focus of this thesis. As a result, Greenland's oceanic setting is now described.

2.2 Climatic conditions

2.2.1 Large-scale ocean setting

Greenland lies in the north Atlantic, spanning latitudes from 60 to 82°N. The ocean water around the coast of Greenland has influences from both polar and tropical regions, and from the ice sheet itself (Fig. 2.4). Polar influences come from the east Greenland current (EGC) which brings cold and relatively fresh polar water (PW) south from the Arctic, hugging the east coast of Greenland in the Nordic seas and continuing to follow the coast around Cape Farewell and into Baffin Bay (Fig. 2.4; *Straneo and Heimbach* (2013)). The tropical influence comes from the Atlantic Meridional Overturning Circulation (or Gulf Stream) which brings subtropical water into the North Atlantic. This warm and relatively salty Atlantic water (AW) flows towards the south-east coast of Greenland in the Irminger current, thereafter following the EGC around the coast (Fig. 2.4; *Rignot et al.* (2012)). The lighter PW tends to occupy Greenland's 200-300 m deep continental shelf immediately adjacent to the coast, with denser AW found beneath PW in deep cross-shelf troughs and at greater depths further offshore

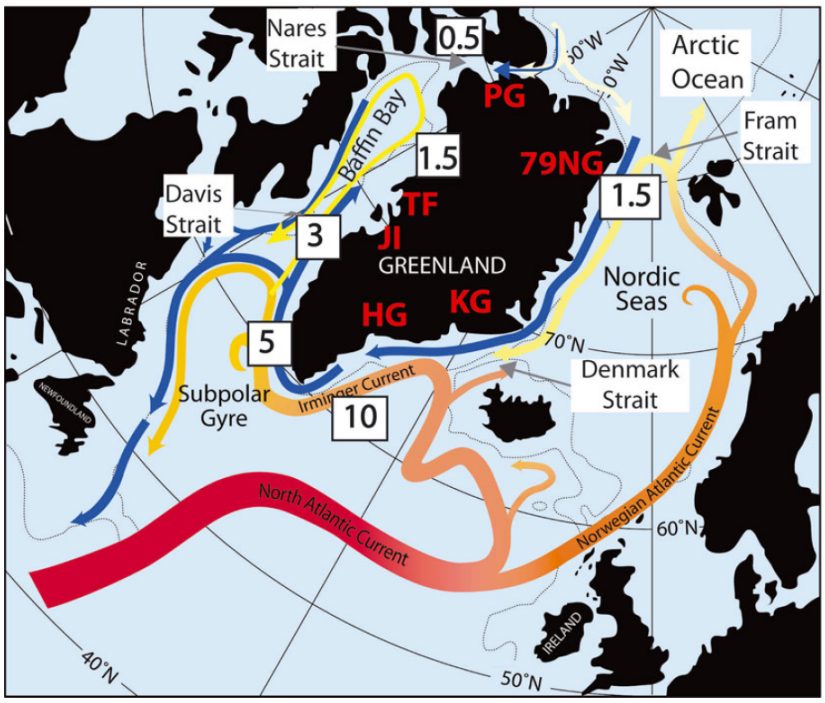

Figure 2.4: Greenland ocean setting reproduced from *Straneo et al.* (2012a). Boxed numbers indicate the typical temperature (°C) of offshore Atlantic Water. Red acronyms are HG - Helheim Glacier, KG - Kangerdlugssuaq Glacier, JI - Jakobshavn Isbrae, TF - Torssukatak Fjord, 79NG - 79 North Glacier and PG - Petermann Glacier.

(*Sutherland and Pickart*, 2008; *Våge et al.*, 2011). Thus the warmest ocean water around Greenland is the AW found at depth in south-east Greenland and subsequently south-west Greenland, with northern Greenland more insulated by cooler PW (*Straneo et al.*, 2012a).

2.2.2 Fjord water properties

Greenland's fjords (e.g. Fig. 2.5) are typically long (up to 100 km), narrow (∼5 km) and deep (>1000 m in places). Many are choked with ice mélange: a mixture of sea ice and icebergs. The waters found in Greenlandic fjords are generally similar to those described on the continental shelf, with cold and fresh PW overlying warm and dense AW (Fig. 2.5; *Straneo et al.* (2010); *Inall et al.* (2014); *Gladish et al.* (2015); *Bartholomaus et al.* (2016)). The temperature of AW found in fjords varies with the

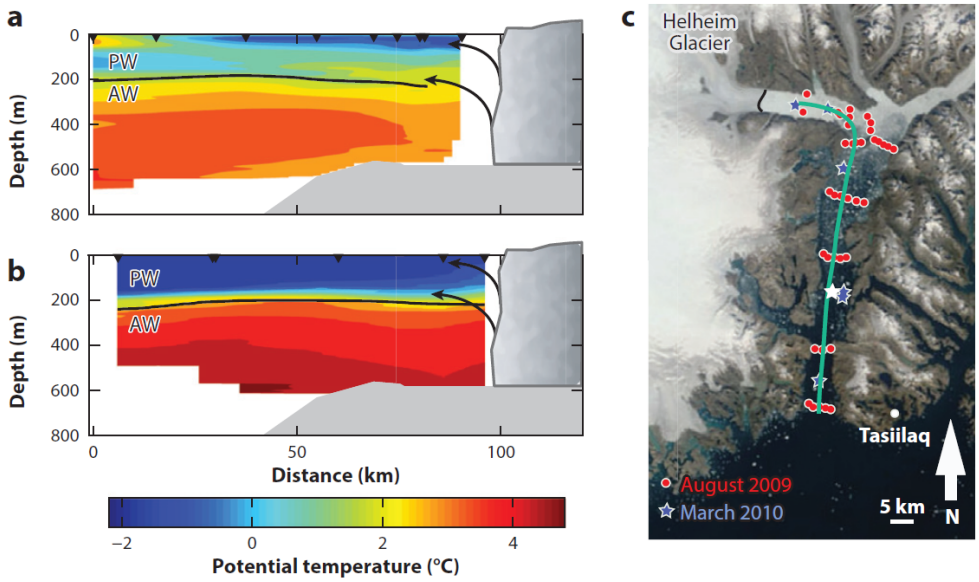

Figure 2.5: Water temperature in Sermilik Fjord, adjacent to Helheim Glacier, reproduced from *Straneo and Cenedese* (2015). Panels (a) and (b) show along-fjord sections from August 2009 and March 2010 respectively.

distance from the source of heat in the Irminger sea (Fig. 2.4), with the warmest waters (∼4°C) found in Sermilik fjord in south-east Greenland (*Straneo et al.*, 2010) and progressively cooler AW found near Jakobshavn Isbrae (∼3°C, *Gladish et al.* (2015)), Kangerdlugssuaq (∼2°C, *Inall et al.* (2014)) and Petermann (∼0°C, *Johnson et al.* (2011)).

Fjord waters are modified by the presence of a tidewater glacier. During summer, meltwater from the ice sheet surface is discharged into the fjord, often flowing down-fjord either at the fjord surface or at the PW/AW interface (*Straneo et al.*, 2011; *Sciascia et al.*, 2013; *Mortensen et al.*, 2014). Melting of the glacier calving front freshens and cools fjord water, with the cooling effect particularly significant due to the large latent heat of ice melt (*Jenkins*, 1999). By adding meltwater to the fjord surface, melting of icebergs may stratify the fjord and, in locations with significant ice mélange, keep the fjord surface close to the freezing point (*Straneo et al.*, 2011; *Gladish et al.*, 2015). Through mixing of heat, iceberg melt may also result in along-fjord cooling of AW, somewhat insulating glaciers from oceanic heat (*Inall et al.*, 2014). In

contrast, at fjords with little ice at the fjord surface, summer insolation can create very warm but shallow surface layers (*Stevens et al.*, 2016).

Key to this thesis is the potential for melting of tidewater glacier calving fronts by fjord waters. Although fjord waters are relatively cold in a global context, the in-situ pressure and salinity dependent freezing point of approximately $-2°C$ at calving fronts means that the deep AW found in Greenlandic fjords (e.g. Fig. 2.5) represents a significant source of heat available for melting of tidewater glaciers.

2.2.3 Temporal variability in ocean forcing

Subsurface waters around Greenland have generally warmed since the mid-90s, manifested as a thickening and warming of the AW layer in west and south-east Greenland (Fig. 2.6; *Myers et al.* (2007); *Straneo and Heimbach* (2013)). This change was driven by increased inflow of warm subtropical water to the north Atlantic, which has in turn been linked to large scale climate indices such as the North Atlantic Oscillation (*Hurrell*, 1995) and the Atlantic Multidecadal Oscillation (*Polyakov et al.*, 2005). Ocean reanalysis suggests a subsurface warming of 1.5°C between 1994 and 2005 in south-east and south-west Greenland and warming of 2°C between 1997 and 2005 in central and north-west Greenland (*Rignot et al.*, 2012). On the west coast, the arrival of a warm subsurface water mass migrating northwards up the coast from the Irminger Sea is seen in 1997, generating subsurface warming of $\sim$1°C in Disko Bay, adjacent to Jakobshavn Isbrae (*Holland et al.*, 2008a).

Hydrographic surveys from 1993 and 2004 inside Kangerdlugssuaq Fjord in east Greenland show a thickening and $\sim$1°C warming of the AW layer by 2004, although surveys from 1991 are the warmest of all (*Christoffersen et al.*, 2011, 2012). Data from Ilulissat Icefjord and fjord mouth, adjacent to Jakobshavn Isbrae, shows that in 2009 and 2011-2013, fjord waters were as warm as in 1997, while 2010 was likely as cold as the 1980s, displaying the potential for significant interannual variability (*Gladish et al.*, 2015). While data from the 90s and early 2000s from within fjords is sparse, the good communication observed between fjords and the continental shelf in recent years (*Jackson et al.*, 2014; *Gladish et al.*, 2015) suggests that the large scale oceanic

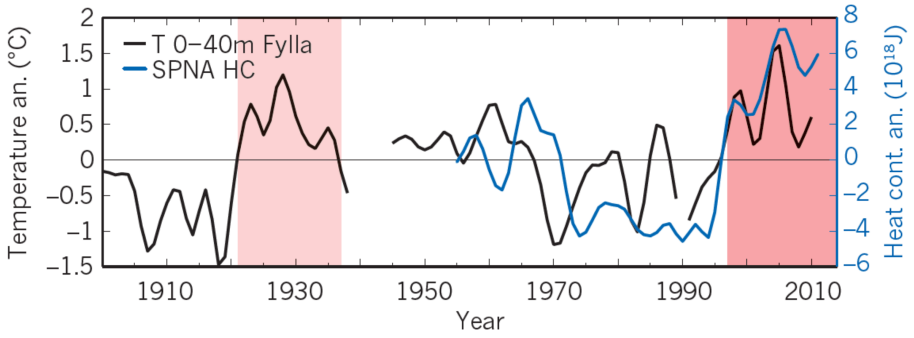

Figure 2.6: Time series of Greenland ocean heat content, reproduced from *Straneo and Heimbach* (2013): near-surface ocean temperature anomaly at Fylla Bank, west Greenland (black) and modelled heat content anomaly of the upper 700 m of the sub-polar North Atlantic (blue).

warming observed from the mid-90s will likely have propagated rapidly into fjords enabling interaction between these warmer waters and tidewater glaciers.

Ocean reanalysis provides a longer term perspective, suggesting that ocean waters in south-east Greenland were cold in the 50s and from 1970 to the mid-90s, and warm in the mid-60s and from the mid-90s onwards (*Straneo and Heimbach*, 2013; *Khan et al.*, 2014). A record of near-surface water temperature in west Greenland is as warm from 1920 to 1935 as it is today (Fig. 2.6; *Andresen et al.* (2012)).

2.2.4 Temporal variability in atmospheric forcing

The past few decades have seen increasing air temperatures and surface melting on the Greenland Ice Sheet. Following a ∼20-year period of relative stability, ice sheet annual surface air temperatures warmed by 1.8°C between 1994 and 2007 (*Box et al.*, 2009). Continuing the trend, regional climate models suggest that surface melting in the years 2007-2012, excepting 2009, was unprecedented in at least the previous 50 years (*van den Broeke et al.*, 2016). In particular, 2012 saw summer air temperatures three standard deviations above the 1979-2011 mean, resulting in the ice sheet contributing a record 1.2 mm to global sea level in 2012 (*Tedesco et al.*, 2013). With a dataset extending to 1840, *Box et al.* (2009) show that warming of similar magnitude (2.4°C) also occurred

between 1919 and 1932, coincident with the inferred warm ocean conditions described above.

Atmospheric variability in past decades, and indeed over longer timescales, therefore shows similar trends to oceanic variability. The tight coupling between atmosphere and ocean makes it hard to isolate which forcing (or perhaps a combination of the two forcings) is driving tidewater glacier dynamics.

2.3 Drivers of tidewater glacier dynamics

2.3.1 Evidence linking ice and ocean

At the broad scale, evidence for a link between the ocean and the ice sheet comes from the coincident timing of ocean and glacier change. In south-east Greenland, both ocean warming and the initiation of glacier change are observed in the mid-90s (Figs. 2.2 and 2.6; *Rignot and Kanagaratnam* (2006); *Straneo and Heimbach* (2013)). The slightly delayed onset of glacier change in west and north-west Greenland is consistent with the lagged ocean warming in the region from 1997 (*Rignot and Kanagaratnam*, 2006; *Holland et al.*, 2008a). Furthermore, the more quiescent phase of glacier dynamics in south-east Greenland from the late-2000s coincides with a stabilisation of ocean temperature, while the more sustained acceleration of glaciers in the north-west occurred under continuing elevated ocean temperature (Fig. 2.2; *Rignot et al.* (2012); *Moon et al.* (2012)).

Over the length of the east coast, examination of glacier terminus position change suggests a distinct boundary in glacier behaviour around 69°N, with glaciers south of this boundary retreating significantly between 2001 and 2005 and those north showing little change (Fig. 2.1; *Seale et al.* (2011)). The boundary at 69°N was found to coincide with a similar boundary in subsurface ocean temperature arising from the delivery of warm ocean water to south-east Greenland in the Irminger current. Looking further back, the initiation of retreat of Kangerdlugssuaq glacier from its Little Ice Age maxima and the retreated position of Helheim glacier in the early 1930s occurred during a period

of warm ocean temperatures in the upstream Irminger current (Fig. 2.4; *Andresen et al.* (2012); *Khan et al.* (2014)).

The initiation of acceleration, thinning and retreat of Jakobshavn Isbrae in 1997 has been attributed to a sudden subsurface ocean warming of ∼1°C (*Holland et al.*, 2008a; *Motyka et al.*, 2011). Assuming a linear relationship between ocean thermal forcing and submarine melt rate of the floating tongue (which is supported by theoretical studies), the sudden ocean warming in 1997 would have increased melt rates by 25% or ∼60 m/yr (*Motyka et al.*, 2011). This increase approximately accounts for the observed thinning of the ice tongue (*Thomas*, 2004), reducing buttressing of the glacier behind and ultimately leading to the break-up of the ice tongue and further acceleration and retreat (*Holland et al.*, 2008a).

Further evidence for the importance of the ocean in tidewater glacier dynamics comes from estimates of toward-glacier heat flux in proglacial fjords. Using fjord hydrography and measurements of circulation velocity, estimates of toward-glacier heat flux amount to >9 m/d of calving front melting at Yahtse Glacier (*Bartholomaus et al.*, 2013) and up to 17 m/d at LeConte Glacier (*Motyka et al.*, 2013), both in Alaska, representing a half to two-thirds of terminus ice flux. Using the same method, *Rignot et al.* (2010) estimate that calving front melting may account for 20-80% of terminus ice flux at three glaciers in west Greenland, while *Inall et al.* (2014) estimate a toward-glacier heat flux of 10 m/d (or 30-60% of terminus ice flux) at Kangerdlugssuaq Glacier. Together, these studies suggest that calving front melting by the ocean can play a very significant role in terminus mass balance, indicating that change in ocean temperature could have a significant effect on glacier dynamics. It is however worth stating that these heat flux estimates should be viewed with some caution (*Jackson and Straneo*, 2016), as will be discussed further below.

Aside from directly impacting glacier mass balance, melting of calving fronts by the ocean may promote calving of icebergs. Idealised modelling studies suggest that changing the calving front shape from vertical by ocean melting may increase calving rate (*O'Leary and Christoffersen*, 2013; *Wagner et al.*, 2016), therefore suggesting that

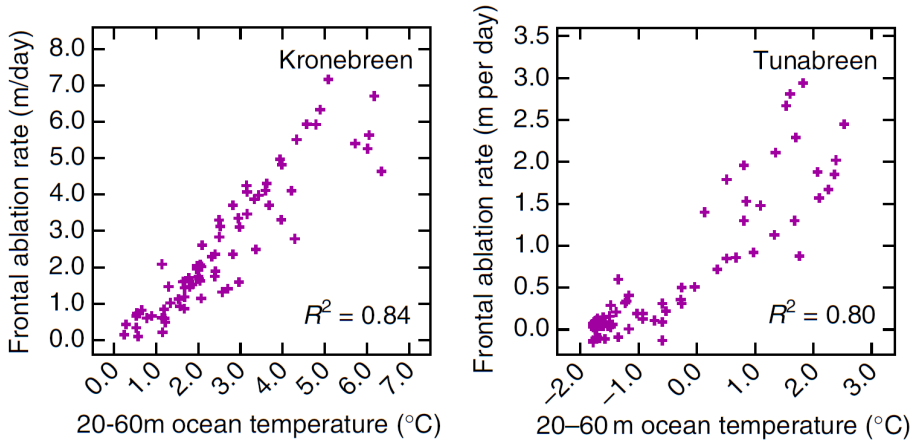

Figure 2.7: Relationship between ocean temperature and satellite-derived frontal ablation rate at two tidewater glaciers in Svalbard, reproduced from *Luckman et al.* (2015).

increased melting due to ocean warming would amplify calving and cause terminus retreat. Compelling field evidence linking the ocean to calving at tidewater glaciers comes from Svalbard, where *Luckman et al.* (2015) find very strong correlations between subsurface ocean temperature and frontal ablation rate at Kronebreen and Tunabreen (Fig. 2.7). Further background on the calving process is provided below. There is therefore much evidence, at ice-sheet and individual glacier scales, and in idealised numerical modelling, linking ocean warming to tidewater glacier acceleration, thinning and retreat.

2.3.2 Confounding factors

Despite the strong body of evidence linking tidewater glaciers to the ocean, there are also confounding factors and suggestions of a lack of feedback between the ocean and ice. Firstly, the described close coupling between atmospheric and oceanic temperatures means that much of the discussion on the coincident timing of oceanic warming and glacier response applies equally to atmospheric temperature, complicating the isolation of a dominant driver of glacier dynamics.

Statistical comparison of climate with glacier change does not elucidate a clear link. For example, *Jensen et al.* (2016) found some regional correlation between climate and the

annual area change of 42 marine-terminating glaciers around Greenland over the period 1999-2013, with glacier change in south-east Greenland correlating with sea surface temperature and sea ice concentration, and glacier change in north-west Greenland correlating with the magnitude of surface melting. For a larger glacier population of 199 and more frequent measurements of terminus position, *Murray et al.* (2015) find no significant correlation of glacier change with any of air temperature, sea surface temperature or sea ice concentration. They do, however, find a significant correlation of glacier terminus position in south-east Greenland with subsurface Irminger current temperature lagged by one year (*Murray et al.*, 2015). These large spatial and long timescale datasets do not therefore indicate a clear link between the ocean and tidewater glaciers. This may be because no such link exists, or may be related to the common use of sea surface temperature as a proxy for ocean temperature, when in fact process understanding suggests glaciers are more likely to respond to subsurface temperature (e.g. *Jenkins*, 2011; *Luckman et al.*, 2015), which may differ from sea surface temperature.

The lack of correlation of glacier dynamics with climate is embodied by the contrasting behaviour of geographically close glaciers (e.g. Fig. 2.1). For example, Umiamako Isbrae, located in west Greenland, retreated by 4 km and more than doubled in velocity between 2000 and 2010 (*Howat et al.*, 2010; *McFadden et al.*, 2011). Store Glacier, located ∼150 km south and connected to the same fjord system, and therefore experiencing similar air and ocean temperatures, showed essentially no change in terminus position or velocity over the same period (*Howat et al.*, 2010). This glacier-specific response to a similar forcing has been attributed to topography and specifically, variations in fjord/glacier width and bed topography. Study of the terminus position of 10 glaciers in north-west Greenland between 2001 and 2005 suggests that rapid retreat is promoted by the loss of contact with lateral or basal pinning points and by significant widening of the fjord during retreat (*Carr et al.*, 2013), conclusions which are also supported by flowline glacier modelling (*Enderlin et al.*, 2013). Furthermore, theoretical considerations (*Schoof*, 2007), flowline modelling of real glaciers (*Nick et al.*, 2013) and observations (*Joughin and Smith*, 2013) all suggest that once terminus retreat

is initiated, tidewater glaciers retreat very rapidly down reverse bed slopes. These considerations indicate that glacier-specific geometry will modulate a glacier's response to climate forcing, so that oceanic or atmospheric warming should perhaps be seen as a perturbation to the glacier, with the magnitude of response ultimately determined by glacier geometry. These glacier specific factors may explain why adjacent glaciers respond very differently to the same climate forcing, and why correlation of terminus position with climate has limited success.

A further complication to the evidence linking ice and ocean comes from numerical modelling of large tidewater glaciers in Greenland. Three studies present full-Stokes flowline modelling of large Greenlandic tidewater glaciers, incorporating submarine melting of glaciers by the ocean (*Cook et al.*, 2014; *Todd and Christoffersen*, 2014; *Krug et al.*, 2015). All three find that submarine melting at reasonable rates has little effect on terminus position and glacier dynamics. It is only by increasing submarine melt rates to over 20 m/d, a rate which is not currently supported by the literature, that the model of Helheim glacier shows significant response (*Cook et al.*, 2014). Furthermore, a vertically-integrated plan-view model of Store Glacier suggests that a submarine melt rate of 12 m/d, approximately a factor of 4 larger than suggested by heat flux estimates, is required to initiate glacier retreat (*Rignot et al.*, 2010; *Morlighem et al.*, 2016). These models therefore find little role for submarine melting in the dynamics of the modelled glaciers. There are, however, reasons to remain cautious about the conclusions from these studies. The effect of concentrating high rates of submarine melting in one location on a calving front has not yet been investigated due to the difficulties of simulating calving in three dimensions. The range of glaciers which have been modelled remains limited, with all of the above studies focussing on large, fast-flowing glaciers. Furthermore, all of the above models apply some variant of a stretching-threshold based calving law (*Benn et al.*, 2007), which may not capture the possible coupling between submarine melting and calving.

2.3.3 Other potential drivers of tidewater glacier dynamics

There are a number of other possible drivers of rapid change at tidewater glaciers. Leading candidates include increasing basal lubrication and changes in backstress from ice mélange and sea ice. Considering first basal lubrication, the role of water at the ice-bed interface in modulating ice velocity has long been studied in Alpine systems (e.g. *Iken and Bindschadler*, 1986) and over the past decade at land-terminating glaciers in Greenland (*Zwally et al.*, 2002; *Bartholomew et al.*, 2010). These land-terminating systems undergo short-term increases in ice velocity in response to increased surface melting, but ice velocities often subsequently decrease due to the establishment of efficient subglacial drainage pathways which result in decreasing subglacial water pressure (e.g. *Cowton et al.*, 2013).

Despite increasing atmospheric temperature and ice sheet surface melting in recent decades, annual ice velocity at land-terminating systems in Greenland has decreased (*Tedstone et al.*, 2015). This is thought to result from the persistence of efficient subglacial drainage into the winter months, leading to widespread dewatering of the ice-bed interface, such that warm summers with high ice velocity are compensated by decreased ice flow in the following winter (*Sole et al.*, 2013; *Tedstone et al.*, 2013). At land-terminating margins therefore, increasing atmospheric temperature has not resulted in interannual glacier acceleration. The applicability of these results to tidewater glaciers, however, remains uncertain.

At marine-terminating KNS, *Sole et al.* (2011) show that ice velocity >35 km from the calving front responds to surface melting in a similar fashion to land-terminating margins. Subsequent observations would appear to extend this conclusion to within a few kilometres of the terminus (*Ahlstrom et al.*, 2013; *Moon et al.*, 2014). A study of seasonal evolution of ice velocity at a large number of tidewater glaciers around Greenland shows that some exhibit land-terminating glacier-type behaviour with late summer deceleration, while at others ice velocity scales with surface melting (*Moon et al.*, 2014). Glacier Perito Moreno in Patagonia - though freshwater lake-terminating rather than tidewater - appears to be of the latter type; an excellent correlation is

obtained between air temperature and ice velocity (*Sugiyama et al.*, 2011). The role of subglacial hydrology in modulating tidewater glacier velocity is further complicated by calving front processes such as terminus retreat. *Joughin et al.* (2008b) show that at Jakobshavn Isbrae, the terminus position exerts a greater control on ice velocity than surface melting.

There are theoretical reasons to suspect that subglacial hydrology may differ between marine and land-terminating systems. Simple models of subglacial hydrology consider drainage through channels and cavities under basal sliding (e.g. *Schoof*, 2010). The threshold separating drainage in channels and cavities, and thus low and high basal water pressure respectively, is found to depend on the magnitude of subglacial discharge and the sliding velocity (*Kamb*, 1987; *Fowler*, 1987; *Schoof*, 2010). High discharge and little sliding favours drainage through channels while low discharge and rapid sliding favours drainage through cavities. One can therefore argue that the rapid basal sliding near the calving fronts of tidewater glaciers might inhibit the formation of efficient subglacial channels, such that drainage occurs predominantly through inefficient cavities and that ice velocity will therefore scale with surface melting.

Such arguments may explain the observations of *Sugiyama et al.* (2011) from Glacier Perito Moreno. The arguments are also supported by satellite observations of Helheim Glacier, which show seasonal dynamic thinning of nearly 20 m, apparently driven by surface melting and increased basal lubrication rather than by terminus retreat (*Bevan et al.*, 2015). *Pfeffer* (2007) theorise that such a mechanism can lead to irreversible glacier retreat if during thinning the loss of bed traction exceeds the loss of driving stress. This offers an alternative mechanism driving tidewater glacier retreat in Greenland; greater surface melting increases basal lubrication, resulting in dynamic thinning which is either itself a runaway process (*Pfeffer*, 2007) or may increase buoyancy-driven calving (*James et al.*, 2014).

The role of basal lubrication in modulating interannual velocity change at tidewater glaciers remains highly uncertain. Together, the above studies suggest that while ocean forcing may be the current leading hypothesis for initiating recent change at tidewater

glaciers around Greenland, there may yet be a role for increased basal lubrication resulting from increased surface melting as an alternative or complementary factor.

There is much evidence that the presence or absence of sea ice and ice mélange in the proglacial fjord plays a role in tidewater glacier dynamics. Based on five years of velocity, terminus position and mélange observations at 16 glaciers in north-west Greenland, *Moon et al.* (2015) find a strong correspondence between glacier dynamics and mélange conditions, with strong and rigid mélange associated with glacier slow-down and advance, and open water (the absence of mélange) associated with acceleration and retreat. At Kangerdlugssuaq Glacier in south-east Greenland, *Christoffersen et al.* (2012) note that ice mélange and sea ice was absent from Kangerdlugssuaq Fjord during winter 2004/2005. These highly unusual fjord conditions were linked to a particularly warm and windy winter, and it is hypothesised that the lack of ice mélange led to the coincident rapid retreat of 7 km (*Christoffersen et al.*, 2012).

Models also support the hypothesis that ice mélange plays an important role in terminus stability; the afore-mentioned full-Stokes flowline models suggest that the presence or absence of ice mélange exerts a greater control on glacier dynamics than submarine melting (*Todd and Christoffersen*, 2014; *Krug et al.*, 2015). In these models, the backstress exerted on the glacier by the ice mélange helps to balance the driving stress, reducing longitudinal stretching and therefore, by the calving criteria used, inhibiting calving. Over the decadal timescales of tidewater glacier change in Greenland, it could therefore be the case that increased air and ocean temperatures have restricted sea ice growth and/or loosened ice mélange, reducing backstress on tidewater glaciers and leading to widespread acceleration and retreat.

In summary, recent decades in Greenland have been a time of substantial change, both in terms of climate (Fig. 2.6) and ice sheet dynamics (Figs. 2.1 and 2.2). It is clear from the widespread and synchronous nature of change at Greenland's tidewater glaciers that they have responded to a climatic forcing; identifying this forcing and elucidating the processes responsible is however challenging. At present, the leading hypothesis

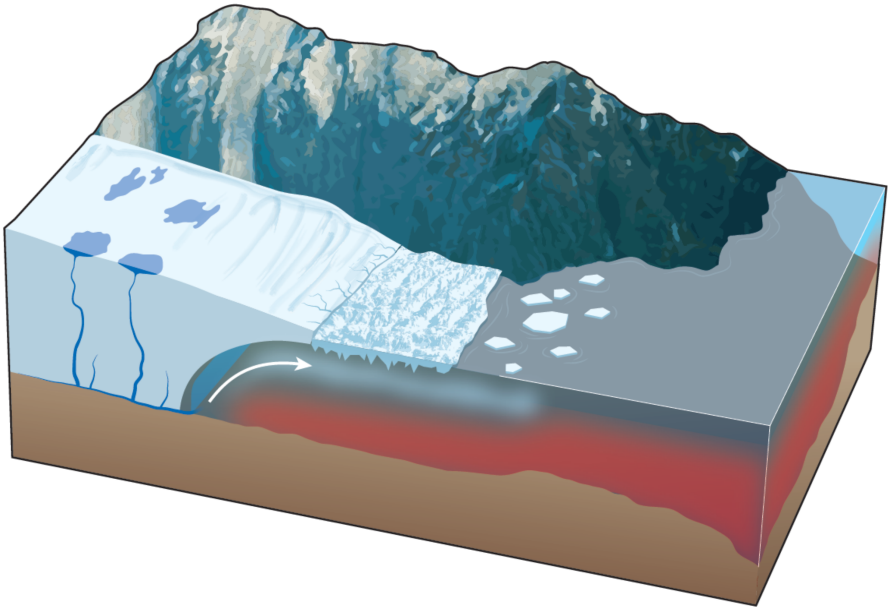

Figure 2.8: Schematic of ice-ocean interaction processes, adapted from *Straneo and Heimbach* (2013). The white arrow represents the rising buoyant plume.

links the ocean with the ice sheet, possibly by submarine melting of tidewater glacier calving fronts. As discussed, there are however other potentially important factors. What is clearly lacking is a detailed understanding of the processes through which climatic change impacts tidewater glacier dynamics. This thesis aims to address one such process in detail, that of submarine melting, and this background section now focusses on ice-ocean interaction and submarine melting.

2.4 Ice-ocean interaction processes

2.4.1 Plumes

During the Greenland summer, large volumes of meltwater from the ice sheet surface penetrate the ice through crevasses and moulins to enter the subglacial hydrological system at the ice-bed interface (Fig. 2.8). Once beneath the ice, water generally flows towards the ocean, in a direction defined by both the bed topography and the ice thickness (*Shreve*, 1972). As touched on above, subglacial water may flow through

Figure 2.9: Example surface expressions of plumes at Kangiata Nunata Sermia, south-west Greenland. Images from *Sole et al.* (2011) with (a) taken on 12 July 2009 and (b) on 19 July 2009.

arborescent and efficient subglacial channels, evacuating water rapidly and at low pressure, or through inefficient linked cavities or subglacial till, transporting water slowly and at high pressure (e.g. *Fountain and Walder*, 1998). At a tidewater glacier, either system will eventually release water into the ocean at the grounding line at the base of the calving front (Fig. 2.8).

Plumes form adjacent to calving fronts where this subglacial discharge is released into the ocean (Figs. 2.8 and 2.9). The dynamics of such plumes have now been studied in detail using two modelling approaches. The first uses buoyant plume theory (e.g. *Jenkins*, 2011; *Cowton et al.*, 2015; *Slater et al.*, 2016; *Carroll et al.*, 2016), a simple and computationally cheap method of capturing plume dynamics. An alternative is to use a general circulation model (*Xu et al.*, 2013; *Sciascia et al.*, 2013; *Kimura et al.*, 2014; *Carroll et al.*, 2015; *Slater et al.*, 2015); a flexible but more complex approach.

These two approaches are introduced in more detail in Chapter 3. Together, the above studies encapsulate the following qualitative description of plume dynamics.

Being derived from melting of the ice sheet surface, the subglacial discharge emerging from the grounding line has low salinity. In contrast, the ocean into which this water emerges is salty and dense. The subglacial discharge is thus highly buoyant and will rise towards the fjord surface as a buoyant plume (Fig. 2.8). The shear in water velocity, which results between the rapidly rising subglacial discharge and still ambient fjord water, generates turbulent mixing at the edges of the plume, so that the plume entrains surrounding fjord water. The volume flux of the plume therefore grows as it rises, diluting the buoyancy of the plume. If the fjord is stratified, so that the fjord water density (as defined by the temperature and salinity) increases with depth, the plume and ambient water densities may become equal at some depth termed the neutral buoyancy level. Above this level the buoyancy of the plume reverses, but momentum ensures it continues rising, eventually slowing and reaching a maximum height before flowing away from the glacier (Fig. 2.10).

Many of the afore-mentioned studies show that the neutral buoyancy level and height reached by the plume increase with the magnitude of subglacial discharge initiating the plume (e.g. Fig. 2.10). *Carroll et al.* (2015) further show that plumes will often find neutral buoyancy at a strong pycnocline - a depth at which the fjord water density changes rapidly - as is often found in Greenlandic fjords at the interface between the AW and PW (e.g. *Sciascia et al.*, 2013). The height reached by a plume is therefore determined by the magnitude of subglacial discharge and the fjord stratification. Based on this understanding, three possible situations arise. For small subglacial discharges and strongly stratified, deep fjords, plumes will not reach the fjord surface (Fig. 2.10, left and centre). In the intermediate case, a plume may reach the fjord surface but be denser than the fjord surface water, and will therefore subduct as it flows away from the glacier (Figs. 2.9a and 2.10, right). Finally, for high subglacial discharges and weakly stratified, shallow fjords, plumes may often reach the surface and be less dense than the fjord surface water, enabling the plume to remain at the surface as it flows away from the glacier (Fig. 2.9b).

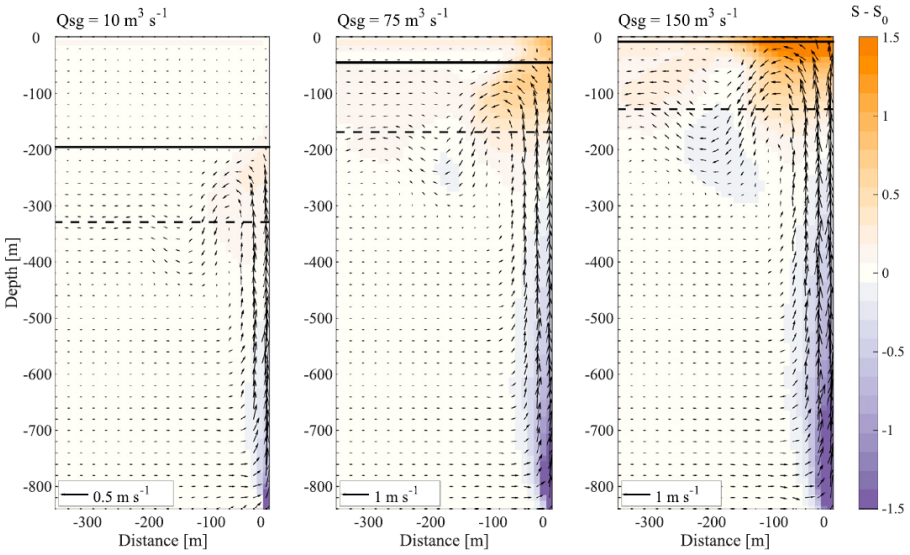

Figure 2.10: Modelled plume dynamics for three subglacial discharges, reproduced from *Carroll et al.* (2015). Left and centre: weak plumes which do not reach the fjord surface. Right: strong plume which reaches the fjord surface but is denser than ambient surface water so subducts as it flows away from the glacier. Solid lines indicate maximum height reached by the plume, dashed lines are the neutral buoyancy level. Colours indicate difference between plume and ambient salinity.

It is clear that the density of the plume plays a key role in its dynamics. Plume density is in turn determined by its temperature and salinity (e.g. *Fofonoff and Millard*, 1983). In fact, within the range of water temperature and salinity encountered in Greenland, density is largely controlled by salinity (e.g. *Jenkins*, 2011). Plume temperature is instead a key control on submarine melt rate, as will be described below. Plume modelling (e.g. *Carroll et al.*, 2015) suggests the following description of plume temperature and salinity. At the grounding line, water in the plume is assumed to be purely subglacial discharge and is therefore at the in-situ freezing point and has zero salinity. Turbulent entrainment of ambient fjord water increases the temperature and salinity of the plume as it rises (Fig. 2.10). The entrained water is subsequently advected (vertically) within the plume, so that the plume transports deep water towards the fjord surface. Since fjords in Greenland often contain warm salty water at depth and cold fresh water at the surface, plumes can therefore bring anomalously warm and

salty water to the fjord surface (Fig. 2.10; *Carroll et al.* (2015)). Alternatively, where fjord surface water has been warmed by solar insolation, plume water may appear as a cold anomaly at the fjord surface (*Mankoff et al.*, 2016).

Much of this description of plume dynamics is based on modelling rather than data; observations of water velocities and properties from within plumes in Greenland are rare due to the difficulties of collecting data from these highly turbulent and dangerous regions of the fjord. *Bendtsen et al.* (2015) present a single CTD cast from a plume adjacent to KNS in south-west Greenland. This cast showed anomalously warm and saline surface water, consistent with the vertical transport and overshoot of deep water within the plume. The subglacial discharge content of the plume at the surface was 7%, indicative of significant dilution by entrainment of ambient fjord water. Perhaps the most detailed observations of a plume to date come from Sarqardleq Fjord (*Mankoff et al.*, 2016), data which includes velocity, temperature and salinity from either inside the plume itself or within the surface expression of the plume. These data again confirm the dilution of subglacial discharge (which comprises 10% volume in this case), and show that the submarine meltwater content of the plume is likely less than 0.1%. These limited datasets show qualitative agreement with models of plume dynamics, but are not yet of sufficient detail to rigorously interrogate key parameterisations within plume models, such as for the rate of entrainment or submarine melting.

A particularly poorly understood aspect of glacial plumes is the spatial pattern of emergence of subglacial discharge at the grounding line (i.e. whether subglacial discharge emerges in a focussed or more diffuse fashion). Some clues are offered by the turbid expression of plumes on the fjord surface. Approximately half conical, well-confined surface expressions (*Mankoff et al.* (e.g. 2016); Fig. 2.9a) may be taken as evidence of focussed delivery of subglacial discharge into the fjord. Furthermore, recent side-scan sonar surveys of calving fronts in west Greenland show deeply incised, narrow chimney features which are likely created by plume-enhanced submarine melting (Fig. 2.11; *Fried et al.* (2015); *Rignot et al.* (2015)), again indicative of focussed delivery of subglacial discharge. On the other hand, turbid surface water occupying a significant

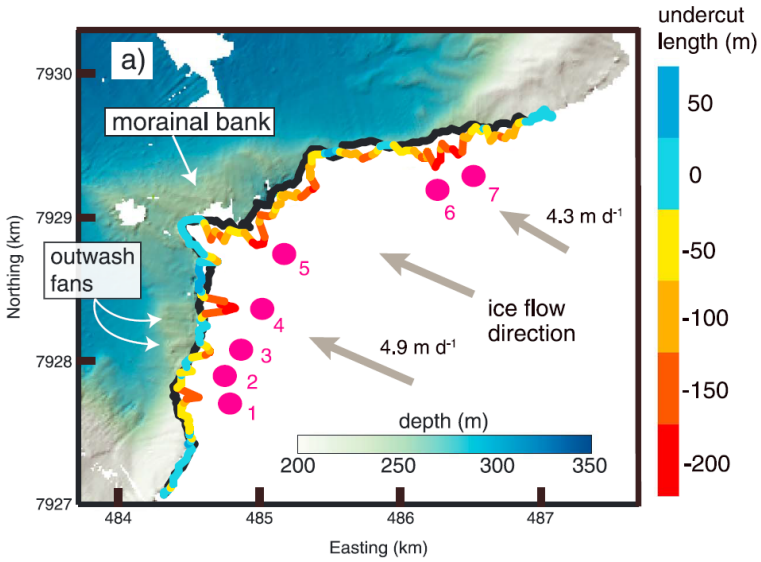

Figure 2.11: Calving front undercutting at Kangerlussuup Sermia, west Greenland, reproduced from *Fried et al.* (2015). Black line indicates location of calving front at the fjord surface, while the coloured line illustrates the subsurface ice topography.

width of the calving front (e.g. Fig. 2.9b) might be taken as evidence of much more diffuse subglacial drainage.

The importance of plumes in the topic of ice-ocean interaction is twofold. Plumes drive high water velocities adjacent to the calving front thereby significantly influencing submarine melt rates. Plumes are also, however, an integral driver of wider fjord circulation.

2.4.2 Fjord circulation

Fjord circulation provides an essential link between the ice sheet and the ocean, responsible for transporting the warm AW from the continental shelf and fjord mouth up to glaciers at the fjord head, and for the renewal of fjord waters; in the absence of this renewal, melting of ice would eventually cool the fjord to the freezing point.

Several classifications of circulation have been proposed and observed to operate in glacial fjords (e.g. *Straneo and Cenedese*, 2015). The first, buoyancy-driven circulation,

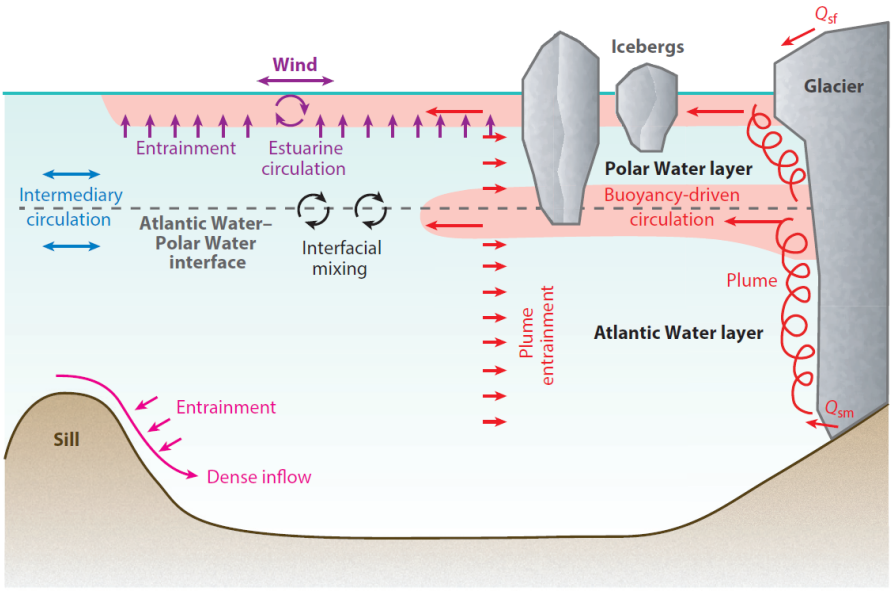

Figure 2.12: Fjord circulation schematic, reproduced from *Straneo and Cenedese* (2015), illustrating the key circulation types (buoyancy-driven and intermediary).

is driven by plumes initiated by subglacial discharge. The entrainment of surrounding fjord water into these plumes pulls water towards the glacier at depth, while water from the plume itself flows away from the glacier closer to the fjord surface (Figs. 2.8, 2.10 and 2.12). This circulation is perhaps most obviously illustrated by water velocity observations from in front of LeConte Glacier in Alaska (*Motyka et al.*, 2013), while it has also been observed at a couple of smaller glaciers in west Greenland (*Rignot et al.*, 2010). A slight variant on the described mechanism may occur at deep and strongly stratified fjords. In such fjords, plumes often find neutral buoyancy and flow away from the glacier at some depth below the surface, leaving room for a second circulation cell above (Figs. 2.5 and 2.12; *Straneo et al.* (2011); *Sutherland and Straneo* (2012); *Sciascia et al.* (2013)). Note that while in summer months the buoyancy source driving this circulation is provided by subglacial discharge originating from surface melting, a similar (albeit weaker) circulation may continue to operate in winter due to the emergence of subglacial meltwater produced by basal friction (*Christoffersen et al.*, 2012) and due to the buoyancy provided by continued submarine melting of the calving front (e.g. *Sciascia et al.*, 2013).

A second form of circulation is 'intermediary circulation', in which water density differences between the fjord and shelf drive rapid exchange of water throughout the fjord (Fig. 2.12). This circulation is thought to be particularly active during winter in Sermilik and Kangerdlugssuaq fjords in south-east Greenland (*Jackson et al.*, 2014). Here, strong along-shore winds depress isopycnals at the fjord mouth, resulting in a density gradient between the fjord and shelf which drives water from the shelf towards the glacier near the surface, and water from the fjord out to the shelf at depth. Once winds relax, the opposite circulation may occur to restore equilibrium (*Straneo et al.*, 2010; *Jackson et al.*, 2014). Moorings located in Sermilik and Kangerdlugssuaq fjords over winter suggest that this mechanism drives rapid exchange between fjord and shelf, characterised by pulses of water velocity exceeding 0.5 m/s, periodically reversing on timescales of several days (*Jackson et al.*, 2014). These pulses can exchange upwards of 25% of the fjord volume (*Jackson et al.*, 2014; *Cowton et al.*, 2016), though *Cowton et al.* (2016) suggest that the exchange happens mostly in the outer part of the fjord, with the effect diminished at the fjord head where the glacier is located. While the focus has been on along-shore winds as a source of intermediary circulation, other drivers of shelf variability, for example due to larger-scale ocean dynamics might also result in fjord-shelf density contrast and drive similar exchange.

Mortensen et al. (2011) find evidence for two additional circulation modes operating in Godthåbsfjord, a fjord system in west Greenland characterised by several shallow sills. The first stems from periodic inflows of dense water from the shelf into the fjord (Fig. 2.12). The second is a form of intermediary circulation where along-fjord density gradients are set up by intense tidal mixing of the water column over the shallow sills. Further possible drivers of fjord circulation which have not received much attention in the literature include terrestrial runoff and along-fjord winds (Fig. 2.12).

The prevalence of the described forms of circulation in fjords around Greenland, and their importance in the delivery of warm water to tidewater glaciers remains unclear. Certainly, all tidewater glaciers around Greenland experience seasonal surface melting and therefore buoyancy-driven circulation will widely operate in summer, at least close to tidewater glaciers. Down-fjord and in winter, the influence of subglacial discharge is

diminished and shelf-driven circulation may play a greater role. Numerical modelling of Kangerdlugssuaq Fjord suggests that while buoyancy-driven circulation is weaker in terms of flow velocity than intermediary circulation, it is consistent over time and therefore more effective at transporting water all the way to the calving front, at least during summer months (*Cowton et al.*, 2016). The presence of shallow sills is also likely to influence circulation dynamics (*Mortensen et al.*, 2011; *Jackson et al.*, 2014). For example, in Ilulissat Icefjord (into which flows Jakobshavn Isbrae), the entrance sill blocks the warmest AW from reaching the glacier and disrupts possible intermediary circulation (*Gladish et al.*, 2015).

Returning to the importance of fjord circulation, the described modes provide a means for transporting warm water up-fjord to drive submarine melting of tidewater glaciers. For deep-silled fjords, the combination of buoyancy-driven and intermediary circulation appears to keep the fjord and shelf in good communication (e.g. *Jackson et al.*, 2014), so that warm AW on the shelf has easy access to the calving fronts of tidewater glaciers. Shallow sills may impede this communication, to a certain extent isolating the fjord from the shelf so that water within the fjord may be somewhat cooler than outside (e.g. *Mortensen et al.*, 2013; *Gladish et al.*, 2015).

2.4.3 Submarine melting

The key process studied throughout this thesis and, as described above, the leading contender for a driver of tidewater glacier retreat, is submarine melting. Submarine melting refers to melting of ice by the ocean both at the near-vertical calving fronts of tidewater glaciers and beneath floating ice tongues and ice shelves. Submarine melting occurs when water above the pressure and salinity-dependent freezing point encounters submerged ice (*Jenkins*, 1999). Melting also however requires water motion to drive the transfer of heat from ocean to ice (*Holland and Jenkins*, 1999). The source of motion may be the melting itself, which introduces buoyant meltwater into the ocean and drives 'melt-driven convection' (*Magorrian and Wells*, 2016). Plumes initiated by subglacial discharge (Fig. 2.10) provide an alternative source of motion. High water velocities in these plumes can drive rapid submarine melting termed 'convection-driven

melt' (*Jenkins*, 2011). Further sources of motion may include wider fjord circulation or tides (e.g. *Jenkins et al.*, 2010). The dominant source of motion may also vary from location to location and from season to season. Antarctic ice shelves are low discharge environments where tides and melt-driven convection are dominant. In contrast, the high subglacial discharge experienced in summer by tidewater glaciers is likely to be the dominant source of water motion through initiation of plumes and wider fjord circulation, though there may still be a role for melt-driven convection away from plumes or in winter.

Observations of submarine melting

Due to the extreme difficulty and danger inherent in surveying calving fronts, there have been no direct observations of submarine melting at the near-vertical calving fronts of tidewater glaciers. Estimates of submarine melting at these systems have, to date, relied on inference based on fjord hydrography and circulation or on calving front evolution. In the first method, detailed knowledge of fjord temperature, salinity and velocity at an across-fjord section (or 'flux gate') can in theory be combined to calculate a net toward-glacier heat flux. This net heat flux may then be converted to a submarine melt volume and thereafter a submarine melt rate by dividing the estimated melt volume by the submerged calving front area. This method has seen extensive use, resulting in melt rate estimates of 1.8 m/d and 10 m/d at Helheim and Kangerdlugssuaq Glaciers, east Greenland (*Sutherland and Straneo*, 2012; *Inall et al.*, 2014); 0.7-5 m/d at five glaciers in west Greenland (*Rignot et al.*, 2010; *Xu et al.*, 2013); and respectively 9-17 m/d and >9 m/d at LeConte and Yahtse Glaciers in Alaska (Fig. 2.13; *Motyka et al.* (2003, 2013); *Bartholomaus et al.* (2013)).

There are, however, compelling reasons to view these flux gate estimates with caution. The measured fjord hydrographies are usually just snapshots of systems which show significant variability on short timescales (*Motyka et al.*, 2013; *Jackson et al.*, 2014), so that it is not clear how the estimated melt rate may be indicative of the longer-term forcing experienced by the glacier. Furthermore, sparse data is often spatially extrapolated, neglecting the potentially complex and three-dimensional nature of fjord

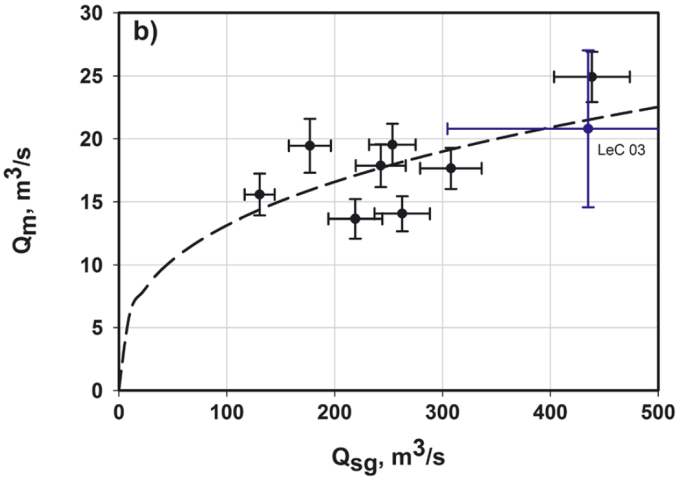

Figure 2.13: Relationship between modelled subglacial discharge Q_{sg} and fjord heat flux-estimated submarine melt rate Q_m at LeConte Glacier, Alaska, reproduced from *Motyka et al.* (2013).

circulation (e.g. *Rignot et al.*, 2010). Finally, these estimates assume that all of the calculated heat flux is used for submarine melting of the calving front. In reality, a significant proportion may be lost to melting of proglacial ice mélange (*Enderlin et al.*, 2016), or simply re-exported from the fjord at a later time. A rigorous analysis of heat flux estimates has been conducted by *Jackson and Straneo* (2016). They emphasize the great difficulty of constraining heat budgets and note the importance of temporal averaging (to account for temporal variability) and the potential re-export of heat, factors largely neglected in the above studies. In an application to Sermilik fjord (containing Helheim glacier), the net toward-glacier heat flux is indistinguishable from zero in winter, and equivalent to 1500±500 m^3/s of submarine meltwater in late summer (*Jackson and Straneo*, 2016).

An alternative method of investigating melt rates is to track terminus position and assume that what happens above the water is in some way representative of the submerged part of the calving front. The afore-mentioned study of *Luckman et al.* (2015) calculated frontal mass loss as the difference between ice velocity and terminus position change. If the same losses occur underwater, and are assumed to occur entirely by submarine melting (as is supported by observations suggesting infrequent subsurface

calving), then the above-water frontal mass loss gives an estimate of submarine melt rate. Application of this technique suggests a seasonally variable submarine melt rate of 0-8 m/d at three glaciers in Svalbard (Fig. 2.7; *Luckman et al.* (2015)). A similar technique is employed by *Fried et al.* (2015), who additionally present terminus morphology from side-scan sonar at Kangerlussuup Sermia in west Greenland (Fig. 2.11), giving maximum melt rates of 3.7 m/d and a calving front average of 2 m/d. These methods are only useful for estimating submarine melt rate at glaciers with infrequent subsurface calving. The fastest-flowing glaciers in Greenland, moving at rates >15 m/d, are dominated by full-depth calving (e.g. *James et al.*, 2014), so that melt rate cannot be estimated using this technique.

In spite of the difficulties of quantifying melt rate, one may draw qualitative conclusions from the side-scan sonar surveys of calving fronts (*Fried et al.*, 2015; *Rignot et al.*, 2015). These studies show extensively undercut calving fronts with deeply incised narrow chimney features (Fig. 2.11), measuring a few hundred metres in width and extending several hundred metres beneath the glacier. These chimney features align with predicted subglacial drainage pathways and therefore provide strong evidence that plumes drive rapid submarine melting and enhance melt rate relative to adjacent sections of calving front not in contact with a plume.

Estimates of submarine melting beneath ice shelves, ice tongues and icebergs may be more reliable. Melt rates beneath ice shelves and ice tongues may be calculated based on ice flux divergence, a technique which has seen extensive application in Antarctica (e.g. *Rignot et al.*, 2013) and Greenland (e.g. *Enderlin and Howat*, 2013). Submarine melt rates beneath the now-disintegrated ice tongue of Jakobshavn Isbrae were estimated at 0.6 m/d in 1984-1985 (*Motyka et al.*, 2011). *Rignot and Steffen* (2008) calculate maximum melt rates of 0.1 m/d beneath Petermann Glacier in northern Greenland. For 13 glaciers around Greenland in the period 2000-2010, *Enderlin and Howat* (2013) infer submarine melt rates varying from 0.03 m/d (Petermann Glacier) to 3 m/d (Jakobshavn Isbrae ice tongue). Furthermore, ice mélange melt rates in the range 0.1-0.8 m/d have recently been estimated using repeat high-resolution DEMs (*Enderlin et al.*, 2016). Focussing on Helheim Glacier, the same study estimates the submerged surface area

of the proglacial ice mélange to lie in the range 132-261 km^2, at least an order of magnitude larger than the calving front surface area. This huge surface area leads to total meltwater flux estimates of 126-494 m^3/s, confirming the suggestion that a large fraction of toward-glacier heat flux in the fjord may result in iceberg melting rather than calving front melting.

Modelling of submarine melting

Modelling of submarine melting (e.g. Fig. 2.14) provides a complementary approach, using the previously introduced buoyant plume theory or general circulation models to estimate water velocity, temperature and salinity adjacent to the calving front. These properties are converted to a melt rate using a submarine melt rate parameterisation (*Holland and Jenkins*, 1999) which accounts for the turbulent transfer of heat and salt between the ice and ocean. Under the most commonly used 'three-equation' melt parameterisation (*Holland and Jenkins* (1999); see also section 3.3 below), melt rate increases with both water velocity and temperature, which increase the turbulent transfer of heat. Melt rates also increase weakly with salinity and depth due to the dependence of the melting point on salinity and pressure (*Holland and Jenkins*, 1999).

Considering first convection-driven melt, in which the source of water motion is the release of subglacial discharge at the grounding line, numerous studies have investigated the effect on melting of subglacial discharge, water temperature, and subglacial channel geometry. Absolute values of modelled melt rate vary strongly with these factors, from minimum values of <0.1 m/d (e.g. *Sciascia et al.*, 2013) for low subglacial discharges to maximum values exceeding 10 m/d for high subglacial discharges in warm fjords (Fig. 2.14a; *Carroll et al.* (2016)). These factors are now discussed in turn.

Submarine melt rate (both spatially averaged and at a given location) is found to respond sub-linearly to increasing subglacial discharge, regardless of the geometry of the subglacial channel (e.g. Fig. 2.14b). Models in which across-fjord variability in dynamics is neglected (i.e. 2D or 'flowline' models) suggest submarine melt rate increases with the magnitude of subglacial discharge raised to the power 1/3 (*Jenkins*, 2011; *Xu et al.*, 2012) or 1/3 to 1/2 (*Sciascia et al.*, 2013). Models taking account

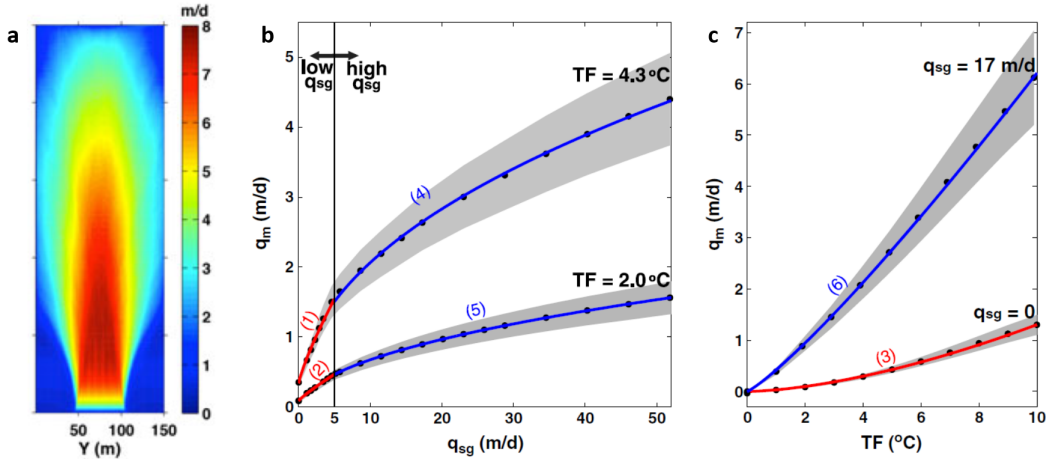

Figure 2.14: Modelled submarine melt rates in a general circulation model: (a) face-on view of the calving front with colours indicating submarine melt rate; (b) modelled relationship between submarine melt rate q_m and subglacial discharge q_{sg} for two fjord temperature profiles; (c) modelled relationship between submarine melt rate q_m and fjord temperature TF for two subglacial discharges. Figures adapted from *Xu et al.* (2013).

of across fjord variability (i.e. 3D general circulation models or conical plume models) suggest a similar relationship where the exponent takes a value 0.5-0.9 (Fig. 2.14b; *Xu et al.* (2013)) and ∼1/3 (*Kimura et al.*, 2014).

Most studies find that melt rate responds approximately linearly to increasing water temperature for convection-driven melt, regardless of plume geometry (*Jenkins*, 2011; *Xu et al.*, 2012; *Sciascia et al.*, 2013). *Xu et al.* (2013) suggest a slightly more sensitive relationship where melt rate scales with water temperature raised to the power 1.2-1.6 (Fig. 2.14c). Investigations of the sensitivity of melt rate to the shape of the subglacial channel suggest that total submarine melt rate increases by 15-40% if a wide (rather than narrow) subglacial channel is assumed (*Xu et al.*, 2013; *Kimura et al.*, 2014).

Models also illuminate spatial patterns in submarine melt rate. Melt rates are found to be substantially elevated above subglacial channels where plumes are in contact with the calving front, and are generally highest in the core of the plume where water velocities are highest (Fig. 2.14a; *Xu et al.* (2013); *Kimura et al.* (2014)). There is

often a region of lower melting close to the grounding line where plumes retain the cold signature of the emerging subglacial discharge (Fig. 2.14a; *Xu et al.* (2012); *Sciascia et al.* (2013); *Xu et al.* (2013); *Kimura et al.* (2014); *Carroll et al.* (2016)). Excepting this region, and in models which use stratified fjord conditions, melt rates are generally higher at depth due to (i) higher water temperature at depth, (ii) the slowing of the plume with height as it encounters less dense surface water and (iii) for 3D models, the slowing of the plume due to entrainment of ambient water (*Xu et al.*, 2012; *Sciascia et al.*, 2013; *Xu et al.*, 2013; *Cowton et al.*, 2015; *Carroll et al.*, 2016). For unstratified fjords, melt rates can instead decrease with depth (*Kimura et al.*, 2014).

There are few studies of melt-driven convection focussing on Greenland; most concern the lower-discharge environment of Antarctica (e.g. *Holland et al.*, 2008b). Plumes arising from melt-driven convection are much weaker than subglacial discharge-initiated plumes, with water velocities at least an order of magnitude smaller (*Sciascia et al.*, 2013; *Magorrian and Wells*, 2016). Such plumes may therefore only rise a short distance and it has been suggested a series of stacked circulation cells with typical heights of 10-100 m may form, in which melt rates are on the order of 0-0.3 m/d (*Magorrian and Wells*, 2016). Again melt rates are found to be higher at depth where the fjords are warmer and less stratified.

A pervasive issue with modelling of submarine melt rate is uncertainty in the values of parameters which appear in the submarine melt rate parameterisation (*Holland and Jenkins*, 1999). Values for these parameters are highly uncertain and at present are based on studies of sea ice (e.g. *McPhee et al.*, 2008) or a tidally-dominated ice shelf (*Jenkins et al.*, 2010). As such it is not clear how appropriate these values are to the rather different conditions associated with plumes driven by subglacial discharge at tidewater glaciers (*Straneo and Heimbach*, 2013). In theory, the important parameters could be validated by comparing the described models with observations. In practice, the uncertainties on both sides of this comparison are large so that it is difficult to obtain strong conclusions. At present, perhaps the strongest statement that can be made is that model and observation display order of magnitude agreement in absolute values of submarine melt rate.

Due to the scarcity of melt rate observations, it is even harder to observe variability in submarine melt rate due to variation in, for example, fjord temperature. Two previously described studies are, however, relevant. *Luckman et al.* (2015) find a strong linear relationship between frontal ablation (which is likely representative of submarine melt rate) and ocean temperature (Fig. 2.7), supporting suggestions from the models. Observations from in front of LeConte Glacier also support the modelled sublinear relationship between melt rate and subglacial discharge (Fig. 2.13; *Motyka et al.* (2013)). While detailed predictions of submarine melt rate from models should be viewed with caution, there is emerging evidence supporting the broader conclusions of modelling studies.

2.4.4 Links between submarine melting and calving

Removal of ice by submarine melting may in some cases account for a significant fraction of the terminus ice flux. Observations suggest this is the case at least for some glaciers in Svalbard and Alaska (*Motyka et al.*, 2013; *Bartholomaus et al.*, 2013; *Luckman et al.*, 2015). For the fastest-flowing glaciers in Greenland, the balance of observational and modelling evidence instead suggests that ice velocity substantially exceeds submarine melt rate (e.g. *Sutherland and Straneo*, 2012). If submarine melting plays an important role in glacier dynamics in these locations, then it must be through a sensitive coupling between submarine melting and calving. It is therefore worth briefly reviewing the process of calving, to consider the potential importance of submarine melting on calving processes and ultimately tidewater glacier dynamics.

Benn et al. (2007) provide an authoritative overview of the great variety of calving styles and processes observed at marine-terminating glaciers and ice shelves. They suggest four principal mechanisms driving calving: (i) longitudinal stretching of ice as it approaches the calving front, (ii) the force imbalance which necessarily exists at calving fronts due to the differing densities of ice and water, (iii) melt-undercutting of the calving front, and (iv) torque exerted on the calving front by buoyancy.

Addressing each in turn, ice will often experience longitudinal (along-flow) stretching as it approaches the calving front, often manifested through the formation of crevasses, a

process which may also be promoted by hydrofracture. These crevasses are an obvious weak spot at which calving could occur, and thus most models of calving incorporate stretching-threshold based calving criteria (*Benn et al.*, 2007; *Nick et al.*, 2010; *Todd and Christoffersen*, 2014).

The force imbalance resulting from differing hydrostatic ice and ocean pressure at calving fronts manifests itself as a maximum of tensile stress located at the glacier surface approximately one ice thickness behind the calving front (Fig. 2.15; *Reeh* (1968)). *O'Leary and Christoffersen* (2013) have shown that the location of maximum stress is displaced up-glacier if the calving front is undercut, suggesting that undercutting by submarine melting could increase calving rate (Fig. 2.15). They further show that the displacement of the stress field is several times larger than the length of undercutting, indicating the potential for submarine melting to drive calving at a rate several times larger than the melt rate, as is required if submarine melting is to explain dynamic change at the fastest-flowing glaciers in Greenland.

A less dynamic aspect of the potential coupling between submarine melting and calving is how undercutting by submarine melting will destabilise ice above the undercut (*Benn et al.*, 2007). In this case, there may be no direct dynamic feedback of submarine melting on calving, it is simply that ice below the water is removed by submarine melting, while ice above calves at a rate controlled by submarine melting. Thus, frequent and small above-water calving events would be observed, with infrequent subsurface calving. As already described, a number of glaciers in west Greenland are indeed substantially undercut due to submarine melting (*Fried et al.*, 2015; *Rignot et al.*, 2015) and calving rate at three glaciers in Svalbard is well correlated with ocean temperature (*Luckman et al.*, 2015), lending support to the prevalence of this calving mechanism in some locations.

Finally, buoyancy-driven calving currently appears to be the dominant style of calving at the fastest-flowing glaciers in Greenland, such as Helheim Glacier and Jakobshavn Isbrae (*James et al.*, 2014; *Xie et al.*, 2016), characterised by calving of kilometre-scale full-depth blocks of ice which often rotate after detaching from the glacier. These

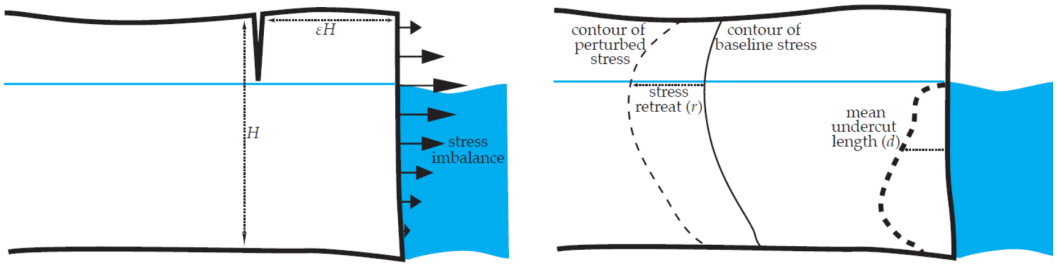

Figure 2.15: Schematic effect of undercutting by submarine melting on calving, adapted from *O'Leary and Christoffersen* (2013). Undercutting displaces the stress field up-glacier, potentially increasing calving rate.

events have been attributed to the flow of the glacier into deeper water, forcing the glacier below flotation and inducing a buoyant torque, promoting the formation of basal crevasses (*James et al.*, 2014; *Wagner et al.*, 2016). Submarine melting may play a role by melting the base of the block (*Xie et al.*, 2016) or by shaping the calving front to have a toe near the grounding line, increasing the buoyant torque (*Wagner et al.*, 2016).

It is also of course possible that multiple mechanisms operate at the same glacier, either at different times in the year or at different locations on the calving front. For example, if has been suggested that at Store Glacier, differential submarine melting creates undercut embayments and protruding headlands, with frequent smaller calving events in the embayments driven by submarine melting and infrequent but large buoyancy-driven events removing the headlands (*Chauché et al.*, 2014; *Todd and Christoffersen*, 2014; *Ryan et al.*, 2015).

2.4.5 Models of tidewater glaciers incorporating submarine melting

If the ultimate purpose of understanding ice-ocean interaction is to constrain future sea level rise, then we require models which capture the essential processes and allow us to run projections of glacier dynamics. There are now several studies incorporating calving parameterisations into simulations of tidewater glacier dynamics, ranging from simple depth-integrated flowline models (e.g. *Nick et al.*, 2009) to two-dimensional full-Stokes flowline models (e.g. *Cook et al.*, 2014) to depth-integrated plan-view models (e.g.

Bondzio et al., 2016). Almost all of these models incorporate an along-flow stretching threshold based calving criteria, where the threshold may depend on crevasse water depth (*Benn et al.*, 2007) and basal water pressure (*Nick et al.*, 2010). An exception is the study of *Nick et al.* (2009), which employed a flotation-based calving criterion to model Helheim Glacier in south-east Greenland.

Each of these models includes some representation of submarine melting. Melting may be imposed beneath ice shelves or tongues in depth-integrated flowline models (e.g. *Nick et al.*, 2013), but these simple models cannot take account of the vertical variation in stress induced by changing calving front shape, potentially a key process in ice-ocean interaction (Fig. 2.15; *O'Leary and Christoffersen* (2013)). Models with a vertical dimension are able to incorporate undercutting by submarine melting. Three such studies (*Cook et al.*, 2014; *Todd and Christoffersen*, 2014; *Krug et al.*, 2015) in fact find little role for submarine melting in glacier dynamics when a stretching-threshold based calving law is used. This appears to contrast with the findings of *O'Leary and Christoffersen* (2013) described above. The difference between these studies has been attributed to the diagnostic versus prognostic nature of the models used. In the prognostic (time-evolving) models, the surface geometry of the glacier may adjust to the undercutting, reducing the sensitivity of the stress field to undercutting (*Cook et al.*, 2014). Finally, plan-view models of tidewater glaciers represent submarine melting by moving the calving front according to the competition between ice velocity, submarine melting and calving, where submarine melt rate is imposed and calving rate is again based on a stretching-threshold criterion (*Bondzio et al.*, 2016; *Morlighem et al.*, 2016).

It is not yet clear whether these models accurately capture the possible interaction between submarine melting and glacier dynamics. It should be noted that some of the simplified models above are very successful at simulating the observed changes in tidewater glaciers in recent decades (e.g. *Nick et al.*, 2009). However, many of the key processes remain poorly understood and are very heavily parameterised, reducing confidence in future projections. There is therefore a pressing need for better understanding of submarine melting and its effect on glacier dynamics, and it is to these topics which this thesis aims to contribute.

Chapter 3

Methods

This chapter provides a brief overview of the methods used in this thesis. The principal tool used is plume modelling and much of what follows below is therefore a description of two contrasting models; one a general circulation model and the other a simple analytical model enabling the study of plumes. Chapters 4-6 present idealised modelling while in Chapter 7, the models are applied to a real glacial fjord system in west Greenland; this study site is introduced below. The intention of this chapter is to provide an overview rather than an exhaustive description since the full methodological details are given in the individual chapters and relevant supporting information.

3.1 MITgcm

The Massachusetts Institute of Technology general circulation model (MITgcm) is a flexible tool for the simulation of oceanic and atmospheric dynamics. The model solves the Boussinesq form of the Navier-Stokes equations discretized on an Arakawa-C grid, and has both hydrostatic and non-hydrostatic capabilities (*Marshall et al.*, 1997a,b). The MITgcm is used by a large community of researchers around the world with wide-ranging applications, but has perhaps seen most frequent use in the study of large scale ocean dynamics (e.g. *Losch et al.*, 2010; *Forget et al.*, 2015). Beginning with the study of *Xu et al.* (2012), the MITgcm has become the most popular tool for complex plume

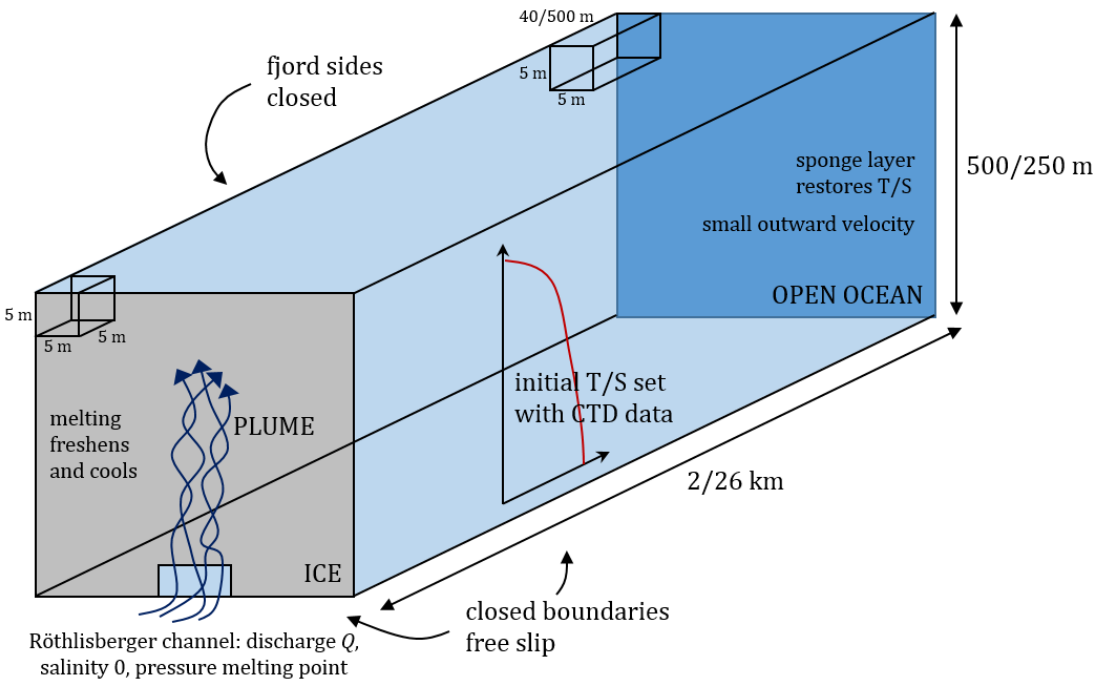

Figure 3.1: Schematic of model set-up in the MIT general circulation model.

and fjord modelling in glacial settings (e.g. *Sciascia et al.*, 2013; *Carroll et al.*, 2015; *Slater et al.*, 2015; *Cowton et al.*, 2015). In this thesis the MITgcm is used in Chapters 4 and 7 to model proglacial plumes rising up the calving fronts of tidewater glaciers. A degree of customisation of the model to these purposes is required.

3.1.1 Model bathymetry

In Chapters 4 and 7, idealised fjord bathymetry is assumed, consisting of flat-bottomed fjords with vertical sides (Fig. 3.1). Fjord depth was taken to be 500 m and 250 m in Chapters 4 and 7 respectively, the former taken as representative of typical deep Greenlandic fjords, and the latter thought to be appropriate for Kangiata Nunata Sermia in south-west Greenland (section 3.5). Fjord length was taken to be 2 km and 26 km in Chapters 4 and 7 respectively, the much longer fjord in Chapter 7 helping to reduce the reflection of internal waves from the boundaries of the model.

3.1.2 Initial conditions

All of the applications of MITgcm in this thesis use initial temperature and salinity profiles obtained from conductivity-temperature-depth (CTD) casts into fjords in Greenland. Chapter 4 uses profiles from Store Glacier in west Greenland collected during August 2009 and 2010 (*Chauché et al.*, 2014). Chapter 7 uses profiles from Godthåbsfjord (section 3.5) collected throughout 2009 (*Mortensen et al.*, 2013). In all the simulations, the fjord is initially at rest, with the model then run subject to the boundary conditions described below and allowed to reach a 'steady state' before conclusions are drawn, with 'steady state' defined by stabilisation of the quantity of interest (e.g. submarine melt rate in Chapter 4).

3.1.3 Boundary conditions

For all the simulations presented in this thesis, fjord sides are taken to be closed boundaries with a free slip condition (Fig. 3.1), so that water may not flow through these boundaries but may flow parallel to the boundary without resistance. At the open ocean boundary, a 'sponge layer' is imposed (e.g. *Sciascia et al.*, 2013) in which the temperature and salinity are relaxed towards the initial conditions and where the water velocity is relaxed towards a prescribed value (Fig. 3.1). This is a very small non-zero value ($< 5 \times 10^{-4}$ m/s in Chapter 4) which is directed out of the model domain. This sponge layer helps to prevent unphysical reflections of waves from the open ocean boundary and balances the input of subglacial discharge at the glacier end of the domain, ensuring that the modelled fjord does not fill up during simulations.

In Chapters 4 and 7, the glacier boundary is closed except for subglacial channels at the grounding line through which flows fresh (salinity = 0) subglacial discharge at the pressure melting point (-0.29°C for a fjord depth of 500 m). The magnitude of subglacial discharge is prescribed and varied based on representative values from surface energy balance modelling. For a given subglacial discharge, the cross-sectional area of the subglacial channel (and thus the through-channel water velocity) is estimated assuming the channels are steady state Röthlisberger channels in which creep closure from the weight of ice is balanced by wall melting (*Röthlisberger*, 1972). In actuality

the estimated channel sizes must be rounded to the nearest 25 m^2 due to the model resolution of 5 m.

At the glacier boundary, submarine melt rates are calculated from modelled water temperature and velocity based on the parameterisation described below (section 3.3). The input of the resulting submarine meltwater into the fjord is 'virtual'; model cells adjacent to the ice are freshened and cooled by the melting but no mass is added to the domain (*Losch*, 2008; *Xu et al.*, 2012).

3.1.4 Resolution

In order to accurately capture plume dynamics, model resolution close to the glacier is 5 m and isotropic (the same in each of the x, y and z directions; Fig. 3.1). This high resolution is maintained for the 250 m closest to the glacier, thereafter increasing to reach 40 m and 500 m at the open ocean boundary in Chapters 4 and 7 respectively (Fig. 3.1). The modelled plumes in these chapters are contained within the high resolution section of the domain close to the glacier. Resolution in the y and z directions remains at 5 m throughout the domain, which is computationally inefficient given that the far-fjord dynamics are of little interest, but is unavoidable given the structured grid and lack of nesting ability of MITgcm.

Due to the high resolution employed to simulate plumes, and the high modelled vertical velocities (> 6 m/s), a timestep as small as 0.25 s is used in Chapters 4 and 7. These short timesteps place restrictions on the achievable length of simulation time, even when simulations are undertaken in parallel (simulations in Chapters 4 and 7 were undertaken on 16 cores).

3.1.5 Subgrid-scale mixing

A key aspect of any general circulation simulation is the consideration of subgrid-scale mixing, that is, turbulent mixing which occurs at scales smaller than the resolution of the model. Fully resolving the turbulent mixing within plumes (direct numerical simulation) would require a model resolution less than 1 mm (e.g. *Moin and Mahesh*, 1998) and is therefore completely impractical for geophysical-scale simulation. At the

still relatively high resolution of 5 m used in Chapters 4 and 7, geophysical scale models are computationally manageable and plumes are fairly well resolved (having a typical width of 10 to 100 m, or 2 to 20 grid cells). Much of the dynamically important turbulent mixing at the edges of the plume does however occur at the subgrid scale. In order to correctly represent the dynamics of the plumes, consideration of subgrid-scale mixing is therefore vitally important.

For the MITgcm plume modelling presented in this thesis, a simple isotropic constant eddy viscosity model (e.g. *Kämpf*, 2010) is assumed for subgrid-scale mixing of momentum, heat and salt with the Prandtl number set to 1 (*Sciascia et al.*, 2013) leaving a single free eddy viscosity/diffusivity parameter K. This parameter is tuned by comparing plumes modelled in MITgcm to those obtained using a simpler analytical approach (buoyant plume theory, section 3.2 below). Loosely speaking, higher values of K give smoother, more diffuse simulations in which subgrid-scale mixing is heavily parameterised, while smaller values of K give more 'turbulent' simulations, sometimes at the expense of numerical stability, in which a greater degree of mixing is resolved.

The choice of K for plume modelling is described in Chapter 4, and it is seen that the most appropriate value of K depends on the magnitude of subglacial discharge. Intuitively, the degree of mixing between the rapidly rising plume and the relatively still ambient fjord water will depend on the velocity shear between the two regions. Since the plume velocity increases with the subglacial discharge (Chapter 5), it should be expected that the most appropriate value of K depends on the magnitude of subglacial discharge. Although intuitive, in retrospect the described approach is not the most practical as the value of K has to be varied with subglacial discharge, making seasonal simulations, or simulations with two plumes of differing subglacial discharge, rather difficult. A more sophisticated approach would use a subgrid-scale mixing parameterisation which accounts for the dependence of mixing on velocity shear; such schemes are under development in the MITgcm and may be the way to go for future simulations.

3.2 Buoyant plume theory

Buoyant plume theory (BPT) provides a simpler, more analytical model of plume dynamics, based on the conservation of plume volume, momentum and buoyancy as the plume rises. The long and very extensive literature on BPT describes how the theory has proven highly successful at capturing the dynamics of both laboratory plumes (e.g. *Batchelor*, 1954; *Morton et al.*, 1956) and geophysical plumes, such as volcanic ash clouds (e.g. *Baines and Sparks*, 2005) and dense overflows (e.g. *Wells and Wettlaufer*, 2007). As such it seems reasonable to place some confidence in the ability of BPT to capture the essential dynamics of plumes adjacent to tidewater glaciers.

The first applications of BPT in a glacial setting were *MacAyeal* (1984) and *Jenkins* (1991), in which BPT was coupled to a parameterisation for submarine melting of the ice by the ocean. The recent great interest in ice-ocean interaction has resulted in a number of studies employing BPT, focussed on Antarctic ice shelves (*Holland and Feltham*, 2006; *Payne et al.*, 2007; *Jenkins*, 2011), Greenlandic tidewater glaciers (*Carroll et al.*, 2016; *Magorrian and Wells*, 2016; *Slater et al.*, 2016), and used for forcing of fjord models (*Cowton et al.*, 2015, 2016). An important point of difference between Antarctic and Greenlandic applications, which features at a number of points in this thesis, is that in the Antarctic case, the buoyancy of the plume is provided largely by submarine melting itself, whereas within discharge plumes in Greenland, the buoyancy of the plume is overwhelmingly provided by subglacial discharge at the base and is therefore closer to classical BPT (*Morton et al.*, 1956).

In this thesis BPT is used in four contexts. It is used firstly in Chapter 4 to calibrate the discussed subgrid-scale mixing parameters in MITgcm. In Chapter 5, BPT is used to explore the sensitivity of plume dynamics and submarine melting to variation in subglacial discharge and fjord conditions, and ultimately to develop simple parameterisations for submarine melting of calving fronts by plumes. BPT is employed in Chapter 6 to explore feedbacks between calving front shape, plume dynamics and submarine melting at tidewater glaciers. BPT is finally used in Chapter 7 to explore the subglacial discharge required for a plume to reach the fjord surface, thus giving

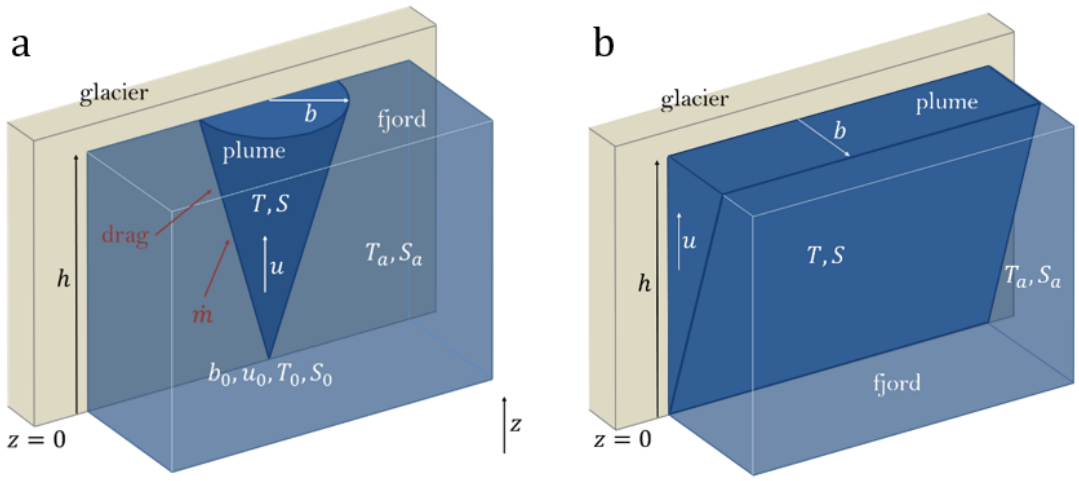

Figure 3.2: Schematics of modelling with buoyant plume theory for (a) point source plumes and (b) line source plumes, as described in the text.

information on the state of the subglacial hydrological system at a west Greenland tidewater glacier.

3.2.1 Defining equations

Two differing plume geometries are considered in this thesis. In each, a 'top-hat' profile for plume properties is assumed such that plume velocity, temperature and salinity do not vary in the plume cross-section. The first geometry, referred to throughout as a point source plume, has a half-conical shape with flat side against the vertical glacier and curved side open to the fjord (Fig. 3.2a). The defining equations ensure conservation of volume, momentum, heat and salt flux as the plume rises and may be written

$$\frac{d}{dz}\left(\frac{\pi}{2}b^2u\right) = \pi b\dot{e} + \Delta V^p_{melt} \tag{3.1a}$$

$$\frac{d}{dz}\left(\frac{\pi}{2}b^2u^2\right) = \frac{\pi}{2}b^2g' - 2C_dbu^2 \tag{3.1b}$$

$$\frac{d}{dz}\left(\frac{\pi}{2}b^2uT\right) = \pi b\dot{e}T_a + \Delta T^p_{melt} \tag{3.1c}$$

$$\frac{d}{dz}\left(\frac{\pi}{2}b^2uS\right) = \pi b\dot{e}S_a + \Delta S^p_{melt} \tag{3.1d}$$

where b, u, T and S are respectively plume radius, velocity, temperature and salinity. The rate of entrainment of ambient fjord water of temperature T_a and salinity S_a into the plume is denoted $\dot{e}$ (in units m/s). The plume experiences quadratic drag at the ice-ocean interface with coefficient C_d. The addition of volume to the plume due to submarine melting is represented by the term ΔV^p_{melt}, with the effect of submarine melting on plume temperature and salinity represented by similar terms in Eqs. 3.1c and 3.1d. The reduced gravity of the plume is denoted g' and is given by

$$g' = g\left[\rho(T_a, S_a) - \rho(T, S)\right]/\rho_{ref} \tag{3.2}$$

where g is gravitational acceleration and ρ_{ref} is a reference density. The densities in the numerator are calculated as a function of temperature and salinity according to an equation of state, either non-linear (*Fofonoff and Millard*, 1983) or linear (*Jenkins*, 2011). Eq. 3.1a therefore states that the rate of change of plume volume flux is given by entrainment of ambient water over the curved side of length πb and the addition of submarine meltwater. Eq. 3.1b states that change in plume momentum flux is driven by plume buoyancy and plume-ice drag. Eqs. 3.1c/3.1d ensure that change in plume heat/salt flux is due to entrainment of ambient heat/salt and the effect of submarine melting on plume heat/salt content.

The second plume geometry, referred to throughout as a line source plume, has a wedge shape with a vertical side against the vertical glacier and an inclined side open to the fjord (Fig. 3.2b). The side margins of the plume are neglected. The defining equations for the line source plume are

$$\frac{d}{dz}(bu) = \dot{e} + \Delta V^l_{melt} \tag{3.3a}$$

$$\frac{d}{dz}\left(bu^2\right) = bg' - C_d u^2 \tag{3.3b}$$

$$\frac{d}{dz}(buT) = \dot{e}T_a + \Delta T^l_{melt} \tag{3.3c}$$

$$\frac{d}{dz}(buS) = \dot{e}S_a + \Delta S^l_{melt} \tag{3.3d}$$

where in this case b measures the width of the plume in the ice-perpendicular direction, and all other variables follow from the point source case (the superscript l in the submarine melt terms indicates a line source rather than point source plume).

The above equations apply for a plume rising up a vertical calving front, an assumption which is relaxed in Chapter 6. The generalisation to a non-vertical calving front - subtending an angle θ with the horizontal - entails replacing the vertical coordinate z with an along-boundary coordinate l, and introducing a factor $\sin\theta$ into the term representing acceleration due to buoyancy (e.g. for the line plume, $bg' \rightarrow bg'\sin\theta$).

3.2.2 Entrainment parameterisation

In order to provide a closed system of equations, the rate of entrainment and submarine melting terms must be expressed in terms of plume variables. The simplest entrainment parameterisation, which has proven highly successful in capturing plume dynamics, has the rate of entrainment of fjord water into the plume proportional to the plume velocity, with constant of proportionality α (*Morton et al.*, 1956)

$$\dot{e} = \alpha u \tag{3.4}$$

Physically, $\dot{e}$ may be thought of as the velocity of water crossing the plume-fjord boundary at the edge of the plume, in a direction perpendicular to the velocity of the plume itself. The value of α must be empirically determined and is usually found to lie in the range 0.08-0.12 (e.g. *Turner*, 1979); in this thesis a value $\alpha = 0.1$ is generally applied and it is demonstrated that plume dynamics are relatively insensitive to this choice (Chapter 5).

For a non-vertical calving front, a factor of $\sin\theta$ is added to the entrainment parameterisation, resulting in a reduction of entrainment when the plume is inclined (*Pedersen*, 1980; *Jenkins*, 2011)

$$\dot{e} = \alpha \sin\theta \, u \tag{3.5}$$

This additional factor aims to take account of the density gradient which has to be overcome when dense ambient water is entrained into the relatively lighter plume lying above. In this context, more complex entrainment parameterisations which take into account the plume Richardson number have also been used for simulating plumes beneath ice shelves (*Holland and Feltham*, 2006; *Payne et al.*, 2007) and are discussed in Chapter 6. Description of the second parameterisation required, that for the terms representing submarine melting, is deferred to section 3.3 below.

3.2.3 Solution of BPT

The plume equations for the point source plume (Eqs. 3.1) and for the line source plume (Eqs. 3.3), together with the reduced gravity (Eq. 3.2), entrainment parameterisation (Eq. 3.4 or 3.5) and the melt rate parameterisation described below (Eqs. 3.6), form a closed system of ordinary differential equations which are integrated numerically in MATLAB. The ambient fjord conditions must be specified at all depths, and this is done either with data from CTD profiles (Chapters 4 and 7) or in an idealised fashion (Chapters 5 and 6). The subglacial discharge must be specified for the point source plume, and equivalently the line source plume requires specification of the subglacial discharge per unit width. These are enforced by choosing appropriate initial plume width and velocity, as described in Chapter 5. Finally, initial plume salinity and temperature are set to zero and the pressure melting point respectively, as in MITgcm.

3.2.4 Suitability of plume geometry

Point source plumes are best applied where subglacial discharge emerges in a focussed fashion, essentially from a point at the glacier grounding line (Fig. 3.2a). As such, the

point source model is likely appropriate where subglacial discharge emerges from an approximately semi-circular Röthlisberger channel. In contrast, application of a line source plume model is likely more appropriate either for very wide subglacial channels or where the emergence of subglacial discharge is spread uniformly across a significant width of the calving front. The width of channel required for the line plume model to be appropriate is discussed in Chapter 6; as a rough guide, for a fjord of depth 250 m, a channel should be wider than about 125 m before use of a line plume model would be appropriate. Equally, to apply the point source plume model, the channel should not be too wide, on the order of tens of metres. There may therefore be channels which sit awkwardly between the point and line source plume models, being some combination of the two. As has been described in the background chapter, we do not (in general) have a good understanding of the spatial pattern of emergence of subglacial discharge at tidewater glacier grounding lines, so that it is not clear which plume model geometry is most appropriate.

3.3 Melt rate parameterisation

Conversion of modelled plume and fjord dynamics, as given by BPT or MITgcm, to submarine melt rate requires consideration of ice-ocean boundary thermodynamics. A review of melt rate parameterisations is given by *Holland and Jenkins* (1999), and encapsulates the following description of the ice-ocean boundary.

The ice-ocean boundary system may be thought of as three (or even four) distinct layers (Fig. 3.3). At the edges are the ice (or calving front) and the 'mixed layer', also termed the 'outer turbulent region' (*Wells and Worster*, 2008). In this thesis the mixed layer is either the plume itself or simply the water circulating at velocity u past the calving front in the model cells adjacent to the ice. Between the ice and the mixed layer lies the ice-ocean boundary layer. The left edge of this boundary layer forms the physical ice-ocean interface where the water temperature T_b is assumed to be the in-situ freezing point. The right edge of this boundary layer forms the interface with the mixed layer, where the water temperature T is given by the mixed layer temperature (e.g. by the

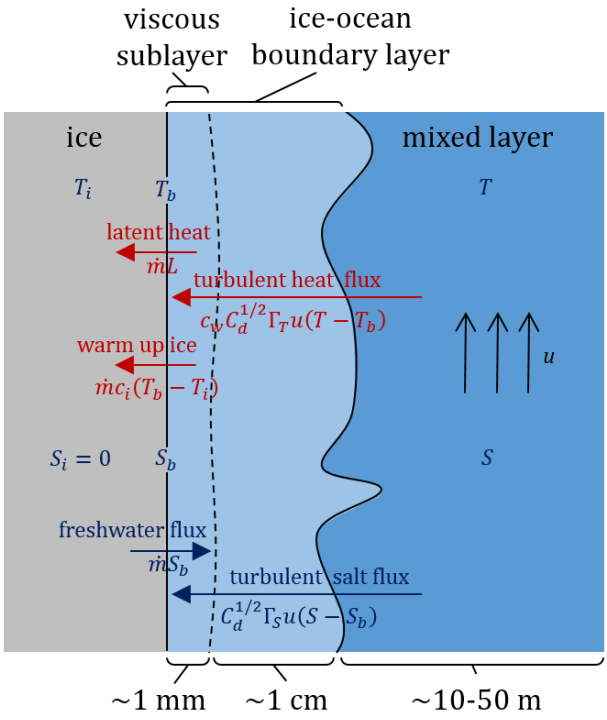

Figure 3.3: Schematic of heat and salt exhange at the ice-ocean boundary.

plume temperature). The resulting temperature (and salinity) gradient across the ice-ocean boundary layer drives heat (and salt) flux from the ocean to the ice. Construction of a melt rate parameterisation involves assuming the ice-ocean boundary layer is in thermodynamic equilibrium and therefore balancing heat and salt flux through this layer.

Heat flux from the ice-ocean boundary layer into the ice consists of the heat required to warm the ice to the melting point and the latent heat of melting (Fig. 3.3). In equilibrium, the sum of these fluxes must be balanced by turbulent heat flux from the mixed layer through the ice-ocean boundary layer. Similarly, the input of freshwater into the ice-ocean boundary layer from melting must be balanced by a salt flux from the mixed layer (Fig. 3.3), so that the boundary layer salinity is maintained. Heat flux from the mixed layer through the ice-ocean boundary layer is assumed to take the form $\gamma_T(T - T_b)$ where γ_T represents the turbulent transfer of heat from the mixed layer through the ice-ocean boundary layer. Within the ice-ocean boundary layer, and

close to the interface, turbulence will be supressed by the interface, creating a viscous sublayer (Fig. 3.3, the possible fourth layer of the system) through which heat flux occurs by molecular diffusion. The presence of this sublayer must also be encapsulated in γ_T, and since heat diffuses more quickly than salt, the equivalent exchange coefficient for salt γ_S is smaller than γ_T. Recognising the role of motion in the mixed layer in generating turbulence in the ice-ocean boundary layer, the exchange coefficients are expressed as $\gamma_{T,S} = \Gamma_{T,S} u^\star$, where $\Gamma_{T,S}$ are heat and salt transfer coefficients and $u^\star = C_d^{1/2} u$ is the friction velocity. The flux of heat and salt from the mixed layer through the ice-ocean boundary layer therefore scales linearly with the velocity of the mixed layer.

Putting the above description together gives the three-equation melt parameterisation (Fig. 3.3; *Holland and Jenkins* (1999); *Jenkins* (2011))

$$\dot{m}\left[c_i\left(T_b - T_i\right) + L\right] = c_w C_d^{1/2} \Gamma_T u \left(T - T_b\right) \tag{3.6a}$$

$$\dot{m} S_b = C_d^{1/2} \Gamma_S u \left(S - S_b\right) \tag{3.6b}$$

$$T_b = \lambda_1 S_b + \lambda_2 + \lambda_3 (h - z) \tag{3.6c}$$

The first equation balances heat flux, the second salt flux and the last ensures the ice-ocean interface itself remains at the in-situ freezing point, together providing three equations for the three unknowns of melt rate $\dot{m}$ and ice-ocean interface temperature T_b and salinity S_b.

Under the three equation melt parameterisation, the submarine melting terms in the point source plume (Eqs. 3.1) become

$$\Delta V^p_{melt} = 2b\dot{m} \tag{3.7a}$$

$$\Delta T^p_{melt} = 2b\left[\dot{m} T_b - \Gamma_T C_d^{1/2} u (T - T_b)\right] \tag{3.7b}$$

$$\Delta S^p_{melt} = 2b\left[\dot{m} S_b - \Gamma_S C_d^{1/2} u (S - S_b)\right] \tag{3.7c}$$

The factors of $2b$ arise from the width of the plume-ice contact. In Eq. 3.7b the two terms represent respectively the heat added to the plume due to the addition of meltwater at temperature T_b and the heat removed from the plume due to turbulent transfer from the plume into the ice-ocean boundary layer. The submarine melting terms in the line source plume (Eqs. 3.3) are the same but for the factors of $2b$.

Much rests on the values of the Stanton numbers $C_d^{1/2}\Gamma_{T,S}$; the melt rate calculated from Eqs. 3.6 is approximately linearly related to the thermal Stanton number $C_d^{1/2}\Gamma_T$ (*Holland and Jenkins*, 1999). Values for these parameters (e.g. Table S1.1) come from measurements made beneath sea ice (e.g. *McPhee et al.*, 2008) and from only one field study beneath the Ronne ice shelf in Antarctica (e.g. *Jenkins et al.*, 2010). As will be discussed in each of the chapters, observations from tidewater glaciers with which to calibrate these parameters are lacking, thus uncertainty in the value of these coefficients is a key and problematic issue in our understanding of ice-ocean interaction, significantly impacting confidence in modelled submarine melt rates.

To gain some insight into the melt rate parameterisation, the dominance of latent heat on the left hand side of Eq. 3.6a may be used to gain the approximation

$$\dot{m} \approx \frac{c_w C_d^{1/2} \Gamma_T}{L} u \left(T - T_b\right) \tag{3.8}$$

It is therefore seen that the submarine melt rate is largely proportional to the product of mixed layer (or plume) velocity u and thermal forcing $T - T_b$. This expression is illustrated in Fig. 3.4; note that the combination of leading parameters equates to approximately 1.1 $(^\circ\mathrm{C})^{-1}$ when melt rate is expressed in m/d and water velocity in m/s, so that a water velocity of $u = 1$ m/s and a thermal forcing of $T - T_b = 1^\circ$C (for example given by water temperature of approximately $T = 0^\circ$C) leads to a melt rate of $\sim$1 m/d (Fig. 3.4).

The melt parameterisation (Eqs. 3.6) is used throughout this thesis to calculate melt rates in both BPT and MITgcm. In BPT the melt rate parameterisation is fully coupled into the equations (e.g. Eqs. 3.1 and 3.3; Chapter 5) so that the potential feedback of

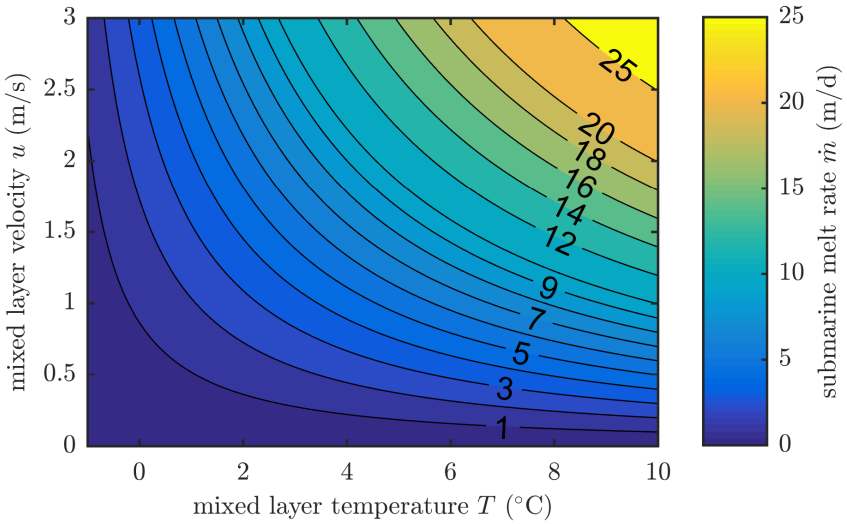

Figure 3.4: Melt rate parameterisation. Note this result is for a water depth of 100 m and a mixed layer salinity $S = 30$ psu. Varying water depth in the range 0 to 1000 m and mixed layer salinity S in the range 25 to 35 psu affects melt rate by at most 35% for $T > 1°C$.

melting on plume dynamics is captured. The velocity and temperature which enter into the melt rate parameterisation are the plume velocity and temperature. In MITgcm, the melt rate parameterisation is used to calculate the magnitude of the freshening and cooling of ice-adjacent cells described above. The velocity and temperature entering into the melt rate parameterisation are taken from the model cell adjacent to the ice. This velocity is largely vertical within plumes, but mostly horizontal on other parts of the calving front.

3.4 Comparison of MITgcm and BPT

Both MITgcm and BPT are used in this thesis for plume modelling, and it is worthwhile to briefly contrast the two methods. MITgcm is very flexible and capable of handling arbitrary geometries, but this comes with significant complexity and computation time measured in hours to days. In contrast, BPT is suitable only for idealised geometries, but is very simple and may be solved in at most a few seconds. Provided MITgcm is carefully set up, in particular with respect to subgrid-scale mixing, MITgcm and

BPT are in excellent agreement as regards cross-section averaged plume dynamics (section S1.2). MITgcm however resolves variation in plume properties within the plume, for example, that water velocities are higher in the core of the plume than at the edges, and that close to the grounding line water temperature is cooler in the core of the plume than at the edges. Furthermore, MITgcm allows for the study of calving front water circulation over a region wider than the plume.

MITgcm and BPT therefore lie at opposite ends of the complexity spectrum but in many situations give comparable results. MITgcm is clearly required if one is interested in the wider melting driven by plume-generated fjord circulation. However, for many purposes BPT is sufficient and is a promising candidate to form the basis for coupled ice-ocean models at ice sheet scales.

3.5 Kangiata Nunata Sermia

In Chapter 7, the described models are applied to Kangiata Nunata Sermia (KNS, Fig. 3.5), a large tidewater glacier in south-west Greenland draining ∼2% of the Greenland Ice Sheet (*Sole et al.*, 2011). The relative accessibility of KNS, located 100 km from Nuuk (Fig. 3.5), means it is well studied, providing a test site for numerous glaciological studies, including investigations of surface mass balance (*Van As et al.*, 2014), subglacial hydrology (*Sole et al.*, 2011), seasonal dynamics (*Moon et al.*, 2014) and long-term evolution (*Lea et al.*, 2014). The calving front of KNS is 4.5 km wide and thought to be grounded in ∼250 m of water (*Mortensen et al.*, 2011). KNS flows at speeds approaching 20 m/d at the terminus into Godthåbsfjord, a narrow fjord extending 160 km from KNS to the open ocean near Nuuk (Fig. 3.5; *Joughin et al.* (2010); *Mortensen et al.* (2011)). The fjord has been extensively studied (*Mortensen et al.*, 2011, 2013, 2014) revealing the presence of warm (1-2°C) water at depth thought to provide a heat source for submarine melting of KNS.

Chapter 7 focusses on proglacial plumes adjacent to the calving front of KNS (e.g. Fig. 2.9). The basic premise of Chapter 7 is to use the relationship between the subglacial discharge initiating a plume and the likelihood of the plume reaching the fjord

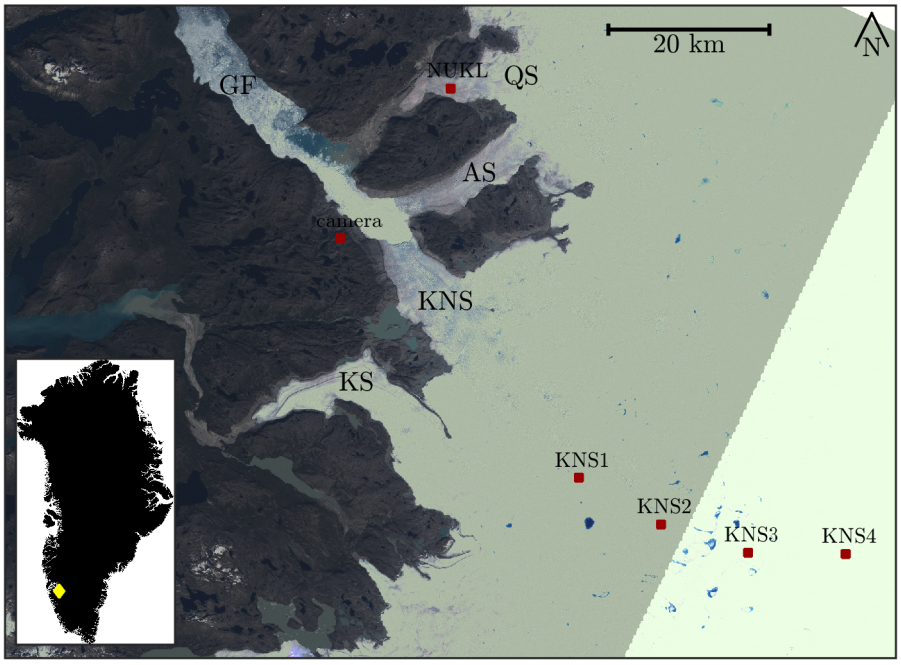

Figure 3.5: Overview of the Kangiata Nunata Sermia system in south-west Greenland. Markers show the location of the time-lapse camera, the four GPS sites described in the text (KNS1-4), and the PROMICE weather station NUKL. Other abbreviations are GF: Godthåbsfjord, QS: Qamanârssûp Sermia, AS: Akugdlerssûp Sermia, KNS: Kangiata Nunata Sermia and KS: Kangaasarsuup Sermia. Background imagery from *Howat et al.* (2014) and *Howat* (2017).

surface. Thus the presence or absence of plumes at the fjord surface can be compared with estimates of catchment runoff, thereby gaining information on the structure of the subglacial hydrological system from which discharge emerges at the terminus.

A time series of plume visibility at the fjord surface is therefore required. Through the summer of 2009, a time-lapse camera located ∼5 km west of the calving front (Fig. 3.5) observed the terminus of KNS, capturing an image every hour from 11 May to 7 September (*Sole et al.*, 2011). As described in Chapter 7, these images were manually classified based on the presence or absence of a plume, resulting in an hourly resolution time series of plume visibility through the summer of 2009.

The second required dataset is the estimated catchment runoff which is acquired using

two modelling approaches. The first is a classic positive degree day (PDD) scheme, which linearly relates the ablation rate of snow or ice to the elevation of air temperature above freezing via degree day factors (*Hock*, 2003). These degree day factors are estimated using measured air temperature and ablation from four GPS sites located on the trunk of KNS (Fig. 3.5; *Sole et al.* (2011)). The modelled PDD ablation rates from across the catchment are then summed to give an estimate of the subglacial runoff through the terminus. Recognising the simplicity of this approach, for example in neglecting refreezing of meltwater in the snowpack, subglacial runoff was also obtained from the more sophisticated regional climate model HIRHAM5 (*Langen et al.*, 2015). In fact, it is found that the two methods agree well in terms of the predicted subglacial runoff (Chapter 7).

This thesis now proceeds to the first results chapter, in which MITgcm is applied to modelling of plume-induced submarine melting of tidewater glacier calving fronts.

Chapter 4

Effect of near-terminus subglacial hydrology on tidewater glacier submarine melt rates

Submarine melting of calving fronts is a potentially important driver of tidewater glacier dynamics, and is thought to be amplified within proglacial plumes (*Straneo and Heimbach*, 2013, Chapter 2). The presence of plumes, and therefore the distribution of submarine melting, is likely dictated by the locations at which subglacial discharge emerges at the grounding line (the near-terminus subglacial hydrology). However, the near-terminus subglacial hydrology at tidewater glaciers is poorly understood. In this first results chapter, the sensitivity of submarine melting to near-terminus subglacial hydrology is quantified by simulating in MITgcm the calving front water circulation induced under subglacial hydrological scenarios ranging from a single channel to a uniformly distributed system. The results illustrate a key control on the spatial distribution of submarine melting and on calving front shape. They also motivate the work in Chapter 7, which provides constraints on near-terminus subglacial hydrology at a west-Greenland tidewater glacier.

Published in **Geophysical Research Letters**, March 2015.

Authors: D. A. Slater[1], P. W. Nienow[1], T. R. Cowton[1,2], D. N. Goldberg[1], and A. J. Sole[2].

1. School of Geosciences, University of Edinburgh, Edinburgh, UK.
2. Department of Geography, University of Sheffield, Sheffield, UK.

Citation: Slater, D. A., P. W. Nienow, T. R. Cowton, D. N. Goldberg, and A. J. Sole (2015), Effect of near-terminus subglacial hydrology on tidewater glacier submarine melt rates, *Geophysical Research Letters, 42*(8), 2861-2868, doi: 10.1002/2014GL062494.

Author contributions: D.A.S., P.W.N., T.R.C. and A.J.S designed the research. D.A.S. set up the MITgcm runs with help from T.R.C., D.N.G. and A.J.S. D.A.S. ran the simulations and analysed the results. D.A.S. wrote the paper, with input from all other authors.

Abstract

Submarine melting of Greenlandic tidewater glacier termini is proposed as a possible mechanism driving their recent thinning and retreat. We use a general circulation model, MITgcm, to simulate water circulation driven by subglacial discharge at the terminus of an idealized tidewater glacier. We vary the spatial distribution of subglacial discharge emerging at the grounding line of the glacier and examine the effect on submarine melt volume and distribution. We find subglacial hydrology exerts an important control on submarine melting; under certain conditions a distributed system can induce a factor 5 more melt than a channelized system, with plumes from a single channel inducing melt over only a localised area. Subglacial hydrology also controls the spatial distribution of melt, which has the potential to control terminus morphology and calving style. Our results highlight the need to constrain near-terminus subglacial hydrology at tidewater glaciers if we are to represent ocean forcing accurately.

4.1 Introduction

Observations of the mass balance of the Greenland ice sheet in recent decades have shown significant losses at the coastal margins (*van den Broeke et al.*, 2009; *Pritchard et al.*, 2009), much of which has been attributed to the thinning (*Pritchard et al.*, 2009), speed-up (*Rignot and Kanagaratnam*, 2006) and retreat (*Jiskoot et al.*, 2012) of tidewater glaciers. During this period, coastal waters were observed to warm (*Holland et al.*, 2008a; *Christoffersen et al.*, 2011) with water from the Irminger current (*Rignot et al.*, 2012), raising the possibility that Greenlandic tidewater glaciers reacted sensitively to ocean forcing.

One way ocean forcing would manifest itself is by melting the calving fronts of tidewater glaciers, which might provide a significant direct contribution to glacier mass balance (*Inall et al.*, 2014), and could also amplify calving rates (*O'Leary and Christoffersen*, 2013). At tidewater glaciers in Greenland, which typically lie at the end of deep and narrow fjords, melt water from the glacier catchment is expected to emerge into the fjord at the glacier grounding line, thereafter rising as a buoyant plume (*Straneo*

et al., 2012b). In combination with the presence of warm subsurface ocean water in Greenlandic fjords (*Straneo et al.*, 2010) these plumes lead to submarine melting of the calving front.

However, the way in which subglacial discharge emerges at the glacier grounding line remains poorly understood. Subglacial drainage is commonly classified as either channelized or distributed; the former characterized by a small number of large channels, routing water quickly beneath a glacier, while the latter is often conceptualized as a network of linked subglacial cavities, providing a tortuous and slow pathway for transit of meltwater (*Fountain and Walder*, 1998). At the terminus of a tidewater glacier, a channelized system would input subglacial discharge to the fjord from one or a few large outlets, while a distributed system would spread the input more uniformly across the grounding line. The effect of this distinction on tidewater glacier submarine melt rates remains largely unstudied, and is the subject of this paper.

Submarine melt rates at tidewater glaciers in Greenland have been estimated from hydrographic data, and by theoretical and numerical modeling. Rates calculated using hydrographic surveys range from 0.7 to 10 m/d (*Rignot et al.*, 2010; *Sutherland and Straneo*, 2012; *Xu et al.*, 2013; *Inall et al.*, 2014). *Jenkins* (2011) proposed a 1-dimensional model which coupled the theory of buoyant plumes with a melt rate parameterization following *McPhee* (1992). *Xu et al.* (2012) and *Sciascia et al.* (2013, 2014) used 2-dimensional numerical models to investigate fjord circulation and submarine melt rate, while *Cowton et al.* (2015) recently combined buoyant plume theory and numerical modeling in a 3-dimensional fjord model. Finally *Xu et al.* (2013) and *Kimura et al.* (2014) presented high resolution models of subglacial discharge plumes in 3 dimensions.

When comparing their hydrographic data and modeled submarine melt rates, *Xu et al.* (2013) implicitly assumed a fairly distributed system consisting of channels spaced at ∼150 m intervals across the grounding line. *Kimura et al.* (2014) suggested that the submarine melt rate per unit subglacial discharge decreases as the subglacial system becomes more channelized, but the system on which this conclusion was based was a

single channel of variable shape or two channels in close proximity. In addition the modeled fjord was unstratified, so that the resulting plumes could never reach neutral buoyancy, which will affect submarine melt (e.g. *Xu et al.*, 2013).

This study investigates the effect of variation in subglacial hydrology on tidewater glacier submarine melt rates in greater detail, and aims to capture the potential complexity and significance of hydraulic structure at the glacier terminus. The fjord is stratified in a fashion which is typical of conditions in Greenland. For three fixed values of total subglacial discharge, we vary the subglacial hydrological configuration between the conceptual end-members of 'channelized' and 'distributed', model the induced near-ice water circulation in three dimensions and study the resulting submarine melt.

4.2 Methods

4.2.1 Model set-up

We use the MITgcm (*Marshall et al.*, 1997a,b) in non-hydrostatic configuration to model water circulation in an idealized fjord. The domain is 2 km in length and width, and 500 m in depth. Resolution is 5 m across-fjord and vertically, while along-fjord resolution is 5 m for the 250 m closest to the glacier, thereafter increasing to ∼40 m and remaining constant for the 1 km closest to the ocean end of the domain. In all experiments the vertical motion of the plumes is contained within the high resolution section of the domain.

Initial temperature (T_a) and salinity (S_a) (Fig. 4.1a) are set throughout the domain with data from *Chauché et al.* (2014), who report CTD casts close to Store and Rink Glaciers. The fjord sides are closed boundaries, while at the ocean boundary we impose a sponge layer (e.g. *Sciascia et al.*, 2013) which restores properties towards the T_a/S_a profiles shown in Fig. 4.1a. The glacier end of the domain consists of a vertical calving front 2 km wide by 500 m high. This boundary is closed, except for subglacial channels at the base of the calving front, through which fresh (0 psu) subglacial discharge is injected at the pressure melting point (-0.29°C). Melting of the calving front is treated using the 'icefront' package (*Losch*, 2008; *Xu et al.*, 2012) with a slightly modified

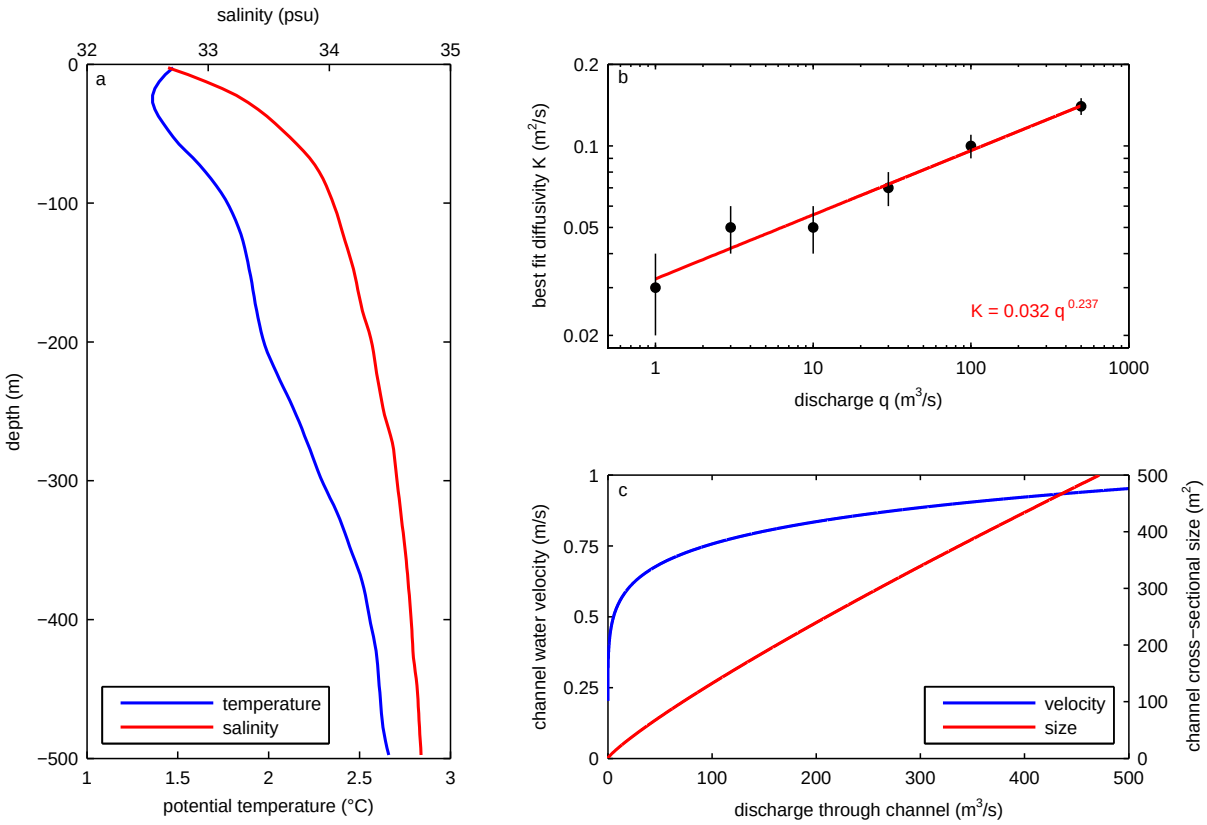

Figure 4.1: (a) Initial and boundary conditions for fjord temperature and salinity. Data are derived from profiles in *Chauché et al.* (2014). (b) The relationship between model diffusivity and per plume discharge, obtained by comparison of plume theory and MITgcm simulations in a simplified set-up, and applied throughout our main simulations. Vertical black bars represent ± 0.01 m^2/s on the best fit diffusivity, which is the increment by which we varied K in the comparison procedure. (c) The relationship between channel discharge, size and velocity obtained by balancing wall melt and creep closure in a Röthlisberger channel.

melt rate parameterization described in section 4.2.3 below. In common with *Xu et al.* (2013) and *Kimura et al.* (2014) we implement a free-slip condition on the calving front. Quoted melt rates are temporal averages over a 7000s period after melt reaches a steady state, which provides a period of sufficient length to smooth out turbulence-induced fluctuations (which are no more than 8% of the mean melt rate).

4.2.2 Subgrid-scale mixing

The turbulent nature of subglacial discharge plumes leads to entrainment of surrounding fjord water, with the rate of entrainment strongly affecting plume dynamics, and therefore the submarine melt and fjord circulation induced. At 5 m resolution, turbulence is not fully resolved, so some parameterization of the entrainment process is required. This is achieved using Laplacian eddy diffusion of momentum, heat and salt. With isotropic model resolution, our diffusivities are isotropic (e.g. *Kimura et al.*, 2014), and further we set the Prandtl number to 1 (e.g. *Sciascia et al.*, 2013) leaving one degree of freedom (K) to set the magnitude of subgrid-scale mixing. In common with previous studies, we calibrate this degree of freedom using buoyant plume theory. Specifically, we model a vertically issuing plume of initial discharge $q = 1$, 3, 10, 30, 100 or 500 m^3/s in a cubic domain of side 500 m, and compare the resulting plume width, velocity, temperature and salinity to the buoyant plume theory of *Morton et al.* (1956). By varying diffusivity K in increments of 0.01 m^2/s, we identify the value of K which gives the best fit to buoyant plume theory for each value of q. We find that this value of K is approximately proportional to $q^{1/4}$, and use a power law fit (Fig. 4.1b) to choose an appropriate value of K for each of our experiments. Further details regarding this procedure are given in section S1.2.

4.2.3 Melt Rate Parameterization

The melt rate parameterization at the calving front is the three equation model (*Holland and Jenkins*, 1999) which has frequently been used in this setting (e.g. *Xu et al.*, 2013; *Sciascia et al.*, 2013; *Kimura et al.*, 2014). Free stream properties for input to the melt rate parameterization are taken from the grid cells adjacent to the ice. We use velocity-dependent turbulent transfer coefficients $\gamma_{T,S} = C_d^{1/2}\Gamma_{T,S}U$ and define $U = \max\left(\sqrt{v^2 + w^2}, U_0\right)$ where v/w are the tangential water velocities in the cells adjacent to the ice. Use of this parameterization introduces a minimum velocity U_0 into the melt calculation, motivated as follows. Laboratory experiments (*Huppert and Turner*, 1980) and theoretical modeling (*Wells and Worster*, 2008; *Jenkins*, 2011) suggest that in the absence of subglacial discharge or away from discharge-driven

plumes, the calving front should still melt leading to the formation of weak convection cells. This is the regime of melt-driven convection rather than the convection-driven melt which is the main focus of this paper. *Sciascia et al.* (2013) modeled melt-driven convection in a two-layer stratification, achieving vertical velocities averaging 0.04 m/s. We find that with a model resolution of 5 m, and even at the low values of K used in this study, we do not resolve the delicate plumes formed in the absence of subglacial discharge. Thus in order to represent this 'zero-discharge' or background melt, we impose a minimum velocity $U_0 = 0.04$ m/s in the melt calculation.

4.2.4 Subglacial Hydrology

Input of a total subglacial discharge Q into the fjord beneath the vertical calving front of the glacier requires the choice of the number of discharging channels n, channel size X, velocity V and channel shape. In this study we vary n and assume the channels are approximately semi-circular in shape. In order to relate X and V to a discharge $q = Q/n$ in each channel, we balance wall melt and creep closure in a Röthlisberger channel (*Röthlisberger*, 1972; *Schoof*, 2010), giving relationships $X \propto q^{6/7}$ and $V \propto q^{1/7}$ (Fig. 4.1c, see also section S1.4). Note that this calculation is only applicable to grounded termini; indeed the assumption of a vertical calving front with discrete subglacial channels may only be relevant to grounded termini.

4.2.5 Description of Experiments

This study aims to determine the effect of variation in near-terminus subglacial hydrology on tidewater glacier submarine melt rates. We use three values of total subglacial discharge Q = 125, 250 and 500 m^3/s, and vary the subglacial hydrology between the end members of 'channelized' and 'distributed' drainage. We split the discharge Q over a number n = 1, 2, 3, 5, 10 or 50 identical channels spaced evenly along the glacier grounding line. These runs are indexed by the parameter $\alpha = 1/n$. To refer to a certain simulation we introduce some notation; $Q_{250}\alpha_{0.1}$ refers to the simulation with a total discharge of 250 m^3/s emerging through 10 identical channels spaced evenly. We also include experiments in which the discharge is uniformly distributed across

the grounding line (identified with $\alpha = 0$) and a number of sensitivity experiments, discussed in section 4.3.2. A full list of model parameters is given in Table S1.1.

4.3 Results and Discussion

Velocity, temperature and submarine melt rate distributions for various experiments are shown in Fig. 4.2, with rates spatially averaged over the 2 km wide by 500 m high calving front displayed in Fig. 4.3. When $Q = 0$ m^3/s, and at the lowest diffusivity used in any of the experiments (0.025 m^2/s), water velocities in the cells adjacent to the ice do not exceed U_0, thus U_0 is the velocity used in the melt parameterization. Melt rate is then determined by water temperature and is therefore greater at depth. Averaged over the calving front, we obtain 0.12 m/d of background melt in this case (Fig. 4.3).

4.3.1 Varying channel number (α)

Model snapshots of ice-tangential water velocity at the calving front are shown in Figs. 4.2a-d. After emerging from a subglacial channel, the plumes rise turbulently and spread to form a conical shape. For each plume, maximum velocities are achieved at depth. Weak plumes ($q < 2.5$ m^3/s) reach neutral buoyancy before the surface, giving low near-surface velocities (Fig. 4.2d). Water velocities increase with increasing discharge per plume.

For $\alpha > 0.02$, high water velocities are contained within the conical plumes. Thus in the $Q_{500}\alpha_1$ simulation, water velocities exceed U_0 over just 29% of the calving front. Furthermore, the plumes remain visibly independent as their spacing is decreased until $\alpha = 0.2$ (Figs. 4.2b, c). In contrast, for $Q_{125}\alpha_{0.02}$ (Fig. 4.2d) the plumes coalesce within 200 m above the grounding line, and water velocities exceed U_0 over 92% of the calving front.

Snapshots of ice-adjacent water temperature are shown in Figs. 4.2e-h. After emerging from a channel, plume temperature increases due to mixing with ambient water. Consistent with plume theory, plumes with a higher initial discharge stay colder until

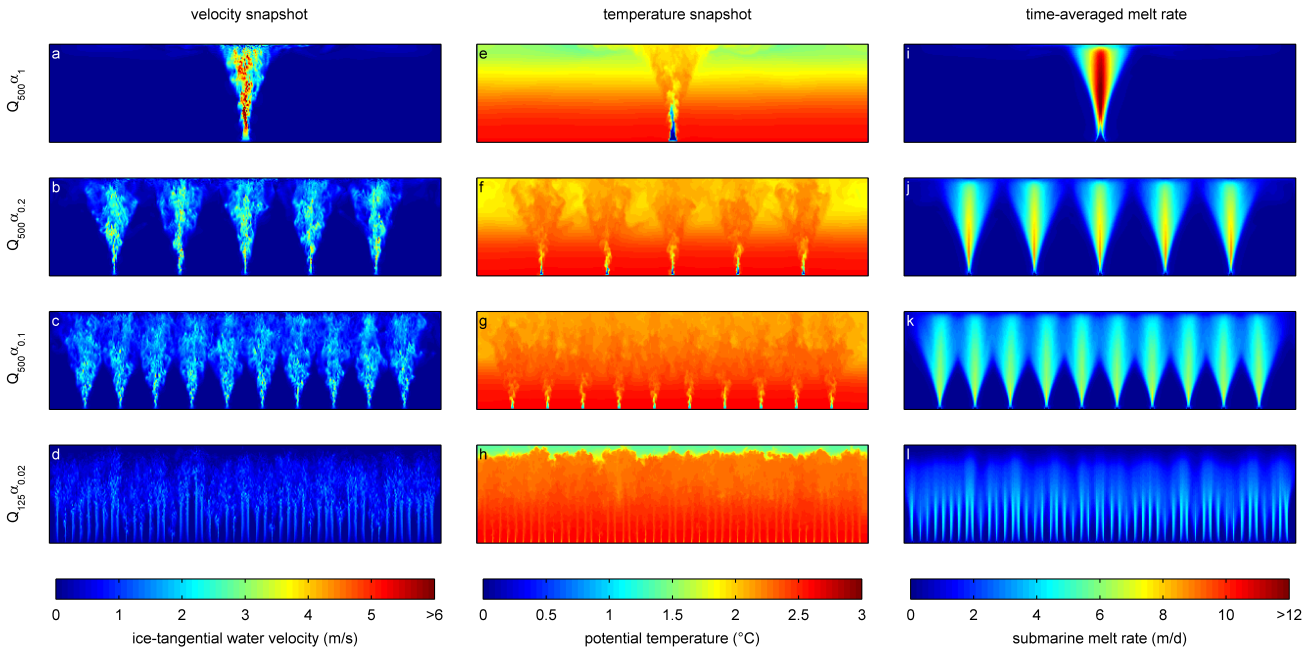

Figure 4.2: Left and centre columns: snapshots, 10000s after model initiation, of the magnitude of ice-tangential water velocity ($\sqrt{v^2 + w^2}$) and temperature. Right column: submarine melt rate, time-averaged over the period between 3000s and 10000s after model initiation. Plots are face-on views of the calving front, which is 2 km wide by 500 m high. Equivalent plots for all other experiments are shown in Figs. S1.3-S1.5.

closer to the surface, for example the $Q_{500}\alpha_1$ plume (Fig. 4.2e) remains colder than 1°C for ∼200 m while the $Q_{500}\alpha_{0.1}$ plumes are warmer than 1°C within 30 m above the grounding line (Fig. 4.2g).

All of the plumes simulated advect the warm and deep ambient water upwards, resulting in warming where the plumes reach the surface. Most of this warm plume water subsequently flows down-fjord and away from the ice, though there is also some lateral spreading across the calving front resulting in slight surface warming away from the plumes (e.g. Fig. 4.2e). With many plumes ($\alpha = 0.33$ or below, Fig. 4.2f), the cold surface water is replaced by warm plume water across most of the calving front, except when the plumes do not reach the surface (e.g. Fig. 4.2h). In the $Q_{125}\alpha_{0.02}$ simulation (Fig. 4.2h), water warmer than 2°C covers almost the entire calving front, and in

general an increased number of plumes results in a larger fraction of the calving front experiencing warm water.

Submarine melt resulting from the distribution of velocity and temperature is shown in Figs. 4.2i-l. Elevated melt rates are contained within a conical region above each subglacial channel. Maximum melt rates are generally achieved between 350 m and 450 m depth, coinciding with maximum velocities. In the $Q_{500}\alpha_1$ experiment (Fig. 4.2i), maximum velocities are obtained at ∼375 m depth, but the plume remains colder until closer to the surface and this shifts the maximum melt location up the calving front to ∼300 m depth. When plumes reach neutral buoyancy before the surface (Fig. 4.2l), melt rates are low near the surface. The melt distributions emphasize the independence of the plumes for $\alpha \geq 0.2$ (Figs. 4.2j, k). In general the distribution of melt follows that of velocity; areas of the glacier in contact with warm water but low velocities undergo little melt (e.g. Fig. 4.2e, i). This highlights that the melt rate parameterization used in this study is strongly dependent on water velocity, a dependence which has yet to be tested with observations from a real system.

Spatial averaging of the submarine melt rate gives the results displayed in Fig. 4.3. For all three total discharges considered, the spatially averaged submarine melt rate increases rapidly as the subglacial drainage system becomes more distributed. For $Q = 500$ m^3/s, the presence of 50 subglacial channels increases total submarine melt by a factor 4.5 over the single channel case. Such a trend can be motivated theoretically: *Cowton et al.* (2015) suggest melt rate for a single plume scales with discharge as $\dot{m} \propto Q^{2/5}$. If the plumes remain independent, splitting Q over n channels gives a per plume melt rate $(Q/n)^{2/5}$ and a total melt rate $n(Q/n)^{2/5} = \alpha^{-3/5}Q^{2/5}$. Then for a fixed total discharge but varying number of channels, melt should scale as $\alpha^{-3/5}$. Application to our $Q = 500$ m^3/s results provides a good fit from $\alpha = 1$ to 0.1, the latter of which is the point in our simulations when the plumes first merge. Finally the $\alpha = 0$ experiments are effectively two-dimensional (Figs. S1.3-S1.5) and give the highest total melt of all, reaching 3.6 m/d for $Q_{500}\alpha_0$. We argue that it is unlikely that water would emerge in a sufficiently uniform fashion that this case is realistic, and thus our sensitivity experiments use $\alpha = 0.02$ as a distributed end member.

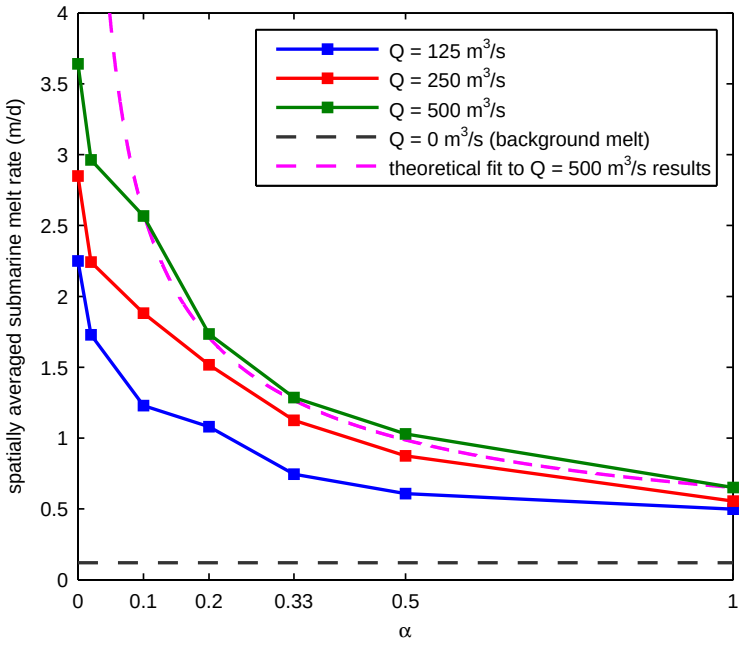

Figure 4.3: Spatially averaged melt rates for each of the model experiments. Also shown in grey is the $Q = 0$ m^3/s case, while a theoretical fit for $Q = 500$ m^3/s described in the text is shown in dotted pink.

The increase in total melt as discharge becomes more distributed can be viewed as arising from the sub-linear dependence of melt on discharge for a single plume. In terms of our modeled distributions of velocity and temperature, it arises because a distributed drainage system leads to both water motion and warmer water over a larger proportion of the calving front. We also note that the spatially averaged submarine melt rate is sensitive to glacier width when there is a single plume, while more distributed cases will be less sensitive to variation in glacier width. The theoretical argument above suggests that melt rate will increase with the number of plumes provided these plumes remain independent. As such, our results apply to 'wide' glaciers, where the glacier width is much larger than the width of a single plume. We expect the vast majority of tidewater glaciers in Greenland to satisfy this condition.

Input varied (units)	Values			Effect on $Q_{250}\alpha_{0.02}$ melt rate (%)		Effect on $Q_{250}\alpha_{1.00}$ melt rate (%)	
	default	low	high	low	high	low	high
T_i (°C)	-25	-35	-15	-5.5	+3.8	-4.7	+3.6
$C_d^{1/2}\Gamma_T$ (-)	1.10×10^{-3}	8.25×10^{-4}	1.38×10^{-3}	-23.0	+19.7	-22.4	+21.0
$C_d^{1/2}\Gamma_S$ (-)	3.10×10^{-5}	2.33×10^{-5}	3.88×10^{-5}	-4.5	+1.2	-4.5	+3.6
ΔT_a (°C)	0	-1	1	-26.2	+23.4	-26.5	+26.7
ΔS_a (psu)	0	-0.5	0.5	-2.1	+1.5	-0.9	+0.1
channel width (m)	20	10	60	n/a	n/a	-6.5	+8.8
slip condition	free slip	no slip	n/a	-35.9	n/a	-31.6	n/a
U_0 (m/s)	0.04	0	0.08	-1.4	-1.0	-12.4	+16.9
velocity (m/s)	0.83	0.42	1.67	n/a	n/a	+5.1	-2.7
K (m^2/s)	0.047/0.119	0.027/0.099	0.067/0.139	-3.7	0.0	4.8	-4.8
resolution (m)	5	10	2.5	-13.3	+8.3	-15.0	+3.7

Table 4.1: Results of sensitivity experiments: variation in model inputs and the effect on spatially averaged submarine melt rate in each of the two default cases $Q_{250}\alpha_{0.02}$ and $Q_{250}\alpha_1$, expressed as a percentage of the default case melt rate. Values of K in the default, low and high columns are for $\alpha = 0.02/\alpha = 1$ respectively.

4.3.2 Sensitivity Experiments

Numerical modeling of tidewater glacier submarine melt rates involves choice of several inputs which are poorly constrained. We therefore present a number of experiments designed to test the sensitivity of our results to variation in these inputs (Table 4.1). As base cases we take the $Q_{250}\alpha_{0.02}$ and $Q_{250}\alpha_1$ simulations. A brief discussion of the results is presented here with more detail in section S1.5.

The sensitivity of our results to the melt calculation parameters T_i, $C_d^{1/2}\Gamma_{T,S}$ and to a uniform shift in ambient temperature by ΔT_a at all depths can be understood largely by consideration of the melt calculation alone (*Holland and Jenkins*, 1999). Sensitivity to channel width and the slip condition are in line with results from *Kimura et al.* (2014).

Of relevance specifically to this study are the sensitivities to U_0, V, K and resolution. Sensitivity to U_0 is related to the proportion of the calving front which is significantly

affected by a plume, thus the $Q_{250}\alpha_{0.02}$ case is insensitive to a doubling of U_0, while $Q_{250}\alpha_1$ experiences a 17% increase in total melt (Table 4.1). Total melt proves relatively insensitive to channel velocity V; change in velocity by a factor two affects melt by at most 5% (Table 4.1).

Change in the diffusivity (K) affects the rate at which the plumes entrain ambient fjord water. We have fitted K to our experiments with a precision of 0.01 m^2/s, and variation in K by 0.02 m^2/s affects total melt by at most 5%. We also investigate resolutions of 2.5 and 10 m with diffusivities again chosen to fit plume theory. A decrease in resolution to 10 m results in decreases in total melt reaching ∼15%, while increasing resolution to 2.5 m gives modest increases in melt. In general, none of the sensitivity experiments performed suggest that the main conclusions of this paper would be affected by variation in our choice of model inputs.

4.4 Implications for Greenland Tidewater Glaciers

4.4.1 Melt rates

The results of this study suggest that the configuration of the near-terminus subglacial hydrological system is an important factor controlling tidewater glacier submarine melt rates. For a fixed total discharge, we predict that spatially averaged submarine melt rates increase quickly as discharge becomes more distributed. In particular the modeling suggests that, for the temperature and salinity profiles used in this study, a plume resulting from a single large subglacial channel is unable to induce spatially averaged submarine melt rates exceeding ∼0.65 m/d, or lower if a wider calving front was considered. However, numerous small plumes of subglacial discharge can induce significant submarine melt, but may not reach the fjord surface. Therefore plumes visible at the fjord surface may not be the dominant contributors to total submarine melt.

The melt rates achieved in this study display order of magnitude agreement with estimates from hydrographic data. However, it is important to stress that significant uncertainty exists in the submarine melt calculation outlined in section 4.2.3, notably

within the turbulent transfer coefficients $C_d^{1/2}\Gamma_{T,S}U$ (e.g. *Jenkins*, 2011), and regarding the relative importance of temperature and water velocity. It is also important to acknowledge that hydrographic data provide a snapshot of conditions in fjords which display significant short-term variability (*Straneo et al.*, 2010; *Jackson et al.*, 2014), such that calculated heat transport may not be representative of the mean (*Sutherland et al.*, 2014). Finally we emphasize that this study focuses in high resolution on a small section of fjord adjacent to the glacier terminus, using fixed T_a/S_a profiles. As such, we have neglected the potential effect of variations in subglacial hydrology on wider fjord circulation which might in turn affect melt rates (*Jackson et al.*, 2014; *Sciascia et al.*, 2014).

4.4.2 Calving

Aside from influencing total melt, variations in subglacial hydrology might also influence calving rate and style due to spatially varying melt. In general, within the modeled plumes, melt rates are greater at depth, which could lead to undercutting of the terminus and amplification of calving (*O'Leary and Christoffersen*, 2013). Considering across-ice variation in melt rate, isolated plumes (e.g. $Q_{500}\alpha_1$) might lead to the formation of calving bays and unstable headlands, consistent with the calving style observed at Store Glacier (*Chauché et al.*, 2014). It is also possible that calving front morphology might impact plume dynamics, with the potential for important feedbacks between plume dynamics, submarine melt and calving. Indeed the melt rates modeled in this study are not sufficient to directly explain the observed retreat of tidewater glaciers in Greenland, thus if ocean forcing is the key driver of this retreat, it is likely a result of a close coupling between submarine melt and calving mechanics.

4.5 Conclusion

A general circulation model, MITgcm, has been used to model near-ice water circulation and submarine melt rates driven by buoyant subglacial discharge at the terminus of an idealized tidewater glacier. The emergence of discharge at the grounding line of the

glacier is varied between the end members of a 'distributed' and 'channelized' subglacial hydrological system, focusing on the effect of this variation on submarine melt.

The results suggest that variation in subglacial hydrology results in large changes in both the distribution and total volume of submarine melt. In particular we find that (i) total melt volume is greater when discharge emerges in a distributed rather than channelized fashion, with enhancement by a factor 5 possible under certain conditions, (ii) strong plumes emerging from large subglacial channels are not, in isolation, able to induce large total melt volumes, but (iii) numerous and distributed small inputs of subglacial discharge are able to drive significant submarine melt. The distribution of melt rate has the potential to influence calving front morphology and calving style, a coupling which remains poorly understood but is likely important for tidewater glacier dynamics. Our results identify a need to constrain near-terminus subglacial hydrology at tidewater glaciers if we are to represent ocean forcing accurately and ultimately to understand and even predict the behaviour of Greenland's outlet glaciers.

Chapter 5

Scalings for submarine melting at tidewater glaciers from buoyant plume theory

The previous chapter showed that near-terminus subglacial hydrology strongly influences submarine melting at tidewater glaciers by controlling the geometry and number of proglacial plumes operating at the ice-ocean interface. The approach taken in Chapter 4 - simulation of plumes using MITgcm - is however computationally intensive, and for the understanding of plume dynamics across a wide range of physical settings, a more efficient approach is preferable. This chapter therefore applies the far quicker buoyant plume theory (*Morton et al.*, 1956) to investigate plume behaviour at tidewater glaciers.

In contrast to previous work (e.g. *Jenkins*, 2011), the focus here is explicitly on plumes in which the buoyancy of the plume is dominated by the subglacial discharge, as is likely the case for vigorous plumes at tidewater glaciers where inputs from subglacially emerging meltwater are substantial. This chapter seeks to develop simple relationships between plume dynamics, submarine melting and key physical parameters such as the magnitude of subglacial discharge and the fjord stratification. The understanding

developed provides a foundation for each of the subsequent chapters; Chapter 6 relies on the limited effect of submarine melting on plume dynamics, Chapter 7 builds on the identified controls which determine the height to which a plume rises, and Chapter 8 further develops the simple estimates of submarine melt rate introduced here.

Published in **Journal of Physical Oceanography**, June 2016.

Authors: D. A. Slater[1], D. N. Goldberg[1], P. W. Nienow[1], and T. R. Cowton[1].

1. School of Geosciences, University of Edinburgh, Edinburgh, UK.

Citation: Slater, D. A., D. N. Goldberg, P. W. Nienow, and T. R. Cowton (2016), Scalings for submarine melting at tidewater glaciers from buoyant plume theory, *Journal of Physical Oceanography, 46*(6), 1839-1855, doi: 10.1175/JPO-D-15-0132.1.

Author contributions: All authors guided the research. D.A.S. performed the calculations with guidance from D.N.G. D.A.S. wrote the paper, with input from all other authors.

Abstract

Rapid dynamic changes at the margins of the Greenland Ice Sheet, synchronous with ocean warming, have raised concern that tidewater glaciers can respond sensitively to ocean forcing. Our understanding of the processes encompassing ocean forcing nevertheless remains embryonic. We use buoyant plume theory to study the dynamics of proglacial discharge plumes arising from the emergence of subglacial discharge into a fjord at the grounding line of a tidewater glacier, deriving scalings for the induced submarine melting. Focusing on the parameter space relevant for high discharge tidewater glaciers, we suggest that in an unstratified fjord the often quoted relationship between total submarine melt volume and subglacial discharge raised to the power 1/3 is appropriate regardless of plume geometry provided discharge lies below a critical value. In these cases it is then possible to formulate a simple equation estimating total submarine melt volume as a function of discharge, fjord temperature and calving front height. However once linear stratification is introduced - as may be more relevant for fjords in Greenland - the total melt rate-discharge exponent may be as large as 3/4 (2/3) for a point (line) source plume and displays more complexity. Our scalings provide a guide for more advanced numerical models, inform understanding of the processes encompassing ocean forcing, and facilitate assessment of the variability in submarine melting both in recent decades and under projected atmospheric and oceanic warming.

5.1 Introduction

Loss of ice from the Greenland Ice Sheet contributed ∼8 mm to global sea level between 1992 and 2012 (*Shepherd et al.*, 2012; *Vaughan et al.*, 2013), with the rate of loss accelerating over the same period (*Rignot et al.*, 2011) such that between 2009 and 2012, Greenland contributed ∼1 mm yr^{-1} to global sea level (*Enderlin et al.*, 2014). Driven by a period of tidewater glacier acceleration and retreat (*Moon et al.*, 2012; *Jiskoot et al.*, 2012), ice flux into the ocean from tidewater glaciers accounted for approximately half of Greenland's mass balance deficit in the early 2000s (*van den Broeke et al.*, 2009). Tidewater glacier dynamics can therefore have a significant impact on Greenland Ice Sheet mass balance.

The dramatic changes observed at many of Greenland's outlet glaciers occurred during a period of atmospheric and oceanic warming (*Mernild et al.*, 2014; *Rignot et al.*, 2012); however a conclusive attribution of the response of tidewater glaciers to one of these factors remains elusive. Indeed many of the processes affecting tidewater glaciers are promoted by both of these forcings, such that a full understanding of the dynamics likely requires consideration of both atmospheric and oceanic factors (*Straneo and Cenedese*, 2015). One such process is submarine melting of the calving front, on which this paper is focused.

Submarine melting may contribute to mass loss either directly via melting of submerged ice (*Motyka et al.*, 2013; *Bartholomaus et al.*, 2013; *Inall et al.*, 2014), or indirectly by controlling calving style and rate (*O'Leary*, 2011; *Chauché et al.*, 2014) or grounded ice flux (*Holland et al.*, 2008a). Submarine melting is thought to be promoted by both the presence of warm water of subtropical origin in Greenlandic fjords (*Straneo et al.*, 2010; *Mortensen et al.*, 2011) and the emergence of subglacial discharge at the grounding line of the glacier (*Jenkins*, 2011). Presence of the latter results in proglacial plumes as the discharge rises buoyantly, and the high ice-adjacent water velocities generated increase the turbulent transfer of heat to the ice. These proglacial plumes are the focus of this study.

Given the difficulties of directly measuring submarine melt rates, estimates have to date relied either on modelling or on hydrographic data taken some distance from the glacier terminus. The hydrographic data can in theory be used to calculate a net toward-glacier heat flux. This method has been applied around Greenland to obtain submarine melt rates ranging from 0.7 to 10 $\mathrm{m\,d^{-1}}$ (*Rignot et al.*, 2010; *Sutherland and Straneo*, 2012; *Xu et al.*, 2012; *Inall et al.*, 2014). Such estimates should however be viewed with caution as fjord dynamics can display significant short term variability (*Jackson et al.*, 2014; *Straneo and Cenedese*, 2015) such that a calculated melt rate may not be indicative of a longer term mean. There may also be considerable loss of heat between the flux gate and calving front due to the melting of submerged proglacial ice mélange (*Inall et al.*, 2014).

An alternative approach uses high-resolution numerical modelling to predict ice-adjacent water velocities and temperatures, which are then converted to a submarine melt rate using a melt parameterisation (*Holland and Jenkins*, 1999). This has been undertaken in both two (*Xu et al.*, 2012; *Sciascia et al.*, 2013, 2014) and three dimensions (Chapter 4; *Xu et al.*, 2013; *Kimura et al.*, 2014; *Slater et al.*, 2015; *Carroll et al.*, 2015). These models have facilitated investigation of the spatial distribution of submarine melting, and of how submarine melting responds to variations in subglacial discharge, fjord temperature and near-terminus subglacial hydrology. A key result from these studies is that per plume, submarine melt rate responds sublinearly to increasing subglacial discharge. Specifically these studies suggest a relation $\dot{m} \propto Q^{\gamma}$ between submarine melt rate $\dot{m}$ and subglacial discharge Q, with γ taking various values from $\gamma < 1/3$ (*Kimura et al.*, 2014) to $1/3$ (*Xu et al.*, 2012; *Sciascia et al.*, 2013; *Kimura et al.*, 2014), $1/2$ (*Sciascia et al.*, 2013; *Xu et al.*, 2013) and ~ 0.85 (*Xu et al.*, 2013). All studies show a linear response of melt rate to variation in water temperature (*Sciascia et al.*, 2013; *Xu et al.*, 2013). Finally Chapter 4; *Slater et al.* (2015) suggested that the total submarine melt volume is greater if the subglacial discharge emerges via drainage which is distributed across the grounding line rather than concentrated in a few large channels. Numerical models however rely on a melt parameterisation which has as yet been validated only beneath an Antarctic ice shelf (*Jenkins et al.*, 2010) which is likely a substantially different setting to vertical calving fronts at tidewater glaciers.

A final method of investigating submarine melt rates - and the approach taken in this study - is buoyant plume theory (BPT). BPT has been successfully applied to a wide range of environmental phenomena, traceable back to the classic paper by *Morton et al.* (1956). BPT describes the evolution of a source of buoyancy as it rises through an ambient fluid. In this glacial application we use BPT to describe ice-adjacent water velocity and temperature within a proglacial plume. This approach avoids recourse to computationally expensive numerical simulations but is limited to idealised geometries. BPT has previously been applied to tidewater glaciers. *MacAyeal* (1985) and *Jenkins* (1991) were pioneering papers on the glacial application of BPT. *Wells and Worster* (2008) developed the theoretical basis of coupling plume theory

with submarine melting while *Jenkins* (2011) used BPT to propose, in advance of the numerical studies reported above, a cube root dependence of submarine melt rate on subglacial discharge and a linear dependence on fjord temperature. *O'Leary* (2011) applied BPT to obtain submarine melt rates for three glaciers in West Greenland and *Cenedese and Linden* (2014) have used laboratory experiments to investigate plume dynamics with a glacial motivation. Most recently, *Cowton et al.* (2015) used BPT to force the glacier boundary of an ocean general circulation model adapted to a fjord and *Carroll et al.* (2015) employed BPT to investigate plume outflow depth in a fjord.

In spite of the increasing body of research on submarine melting, there remain significant gaps in our understanding, both observationally (there has yet to be a direct measurement of submarine melting at a tidewater glacier), and in the modelling (for example the wide range of melt-discharge exponent γ values present in the literature). Given the potential importance of submarine melting for tidewater glacier dynamics, there is a need for further investigation of ice-ocean interaction, of which this study is an example.

This study uses BPT to investigate the dynamics of plumes in contact with the vertical calving fronts of tidewater glaciers with a focus on the submarine melt induced by the plume. We investigate both point and line plume sources and consider a fjord which is uniformly or linearly stratified. We also explore under what conditions a plume will reach the fjord surface. In undertaking these investigations we aim to (i) explain the variation in the value of the melt-discharge exponent γ found in the literature, (ii) suggest under what conditions a certain melt exponent may apply and (iii) facilitate assessment of the likely variation in submarine melt at tidewater glaciers, both in recent decades and under future climate scenarios.

5.2 Methods

5.2.1 Introduction to the model

In this paper we consider mainly a half-conical geometry for proglacial plumes (Fig. 5.1) which we believe to be appropriate for plumes arising from channelized subglacial

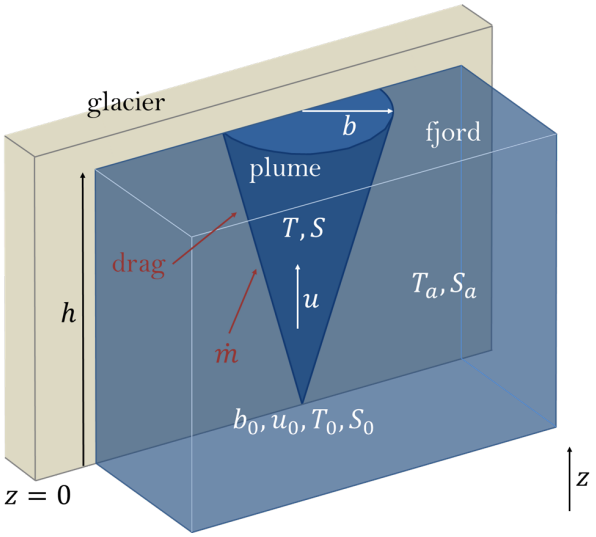

Figure 5.1: The half-conical plume considered in this study. The plume emerges into the fjord at the grounding line of the glacier and rises buoyantly, growing through entrainment of ambient fjord water.

drainage. The glacier terminates in a fjord of depth h and is assumed to have a vertical calving front in contact with the flat side of the plume. The plume has radius $b(z)$, vertical velocity $u(z)$, temperature $T(z)$ and salinity $S(z)$, assumed uniform across the radius of the plume. It experiences drag (coefficient C_d) and induces submarine melt $\dot{m}(z)$ where in contact with the ice. The proglacial fjord has temperature $T_a(z)$ and salinity $S_a(z)$, referred to as ambient conditions.

The plume is initiated at the glacier grounding line by a source of cold and fresh subglacial discharge. With a Greenlandic application in mind, the proglacial fjord is saline. Thus the density $\rho(z)$ of the plume - defined through an equation of state as a function of its temperature and salinity - is initially less than that of the ambient water $\rho_a(z)$ and the plume rises buoyantly. We assume that the plume is turbulent at the source. Turbulence causes the plume to entrain ambient water so that it grows as it rises. Following *Morton et al.* (1956) and numerous other successful applications of BPT, we assume that the rate of entrainment into the plume is proportional to plume velocity u, with a constant of proportionality α.

The entrainment of ambient water means that the temperature and salinity (and therefore density) of the plume are diluted towards the ambient conditions, thereby altering the plume buoyancy. If as a result the plume density exceeds the ambient water density, the plume is then negatively buoyant, will slow down and may not reach the fjord surface.

5.2.2 Defining equations

In order to quantify the evolution of the plume as it rises we introduce a set of equations with the half-conical geometry modified from *Morton et al.* (1956) and the coupling to submarine melt by *Jenkins* (2011) (though the plume considered therein was a two-dimensional line plume). The equations have been previously applied by *Cowton et al.* (2015) and conserve respectively the volume, momentum, heat and salt flux of the plume

$$\frac{d}{dz}\left(\frac{\pi}{2}b^2u\right) = \pi\alpha bu + 2b\dot{m} \tag{5.1a}$$

$$\frac{d}{dz}\left(\frac{\pi}{2}b^2u^2\right) = \frac{\pi}{2}b^2g' - 2C_dbu^2 \tag{5.1b}$$

$$\frac{d}{dz}\left(\frac{\pi}{2}b^2uT\right) = \pi\alpha buT_a + 2b\dot{m}T_b - 2C_d^{1/2}\Gamma_T bu\left(T - T_b\right) \tag{5.1c}$$

$$\frac{d}{dz}\left(\frac{\pi}{2}b^2uS\right) = \pi\alpha buS_a + 2b\dot{m}S_b - 2C_d^{1/2}\Gamma_S bu\left(S - S_b\right) \tag{5.1d}$$

where $g' = g(\rho_a - \rho)/\rho_{ref}$ is the reduced gravity of the plume, denoted g'_0 when evaluated at the glacier grounding line. ρ_{ref} is a Boussinesq reference density. C_d is the drag coefficient, while Γ_T and Γ_S are heat and salt transfer coefficients. Submarine melt rate $\dot{m}$, and ice-ocean boundary temperature T_b and salinity S_b are defined by the three-equation melt formulation (*Holland and Jenkins*, 1999).

$$\dot{m}\left(c_i\left(T_b - T_i\right) + L\right) = c_wC_d^{1/2}\Gamma_T u\left(T - T_b\right) \tag{5.2a}$$

$$\dot{m}S_b = C_d^{1/2}\Gamma_S u\left(S - S_b\right) \tag{5.2b}$$

$$T_b = \lambda_1 S_b + \lambda_2 + \lambda_3(h - z) \tag{5.2c}$$

Here the λ_i's describe the variation of freezing point with salinity, constant offset and variation with depth. c_i and c_w are the heat capacities of ice and water, and T_i is ice temperature (ice salinity is zero).

With a non-linear equation of state (e.g. *Fofonoff and Millard*, 1983), Eqs. 5.1a-5.2c are referred to in this paper as the full model (FM), solution of which is achieved by numerical integration. In order to develop scalings for plume variables and submarine melt under variation in the inputs, we require the model to be analytically tractable, and we thus now describe some simplifications.

5.2.3 Analytical model

The first simplification is to neglect the feedback of submarine melting on the plume. This entails removing the last term on the right hand side of Eq. 5.1a, representing the volume added by submarine melting, and the last two terms on the right hand sides of Eqs. 5.1c and 5.1d, representing the cooling and freshening effect of submarine melting, and heat and salt transfer out of the plume to the ice-ocean interface. Thus we are limiting ourselves to considering convection-driven melt rather than melt-driven convection; that is, we assume that the buoyancy provided by subglacial discharge dominates over the buoyancy added by submarine melting. It can be shown (section S2.1.1) that for ambient water of temperature T_a and subglacial discharge Q_{0m} at temperature T_0, this is the case for length scales $z < Z_m$ above the grounding line, where Z_m is given by

$$Q_{0m}^{2/3} \approx \frac{c_w C_d^{1/2} \Gamma_T}{L} \left(\frac{9 \alpha g_0'}{5\pi} \right)^{1/3} (T_a - T_0) \, Z_m^{5/3} \tag{5.3}$$

Equivalently, at a calving front of height Z_m, Eq. 5.3 gives the subglacial discharge Q_{0m} above which we may neglect the melt feedback. For a calving front which is 500 m high and for a fjord with $T_a = 3°\mathrm{C}$ and $S_a = 34$ psu we obtain $Q_{0m} \approx 0.2$ m^3 s^{-1}. For the largest calving front considered in this study (900 m) and for the warmest water ($T_a = 6°\mathrm{C}$) we obtain $Q_{0m} \approx 2$ m^3 s^{-1}. In summary a conservative estimate for the subglacial discharge below which submarine melting has an important feedback on the plume at real tidewater glaciers is $Q_{0m} \approx 5$ m^3 s^{-1}; in many cases it will be somewhat

smaller. Above this critical discharge, numerical results show that the melt feedback affects plume temperature by $< 2\%$ and salinity by $< 0.5\%$. Note that our focus in this paper on discharges significantly larger than Q_{0m} is equivalent to focussing on length scales z satisfying $z \ll Z_m$. This marks an important difference with the paper of *Jenkins* (2011), which focussed on a line plume in the region $z \sim Z_m$.

Further simplification is achieved by neglecting the plume-ice frictional drag which appears as the second term on the right hand side of Eq. 5.1b; inclusion of this term reduces plume velocity by only $\sim$2.5% in a uniform stratification (section S2.1.2). We also make use of a linear equation of state as in *Jenkins* (2011)

$$\rho = \rho_{ref}\left(1 + \beta_S(S - S_{ref}) - \beta_T(T - T_{ref})\right) \tag{5.4}$$

The simplified system of equations, consisting of Eqs. 5.1a-5.1d with only the first term on each of the right hand sides, together with Eqs. 5.2a-5.2c and the equation of state Eq. 5.4 will be referred to as the analytical model (AM).

5.2.4 Initial conditions

Solution of Eqs. 5.1a-5.1d requires initial conditions for plume radius b_0, velocity u_0, temperature T_0 and salinity S_0. Since the plume is initiated by fresh subglacial discharge at the pressure melting point, we take $T_0 = \lambda_2 + \lambda_3 h$ and $S_0 = 0$ psu. It is less clear how to choose b_0 and u_0.

The simplicity of this model requires that the subglacial discharge emerges into the fjord vertically, a situation which is unlikely to occur at a tidewater glacier. Horizontal emergence may be more realistic as the subglacial channel feeding the plume presumably lies along the ice-bed interface prior to reaching the grounding line. Horizontal emergence has been implemented in previous models, with choice of channel size and flow velocity based on the Manning equation (*Mugford and Dowdeswell*, 2011) or balance of wall melt and creep closure (Chapter 4; *Slater et al.*, 2015). Numerical models suggest that discharge emerging horizontally quickly transitions to vertical flow,

after which point our model should be applicable. We should therefore treat our results near the grounding line with caution.

One constraint on b_0 and u_0 is provided by specifying the subglacial discharge $Q_0 = \pi b_0^2 u_0/2$, but this does not uniquely fix b_0 and u_0; a discharge Q_0 can be achieved with a plume which is initially slow and wide, or one which is fast and narrow. These possibilities are distinguished by their ratio of buoyancy to momentum, a property quantified by a dimensionless number $\Gamma = 5bg'/8\alpha u^2$ (e.g. *Morton*, 1959; *Turner*, 1979; *Kaye*, 2008). A plume with $\Gamma = 1$ is described as pure, having a balance of buoyancy and momentum. Choice of the source value, Γ_0, provides a second constraint to uniquely fix b_0 and u_0. In a uniform stratification, a plume will quickly tend towards $\Gamma = 1$ as it rises (*Hunt and Kaye*, 2005). The plume is therefore quickly insensitive to the value of Γ_0, and we choose $\Gamma_0 = 1$ throughout this paper. Relaxing this assumption does not significantly affect our results, particularly when not close to the grounding line. Solving the two constraints provided by Q_0 and Γ_0, initial plume radius and velocity are given by

$$b_0 = \left(\frac{32\alpha\Gamma_0 Q_0^2}{5\pi^2 g_0'}\right)^{1/5} \qquad u_0 = \frac{2}{\pi}\left(\frac{5\pi^2 g_0'}{32\alpha\Gamma_0}\right)^{2/5} Q_0^{1/5} \tag{5.5}$$

where, as discussed above, we set $\Gamma_0 = 1$ unless stated otherwise.

To solve the model we now require only ambient conditions $T_a(z)$ and $S_a(z)$ and subglacial discharge Q_0. For two classes of ambient stratification (uniform and linear) we proceed with the analytical model to obtain fundamental scalings for plume properties and submarine melt under variation in the inputs. Values of the physical parameter values used are provided in Table S2.1.

5.3 Uniform stratification

5.3.1 Solution of defining equations

The simplest ambient conditions we can consider are those of a uniformly stratified fjord, where temperature and salinity do not vary with depth. This situation is

relevant typically to proglacial fjords in Alaska (*Bartholomaus et al.*, 2013) and also at depth in Greenland (*Chauché et al.*, 2014). In addition plume dynamics in a uniform stratification provide a good approximation to the initial rise of a plume in a linear stratification (*Morton*, 1959), and many of the results regarding submarine melting carry over to the linearly stratified case.

The solution to the analytical model in a uniform stratification (T_a, S_a), for a source of discharge Q_0, satisfying $T(0) = T_0$ and $S(0) = 0$ and with initial radius and velocity as defined in Eqs. 5.5 is (e.g. *Morton et al.*, 1956; *Turner*, 1979; *Straneo and Cenedese*, 2015)

$$b = \frac{6}{5}\alpha\,[z + z_0] \qquad u = \frac{5}{6\alpha}\left(\frac{9\alpha Q_0 g_0'}{5\pi}\right)^{1/3}[z + z_0]^{-1/3} \tag{5.6a}$$

$$T = T_0 + (T_a - T_0)\left(1 - \left[\frac{z_0}{z + z_0}\right]^{5/3}\right) \qquad S = S_a\left(1 - \left[\frac{z_0}{z + z_0}\right]^{5/3}\right) \tag{5.6b}$$

where

$$z_0 = \frac{5}{6\alpha}\left(\frac{32\alpha Q_0^2}{5\pi^2 g_0'}\right)^{1/5} \qquad \text{and} \qquad g_0' = g\left(\beta_S S_a - \beta_T (T_a - T_0)\right) \tag{5.6c}$$

Some example solutions are plotted in Fig. 5.2. Note that this solution holds regardless of the sign of $T_a - T_0$, though we focus here on the $T_a > T_0$ case, which is not a significant restriction for vertical calving fronts. The solution in Eqs. 5.6, including the split of buoyancy into temperature and salinity, is now entirely specified by the four parameters Q_0, T_a, S_a and h. Note that after setting $\Gamma_0 = 1$, z_0 is the one remaining independent characteristic length scale of the problem (e.g. *Kaye*, 2008), and ranges between 0 and 100 m for Q_0 between 0 and 1000 $\mathrm{m^3\,s^{-1}}$. An established result (*Morton*, 1959) is that a finite source pure plume (of which ours is an example since $Q_0 \neq 0$ and $\Gamma_0 = 1$) is equivalent to a plume emanating from a point source of buoyancy only situated a distance z_0 below the finite source. Furthermore, z_0 may be interpreted as the length scale over which the initial conditions influence plume dynamics (*Morton*, 1959; *Wright and Wallace*, 1979). Therefore for $z \ll z_0$ (i.e. close to the grounding line) plume properties are dominated by the initial conditions while for $z \gg z_0$ (i.e. far from the grounding line, or the point source limit) the plume has 'forgotten' its initial

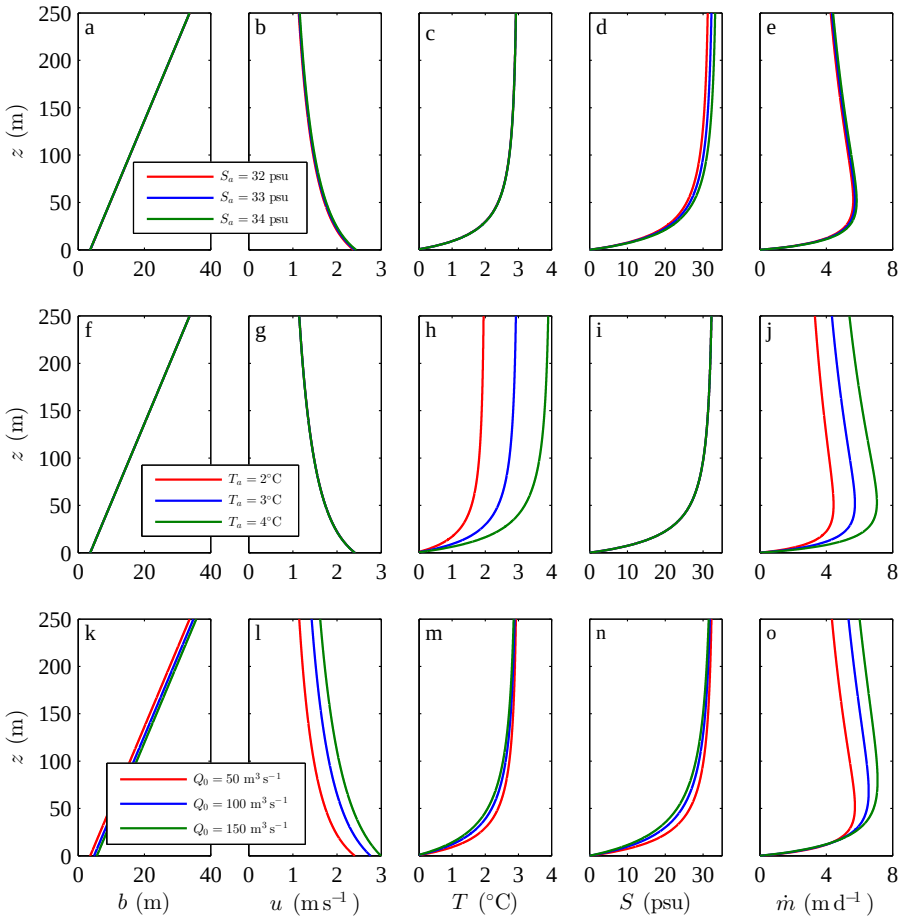

Figure 5.2: (a)-(e): effect of change in S_a, (f)-(j) T_a and (k)-(o) Q_0 on the half-conical plume in a uniform stratification. Unless being varied, the forcing parameters take values $Q_0 = 50$ m^3 s^{-1}, $T_a = 3°$C, $S_a = 33$ psu. Results shown are for the analytical model.

properties. In particular z_0 provides the characteristic length scale which determines how quickly plume temperature and salinity approach ambient values.

5.3.2 Local submarine melt rates

Local submarine melt rates are calculated by substituting Eqs. 5.6a-5.6c into Eqs. 5.2a-5.2c and are plotted in Figs. 5.2e, j and o. Immediately above the grounding line, melt increases quickly with height as the plume warms through entrainment of ambient water. Far from the grounding line, when plume temperature is close to the ambient,

variation in melt with height is dominated by velocity and decays as the inverse cube root of distance above the virtual source. The maximum melt rate is located at depth between these two regions. We now discuss the effect of Q_0, T_a and S_a on melt rates. Qualitatively, melt appears insensitive to S_a (Fig. 5.2e), linearly sensitive to T_a (Fig. 5.2j) and sublinearly sensitive to Q_0 (Fig. 5.2o).

Consider first the dependence of melt on S_a. Plume velocity is weakly affected and plume salinity responds approximately linearly to S_a (Eqs. 5.6 and Fig. 5.2). The submarine melt parameterisation does respond to change in plume salinity through S_b and T_b, however percentage changes in S_a in glacial settings are typically small (e.g. *Straneo and Cenedese*, 2015) and therefore do not result in significant variability in melt rates (Figs. 5.2e and 5.4d). Turning to the response of submarine melt rate to change in T_a, Eqs. 5.6 and Fig. 5.2 show that the only plume variable which responds significantly to T_a is plume temperature, and that it does so in an approximately linear fashion. The submarine melt parameterisation is also close to linear in plume temperature (*Holland and Jenkins*, 1999), and it therefore follows that melt rates respond linearly to T_a.

Sensitivity to subglacial discharge Q_0 is more complex. Previous studies (e.g. *Jenkins*, 2011) have motivated a power law relationship between local submarine melt rate and subglacial discharge, $\dot{m} \propto Q_0^{\gamma}$. Supposing γ were constant, we'd have $\gamma = (Q_0/\dot{m})\, d\dot{m}/dQ_0$, therefore it is useful to consider

$$\frac{Q_0}{\dot{m}}\frac{d\dot{m}}{dQ_0} = \frac{Q_0}{u}\frac{du}{dQ_0} + \frac{Q_0}{T-T_b}\frac{d}{dQ_0}\left(T - T_b\right) \tag{5.7a}$$

$$= \frac{1}{3}\left(1 - \frac{2}{5}\frac{z_0}{z+z_0}\right) + \frac{Q_0}{T-T_b}\left(\frac{dT}{dQ_0}\left[1 - \frac{dT_b}{dT}\right] - \frac{dS}{dQ_0}\frac{dT_b}{dS} - \frac{du}{dQ_0}\frac{dT_b}{du}\right) \tag{5.7b}$$

where we have used the fact that $c_i(T_b - T_i) \ll L$ in Eq. 5.2a. Note that in general Eq. 5.7b retains dependence on z and Q_0 and there is therefore no single value for γ which applies universally. Differentiation of Eq. 5.6b gives the response of plume temperature to change in subglacial discharge

$$\frac{dT}{dQ_0} = -\frac{2(T_a - T_0)}{3Q_0}\left(\frac{z_0}{z+z_0}\right)^{5/3}\frac{z}{z+z_0} \tag{5.8}$$

which, provided $T_a > T_0$, is always negative. This means that at a fixed depth, plume temperature decreases as initial flux increases. This arises because it takes longer to dilute the initial temperature through entrainment when there is a larger initial volume flux. A similar conclusion holds for dS/dQ_0.

We can use the melt rate parameterisation Eqs. 5.2a-5.2c to show that $dT_b/du = 0$, $0 < dT_b/dT < 1$ and $dT_b/dS < 0$ (section S2.2.1). Therefore, if $T_a > T_0$, the second term on the right hand side of Eq. 5.7a is negative (i.e. the effect of increasing subglacial discharge on plume thermal forcing causes a decrease in local melt rate). Conversely the first term in Eq. 5.7a is positive, which says that the effect of increasing subglacial discharge on plume velocity causes an increase in local melt rate.

In the point source limit ($z \gg z_0$) of Eq. 5.7a, the second term tends to zero and the first term tends to 1/3. This is the region in which the effect of initial volume flux on plume temperature has been 'forgotten' and therefore $\dot{m} \propto Q_0^{1/3}$ with the exponent of 1/3 arising from the plume velocity. Away from the point source limit we must consider both plume velocity and temperature and Eq. 5.7a is best investigated numerically using the full model.

Taking $T_a = 3°\text{C}$ and $S_a = 33$ psu, we plot the value of Eq. 5.7a as a function of z and Q_0 in Figs. 5.3a and 5.3c where $h = 300$ m and $h = 1000$ m respectively. We see that $0.30 < \gamma < 0.35$ for $z \gtrsim 8z_0$ and that γ is close to zero or negative for $z \lesssim z_0$, meaning that local melt rates decrease with increasing subglacial discharge. This occurs because, provided $T_a > T_0$, an increase in subglacial discharge decreases plume temperature and salinity, reducing thermal forcing $T - T_b$. This effect dominates over the change in plume velocity for $z \lesssim z_0$ (Figs. 5.3a and 5.3c). Note however that this statement is somewhat sensitive to plume initial conditions chosen at the grounding line; for $\Gamma_0 > 1$ local melt rates near the grounding line decrease more significantly with increasing subglacial discharge while for $\Gamma_0 < 1$ the effect is less significant. In general however it is a good approximation that local melt rates scale with $Q_0^{1/3}$ provided $z \gtrsim 8z_0$; otherwise the exponent is smaller than 1/3 and may even be negative.

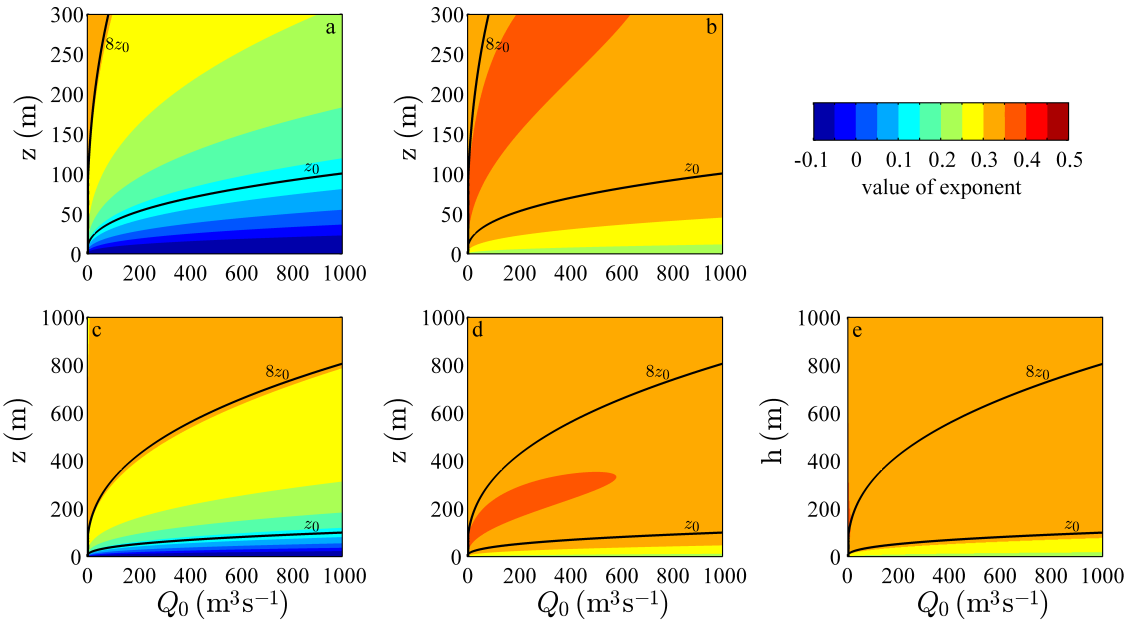

Figure 5.3: (a) and (c): plots of local melt rate-discharge exponent (i.e. γ in the relationship $\dot{m} \propto Q_0^{\gamma}$) as a function of subglacial discharge Q_0 and height above grounding line z. (b) and (d): exponent of the integrand in Eq. 5.9 (i.e. γ in the relationship $b\dot{m} \propto Q_0^{\gamma}$). Calving front height $h = 300$ m in (a) and (b) and $h = 1000$ m in (c) and (d). Note that (a) and (b) are not quite 'zoomed' versions of (c) and (d) due to the weak dependence of melt rate on pressure. (e) shows total melt rate-discharge exponent (i.e. γ in the relationship $\dot{M} \propto Q_0^{\gamma}$) as a function of Q_0 and h. Black lines show multiples of z_0. We take $T_a = 3°$C and $S_a = 33$ psu throughout. Results are generated using the full model.

5.3.3 Total submarine melt rates

It is important to distinguish between local and total submarine melt rates. The latter is here defined by

$$\dot{M} = \int_0^h 2b\dot{m}\, dz \tag{5.9}$$

and is the quantity measured by the heat flux gate estimates described in the introduction. We have discussed the character of $\dot{m}$ in the previous section, now we need also to consider plume radius b. Plume radius is insensitive to change in fjord

temperature and salinity. Noting that

$$\frac{Q_0}{b}\frac{db}{dQ_0} = \frac{2}{5}\left(1 - \frac{z}{z+z_0}\right) \tag{5.10}$$

we see that $b \propto Q_0^{2/5}$ near the grounding line while b becomes independent of Q_0 in the point source limit. The discharge exponent of the integrand in Eq. 5.9 is obtained by summing Eq. 5.7a and Eq. 5.10 and is plotted in Figs. 5.3b and d. For $z \lesssim z_0$, b dominates the exponent of the integrand while in the point source limit it does not contribute. Therefore the presence of plume radius b in Eq. 5.9 rather effectively cancels out the parameter space in which the local melt rate exponent is small and so except for very small z, the exponent of the integrand in Eq. 5.9 lies in the range 0.3 to 0.4 (Figs. 5.3b and d).

We seek lastly a value for the exponent in the relationship $\dot{M} \propto Q_0^{\gamma}$, plotted in Fig. 5.3e. This exponent is thus an integrated version of the exponents shown in Figs. 5.3b and d. For almost the full parameter space we have $0.3 < \gamma < 0.35$ (Fig. 5.3e). $\gamma < 0.3$ is only achieved when $h < z_0$. This occurs because the area of negative exponent seen in Fig. 5.3a becomes more dominant for smaller h. Since to our knowledge the vast majority of tidewater glaciers will satisfy $h > z_0$ it follows that the relationship $\dot{M} \propto Q_0^{1/3}$ will be a good approximation for total melt induced by half-conical plumes at tidewater glaciers.

We know from Eqs. 5.6a and preceding discussion that in the point source limit ($z \gg z_0$) and at the fjord surface, $b \propto h$ and $\dot{m} \propto h^{-1/3}$, and thus $\dot{M} \propto h^{5/3}$. In sum we can motivate a relationship between total submarine melt, forcings and calving front height which reads

$$\dot{M} = A_1 \left[1 + A_2(T_a - T_0)\right] Q_0^{1/3} h^{5/3} \tag{5.11}$$

valid for $h > z_0$. A_1 and A_2 are two constants whose value can be obtained numerically by minimising disagreement between Eq. 5.11 and the full model. For the ranges of Q_0, h, T_a and S_a indicated in Fig. 5.4, this yields $A_1 = 4.05 \times 10^{-6}$ $\mathrm{m^{1/3}s^{-2/3}}$ and $A_2 = 0.75$ $^{\circ}\mathrm{C}^{-1}$. Agreement of Eq. 5.11 with the full model is then excellent (Fig. 5.4) within the parameter range considered (maximum relative error 25%), suggesting that

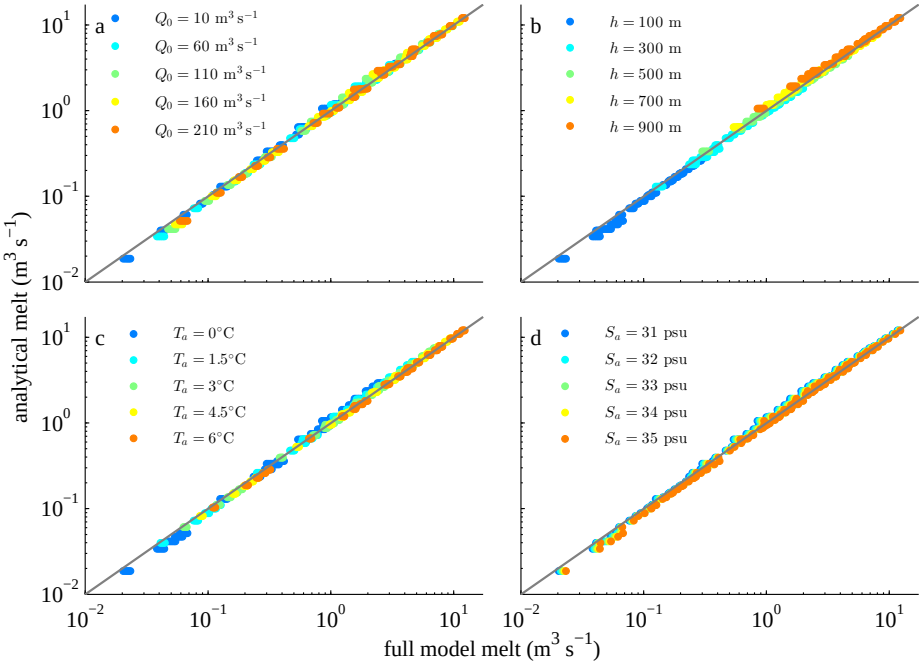

Figure 5.4: Comparison of total melt from the full model (x axes) with total melt from Eq. 5.11 (y axes). Each data point represents a particular choice of parameters from the ranges indicated (thus there are 625 data points on each plot). In (a) we distinguish data points by subglacial discharge Q_0, (b) calving front height h, (c) fjord temperature T_a and (d) fjord salinity S_a.

Eq. 5.11 is useful for estimating total melt without recourse to numerical integration of the full equations. Note that within the parameter range considered, h has the strongest influence on total melt (Eq. 5.11 and Fig. 5.4b), followed by T_a, Q_0 then S_a (Figs. 5.4c, a and d respectively). Note also that Eq. 5.11 remains a good estimate even if we relax the assumption $\Gamma_0 = 1$; the maximum relative error is less than 33% for $1/4 < \Gamma_0 < 30$.

We next consider a linearly stratified fjord, where plumes may not reach the fjord surface and the relationship between submarine melt and subglacial discharge is modified.

5.4 Linear stratification

5.4.1 Defining equations

We now consider linear stratification in temperature or salinity (or both). Continuing to neglect the melt feedback, Eqs. 5.1c and 5.1d may be rewritten (*Morton et al.*, 1956)

$$\frac{d}{dz}\left(\frac{\pi}{2}b^2 u g'_T\right) = -\frac{\pi}{2}b^2 u N_T^2 \tag{5.12a}$$

$$\frac{d}{dz}\left(\frac{\pi}{2}b^2 u g'_S\right) = -\frac{\pi}{2}b^2 u N_S^2 \tag{5.12b}$$

where $g'_T = -g\beta_T(T_a - T)$ and $g'_S = g\beta_S(S_a - S)$ are the reduced gravity of the plume due to temperature and salinity. $N_T^2 = g\beta_T\, dT_a/dz$ and $N_S^2 = -g\beta_S\, dS_a/dz$ are the constant squared buoyancy frequencies due to linear stratification in temperature and salinity. Since fjords in Greenland are warmer and saltier at depth we have $dT_a/dz < 0$ and $dS_a/dz < 0$ and thus $N_T^2 < 0$ and $N_S^2 > 0$. Using the linear equation of state Eq. 5.4 we can combine Eqs. 5.12a and 5.12b into one equation for the evolution of plume buoyancy

$$\frac{d}{dz}\left(\frac{\pi}{2}b^2 u g'\right) = -\frac{\pi}{2}b^2 u N^2 \tag{5.13}$$

where $g' = g'_T + g'_S$ and $N^2 = N_T^2 + N_S^2$. As previously noted it is salinity which dominates density variation in proglacial fjords and therefore N^2 is dominated by N_S^2. Eqs. 5.1a, 5.1b and 5.13 are equivalent to the equations considered in *Morton et al.* (1956). We now consider the effect of stratification on plume dynamics and submarine melt rates in three cases.

5.4.2 Stratification in temperature but not salinity

As a limiting case we consider stratification in temperature but not salinity. Since ambient temperature has a very weak effect on plume dynamics and provided the stratification is not too strong ($|N_T^2|^{3/8} < (2\pi)^{-1/4}\alpha^{-1/2}(Q_0 g'_0)^{1/4}h^{-1}$, see below), we can approximately use the uniform stratification solution from section 5.3 for b and u

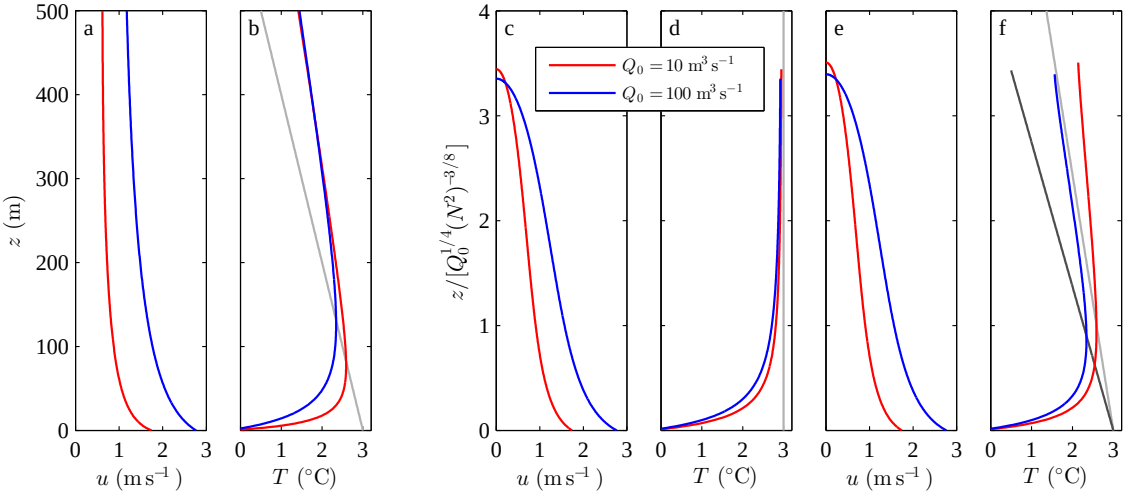

Figure 5.5: Plume velocity and temperature in the linear stratification cases described in the text. (a) and (b) have $dT_a/dz = -0.005$°C m^{-1} and $dS_a/dz = 0$ psu m^{-1}. (c) and (d) have $dT_a/dz = 0$°C m^{-1} and $dS_a/dz = -0.005$ psu m^{-1}. (e) and (f) have $dT_a/dz = -0.005$°C m^{-1} and $dS_a/dz = -0.005$ psu m^{-1}. Note that in (c)-(f) we plot non-dimensionalised z on the y-axis. Grey lines show the ambient temperature; in (f) the plotting of non-dimensional z on the y-axis leads to two ambient temperature lines: the lighter grey applies for $Q_0 = 10$ m^3 s^{-1}, the darker grey for $Q_0 = 100$ m^3 s^{-1}. Ambient values at the grounding line are $T_{a,0} = 3$°C and $S_{a,0} = 33$ psu.

to integrate Eq. 5.12a, obtaining

$$T_a - T = \frac{Q_0}{Q}(T_{a,0} - T_0) + \frac{3}{8}\frac{dT_a}{dz}\left(z + z_0\left[1 - \left(\frac{z_0}{z+z_0}\right)^{5/3}\right]\right) \tag{5.14}$$

where $T_{a,0}$ is the ambient temperature at the grounding line. The first term on the right hand side represents the uniform stratification solution, the second term is the modification due to stratification. Note that with stratification in temperature, we no longer have $T_a - T \to 0$ in the point source limit (Fig. 5.5b) as in the uniform stratification case (Fig. 5.2).

Since local melt rates scale linearly with plume temperature, it follows from Eq. 5.14 that local and therefore total melt rates decrease linearly as $|dT_a/dz|$ increases (with

ambient temperature at the grounding line held fixed). The second term on the right hand side of Eq. 5.14 is an increasing but weak function of Q_0. Indeed in the point source limit we obtain $T_a - T \approx (3/8)\, z\, dTa/dz$ which is independent of Q_0. Therefore the presence of stratification in temperature slightly increases the sensitivity of plume temperature to subglacial discharge, but temperature is independent of Q_0 in the point source limit. The exponent γ in the relationship $\dot{M} \propto Q_0^{\gamma}$ (Fig. 5.6a) therefore shows only minor differences to the uniform stratification case (Fig. 5.3e).

5.4.3 Stratification in salinity but not temperature

In this case we may no longer ignore the effect of stratification on plume dynamics, and the plume may become neutrally buoyant before the fjord surface (Fig. 5.5c, see also section S2.3.1). Consider a point source with buoyancy flux $B_0 = Q_0 g_0'$ in linear stratification $N^2 = N_S^2$. Scaling of plume properties with these parameters can be obtained by non-dimensionalising Eqs. 5.1a, 5.1b and 5.13 following e.g. *Morton et al.* (1956); *Turner* (1979). We obtain

$$b \propto B_0^{1/4}(N^2)^{-3/8} \qquad u \propto B_0^{1/4}(N^2)^{1/8} \qquad g' \propto B_0^{1/4}(N^2)^{5/8} \qquad z \propto B_0^{1/4}(N^2)^{-3/8} \tag{5.15}$$

The characteristic length scale $B_0^{1/4}(N^2)^{-3/8}$ may be interpreted as the height through which the plume rises before stratification becomes important and may be motivated as the height over which a depth integral of the right hand side of Eq. 5.13 becomes comparable to B_0. This scaling therefore represents a balance between dynamics dominated by the initial flux of buoyancy and dynamics dominated by the ambient stratification.

These scalings assume a point source for the plume located at $z = 0$, however plumes at tidewater glaciers are initiated by finite sources. As motivated above, there is a region $z < z_1 = (2\pi)^{-1/4}\, \alpha^{-1/2} B_0^{1/4}(N^2)^{-3/8}$ (*Morton* (1959) and Fig. S2.1) in which a plume in a linear stratification behaves as if in a uniform stratification. Provided our finite source lies within this region (i.e. $z_0 < z_1$, which will be the case for glacial applications) we may trace back to a virtual point source as in the uniform stratification

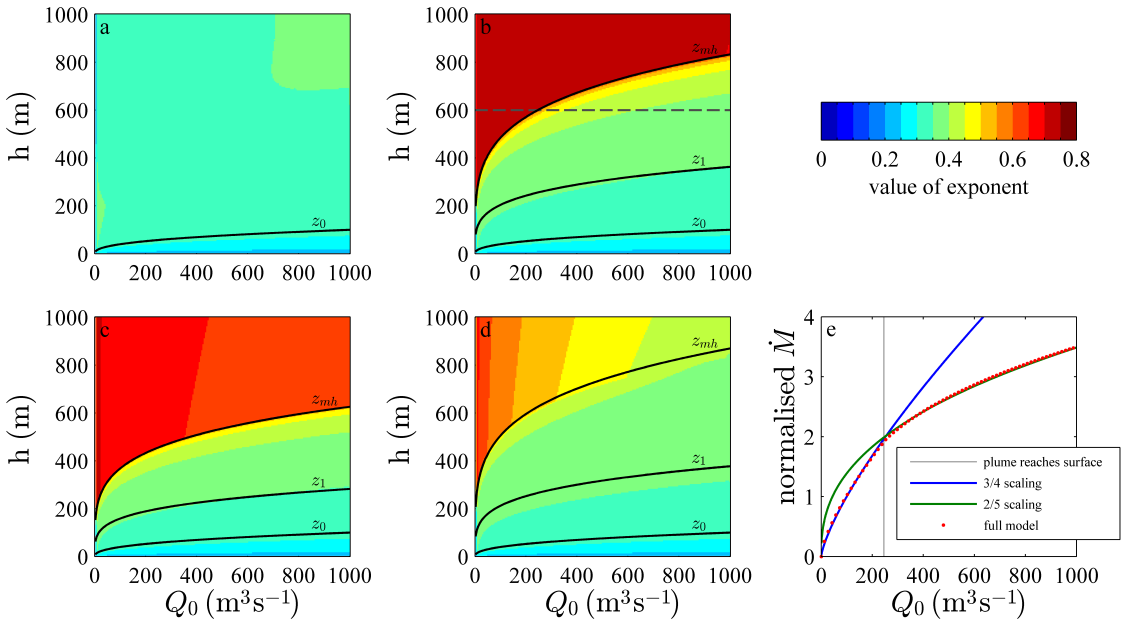

Figure 5.6: (a)-(d): total melt rate-discharge exponent (i.e. γ in the relationship $\dot{M} \propto Q_0^{\gamma}$) for linear stratifications. (a) has $dT_a/dz = -0.005°\text{C m}^{-1}$ and is unstratified in salinity, (b) has $dS_a/dz = -0.005$ psu m^{-1} and is unstratified in temperature, (c) has $dT_a/dz = -0.005°\text{C m}^{-1}$ and $dS_a/dz = -0.01$ psu m^{-1} and (d) has $dT_a/dz = -0.01°\text{C m}^{-1}$ and $dS_a/dz = -0.005$ psu m^{-1}. (e) shows a specific example of the total melt rate-discharge relationship for $h = 600$ m, and corresponds to the horizontal dashed line in (b). Solid black lines depict the three length scales which control melt rate exponent as discussed in the text. Ambient values at the grounding line are $T_{a,0} = 3°\text{C}$ and $S_{a,0} = 33$ psu. Results are generated using the full model.

case and in particular identify the point source buoyancy flux B_0 with the finite source flux $Q_0 g_0'$ (*Morton*, 1959; *Hunt and Kaye*, 2001).

Beyond the region in which the uniform stratification solution is a good approximation, plume density approaches ambient values and the linear stratification solution departs from the uniform equivalent. The plume then undergoes buoyancy reversal at a height z_{br} and thereafter reaches a maximum height z_{mh} above the grounding line given by

(e.g. *Turner* (1979); *Hunt and Kaye* (2001), see also section S2.3.1)

$$z_{br} = 1.95\,(N^2)^{-3/8}\left(\frac{Q_0 g_0'}{2\pi\alpha^2}\right)^{1/4} - \frac{5}{6\alpha}\left(\frac{32\alpha Q_0^2}{5\pi^2 g_0'}\right)^{1/5} \tag{5.16a}$$

$$z_{mh} = 2.57\,(N^2)^{-3/8}\left(\frac{Q_0 g_0'}{2\pi\alpha^2}\right)^{1/4} - \frac{5}{6\alpha}\left(\frac{32\alpha Q_0^2}{5\pi^2 g_0'}\right)^{1/5} \tag{5.16b}$$

Scaling of z_{br} and z_{mh} with Q_0 and N^2 is complicated by the finite source correction term appearing second in Eqs. 5.16. However the first term dominates for parameter values relevant to tidewater glaciers and characteristic plume heights scale approximately with $Q_0^{1/4}(N^2)^{-3/8}$.

Evolution of plume temperature contrast is given by Eq. 5.14 with $dT_a/dz = 0$. The response of plume temperature to change in subglacial discharge (Fig. 5.5d) is therefore similar to the uniform stratification case. It follows that in the point source limit $z \gg z_0$ (if the plume reaches this far) the response of melt rates to varying subglacial discharge is dominated by the effect on plume velocity.

Total submarine melt rate is given by

$$\dot{M} = \int_{z_0}^{z_{mh}+z_0} 2b\dot{m}\,dz \qquad \text{or} \qquad \dot{M} = \int_{z_0}^{h+z_0} 2b\dot{m}\,dz \tag{5.17}$$

where the first expression applies when the plume does not reach the surface ($z_{mh} < h$) and the second when it does ($z_{mh} > h$).

Assuming then that under change in Q_0, local melt rates are controlled by plume velocity, it follows from Eqs. 5.15 that local melt rates would scale with $Q_0^{1/4}(N^2)^{1/8}$. The area of contact between the plume and ice scales with $bz_{mh} \propto Q_0^{1/2}(N^2)^{-3/4}$ when the plume does not reach the surface and $bh \propto Q_0^{1/4}(N^2)^{-3/8}$ when it does, where we have neglected the point source correction.

The exponent in the relationship $\dot{M} \propto Q_0^{\gamma}$ (Fig. 5.6b) therefore varies depending on where calving front height h falls in relation to the three length scales $z_0 < z_1 < z_{mh}$. When $h < z_1$, plume dynamics are well approximated by the uniform stratification

solution and we may apply our results from section 5.3. For $z_1 < h < z_{mh}$ we lie in a transition regime where total melt rates combine the $Q_0^{1/2}(N^2)^{-1/4}$ velocity-induced scaling for total melt with the effect of Q_0 on plume temperature (the latter cannot be ignored because we do not satisfy $h \gg z_0$). Therefore the total melt rate-discharge exponent is reduced and ∼2/5 provides an approximate value (Fig. 5.6e). Finally, when $h > z_{mh}$ we'll also have $z \gg z_0$ for much of the calving front, therefore local melt rates are controlled by plume velocity and total melt rates scale as $Q_0^{3/4}(N^2)^{-5/8}$ (Fig. 5.6b and e). Consideration of the point source correction results in only minor modifications to the exponents, discussed in section S2.3.2.

5.4.4 Stratification in both temperature and salinity

While the preceding discussions provide interesting results which allow us to understand this last case, it is more usual to find stratification in salinity in concert with stratification in temperature. Plume width, velocity and reduced gravity scale as in the previous section, with both N_S^2 and N_T^2 contributing to N^2 in this case. Plume temperature however is different. By combining Eqs. 5.12a and 5.12b, evaluating the resulting expression at z_{mh} and noting the dominance of salinity in the equation of state we obtain (section S2.3.3)

$$T_a - T \approx -(1 + |\lambda|)\frac{dT_a/dz}{dS_a/dz}\frac{Q_0}{Q}(S_{a,0} - S_0) \propto Q_0^{1/4}(N_T^2)(N_S^2)^{-3/8} \tag{5.18}$$

where λ is some constant and $S_{a,0}$ is the ambient salinity at the grounding line.

We now compare this to previous sections. With stratification in salinity but not temperature, $T_a - T$ tends to 0 far from the grounding line (section 5.4.3, Fig. 5.5d). With stratification in temperature but not salinity, $T_a - T$ became independent of Q_0 far from the grounding line (section 5.4.2, Fig. 5.5b). The critical difference with stratification in both temperature and salinity is that at the furthest point from the grounding line, $T_a - T$ does not tend to 0 and retains sensitivity to Q_0 (Eq. 5.18, Fig. 5.5f). Therefore when considering the effect of change in Q_0 on submarine melt, we must consider the effect on plume temperature. Eq. 5.18 and Fig. 5.5f show that as Q_0 is increased, and at the point where the plume reaches its maximum height, plume

temperature may be significantly decreased. This effect is less pronounced for small Q_0, small N_T^2 or large N_S^2 (Eq. 5.18).

The total melt rate-discharge exponent may therefore be substantially reduced relative to the case considered in section 5.4.3. For $dT_a/dz = -0.005°\mathrm{C\,m^{-1}}$ and $dS_a/dz = -0.01\ \mathrm{psu\,m^{-1}}$ (Fig. 5.6c) the exponent is only slightly reduced. However if we increase stratification in temperature and decrease stratification in salinity (Fig. 5.6d) the exponent may be reduced to $\sim 1/2$ and is only unaffected at low Q_0. Given the complexity of the relationship between total melt rate and subglacial discharge in the presence of stratification, it is not generally possible to obtain an equivalent of Eq. 5.11 when stratification is present.

5.5 Line plumes

For completeness we now briefly consider the alternative geometry of line plumes. In the line plume case discharge is distributed uniformly across the glacier grounding line and is therefore appropriate for distributed subglacial drainage or low and very wide channels. The results are qualitatively similar to the half-conical geometry and we therefore only highlight areas with interesting differences. The subglacial discharge Q_0 is regarded as a discharge per unit width of glacier. The plume is wedge shaped with the vertical side against the glacier and the inclined face in contact with the fjord (Fig. S2.2). Plume width $b(z)$ is taken as the thickness of the wedge at height z. Note that this is now the same model as considered in *Jenkins* (2011).

For a uniform stratification, an equivalent solution to Eqs. 5.6a-5.6c is easily found (*Linden et al.*, 1990; *Jenkins*, 2011; *Straneo and Cenedese*, 2015), see also section S2.4.1. The point source correction distance is given by $z_0 = (Q_0^2/\alpha^2 g_0')^{1/3}$. As in the half-conical case, the relative magnitude of z and z_0 determines the control on melt rate under change in subglacial discharge. In the point source limit $z \gg z_0$, change in melt due to change in subglacial discharge arises through the effect on velocity (note that this was the region considered by *Jenkins* (2011)). For $z \sim z_0$ plume temperature must also be considered. Plots of the local melt rate exponent (Figs. 5.7a and b) show a

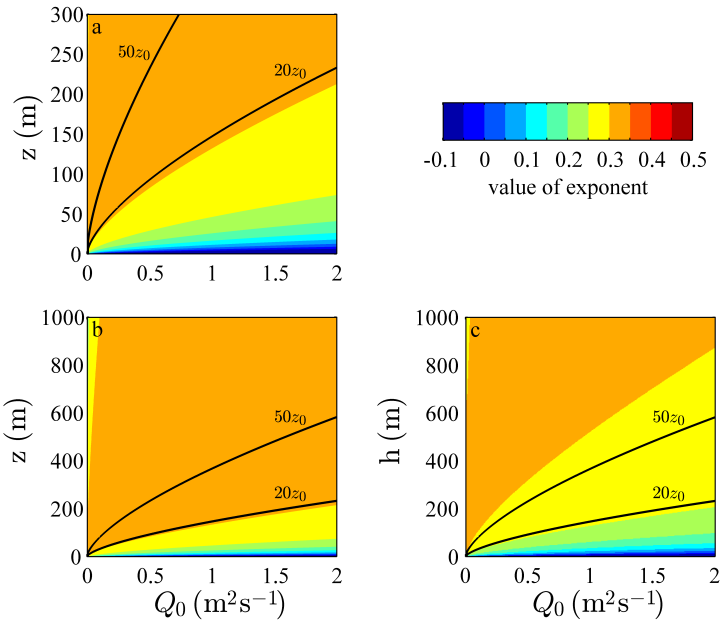

Figure 5.7: (a) and (b): plots of local melt rate-discharge exponent (i.e. γ in the relationship $\dot{m} \propto Q_0^{\gamma}$) for the line plume geometry. Calving front height $h = 300$ m in (a) and $h = 1000$ m in (b). (c) shows total melt rate-discharge exponent (i.e. γ in the relationship $\dot{M} \propto Q_0^{\gamma}$) for the line plume geometry. Black lines show multiples of $z_0 = (Q_0^2/\alpha^2 g_0')^{1/3}$. Note that we do not consider the discharge exponent of $b\dot{m}$ in the line plume case as the total melt integrand - Eq. 5.19 - does not contain b. Ambient values at the grounding line are $T_{a,0} = 3°$C and $S_{a,0} = 33$ psu. Results are generated using the full model.

similar form to the half-conical case, with an exponent of 1/3 (as found in *Jenkins* (2011)) a good approximation for $z \gtrsim 15z_0$. Note that for the half-conical case an exponent of 1/3 was good for $z \gtrsim 8z_0$; the difference in length scales arises because the half-conical plume approaches ambient temperature more quickly than the line plume.

In contrast to the half-conical case, total melt rate per unit width of glacier is defined by

$$\dot{M} = \int_0^h \dot{m}\, dz \tag{5.19}$$

The appearance of plume radius b in the half-conical equivalent definition - Eq. 5.9 -

helped to ensure that the total melt rate exponent was close to 1/3 for $h > z_0$. In the line plume case the differing integrand means that an exponent of 1/3 is only a good approximation for $h \gtrsim 70z_0$ (Fig. 5.7c). Whether or not this provides a significant complication at real glaciers therefore depends on the calving front height and subglacial discharge. For example, at a calving front with $h = 500$ m, a total melt rate exponent of 1/3 is good for $Q_0 \lesssim 1\ \mathrm{m^2\,s^{-1}}$; for higher values of Q_0 the exponent will be reduced.

Finally, considering that melt approaches a constant value with depth, total melt rate is proportional to calving front height h. It follows that the line plume equivalent of Eq. 5.11 is

$$\dot{M} = A_1 \left[1 + A_2(T_a - T_0)\right] Q_0^{1/3} h \tag{5.20}$$

valid for $h \gtrsim 70z_0$. Numerically we obtain $A_1 = 1.56 \times 10^{-5}\ \mathrm{s^{-2/3}}$ and $A_2 = 0.84\ ^\circ\mathrm{C^{-1}}$. Comparison of this equation and the full model is shown in Fig. S2.3 (maximum relative error is 13%).

In a linear stratification line plume variables scale as $b \propto Q_0^{1/3}(N^2)^{-1/2}$, $u \propto Q_0^{1/3}$ and $g' \propto Q_0^{1/3}(N^2)^{1/2}$ while line plume characteristic heights z_{br} and z_{mh} scale as $Q_0^{1/3}(N^2)^{-1/2}$ (*Wright and Wallace* (1979); *Bush and Woods* (1999), see also section S2.4.2).

The character of submarine melting in a linear stratification is analogous to the half-conical case. With stratification in temperature but not salinity, uniform stratification results may be applied (Fig. 5.8a). With stratification in salinity but not temperature, and provided local melt rate follows plume velocity, we have total melt rates scaling with $Q_0^{2/3}(N^2)^{-1/2}$ when the plume does not reach the surface and $Q_0^{1/3}$ when it does (Fig. 5.8b). These exponents may however be reduced due to the effect of change in Q_0 on plume temperature. With stratification in both temperature and salinity we expect a further reduction in exponents as decreasing plume temperature with increasing subglacial discharge reduces submarine melt rates (Fig. 5.8c and d).

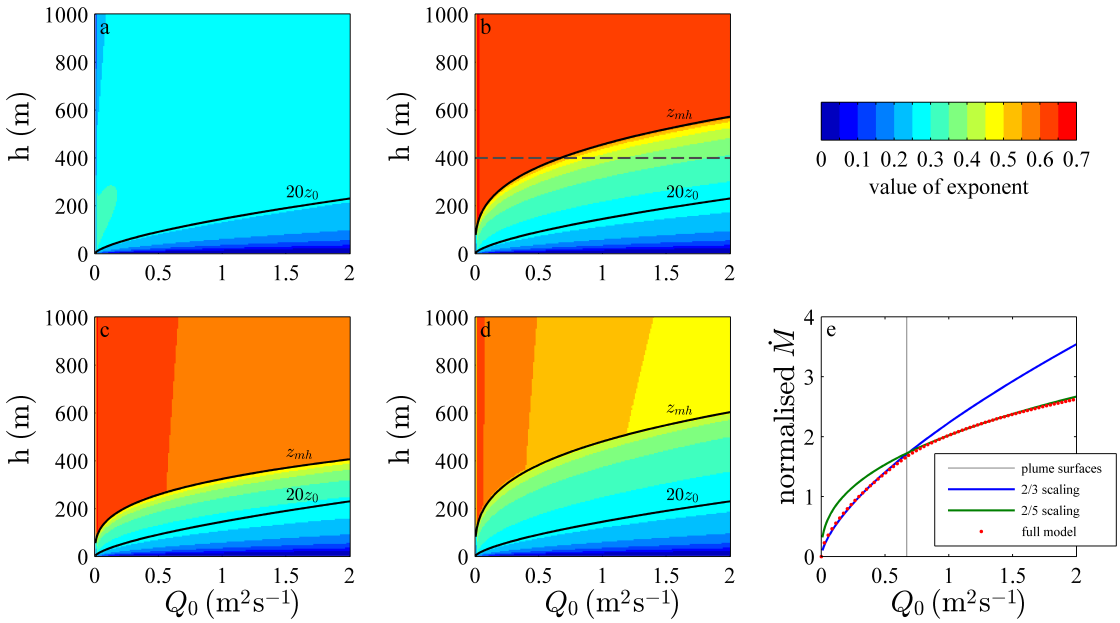

Figure 5.8: Line plume equivalent of Fig. 5.6. (a)-(d): total melt rate-discharge exponent (i.e. γ in the relationship $\dot{M} \propto Q_0^{\gamma}$) for linear stratifications. (a) has $dT_a/dz = -0.005°\text{C m}^{-1}$ and is unstratified in salinity, (b) has $dS_a/dz = -0.005$ psu m^{-1} and is unstratified in temperature, (c) has $dT_a/dz = -0.005°\text{C m}^{-1}$ and $dS_a/dz = -0.01$ psu m^{-1} and (d) has $dT_a/dz = -0.01°\text{C m}^{-1}$ and $dS_a/dz = -0.005$ psu m^{-1}. (e) shows an specific example of the total melt rate-discharge relationship for $h = 400$ m, and corresponds to the horizontal dashed line in (b).

5.6 Discussion

In the following we discuss first the relevance of characteristic plume heights to tidewater glaciers. We then consider the relationship between submarine melt rate and subglacial discharge and use our results to estimate variation in melt rates in recent decades and under projected atmospheric and oceanic warming. We finally discuss the implications for glacier dynamics.

In a linearly stratified fjord, the height of plume buoyancy reversal z_{br} and maximum plume rise z_{mh} scale approximately with subglacial discharge raised to the power 1/4 for a point source plume and 1/3 for a line source plume. We can use these scalings to

comment on the visibility of a plume on the fjord surface. Consider a fjord of depth h. If the stratification and subglacial discharge are such that $z_{br} > h$, the plume will be less dense than the ambient fjord water when it reaches the surface and will thus flow downfjord at the fjord surface, as is often observed in Greenland (e.g. *Tedstone and Arnold*, 2012). If instead $z_{mh} > h > z_{br}$, the plume will reach the fjord surface adjacent to the glacier but will sink before flowing downfjord, likely undergoing some mixing as it sinks. The final possibility is $h > z_{mh}$, in which case the plume does not reach the fjord surface and there may be no visible evidence of discharge emerging at the glacier grounding line.

The scalings can also be used to suggest the magnitude of subglacial discharge required for each of these transitions. To illustrate this, we consider an example from Store Glacier, West Greenland. Application of Eq. 5.16a with $h = 500$ m, $N^2 \sim 2 \times 10^{-5}$ s^{-2} and $g_0' \sim 0.25\ \mathrm{m\,s}^{-2}$ (from Fig. 2 in *Chauché et al.* (2014)) suggests that $Q_0 \sim 140$ $\mathrm{m}^3\,\mathrm{s}^{-1}$ is required before a plume from a single channel would flow away at the fjord surface, while Eq. 5.16b suggests that $Q_0 \sim 40\ \mathrm{m}^3\,\mathrm{s}^{-1}$ is needed before the plume will first be visible at the fjord surface.

Considering now submarine melt, we find that no single scaling for melt with subglacial discharge and stratification can be applied universally. Rather the appropriate scaling depends on a combination of the subglacial discharge, stratification and calving front height. We give here a qualitative summary of our results. In a uniform stratification, local submarine melt rates close to the grounding line may decrease with increasing subglacial discharge when the resulting decrease in plume thermal forcing outweighs the increase in velocity. However it remains the case that total submarine melt rate scales with subglacial discharge raised to the power 1/3 regardless of plume geometry provided discharge does not exceed critical values as discussed in the results. Once linear stratification in salinity is introduced the exponent may be as large as 3/4 (2/3) when a half-conical (line) plume does not reach the fjord surface. As subglacial discharge is increased and temperature stratification is introduced, this exponent is reduced.

Turning to previous work on the melt-discharge exponent, *Xu et al.* (2012) and *Sciascia et al.* (2013) considered line plumes and found total melt rate exponents consistent with 1/3. *Sciascia et al.* (2013) had a two-layer stratification, but melt rates were dominated by the thicker lower layer which was unstratified. *Xu et al.* (2012) did not use a uniform stratification, but because they generated few data points when the plume did not reach the surface, they may not have been able to identify the 2/3 exponent predicted here.

Our half-conical plume results can be compared to three dimensional numerical studies. In a uniform stratification, *Kimura et al.* (2014) found that a total melt rate exponent of 1/3 fitted their results until high initial plume velocities forced the plume away from the ice. With an observed stratification from in front of Store Glacier, *Xu et al.* (2013) suggested an exponent of 0.85 (0.5) at low (high) discharge. We believe the transition between these two values is similar to that which we observe in our results; total melt becomes less sensitive to subglacial discharge once the plume-ice contact area can no longer significantly increase. The slight differences in the exponent between *Xu et al.* (2013) and this paper might be explained by parameterisation of turbulence in the numerical model (Chapter 4; *Slater et al.*, 2015) or the geometry of the plume source (*Kimura et al.*, 2014). We therefore believe that our results regarding the melt-discharge exponent are consistent with previous work, and indeed can offer some explanation for the range of values reported.

Our study is most comparable to that of *Jenkins* (2011), which considered a line plume in the uniform stratification limit, finding a local melt rate-discharge exponent of 1/3. As noted in section 5.2.3, *Jenkins* (2011) focussed on the region where buoyancy input from submarine melting is comparable to the initial buoyancy flux and was therefore able to neglect the region where plume temperature is not close to the ambient value. Our focus in this paper on the region in which the submarine melt feedback is negligible means we need to make explicit consideration of the evolution of plume temperature. For sufficiently small discharges our results are in agreement with *Jenkins* (2011). However for Greenland-relevant parameters we suggest that the local melt rate-discharge exponent can be significantly reduced from 1/3 and may even be negative (Fig. 5.7a).

With the above understanding, we consider under what circumstances a certain exponent should apply. The larger exponents (2/3 for a distributed (line) input, 3/4 for a localised (point) input) apply for total melt rate when plumes do not reach the surface, although these exponents can be reduced by temperature stratification. It is probably necessary to solve the full equations to find an exact exponent. These exponents are likely relevant to glaciers terminating in deep fjords (e.g. Rink Isbrae) or glaciers with a distributed drainage system such that the discharge is split over many channels and is therefore less likely to reach the surface. An exponent of 1/3 applies for glaciers in weakly stratified or shallow fjords when plumes reach the surface (e.g. Svalbard or Alaska) or at large glaciers with high subglacial discharge. In these cases we derived simple expressions - Eqs. 5.11 and 5.20 - for estimating total submarine melt volume.

We can also use our scalings to assess the likely variation in submarine melting in recent decades and in the future. Assuming, for example, a warming of fjord water from 2°C to 3°C (*Holland et al.*, 2008a), Eq. 5.11 suggests an increase in submarine melt of ∼29%. Supposing runoff increased over the same period by ∼25% (*Hanna et al.*, 2011), a melt-discharge exponent of 1/3 (3/4) gives an increase in submarine melting of 8% (18%). In combination, one can suggest that in recent decades submarine melt rates may have increased by up to ∼50% in response to atmospheric and ocean warming. By the end of the century, under a doubling of subglacial discharge (*Fettweis et al.*, 2013) and additional ocean warming of 2°C (*Yin et al.*, 2011), we can estimate an 80% (140%) increase in submarine melting. Such estimates are of course simplistic in that they take no account of possible changes in fjord circulation or subglacial hydrology and rely on uncertain predictions of atmospheric and ocean warming.

When spatially averaged over a glacier terminus, predicted submarine melt rates (e.g. ∼3 $\mathrm{m\,d^{-1}}$, (Chapter 4; *Slater et al.*, 2015)) are generally much smaller than large Greenland tidewater glacier velocities (e.g. ∼20 $\mathrm{m\,d^{-1}}$ at Helheim Glacier, *Bevan et al.* (2015)). It should be noted that this study has focussed on regions of the calving front affected by significant subglacial discharge; regions unaffected by subglacial discharge are still expected to melt (e.g. *Sciascia et al.*, 2013) and may contribute to the spatially

averaged melt rate. The above estimates nevertheless suggest that submarine melting would be unable to solely account for the recently observed retreat of such glaciers. If ocean forcing has been the primary driver of tidewater glacier behaviour in recent decades, we therefore need to invoke a sensitive coupling between submarine melting and glacier dynamics. There is not yet a consensus in the literature on whether this coupling exists.

In a recent model of Store Glacier, *Todd and Christoffersen* (2014) found that terminus position was insensitive to an increase in submarine melt rate of up to 100%, an observation which they attributed to the particular bed and lateral topography at Store. At Helheim Glacier, *Cook et al.* (2014) found an order of magnitude increase in submarine melt was required to make the modelled glacier retreat. These studies therefore suggest that our estimated changes in submarine melting in recent decades would be unable to drive significant glacier retreat. In contrast, other studies (*Weertman*, 1974; *Nick et al.*, 2009; *Enderlin et al.*, 2013) propose that glaciers with beds which deepen inland can respond dramatically to terminus perturbation through the marine ice sheet instability and *O'Leary and Christoffersen* (2013) advocate a sensitive coupling between submarine melting and calving rate which may not be fully captured in models to date. Therefore even with estimates of variation in melt rates in recent decades, the role of submarine melting in the dynamics of Greenland's tidewater glaciers remains ambiguous.

We note one final point regarding our results. The submarine melt rate parameterisation Eqs. 5.2a-5.2c should be used with caution as it has thus far only been validated beneath an Antarctic ice shelf (*Jenkins et al.*, 2010) and there is therefore significant uncertainty in the value of the heat and salt transfer coefficients Γ_T and Γ_S. However, provided the form of the melt rate parameterisation does not change (i.e. $\dot{m} \propto u(T - T_b)$), our scalings are unaffected by this uncertainty.

5.7 Conclusions

In this paper we have used buoyant plume theory to investigate the dynamics of proglacial plumes arising from the input of subglacial discharge at the grounding line of tidewater glaciers, focussing on the induced submarine melting of the calving front. In particular we have aimed to derive scalings for variation in submarine melt rates in terms of subglacial discharge, fjord properties and calving front height.

We find that no simple relationship exists between submarine melt rate, subglacial discharge and fjord stratification. We suggest that the relationship between subglacial discharge and submarine melt rate prevalent in the literature (i.e. submarine melt rate scales with subglacial discharge raised to the power 1/3) is appropriate for local or total melt rates in a uniformly stratified fjord regardless of plume source geometry provided discharge does not exceed a critical value. In these cases it is possible to formulate simple equations for total melt induced - Eqs. 5.11 and 5.20. However, once linear stratification is introduced, the total melt rate-discharge exponent may be as large as 3/4 (2/3) for a point (line) source plume, though the exponent is complicated by stratification in temperature which may reduce the exponent somewhat. These higher exponents are likely representative for large glaciers terminating in deep water in Greenland where plumes are rarely seen, and where submarine melt rates could therefore be more sensitive to the magnitude of subglacial discharge than previously thought. Our findings are also able to explain the range of values of the exponent found in the literature.

We used our melt rate scalings to estimate that submarine melt rates may have increased by $\sim$50% in recent decades, driven by a combination of atmospheric and ocean warming. Whether this is sufficient to explain the observed dynamic changes at tidewater glaciers in Greenland over the same time period remains uncertain; if it is, this would indicate a sensitive coupling between submarine melting and calving dynamics. Since submarine melting is likely to increase in response to predicted atmospheric and ocean warming, it is clear there is the potential for future dynamic response of tidewater

glaciers to submarine melting and thus the need for further research into ice-ocean interaction in Greenland.

Chapter 6

A model for tidewater glacier undercutting by submarine melting

Chapters 4 and 5 quantified the sensitivity of submarine melt rate to the near-terminus subglacial hydrology, the magnitude of subglacial discharge and the fjord stratification. However, these chapters assumed flat and vertical calving fronts. During the course of this thesis, a number of tidewater glaciers in Greenland have been shown to have significantly undercut termini (*Fried et al.*, 2015; *Rignot et al.*, 2015). Motivated by these observations, this chapter seeks to understand the effect of undercutting on plume dynamics and submarine melting, thereby adding undercutting to the relationships which have already been quantified in Chapters 4 and 5.

This chapter also seeks to elucidate the reverse process; the effect of submarine melting on calving front shape. Understanding this relationship is of paramount importance as the link between submarine melting and glacier dynamics may lie in the impact of submarine melting on calving front shape and the subsequent effect on calving (e.g. *O'Leary and Christoffersen*, 2013). As such, this chapter aims to go beyond a simple

estimation of submarine melt rate by considering the time-evolution of calving front shape under depth-varying submarine melting.

Published in **Geophysical Research Letters**, March 2017.

Authors: D. A. Slater[1], P. W. Nienow[1], D. N. Goldberg[1], T. R. Cowton[2], and A. J. Sole[3].

1. School of Geosciences, University of Edinburgh, Edinburgh, UK.
2. School of Geography and Sustainable Development, University of St Andrews, St Andrews, UK.
3. Department of Geography, University of Sheffield, Sheffield, UK.

Citation: Slater, D. A., P. W. Nienow, D. N. Goldberg, T. R. Cowton, and A. J. Sole (2017), A model for tidewater glacier undercutting by submarine melting, *Geophysical Research Letters, 44*(5), 2360-2368, doi: 10.1002/2016GL072374.

Author contributions: D.A.S. designed the research and developed the model under guidance from all other authors. D.A.S wrote the paper with input from all other authors.

Abstract

Dynamic change at the marine-terminating margins of the Greenland Ice Sheet may be initiated by the ocean, particularly where subglacial runoff drives vigorous ice-marginal plumes and rapid submarine melting. Here we model submarine melt-driven undercutting of tidewater glacier termini, simulating a process which is key to understanding ice-ocean coupling. Where runoff emerges from broad subglacial channels we find that undercutting has only a weak impact on local submarine melt rate, but increases total ablation by submarine melting due to the larger submerged ice surface area. Thus the impact of melting is determined not only by the melt rate magnitude but also by the slope of the ice-ocean interface. We suggest that the most severe undercutting occurs at the maximum height in the fjord reached by the plume, likely promoting calving of ice above. It remains unclear however whether undercutting proceeds sufficiently rapidly to influence calving at Greenland's fastest-flowing glaciers.

6.1 Introduction

In recent decades ice loss from Greenland has accelerated due to both decreased surface mass balance and increased ice discharge into the ocean (*van den Broeke et al.*, 2016). Oceanic warming has been widely implicated as a driver of the latter (*Holland et al.*, 2008a; *Straneo and Heimbach*, 2013), yet process understanding of the interaction of the ocean with glaciers remains embryonic, and must be improved to better forecast the contribution of the Greenland Ice Sheet to future sea level rise.

One such poorly understood process is submarine melting, which drives direct ice loss and may also impact glacier dynamics by undercutting calving fronts, amplifying calving, and initiating glacier retreat and acceleration (*Straneo and Heimbach*, 2013). Submarine melting is thought to be amplified where subglacial discharge emerges at the grounding line, forming a buoyant plume rising up the terminus towards the ocean surface (*Jenkins*, 2011). The consequent high ice-adjacent water velocities are expected to enhance heat transfer from ocean to ice (*Holland and Jenkins*, 1999), potentially driving melting at several metres per day (Chapter 4; *Slater et al.*, 2015).

Despite its potential importance, the interaction between submarine melting and terminus shape has not been investigated. Recent side-scan sonar surveys of glaciers in west Greenland have shown that calving fronts can be substantially undercut (*Rignot et al.*, 2015; *Fried et al.*, 2015). It is thought that the most severely undercut sections arise from plume-driven enhanced melting. Existing models of submarine melting however assume vertical and static calving fronts and do not therefore capture the process of melt-driven undercutting.

In this study, we introduce a plume model with a dynamic ice-ocean boundary which evolves in response to calculated submarine melt rates. We investigate the effect of undercutting on plume dynamics, and the effect of submarine melting on terminus morphology. In addressing these questions we aim to elucidate a key link between the ocean and tidewater glacier dynamics.

6.2 Model

We use buoyant plume theory coupled to a melt rate parameterisation to model plume-driven submarine melting. By allowing the ice-ocean boundary to evolve in time we use the model to study feedbacks between plume dynamics and terminus shape. Fig. 6.1a shows a model schematic. The coordinates x, z and l measure along-fjord distance, depth and along-interface distance respectively, taking $z = l = 0$ at the grounding line. The shape of the ice-ocean interface is defined by the angle $\theta(z)$, measured from the horizontal. The glacier flows from the left at velocity v. The plume induces submarine melting at rate $\dot{m}$, which varies with depth, and is defined in the direction perpendicular to the ice-ocean interface. Thus the position and shape of the terminus is determined by the competing influences of ice velocity and submarine melting. There is no calving in this model.

We use the line plume model of *Jenkins* (2011), which ensures conservation of volume, momentum, heat and salt as the plume rises along the ice-ocean interface:

$$\frac{d}{dl}\left(bu\right) = \dot{e} + \dot{m} \tag{6.1a}$$

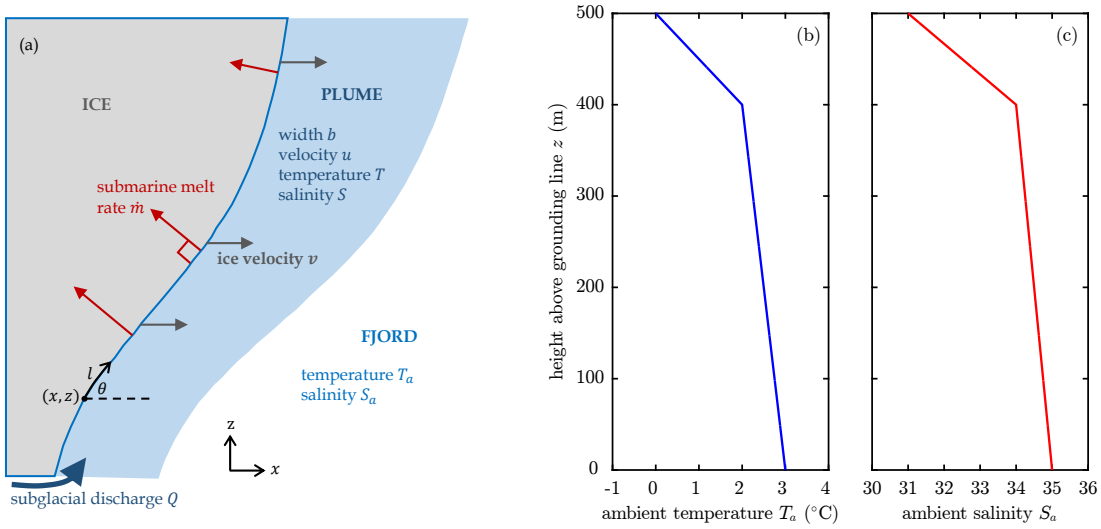

Figure 6.1: (a) Model schematic, (b) fjord temperature and (c) salinity assumed throughout the paper.

$$\frac{d}{dl}\left(bu^2\right) = bg' \sin\theta - C_d u^2 \tag{6.1b}$$

$$\frac{d}{dl}\left(buT\right) = \dot{e}T_a + \dot{m}T_b - C_d^{1/2} u\Gamma_T \left(T - T_b\right) \tag{6.1c}$$

$$\frac{d}{dl}\left(buS\right) = \dot{e}S_a + \dot{m}S_b - C_d^{1/2} u\Gamma_S \left(S - S_b\right) \tag{6.1d}$$

Variables are illustrated in Fig. 6.1a, with b, u, T and S respectively plume width, velocity, temperature and salinity, all assumed uniform in the plume cross-section. The plume entrains fjord water of temperature T_a and salinity S_a at rate $\dot{e}$. The reduced gravity of the plume, g', is defined through an equation of state (*Fofonoff and Millard*, 1983). C_d is a drag coefficient and Γ_T and Γ_S are heat and salt transfer coefficients. Submarine melt rate $\dot{m}$ and interface temperature T_b and salinity S_b are defined using the standard three-equation formulation (Chapter 5; *Holland and Jenkins*, 1999; *Slater et al.*, 2016) in which melt rate is largely proportional to the product of plume velocity and thermal forcing. Finally our entrainment parameterisation follows *Pedersen* (1980) and *Jenkins* (2011), with

$$\dot{e} = \alpha \sin\theta \, u \tag{6.2}$$

where $\alpha = 0.1$ is an experimentally determined coefficient (*Turner*, 1979). Thus the rate of entrainment of fjord water into the plume scales with plume velocity and the slope of the ice-ocean interface.

We depart from the model of *Jenkins* (2011) by allowing the ice-ocean interface to evolve in time. Ice flow moves the interface horizontally forwards at velocity v while submarine melting acts in a perpendicular direction, moving the interface backwards and, if the terminus is undercut, upwards (Fig. 6.1a). At a fixed depth the horizontal movement of the interface may be expressed as (see section S3.1)

$$\frac{\partial x}{\partial t} = v - \frac{\dot{m}}{\sin\theta} = v - \dot{m}\sqrt{1 + \left(\frac{\partial x}{\partial z}\right)^2} \tag{6.3}$$

Some specific parameter choices are required. We assume a terminus fjord depth $h = 500$ m, and idealised ambient fjord conditions (Figs. 6.1b and c) which are generally representative of fjords in Greenland, with warm subtropical water overlain by cold and fresh polar water (*Straneo and Cenedese*, 2015). We consider Greenland-relevant low ($Q = 0.1$ m^2/s) and high ($Q = 2$ m^2/s) subglacial discharge scenarios, which would for example be achieved with respective discharges of 25 m^3/s and 500 m^3/s emerging from a channel measuring 250 m in the across-fjord direction. For each discharge, we choose initial plume width and velocity ensuring the plume has a balance of buoyancy and momentum (Chapter 5; *Slater et al.*, 2016). Initial plume temperature and salinity are set to the in-situ freezing point and zero respectively, appropriate for the emerging subglacial discharge. Numerical details are given in section S3.3.

A few points should be noted regarding the idealised nature of this model. We consider a line plume, neglecting across-fjord variability in plume dynamics. As such this model is only strictly appropriate for 'broad' subglacial channels (i.e. channels with significant size in the across-fjord direction), a fact which is tacit in many similar models (e.g. *Jenkins*, 2011; *Sciascia et al.*, 2013). A definition of 'broad' is discussed in section S3.2; for $h = 500$ m, a channel breadth >250 m might be considered broad, while for $h = 250$ m, a breadth >125 m would suffice. The dimensions of real channels are not well known

at present; however, observations of subsurface terminus morphology do show undercut caverns measuring a few hundred metres in breadth (*Fried et al.*, 2015).

We assume that the plume follows the shape of the undercut terminus. In particular, our plume model does not apply if the terminus becomes overcut, due to the possibility of the plume detaching from the ice. We assume ice velocity is invariant with depth, likely a good approximation for fast-flowing tidewater glaciers (*Meier and Post*, 1987), and neglect other ice-dynamic effects, such as adjustment due to buoyancy or acceleration in the along-flow direction.

6.3 Results

6.3.1 Effect of terminus shape on plume dynamics

We first isolate the feedback of terminus shape on plume dynamics by simulating plumes at static calving fronts of various shapes (Fig. 6.2a) motivated by observations (for example the ∼45° uniform undercutting identified in *Fried et al.* (2015)). It is immediately clear that, when plotted as a function of depth, the ice-perpendicular submarine melt rate $\dot{m}$ is similar for the various terminus shapes (Fig. 6.2b); the melt rates differ by at most 20% near the grounding line for the convex versus vertical terminus, but generally by <5%.

This similarity arises due to a lack of feedback of terminus shape on plume dynamics when considered as a function of depth, which can be understood by rewriting Eqs. 6.1a-6.1d in terms of the vertical coordinate z (putting $d/dl \to \sin\theta\, d/dz$)

$$\frac{d}{dz}(bu) = \alpha u + \frac{\dot{m}}{\sin\theta} \tag{6.4a}$$

$$\frac{d}{dz}\left(bu^2\right) = bg' - \frac{C_d u^2}{\sin\theta} \tag{6.4b}$$

$$\frac{d}{dz}(buT) = \alpha u T_a + \frac{\dot{m}T_b - C_d^{1/2} u \Gamma_T (T - T_b)}{\sin\theta} \tag{6.4c}$$

$$\frac{d}{dz}(buS) = \alpha u S_a + \frac{\dot{m}S_b - C_d^{1/2} u \Gamma_S (S - S_b)}{\sin\theta} \tag{6.4d}$$

Thus when considered as a function of depth, the terminus shape ($\sin\theta$) influences plume dynamics only through the feedbacks of submarine melting (last terms in Eqs. 6.4a, c and d) and plume-ice drag (last term in Eq. 6.4b). In fact, for sufficient subglacial discharge (hence within plumes in Greenland), these feedbacks are negligible (Chapter 5; *Slater et al.*, 2016). Plume dynamics are then independent of terminus shape, with the reduced buoyancy of the plume at an undercut terminus being compensated by reduced entrainment, as both buoyancy and entrainment scale with interface slope (Eqs. 6.1b and 6.2). The neutral buoyancy level and maximum height reached by the plume are therefore little affected by terminus shape, exemplified by the low discharge plumes all reaching a maximum height close to $z = 330$ m (Fig. 6.2b).

We note that use of an alternative Richardson number-dependent entrainment parameterisation (*Kochergin*, 1987; *Holland and Feltham*, 2006) results in a slightly higher dependence of plume dynamics on shape (section S3.7). We also stress that where either subglacial discharge is limited or $\sin\theta$ is small, such as in winter or at ice shelves, terminus shape is expected to influence melt rate (*Magorrian and Wells*, 2016).

Returning to plumes at tidewater glaciers, it is crucial to note that the more undercut calving fronts have a larger surface area (Fig. 6.2a). Therefore, a better measure of the effect of melting on the glacier, which takes into account the surface area, is $\dot{m}/\sin\theta$. This might be thought of as a 'horizontal melt rate' as it is the horizontal displacement of the ice due to melting and can therefore be compared directly to the ice velocity (Eq. 6.3). Due to larger surface area, more undercut calving fronts have higher 'horizontal melt rate' (Fig. 6.2c). Total ablation due to submarine melting, defined as $\int_0^h \dot{m}/\sin\theta\, dz$, is therefore higher at more undercut calving fronts (Fig. 6.2d). To emphasize once more: terminus shape has little effect on ice-perpendicular melt rate $\dot{m}$ (Fig. 6.2b), but undercutting increases the impact of melting (Fig. 6.2c) due to increased ice surface area.

For the remainder of this paper we neglect the feedback of terminus shape on ice-perpendicular melt rate $\dot{m}$, but do account for the increased surface area associated with

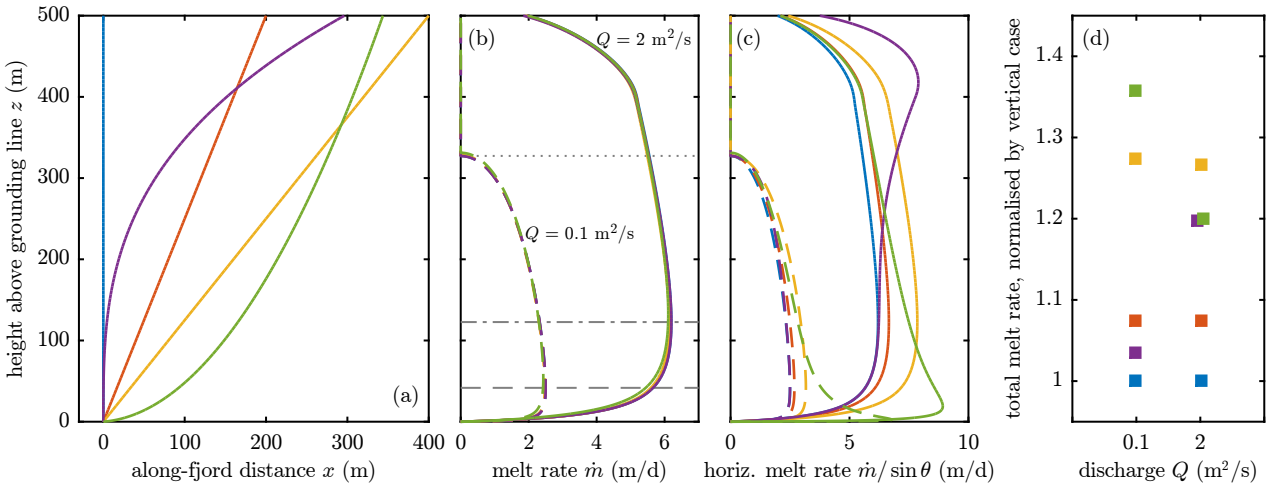

Figure 6.2: (a) Static terminus shapes at which the model is run, including vertical (blue), uniformly undercut (red and yellow), concave (purple) and convex (green). Note that this and all similar plots have an axis aspect ratio of 1:1. (b) Modelled submarine melt rate profiles for the various terminus shapes with colours corresponding to (a), and the low (high) discharge cases in dashed (solid) lines respectively. Blue and red profiles lie largely beneath the purple line. Dashed and dash-dot grey lines indicate the depth of maximum melting for the vertical terminus in the low and high discharge cases respectively. Dotted grey line indicates the maximum height reached by the low discharge plume for the vertical terminus. (c): as (b), but for 'horizontal melt rate' $\dot{m}/\sin\theta$, and (d) total submarine melt rate, normalised by the vertical terminus case for each discharge.

undercutting. When considering the effect of melting on terminus shape we therefore use a fixed ice-perpendicular melt rate profile calculated for a vertical terminus.

6.3.2 Stationary calving fronts

It is instructive to consider whether a terminus may reach a state in which ice flux is balanced by submarine melting. At such a terminus, the 'horizontal melt rate' would equal the ice velocity, with the terminus shape then given by

$$\sin\theta = \frac{\dot{m}}{v} \tag{6.5}$$

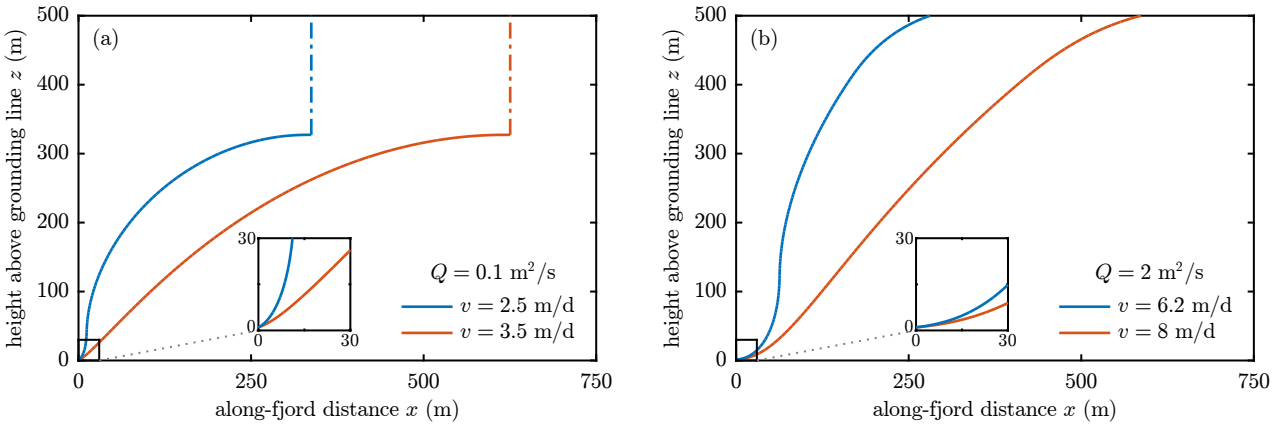

Figure 6.3: Stationary calving fronts obtained by balancing the indicated ice velocity with (a) the low and (b) the high discharge melt profiles from Fig. 6.2b. Insets show near-grounding line details of the subglacial channels imposed in Fig. 6.4.

Based on Eq. 6.5, if at any depth ice-perpendicular melt rate $\dot{m}$ exceeds ice velocity v, there is no stationary solution and the terminus will retreat. Conversely if v exceeds $\dot{m}$, a balance may still be achieved by the terminus becoming undercut; this gives a larger surface area of ice undergoing melting and thus higher total ablation by melting.

Some example stationary calving fronts are plotted in Fig. 6.3. Considering the low discharge case (Fig. 6.3a), the plume does not reach the fjord surface and thus melt rates near the surface are zero (Fig. 6.2b). In this scenario, a balance of ice velocity and melting cannot be achieved in the upper portion of the terminus (plotted in dash-dotted lines in Fig. 6.3a) and here, removal of ice would have to occur by calving or submarine melting not driven by the plume. Where the plume reaches its maximum height the ice-ocean interface approaches horizontal (Fig. 6.3a) as melt rates are low and a large surface area is required to balance the ice flux. The calving fronts are least severely undercut at the depth of maximum melting ($z \sim 50$ m). In Fig. 6.2b, melt rates near the grounding line are low because the plume is cold when emerging into the fjord. At a stationary terminus these low melt rates are compensated by a large surface area and thus the ice becomes more undercut close to the grounding line (Fig. 6.3a).

Similar considerations apply to the high discharge cases (Fig. 6.3b) where the plume

reaches the fjord surface so that the ice flux may be balanced by melting over the full depth. As already motivated by Fig. 6.2c, these stationary examples illustrate how the effect of melting depends on both the melt rate magnitude and on the slope of the ice-ocean interface. Under the same melt rate profile (Fig. 6.2b), both calving fronts in Fig. 6.3b are stationary despite differing ice flux. Finally, the stationary shapes obtained depend on the fjord stratification assumed (Figs. 6.1b and c) with unstratified fjord conditions giving less concave stationary shapes (section S3.4).

6.3.3 Effect of submarine melting on terminus shape and position

We now model the time-evolution of terminus position and shape under plume-driven submarine melting. We run each simulation for a typical melt season length of 100 days assuming for simplicity that subglacial discharge is constant in time. By assuming that terminus shape does not feedback on ice-perpendicular melt rate $\dot{m}$, Eq. 6.3 becomes independent of Eqs. 6.1-6.2. If the plume emerges from a subglacial channel, then near the grounding line $\partial x/\partial z$ will be large and positive; thus, momentarily neglecting ice velocity, Eq. 6.3 gives

$$\frac{\partial x}{\partial t} + \dot{m}\frac{\partial x}{\partial z} \approx 0 \tag{6.6}$$

which is a one-dimensional advection equation with advection velocity $\dot{m}$. Solution of equations of this form requires an initial shape $x(z, 0)$ and a boundary condition on the position $x(0, t)$ or equivalently the slope $\partial x/\partial z(0, t)$ at the bottom (but not top) of the domain. We choose the latter such that solution of Eq. 6.3 requires an initial terminus shape and specification of the slope of the ice-ocean interface near the grounding line through time.

It is not obvious how to specify these conditions. A vertical terminus would seem the default choice for initial shape, but low melt rates near the grounding line (Fig. 6.2b) will then result in an overcut toe rather than the severely undercut features that have been observed (*Fried et al.*, 2015) and which we seek to model. One solution is to include a form of 'subglacial channel' in the initial shape, which is physically reasonable given that we expect severely undercut regions to be associated with plumes emerging from subglacial channels. Thus below the depth of maximum melting, our simulations begin

with a 'subglacial channel' shape taken from one of the stationary solutions previously described. Above maximum melt-depth, the initial terminus shapes merge smoothly to vertical. The stationary solution also sets the slope boundary condition at the grounding line. Full details are in sections S3.3 and S3.5, where we also show that the evolution of terminus shape is insensitive to the details of the imposed subglacial channel.

Figs. 6.4a-c show evolution of calving fronts for the low discharge scenario, with initial subglacial channel shape from the $v = 2.5$ m/d stationary solution (Fig. 6.3a). Above the plume maximum height, melt rates are zero and the ice advances at the ice velocity. Below, the front becomes undercut because melt rates increase closer to the grounding line, until the depth of maximum melting. Below maximum melting, melt rates decrease, but this does not result in a protruding toe because the low melt rates are compensated by the increased surface area associated with the channel. After 100 days, terminus shape approaches that in Fig. 6.3a, blue, which is stationary for an ice velocity of 2.5 m/d. Thus for an ice velocity of 2.5 m/d, the grounding line is stationary, while for ice velocities of 3.5 and 10 m/d the grounding line advances at 1 and 7.5 m/d respectively (Figs. 6.4a-c).

Figs. 6.4d-f show evolution for the same subglacial discharge, but with an initial subglacial channel from the $v = 3.5$ m/d stationary solution (Fig. 6.3a). The channel shape propagates upwards such that the terminus becomes substantially more undercut and retreated than in Figs. 6.4a-c. Terminus shapes in Figs. 6.4d-f approach that in Fig. 6.3a, red, which is stationary for an ice velocity of 3.5 m/d. Thus the grounding line either retreats, is stationary or advances when the ice velocity is less than, equal to or exceeds 3.5 m/d (Figs. 6.4d-f). Figs. 6.4g-l show similar results for the high discharge case, with initial channels included from the $v = 6.2$ and 8 m/d stationary solutions (Fig. 6.3b).

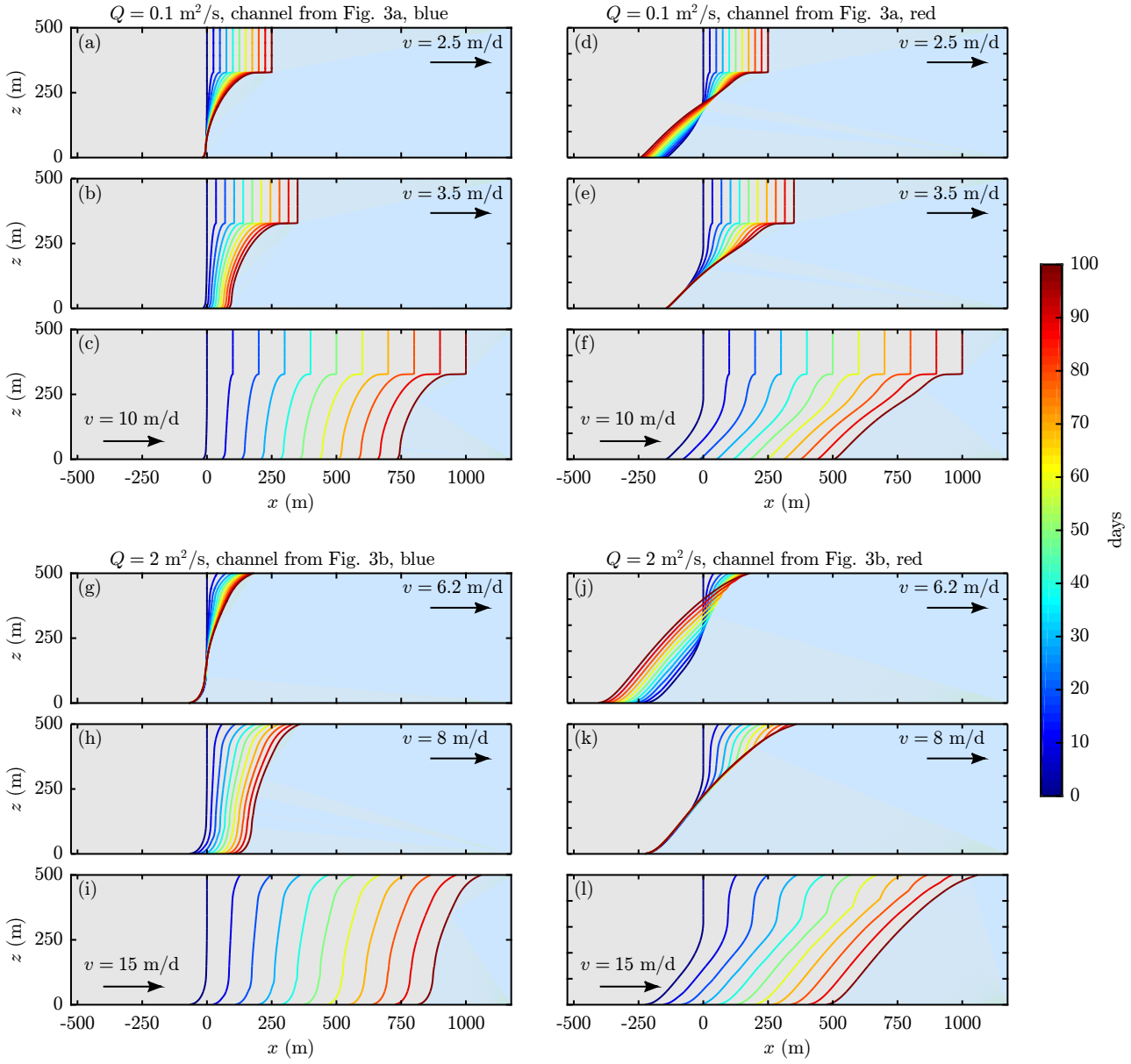

Figure 6.4: Simulation of terminus evolution in the low (a-f) and high (g-l) discharge cases, for the indicated ice velocities and including subglacial channels as described in the text.

6.4 Discussion

6.4.1 Controls on submarine melting

Previous studies investigating controls on submarine melting have considered fjord conditions, fjord depth, subglacial discharge and subglacial hydrology (Chapters 4 and 5;

Xu et al., 2013; *Sciascia et al.*, 2013; *Carroll et al.*, 2015; *Slater et al.*, 2015, 2016). This study adds terminus undercutting demonstrating that for broad subglacial channels and under a commonly used entrainment parameterisation, terminus undercutting does not significantly affect ice-perpendicular submarine melt rates. Total ablation by submarine melting however generally increases with the degree of undercutting due to the increased surface area undergoing melting. Thus the impact of submarine melting depends not only on absolute melt rate but also on the slope of the interface undergoing melting.

Submarine melting may therefore account for a greater fraction of terminus mass balance where calving fronts are severely undercut. Equivalently, the same vertical profile of melting can balance a higher ice flux at a more undercut terminus. In principle this provides a mechanism for melting to balance ice velocity even when ice-perpendicular melt rates are smaller than the ice velocity. The significance of this mechanism depends on the degree of undercutting and the profile of melting; undercutting increases total melt rate by between 3% and 36% in the idealised examples considered here (Fig. 6.2d).

The importance of shape in determining total melt rate means that in our model, evolution of the terminus is sensitive to the slope boundary condition applied at the grounding line. Specifying a boundary condition with θ closer to 0° leads to a more undercut terminus which undergoes greater retreat (Fig. 6.4). Therefore, if we are to simulate the effect of submarine melting on glacier dynamics using our model we need a means of setting this condition. One might argue this could be achieved by considering the dynamics of subglacial channels (*Röthlisberger*, 1972; *Ng*, 1998). While channel dynamics are probably important near the grounding line, it seems unlikely that channel dynamics should exert such influence over the full height of the calving front.

It is perhaps more likely that the sensitivity to this condition arises from our application of a plume model arbitrarily close to the grounding line, a region where channel dynamics should dominate over plume dynamics. Additionally, the confinement of

the plume when close to the grounding line may reduce entrainment, a factor which is not considered in current models. A more sophisticated approach which captures the transition from subglacial channel to plume may be needed to solve these issues.

6.4.2 Inferring melt rate from shape

For a terminus with a steady state shape, Eq. 6.5 may provide a means of determining vertical variation in submarine melting, as $\dot{m}/\sin\theta$ must be constant with height (assuming also that ice velocity does not vary with depth). Given knowledge of terminus shape $\sin\theta$, potentially from side-scan sonar, the vertical variation in melt rate can be calculated. Thus parts of a terminus with little curvature are indicative of depth-invariant melting (e.g. Figs. 6.2b and 6.3b, 100-300 m) while high curvature is indicative of melt rates changing rapidly with depth (e.g. Figs. 6.2b and 6.3b, near grounding line and fjord surface). Determining the absolute melt rate, rather than just vertical variation, requires additional information on terminus movement as a terminus could achieve a steady state shape but not position (e.g. Fig. 6.4c).

This argument relies on the assumption of steady state shape. In reality subglacial discharge varies in time and calving may also impact terminus shape. At glaciers with stable terminus positions and infrequent subsurface calving (e.g. *Luckman et al.*, 2015; *Fried et al.*, 2015), there may however be sufficient time for the terminus to approach steady state. The described method of determining variation in melt rate is independent of entrainment or melt rate parameterisations and so could prove useful in constraining plume models.

6.4.3 Implications for glacier dynamics

The presence of subglacial channels appears to play a key role in determining terminus shape, allowing the calving front to become (or remain) undercut close to the grounding line despite low submarine melt rates, and guiding the calving front towards the stationary shapes. Modelled calving fronts become severely undercut where plumes reach their maximum height, whether at depth (Figs. 6.4a-f) or the fjord surface (Figs. 6.4g-l). Since plumes often find neutral buoyancy at a strong pycnocline (*Carroll*

et al., 2015), this is a likely depth for severe undercutting. Calving of ice above may occur when surface crevasses intersect the undercut terminus cavity (*Fried et al.*, 2015), providing a coupling between calving dynamics and fjord stratification. Such a mechanism is perhaps most likely to occur at glaciers with infrequent subsurface calving, giving sufficient time for the calving front to approach a stationary shape. There is some evidence for this mechanism at glaciers in Alaska, Svalbard and Greenland (*Bartholomaus et al.*, 2013; *Chauché et al.*, 2014; *Luckman et al.*, 2015; *Fried et al.*, 2015).

When ice velocity substantially exceeds submarine melting, as is likely at Greenland's fastest flowing glaciers, the front may advance hundreds of metres over a period of weeks (e.g. Fig. 6.4i). During this period, other calving processes may come into play (*Benn et al.*, 2007), such as the full-depth buoyancy-driven calving identified at Helheim Glacier (*James et al.*, 2014), which may occur before the terminus has had time to become substantially undercut or approach a stationary shape. Ice modelling does not yet provide consensus on the degree of undercutting required to influence full-depth calving, if indeed it does at all (*O'Leary and Christoffersen*, 2013; *Todd and Christoffersen*, 2014; *Cook et al.*, 2014). Alternatively, regularly resetting a terminus to vertical by full-depth calving could increase the likelihood of developing a protruding toe, which may promote buoyancy-driven calving (*Wagner et al.*, 2016).

6.4.4 Limitations and future directions

We have here considered a line plume which is appropriate only for broad subglacial channels. Consideration of point sources is an obvious next step, but would be considerably more complex due to difficulties in capturing the interaction between ice shape, entrainment and plume structure in three dimensions. The sensitivity of our results to the prescribed grounding line boundary condition needs investigation, perhaps by detailed consideration of the subglacial channel to plume transition. Finally, as with all similar studies, we depend on parameterisations of submarine melting and entrainment, which remain untested in Greenland. Detailed field observations of plumes and terminus morphology are essential to constrain these parameterisations.

6.5 Conclusions

We have presented a model coupling buoyant plume theory to an evolving ice-ocean interface, facilitating study of feedbacks between terminus undercutting and submarine melting. We emphasize that the model and conclusions apply only where subglacial discharge emerges from a broad channel.

We find that undercutting has only a weak effect on plume dynamics and local submarine melt rate. All else being equal, local submarine melt rates will therefore not differ between vertical and undercut calving fronts, and undercutting will not affect the height reached by a plume. Undercut glaciers will however experience greater total ablation by submarine melting due to increased ice-ocean surface area. In consequence submarine melting may play a greater role in terminus mass balance and therefore glacier dynamics where calving fronts are severely undercut.

We present steady state terminus shapes in which melting and ice velocity are balanced, and show how terminus shape may in some circumstances be used to infer vertical variation in melt rate. Time-dependent simulations suggest that the presence of subglacial channels plays a key role in driving severe undercutting. Given sufficient time, calving fronts become strongly undercut at the maximum height reached by a plume, which may promote calving of ice above and define calving style at slower-flowing glaciers. It remains unclear however whether undercutting proceeds sufficiently quickly to influence the full-depth calving characteristic of Greenland's fastest-flowing glaciers.

Chapter 7

Spatially distributed runoff at the grounding line of a large Greenlandic tidewater glacier inferred from plume modelling

The foregoing three chapters investigated the effect on submarine melting of variation in the near-terminus subglacial hydrology (Chapter 4), the magnitude of subglacial discharge and the fjord stratification (Chapter 5), and (for a broad channel only) the degree of terminus undercutting (Chapter 6). Application of these key relationships to a real tidewater system requires knowledge of each of these factors. The magnitude of subglacial discharge can be estimated by surface melt modelling (e.g. *Hock*, 2003) and the fjord stratification has now been sampled for numerous tidewater systems around Greenland (*Carroll et al.*, 2016). The results of Chapter 6 suggest that, at least for broad subglacial channels, undercutting has little effect on plume dynamics and submarine melt rate at a given depth, though undercutting does affect total melt rate. Therefore, arguably the least constrained but still highly important control on submarine melting is the near-terminus subglacial hydrology. Side-scan sonar

observations of calving fronts show that tidewater glaciers can have many active subglacial channels (*Fried et al.*, 2015; *Rignot et al.*, 2015), but it is not clear whether this is true of all tidewater glaciers, and furthermore the collection of side-scan sonar observations is difficult and prohibitively dangerous at many glaciers.

In this chapter, a method for constraining near-terminus subglacial hydrology is developed based on the presence or absence of a plume at the fjord surface through incorporating knowledge of the magnitude of subglacial discharge and of plume dynamics. The method is applied to Kangiata Nunata Sermia, a large tidewater glacier in south-west Greenland, providing a real-world application of many of the concepts and models developed in the preceding three chapters.

Published in **Journal of Glaciology**, January 2017.

Authors: D. A. Slater[1], P. W. Nienow[1], A. J. Sole[2], T. R. Cowton[1,3], R. H. Mottram[4], P. L. Langen[4] and D. W. F. Mair[5].

1. School of Geosciences, University of Edinburgh, Edinburgh, UK.
2. Department of Geography, University of Sheffield, Sheffield, UK.
3. School of Geography and Sustainable Development, University of St Andrews, St Andrews, UK.
4. Danish Meteorological Institute, Copenhagen, Denmark.
5. School of Environmental Sciences, University of Liverpool, Liverpool, UK.

Citation: Slater, D. A., P. W. Nienow, A. J. Sole, T. R. Cowton, R. H. Mottram, P. L. Langen and D. W. F. Mair (2017), Spatially distributed runoff at the grounding line of a large Greenlandic tidewater glacier inferred from plume modelling, *Journal of Glaciology, 63*(238), 309-323, doi: 10.1017/jog.2016.139.

Author contributions: D.A.S., P.W.N., A.J.S. and T.R.C. designed the research. P.W.N., A.J.S., T.R.C. and D.W.F.M. collected field observations. A.J.S. processed field observations. R.H.M. and P.L.L. contributed runoff estimates. D.A.S. performed

the analysis and D.A.S., P.W.N., A.J.S. and T.R.C. developed the interpretation. D.A.S wrote the paper with input from all other authors.

Abstract

Understanding the drivers of recent change at Greenlandic tidewater glaciers is of great importance if we are to predict how these glaciers will respond to climatic warming. A poorly constrained component of tidewater glacier processes is the near-terminus subglacial hydrology. Here we present a novel method for constraining near-terminus subglacial hydrology with application to marine-terminating Kangiata Nunata Sermia in south-west Greenland. By simulating proglacial plume dynamics using buoyant plume theory and a general circulation model, we assess the critical subglacial discharge, if delivered through a single compact channel, required to generate a plume which reaches the fjord surface. We then compare catchment runoff to a time series of plume visibility acquired from a time-lapse camera. We identify extended periods throughout the 2009 melt season where catchment runoff significantly exceeds the discharge required for a plume to reach the fjord surface, yet we observe no plume. We attribute these observations to spatial spreading of runoff across the grounding line. Persistent distributed drainage near the terminus would lead to more spatially homogeneous submarine melting and may promote more rapid basal sliding during warmer summers, potentially providing a mechanism independent of ocean forcing for increases in atmospheric temperature to drive tidewater glacier acceleration.

7.1 Introduction

Mass loss from the Greenland Ice Sheet is accelerating, driven both by decreasing surface mass balance and increased ice discharge into the ocean from tidewater glaciers (*van den Broeke et al.*, 2009). From 2000 to 2005, ice discharge accounted for more than half of total mass loss during a period of pronounced acceleration, thinning and retreat of Greenlandic tidewater glaciers (*Pritchard et al.*, 2009; *Moon et al.*, 2012; *Enderlin et al.*, 2014). The widespread nature of this behaviour is indicative of a common climatic forcing, and although substantial ocean warming has been widely implicated as a driver of change at tidewater glaciers (e.g. *Holland et al.*, 2008a; *Christoffersen et al.*, 2011), process understanding of how a warming ocean perturbs a tidewater glacier remains at an early stage. Attribution of a mechanism for observed tidewater glacier change

is confounded by a broadly coincident increase in ice sheet surface melting (*Fettweis et al.*, 2011), which may also impact tidewater glacier dynamics. Due to our incomplete understanding of key tidewater glacier processes, we are currently limited in our ability to make projections of tidewater glacier dynamics and ultimately to quantify their future contribution to global sea level (*Straneo and Heimbach*, 2013).

One process through which the ocean interacts with tidewater glacier termini is submarine melting. Submarine melting is thought to be promoted by the emergence of subglacial discharge at the grounding line, forming plumes which rise buoyantly up the calving front (*Motyka et al.*, 2003, 2013; *Jenkins*, 2011; *Straneo and Cenedese*, 2015). These plumes both increase the transfer of heat from the ocean to the ice and help to draw warm water towards the calving front by setting up an exchange flow in the proglacial fjord (*Straneo et al.*, 2010; *Cowton et al.*, 2015). Progress has recently been made in modelling submarine melting, with the magnitude of subglacial discharge, fjord water properties, grounding line depth and near-terminus subglacial hydrology identified as key controls on the rate and distribution of submarine melting (Chapters 4 and 5; *Jenkins*, 2011; *Xu et al.*, 2013; *Sciascia et al.*, 2013; *Kimura et al.*, 2014; *Slater et al.*, 2015, 2016; *Carroll et al.*, 2016). Of these three controls, near-terminus subglacial hydrology is perhaps the most poorly constrained. Channelised subglacial drainage leads to rapid but localised melting of a calving front, while distributed subglacial drainage leads to slower and more homogeneous melting which results in higher total submarine melt rate (Chapter 4; *Slater et al.*, 2015). It is therefore important to constrain near-terminus subglacial hydrology if we are to understand the role of submarine melting in tidewater glacier dynamics.

A further motivation to study subglacial hydrology at tidewater glaciers comes from its role in modulating basal water pressure and ice velocity. The relationship between subglacial hydrology and ice velocity has long been studied at alpine glaciers (*Iken and Bindschadler*, 1986) and more recently at land-terminating glaciers in Greenland (e.g. *Bartholomew et al.*, 2010). These land-terminating systems typically show transient increases in ice velocity during periods of rapid increase in surface melting (*Bartholomew et al.*, 2010). Once runoff is stable or decreasing, typically in late summer, ice velocity

may fall to levels below pre-melt season values due to the development of efficient subglacial channels which act to reduce water pressure over a significant area of the bed (*Schoof*, 2010; *Cowton et al.*, 2013; *Hewitt*, 2013). At present, however it remains unclear to what extent conclusions from subglacial hydrology at land-terminating glaciers may be transferred to tidewater glaciers.

A number of studies have noted a seasonal evolution of ice velocity at some tidewater glaciers akin to that of land-terminating glaciers, suggesting that the hydrological systems may behave similarly (*Howat et al.*, 2010; *Sole et al.*, 2011; *Moon et al.*, 2014). These studies do not however extend all the way to the glacier terminus and there are indications from other studies that the hydrological systems may behave quite differently. For example, drilling of boreholes to the bed of calving glaciers (*Meier et al.*, 1994; *Sugiyama et al.*, 2011) has shown water pressure can be consistently close to ice overburden. In particular, the results of *Sugiyama et al.* (2011) from Glacier Perito Moreno in Patagonia suggest a lack of evolution towards more efficient subglacial hydrology through the summer, demonstrated by a strong positive correlation between air temperature and ice velocity, and providing a direct link between atmospheric warming and glacier acceleration.

Study of near-terminus subglacial hydrology in the field is however challenging; the terminus region of these fast-flowing glaciers is invariably highly crevassed and it is currently impossible to monitor proglacial discharge as this water flows directly into the fjord at the glacier grounding line. Some insight can be gained with measurements made from the proglacial fjord; side scan sonar can map the morphology of the calving front (*Rignot et al.*, 2015; *Fried et al.*, 2015) while detailed knowledge of ocean properties close to the terminus gives information on locations of subglacial discharge (*Stevens et al.*, 2016). These studies confirm the existence of focussed subglacial discharge at the grounding line but cannot draw conclusions on the emergence of smaller volumes of discharge elsewhere. Furthermore, the data presented in these studies has limited temporal coverage and may be difficult to obtain at glaciers with significant ice mélange.

In this paper we present a method for assessing near-terminus subglacial hydrology with

application to Kangiata Nunata Sermia (KNS), a large tidewater glacier in south-west Greenland. We obtain time series of total catchment runoff and plume visibility at the fjord surface and simulate proglacial plume dynamics using both a simple plume model and the MIT general circulation model (MITgcm). By comparing modelled to observed plume visibility, we attempt to quantify the spatial distribution of subglacial discharge emerging at the grounding line through the 2009 melt season. Two very recent studies have taken a similar approach. *Bartholomaus et al.* (2016) obtained plume visibility from satellite imagery at ∼1.5 week temporal resolution for three glaciers in West Greenland and compared to a simple plume model, but did not consider the effect of subglacial hydrology on plume visibility in any detail. *Schild et al.* (2016) present a 5 year time series of plume visibility and runoff for Rink Glacier, west Greenland, but did not include consideration of plume dynamics. In our study we combine a time series of plume visibility at hourly resolution with a detailed consideration of plume dynamics, enabling a degree of quantification of near-terminus subglacial hydrology. We discuss the extent to which the subglacial hydrology near the terminus of a fast-flowing tidewater glacier may differ from that further inland or at land-terminating glaciers, and consider the implications of our findings for submarine melting and ice dynamics.

7.2 Study area

KNS is the largest tidewater glacier in south-west Greenland (Fig. 7.1), draining approximately 2% of the Greenland ice sheet (*Sole et al.*, 2011). At the calving front, which is 4.5 km wide and grounded ∼250 m below sea level, ice velocity reaches 20 $\mathrm{m\,d^{-1}}$ (*Joughin et al.*, 2010; *Mortensen et al.*, 2011). *Lea et al.* (2014) have reconstructed the dynamics and terminus position of KNS since 1859, showing that the glacier has retreated nearly 10 km since 1921 with only short periods of readvance. Retreat was particularly rapid in the late 1940s when the termini of KNS and the adjacent Akugdlerssûp Sermia separated. Since 2000, KNS has undergone acceleration and thinning, but only modest retreat averaging ∼100 $\mathrm{m\,yr^{-1}}$ (*Rignot and Kanagaratnam*, 2006; *Thomas et al.*, 2009; *Lea et al.*, 2014). Previous hydrological study has inferred that seasonal evolution of ice velocity > 35 km inland from the calving front is controlled

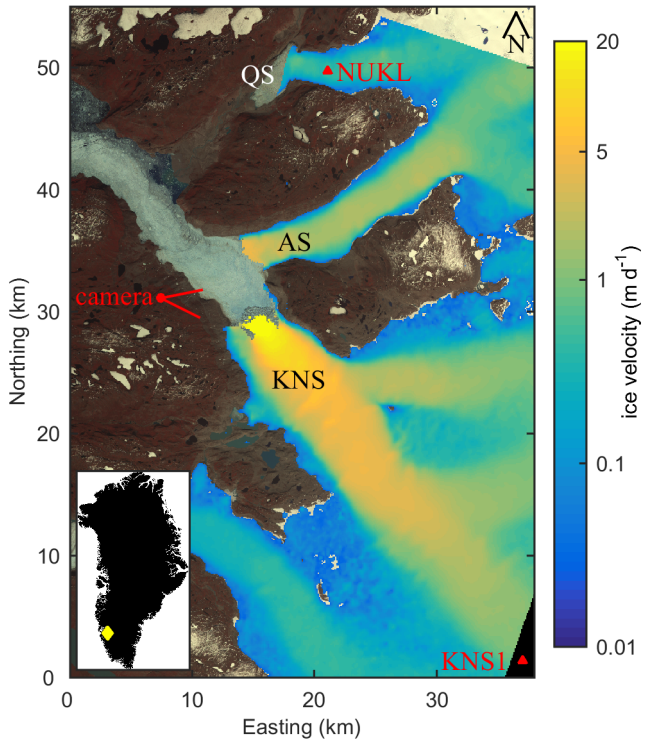

Figure 7.1: Overview plot of study site with Kangiata Nunata Sermia (KNS), Qamanârssûp Sermia (QS) and Akugdlerssûp Sermia (AS) labelled. Background is an ASTER image from 22nd June 2009. Colour overlay shows ice velocities calculated in the interval 21 August 2009 to 1 September 2009 from the NSIDC MEaSUREs dataset (*Joughin et al.*, 2010, 2011). Note the logarithmic velocity colour scale. Also shown is the location and approximate field of view of the time-lapse camera, the GPS station KNS1 and the PROMICE station NUKL. Bottom left inset shows location in south-west Greenland.

by surface melt-induced development of the subglacial drainage system, in a manner similar to land-terminating margins (*Sole et al.*, 2011). More recent work shows late summer deceleration in ice velocity which extends to within a few kilometres of the calving front, presumably induced by the evolution of the subglacial drainage system to an efficient state (*Ahlstrom et al.*, 2013; *Moon et al.*, 2014; *Fahnestock et al.*, 2015).

KNS flows into the Godthåbsfjord system, the oceanography of which has received extensive study (*Mortensen et al.*, 2011, 2013, 2014; *Kjeldsen et al.*, 2014; *Bendtsen*

et al., 2015). During the summer of 2009, which forms the focus of this study, the inner part of this fjord (∼40 km closest to KNS) was characterised by a warm (∼1-2°C) water mass at depths greater than 90 m, resulting from tidally-induced downward mixing of heat in the outer fjord and periodic inflows of dense coastal water (*Mortensen et al.*, 2013). At $<$ 90 m depth the water became cooler and fresher due to an outflowing mixture of subglacial discharge and ambient fjord water, while the fjord surface ($<$ 10 m depth) was characterised by a very fresh layer resulting from terrestrial freshwater runoff and iceberg melting (*Mortensen et al.*, 2013). It should be noted however that these characteristics have been inferred from ocean data taken $>$ 20 km from the calving front as dense ice mélange often prohibits detailed study close to the KNS terminus.

7.3 Methods

7.3.1 Controls on plume visibility

This paper utilises the relationship between the visibility of a plume on the fjord surface and the magnitude of subglacial discharge initiating the plume. This relationship has received extensive study at laboratory scales (e.g. *Morton et al.*, 1956), in theoretical studies (e.g. Chapter 5; *Slater et al.*, 2016) and in numerical modelling (e.g. *Carroll et al.*, 2015). Each of these approaches suggest the following qualitative description of plume dynamics.

Plumes at the margins of tidewater glaciers are initiated by subglacial discharge emerging from the grounding line and rising buoyantly to form a plume. As the plume rises, turbulent entrainment at the plume boundary dilutes the plume with salty ocean water, decreasing the density difference between the plume and fjord (*Morton et al.*, 1956). As a result, there may come a depth where the plume and ambient water density are equal, termed the level of neutral buoyancy. Due to vertical momentum, the plume can continue rising past this depth. However, above the level of neutral buoyancy the plume is negatively buoyant, and thus the plume slows, reaches a maximum height, then dives back downwards as it flows away from the glacier (*Carroll et al.*, 2015).

Alternatively, the plume may reach the fjord surface before reaching neutral buoyancy or running out of vertical momentum (Chapter 5; *Slater et al.*, 2016).

The level of neutral buoyancy and maximum height reached depend on the fjord stratification and magnitude of subglacial discharge (Chapter 5; *Carroll et al.*, 2015; *Slater et al.*, 2016). For small subglacial discharges, the resulting plume mixes rapidly with ambient fjord water and carries little momentum. The plume will thus reach neutral buoyancy and maximum height at some depth below the fjord surface. As subglacial discharge is increased, the resulting plume takes longer to dilute, preserving its positive buoyancy and shifting the level of neutral buoyancy and maximum height to shallower depths. At some critical subglacial discharge the plume has sufficient buoyancy to reach the fjord surface.

If we have a record of when a plume is visible at the fjord surface adjacent to a tidewater glacier, then by considering fjord stratification and plume dynamics we may gain information about the subglacial discharge resulting in the presence or absence of a plume. In addition, if we know the total catchment runoff reaching the terminus, then constraints can be placed on the configuration of the subglacial drainage system near the terminus.

7.3.2 Catchment runoff

We estimate KNS catchment runoff through the summer of 2009 using two standard methods. In the first we use a classic positive degree day sum (PDD) approach (*Hock*, 2003). We use air temperatures and surface ablation recorded at four sites, KNS1-4, sited in the catchment at 1282-1840 m elevation (Fig. 7.1, details in *Sole et al.* (2011)) to obtain degree day factors for snow (ddf_s) and for ice (ddf_i). We delineated the KNS catchment using topographic data from the BedMachine dataset (*Morlighem et al.*, 2014; *Howat et al.*, 2014; *Morlighem et al.*, 2015) and a standard hydropotential analysis (*Shreve*, 1972). In order to run the PDD model we need to extrapolate snow depth, degree day factors and air temperature to the full catchment. We take the simplest approach of using constant snow depth and degree day factors over the full catchment. These constant values are set at the mean values over the four GPS sites,

giving a snow depth of 33 cm, $ddf_s = 4.5$ mm d^{-1}°C^{-1} and $ddf_i = 11.9$ mm d^{-1}°C^{-1}. These degree day factors are comparable to or slightly higher than those obtained at nearby Qamanârssûp Sermia (Fig. 7.1) at an elevation of 790 m (*Braithwaite*, 1995). To obtain air temperature over the full catchment we assume a linear relationship between elevation and air temperature. This linear relationship is calculated at each PDD timestep using data from KNS1-4, and additional data from PROMICE station NUKL (*Ahlstrom et al.*, 2008) located nearby at an elevation of 550 m (Fig. 7.1).

The PDD approach is simplistic in many ways (for example it does not take account of refreezing of meltwater in the snowpack) but compares well with the more sophisticated regional climate model described below. One point which is particularly relevant to this study is that the PDD model outputs an estimate of surface ablation, which is related to but not equivalent to runoff of subglacial discharge at the grounding line. Meltwater from surface ablation may percolate through snow and/or enter a supraglacial drainage system before reaching the glacier bed through a moulin or crevasse. Meltwater may also be stored in surface lakes before drainage to the bed. Runoff resulting from surface lake drainage at KNS has been estimated using MODIS imagery by *Sole et al.* (2011). They estimate that the largest drainage event occurs on day 201 and contributes 70 m^3 s^{-1}. As such, the contribution to runoff from lake drainage is expected to be significantly smaller than surface melting, and we do not make further explicit consideration of lake drainage.

Once in the subglacial drainage system, travel time through the system may vary significantly depending on the state of the hydraulic system (*Fountain and Walder*, 1998). The cumulative effect of all of these processes will be to delay meltwater from production to entering the fjord. There may also be seasonal variation in this delay, with typically faster transit times in late summer (*Campbell et al.*, 2006; *Cowton et al.*, 2013). We attempt to take account of these processes by using transit velocities to delay runoff. We consider end-member transit velocities (*Cowton et al.*, 2013) of 0.05 m s^{-1} ('delayed') and 1 m s^{-1} ('rapid'). Thus meltwater produced 30 km from the terminus would enter the fjord approximately 1 week later in the 'delayed' scenario. It will be seen that our broad conclusions are not sensitive to the choice of transit velocity.

Our second estimate of runoff comes from the regional climate model HIRHAM5, applied to Greenland at 5 km resolution. The model has been described in detail in *Langen et al.* (2015); HIRHAM5 combines the HIRLAM weather forecasting model (*Eorola*, 2006), physics schemes derived from the ECHAM5 general circulation model (*Roeckner et al.*, 2003), and a dynamic snow/ice surface scheme. The model has demonstrated ability to accurately simulate runoff in the Godthåbsfjord region (*Langen et al.*, 2015). An important point for this study is that surface melt from the model runs off with a timescale depending on surface slope as in the regional climate model MAR (*Zuo and Oerlemans*, 1996; *Lefebre et al.*, 2003).

7.3.3 Plume visibility

A time series of plume visibility was created with images from a time-lapse camera. The camera was located on a ridge a few kilometres north-west of the calving front (Fig. 7.1) and captured an image every hour from 11 May 2009 (day 131) until 7 September 2009 (day 250). We manually classified these images into four states (Fig. 7.2). Images showing the presence of an ice tongue were assigned a value -1 (Fig. 7.2a). Images without an ice tongue but with no surface expression of a plume were assigned a value 0 (Fig. 7.2b). Images showing the presence of a plume at the fjord surface were assigned a value of respectively 1 or 2 depending on whether the surface expression of the plume was limited to within a few hundred metres of the calving front (Fig. 7.2c) or whether the plume flowed down-fjord at the surface for a number of kilometres (Fig. 7.2d). We are confident that the open water signatures which we interpret as plumes are not caused by calving or wind events as the open water is visibly turbid (e.g. Fig. 7.2c and d), indicating a subglacial origin. The result is a time series of plume visibility at hourly resolution through the summer of 2009. Data gaps result from camera malfunction or when bad weather obscured the calving front.

7.3.4 Plume dynamics

Plume dynamics are also modelled using two methods. Both have been widely applied to simulate plumes adjacent to glaciers and have been described in detail elsewhere

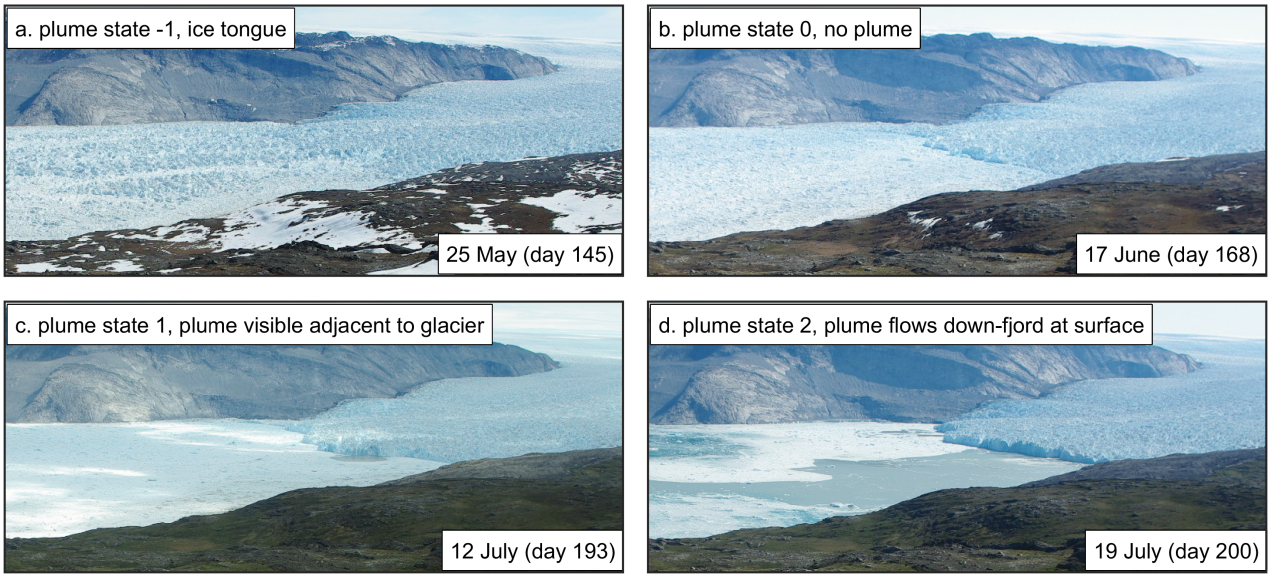

Figure 7.2: Illustrations of plume state classification. (a) Plume state = -1, ice tongue present. (b) Plume state = 0, no ice tongue and no surface expression of a plume. (c) Plume state = 1, plume visible adjacent to glacier terminus but is contained within a few hundred metres of the terminus. (d) Plume state = 2, plume visible and flows down-fjord at surface for a number of kilometres.

(Chapter 5; *Jenkins*, 2011; *Carroll et al.*, 2015; *Slater et al.*, 2016). Here we provide only a brief overview.

The first model we employ is buoyant plume theory (BPT) (*Morton et al.*, 1956). BPT describes the evolution of a plume as it rises by solving conservation equations for volume, momentum and buoyancy. Turbulent mixing of the plume with fjord water is incorporated by assuming entrainment into the plume is proportional to the plume velocity (*Morton et al.*, 1956). The model includes the feedback of submarine melting on plume buoyancy and frictional drag at the ice-ocean interface. We consider two plume geometries; a half-conical shape which we suggest is appropriate for plumes arising from narrow subglacial channels (i.e. point sources), and a wedge shape which we suggest is appropriate for plumes arising from very wide channels or diffuse subglacial

discharge (i.e. line sources). Details of the model for the two geometries can be found in Chapter 5; *Slater et al.* (2016).

While BPT captures much of the essential dynamics, it does not include any consideration of the fjord surface and does not describe what happens to water from the plume after the plume has reached its maximum height. To address these shortcomings and to provide a visual comparison of model and observation, we model the point source plumes in a high resolution non-hydrostatic configuration of the MITgcm (*Marshall et al.*, 1997a,b). Our aim is to accurately simulate near-ice plume dynamics rather than the full fjord circulation, thus the model domain is an idealised version of the proglacial fjord. We use a uniform fjord depth of 250 m, a width of 1 km and a length of 26 km. The domain is designed to be sufficiently wide and long that the boundaries do not affect plume dynamics. We do not expect that the idealised nature of our model domain, and in particular the lack of detailed near-glacier bathymetry, significantly affects the plume dynamics which are the focus of this study. In the near-ice region we employ an isotropic model resolution of 5 m, with subgrid-scale mixing parameters calibrated using BPT. A detailed description of the model configuration can be found in Chapter 4; *Slater et al.* (2015).

Fjord stratification in both BPT and MITgcm is set using a temperature and salinity profile taken in the fjord ∼35 km from KNS on 5 August 2009 (Fig. 7.3c and d, *Mortensen et al.* (2013)). We model plumes resulting from point source discharges of 1 to 500 $m^3\,s^{-1}$ and line source discharge per unit width from 0.01 to 2 $m^2\,s^{-1}$. We observe changes in plume dynamics with a focus on the surface expression of the plume.

Finally, additional data considered in this study includes ice velocity from KNS1 (Fig. 7.1, *Sole et al.* (2011)) which provides information on channelisation of subglacial hydrology higher up in the catchment, and ice velocities over the wider glacier (Fig. 7.1) from the NSIDC MEaSUREs dataset (*Joughin et al.*, 2010, 2011). Unfortunately, subglacial topography is poorly constrained near to the terminus of KNS (*Morlighem et al.*, 2014), preventing the meaningful modelling of drainage pathways for comparison with observed plume locations (e.g. *Fried et al.*, 2015).

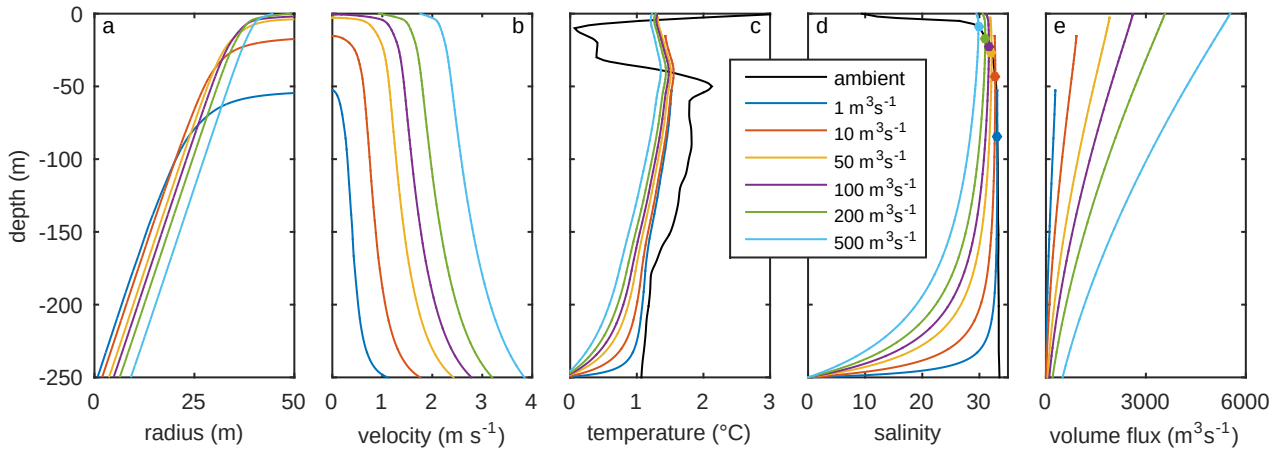

Figure 7.3: Plume modelling with BPT assuming a narrow subglacial channel (point source), for discharges from 1 to 500 $m^3\,s^{-1}$. Grounding line is located at -250 m and the fjord surface at 0 m. (a) shows plume radius, (b) plume velocity, (c) plume temperature, (d) plume salinity and (e) plume volume flux. Ambient fjord temperature and salinity are shown in black in (c) and (d). Salinities are expressed here and throughout this paper using the practical salinity scale. Filled symbols in (d) indicate the height at which the plume salinity exceeds the ambient salinity. Results suggest a plume initiated by a discharge of 1 $m^3\,s^{-1}$ will reach a maximum height ~50 m below the fjord surface, while plumes resulting from discharges upwards of 50 $m^3\,s^{-1}$ reach - or effectively reach - the fjord surface.

7.4 Results

7.4.1 Plume modelling

Results from BPT for point sources of subglacial discharge from 1 to 500 $m^3\,s^{-1}$ are shown in Fig. 7.3. For the smallest discharge considered - 1 $m^3\,s^{-1}$ - the plume mixes rapidly, with plume salinity close to the ambient fjord value within 50 m above the grounding line. However the fjord is very weakly stratified below 50 m depth, and therefore despite this plume being relatively weak, it still reaches to within 50 m of the fjord surface (Fig. 7.3b). As discharge is increased, plume width and velocity increase, plume temperature and salinity approach ambient values more slowly and the plume

reaches closer to the surface. The extremely fresh surface layer, with salinity as low as 10 (Fig. 7.3d), causes plumes to slow as they approach the fjord surface (Fig. 7.3b).

Of particular interest to this study is the critical subglacial discharge at which the resulting plume will be visible at the fjord surface. In Fig. 7.3, discharges of 100 $m^3\,s^{-1}$ or greater reach the fjord surface. However, BPT does not provide any information about the fate of water within the plume after the plume reaches either the surface or its maximum height. For example, the plume resulting from a discharge of 50 $m^3\,s^{-1}$ reaches within 5 m of the fjord surface and carries a volume flux of 2000 $m^3\,s^{-1}$ at its maximum height (Figs. 7.3b and e). This volume flux must flow down-fjord away from the glacier in a layer of finite thickness; therefore it is possible that the plume resulting from a discharge of 50 $m^3\,s^{-1}$ would indeed be visible at the fjord surface. To consider this possibility we turn to our modelling in MITgcm.

Results from point source plume modelling in MITgcm are shown in Fig. 7.4. The plots show side-view cross-sections through the centre of the modelled plumes for discharges from 5 to 500 $m^3\,s^{-1}$. The smallest discharge modelled - 5 $m^3\,s^{-1}$ (Fig. 7.4a) - results in a plume which rises to within ∼20 m of the fjord surface. The majority of plume water finds neutral buoyancy at ∼50 m depth and flows down-fjord at velocities up to 0.1 $m\,s^{-1}$. There are slow compensatory inflows of a few $cm\,s^{-1}$ (below 100 m depth and at the surface). The plume induces some disturbance at the surface; however water velocities here are very small (< 0.05 $m\,s^{-1}$) and if there is ice mélange at the surface we suggest this plume would be unlikely to show any surface expression (c.f. Fig 7.2b).

As subglacial discharge is increased, the modelled plume displays an increasing ability to drive a surface expression. At a discharge of 50 $m^3\,s^{-1}$ (Fig. 7.4e) the plume does indeed reach the fjord surface. Water from within the plume then flows away from the glacier in a layer which is 20 m thick in the vertical and with velocities which exceed 1 $m\,s^{-1}$ at the surface. Due to the entrainment of deeper saltier water, and in agreement with BPT (Fig. 7.3), water in the plume at the surface is denser than the ambient water. Plume water therefore remains at the surface for only ∼100 m from the glacier, thereafter diving back down to a level of neutral buoyancy at ∼40 m depth

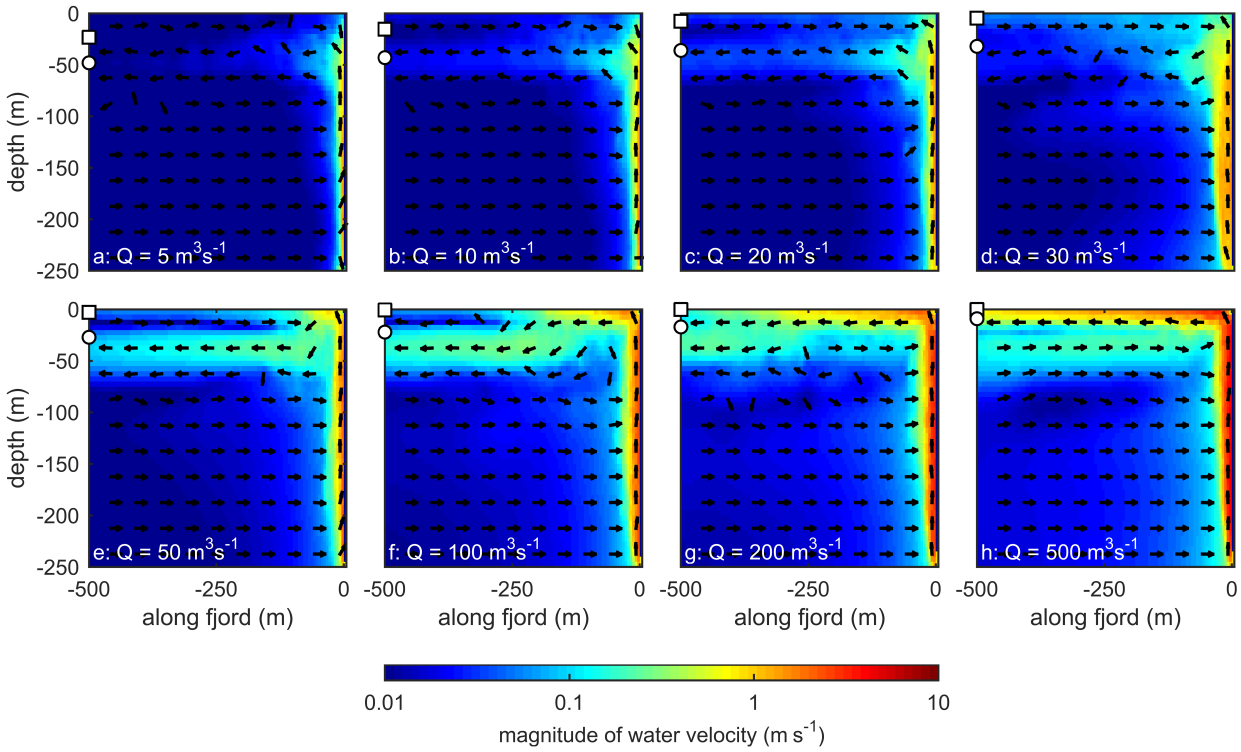

Figure 7.4: Point source plume modelling in MITgcm. Plots show a cross-section along a fjord centreline which passes through the centre of the plume. In each plot the glacier is at the right and runoff enters at the grounding line at the bottom right, producing a plume. Subglacial discharge increases from (a) 5 $m^3 s^{-1}$ to (h) 500 $m^3 s^{-1}$. Note logarithmic velocity colour scale and that arrows indicate direction - but not magnitude - of flow. Circular symbols indicate the height at which the plume salinity is equal to ambient salinity according to BPT (Fig. 7.3d) while square symbols indicate the maximum height reached by the plume according to BPT (Fig. 7.3b). The plots suggest a discharge of 50 $m^3 s^{-1}$ is required before the resulting plume will be visible at the fjord surface.

(Fig. 7.4e). We propose that this modelled situation corresponds to Fig. 7.2c where a plume is visible at the fjord surface but confined within a few hundred metres of the glacier. With a subglacial discharge of 500 $m^3 s^{-1}$ (Fig. 7.4h), the plume drives surface velocities in excess of 3 $m s^{-1}$ close to the glacier, and remains at the fjord surface for a number of kilometres (c.f. Fig. 7.2d).

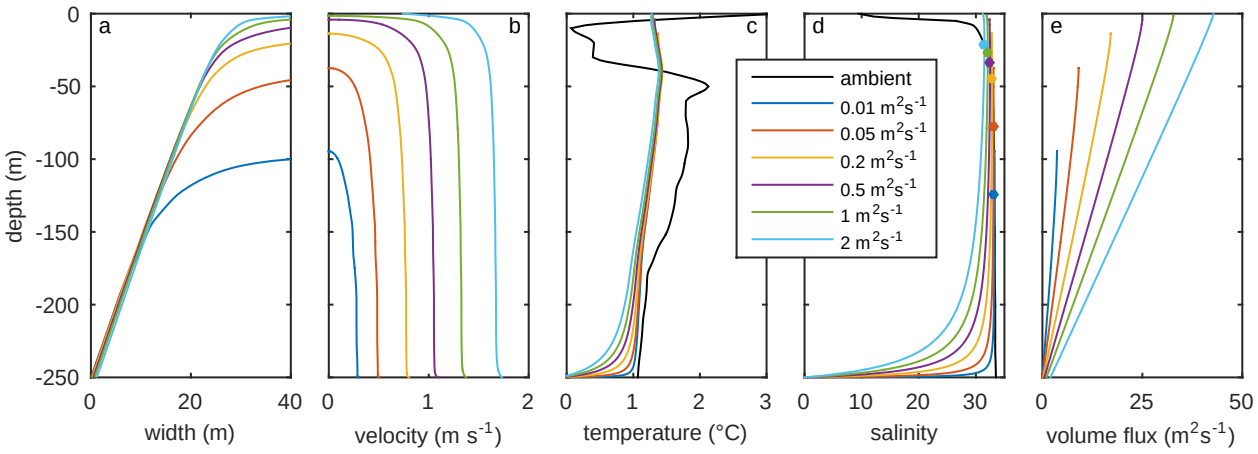

Figure 7.5: Plume modelling in BPT assuming a low and very wide subglacial channel (line source), for discharge per unit width from 0.01 to 2 $m^2\,s^{-1}$. A plume initiated by a discharge of 0.01 $m^2\,s^{-1}$ reaches a maximum height ~100 m below the fjord surface, while plumes resulting from discharges upwards of 0.5 $m^2\,s^{-1}$ will reach - or effectively reach - the fjord surface.

The maximum height reached by the plume according to BPT is plotted as square symbols in Fig. 7.4 while the height at which the plume becomes denser than ambient fjord water according to BPT is plotted as circular symbols. The latter height is thought to be a good estimate of the depth at which a plume finds neutral buoyancy as it flows away from the glacier (*Carroll et al.*, 2015). Comparison of the symbols from BPT with the MITgcm results shows very good agreement between the two methods, though BPT takes no account of mixing of fjord water as it flows away from the glacier, which may explain the slightly deeper outflowing layer for discharges of 50 and 100 $m^3\,s^{-1}$ (Fig. 7.4e and f).

Plots from BPT applied to line sources are shown in Fig. 7.5. The results show the same qualitative features as for point sources, with larger subglacial discharges driving stronger plumes which reach closer to the fjord surface. Plumes initiated by discharges of 1 $m^2\,s^{-1}$ and upwards reach the fjord surface but slow rapidly near the surface due to the fresh surface layer in the ambient fjord (Figs. 7.5b and d). A discharge of 0.5

$m^2\,s^{-1}$ generates a plume which reaches within 5 m of the fjord surface and carries a volume flux of 25 $m^2\,s^{-1}$ at its maximum height.

We now return to the question of the critical subglacial discharge required for the resulting plume to be visible at the fjord surface. Based on BPT, discharges of 100 $m^3\,s^{-1}$ for a point source and 1 $m^2\,s^{-1}$ for a line source are required for the plume to reach the surface (Figs. 7.3 and 7.5). However discharges of 50 $m^3\,s^{-1}$ and 0.5 $m^2\,s^{-1}$ result in plumes which reach within 5 m of the fjord surface and carry significant volume fluxes which must flow away from the glacier in a layer of finite thickness. Modelling in MITgcm indeed suggests that a discharge of 50 $m^3\,s^{-1}$ will drive a surface expression where plume water flows away from the glacier at the surface. By analogy it is reasonable to expect that a line source discharge of 0.5 $m^2\,s^{-1}$ would be sufficient to drive a surface expression.

In this study we consider 50 $m^3\,s^{-1}$ or 0.5 $m^2\,s^{-1}$ to be the critical subglacial discharge at which the resulting point or line source plume will drive an expression visible on the fjord surface. Note that a line source with discharge 0.5 $m^2\,s^{-1}$ and width 100 m carries the same discharge as a point source with discharge 50 $m^3\,s^{-1}$.

We note that if there is ice mélange present at the fjord surface (e.g. Fig 7.2b) then the surface expression of a plume may be inhibited, though this effect is very difficult to quantify. Our images show that ice mélange is present at the fjord surface throughout the summer of 2009. During periods of plume state 2, ice melange in the centre of the fjord is flushed downfjord (Fig. 7.2d), but after these events it quickly returns to cover the full fjord. The ice mélange appears fairly mobile in our time lapse images, especially later in the melt season. In support of our choice of critical subglacial discharge, *Bendtsen et al.* (2015) have estimated surface current velocities within a mélange-free surface plume on the order of 0.5 $m\,s^{-1}$. This indicates that surface velocities of 1 $m\,s^{-1}$, as modelled in our 50 $m^3\,s^{-1}$ case, would be sufficient to locally clear ice mélange from in front of KNS and give a plume visible at the fjord surface.

7.4.2 Plume visibility, catchment runoff and subglacial hydrology

Early melt season (day 110-192)

Significant surface melting begins on day 135 following a rapid rise in air temperature (Figs. 7.6a and b). The ice tongue (Fig. 7.2a) remains structurally intact until rapid disintegration on day 155 following a further increase in surface melting. There follows a period of 37 days during which there is no visible surface expression of a plume (Figs. 7.2b and 7.6d) in spite of substantial modelled surface melting (Fig. 7.6b). Runoff in the 'PDD rapid' case (Fig. 7.6b, purple) is similar to surface melt production (Fig. 7.6b, green) and regularly exceeds 200 $m^3 s^{-1}$ from day 152 to 192. Runoff as predicted by HIRHAM5 peaks at 750 $m^3 s^{-1}$ during a large rainfall event. In the 'PDD delayed' case (Fig. 7.6b, pink), peaks in runoff are delayed and smoothed, but between days 152 and 192, runoff still peaks at 250 $m^3 s^{-1}$ and is sustained at this level for $\sim$15 days.

Modelled runoff in the early melt season therefore frequently exceeds the critical discharge required for a plume to show a surface expression. Considering first point sources, if at a given time there is no surface expression of a plume, our results suggest that no single channel is carrying a discharge greater than 50 $m^3 s^{-1}$. If at the same time runoff from the glacier into the fjord is 250 $m^3 s^{-1}$, there must be at least 5 independent subglacial channels so that no individual plume reaches the fjord surface and creates a visible surface expression. If instead runoff is emerging as a line source and there is no surface expression of a plume, discharge per unit width at the source must not exceed 0.5 $m^2 s^{-1}$. If at the same time catchment runoff is 250 $m^3 s^{-1}$, this implies that the line source has a minimum width of 500 m. Of course, point and line sources are idealised geometries and a realistic system may consist of a complex combination of the two. These idealised geometries nevertheless provide an informative first-order measure of the spatial spreading of runoff at the grounding line.

Modelled plume visibility for various runoff and hydrological scenarios are plotted in Fig. 7.6e. A label P4/L400 indicates 4 independent point sources or a line source of width 400 m. As described above, these are equivalent scenarios in terms of plume

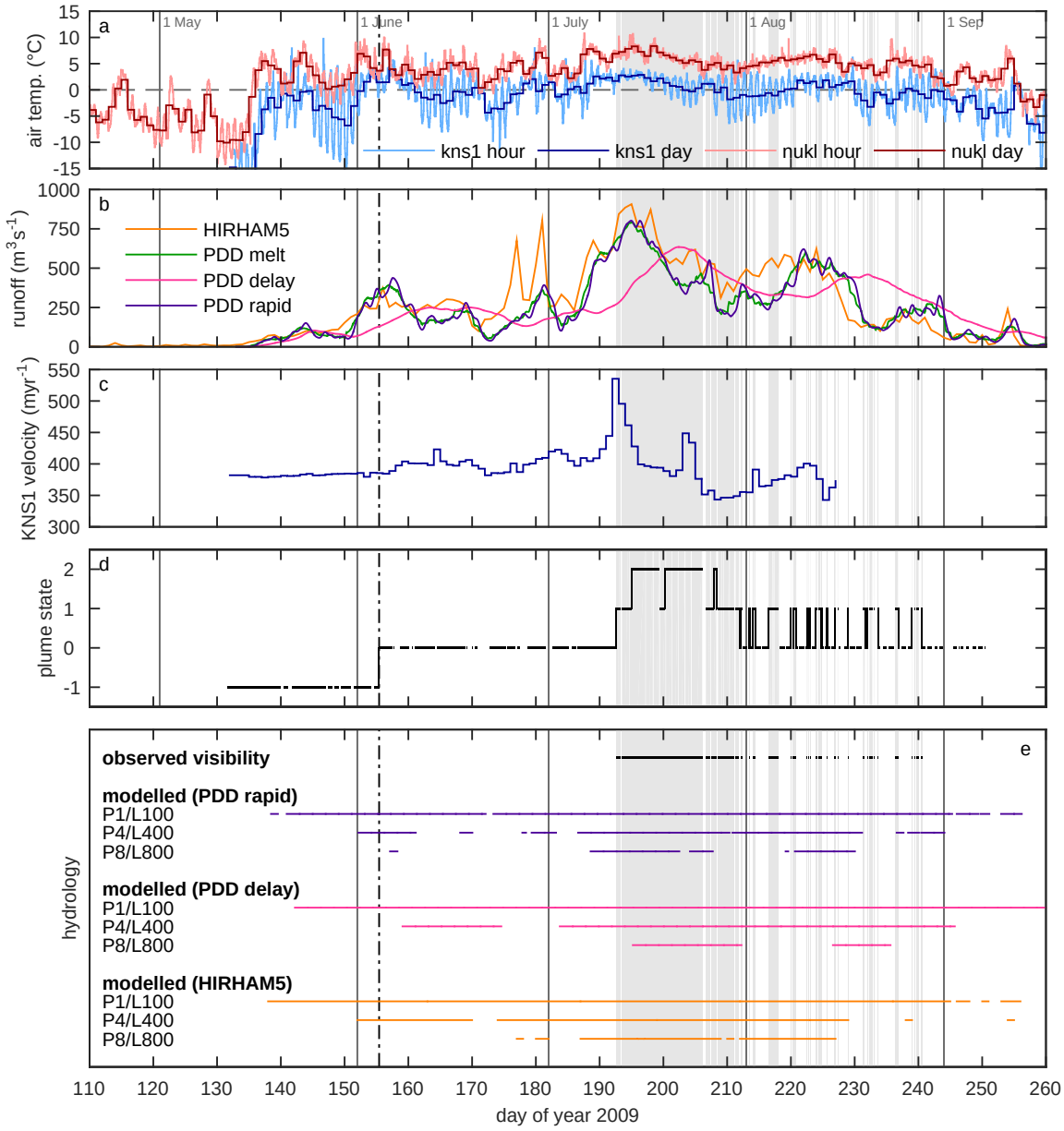

Figure 7.6: (a) air temperature from KNS1 and NUKL PROMICE stations (Fig. 7.1). (b) Modelled runoff. HIRHAM5 (orange) delays runoff using a parameterisation based on surface slope. PDD model (green) assumes instantaneous runoff. PDD delay (pink) uses a transit velocity of 0.05 m s^{-1} from point of production to the terminus. PDD rapid (purple) uses a transit velocity of 1 m s^{-1}. The green curve has been smoothed using a 3 day moving window, the pink and purple curves using... [*Caption continues on next page*]

Figure 7.6: [*Continued*] ...a 6 hour moving window. Large discrepancies between HIRHAM5 and the PDD model arise due to rainfall events (e.g. days 177 and 181). (c) KNS1 daily ice velocity. (d) Plume state as described in Fig. 7.2. (e) Plume visibility under various runoff and hydrological scenarios, for comparison to observed plume visibility (top, black). P4 assumes 4 independent narrow subglacial channels (point sources) while L400 assumes a low and wide subglacial channel of 400 m width (line source). For example, assuming we had a single narrow subglacial channel and runoff according to the PDD delay scenario, a plume would be visible at the fjord surface continuously from day 142 to 260. Dash-dot black line shows timing of ice tongue break-up.

visibility. We expect that the structural integrity of the ice tongue would prevent a plume from reaching the surface before day 155. The lack of plume visibility from day 155 to 192 can be reproduced by a drainage system consisting of 8 independent point sources or a line source of width 800 m (Fig. 7.6e, P8/L800). It is certainly clear that in any runoff scenario, there cannot be a single large subglacial channel routing the majority of the runoff, as the resulting plume would be visible at the fjord surface continuously through the early melt season (Fig. 7.6e, P1/L100). We therefore argue that during the early melt season, the input of runoff into the fjord from beneath the glacier occurs in a spatially distributed fashion consisting of either numerous point sources, a wide line source, or some combination of the two.

Mid melt season (day 192-211)

Surface melting increases from day 185 to a peak on day 195, driven by air temperatures above zero even at high elevations (Fig. 7.6a). Over the following days surface melting decreases but runoff remains high (> 250 m^3 s^{-1}). A plume is first visible on day 192 in state 1 (Fig. 7.2c) before expanding to state 2 (Fig. 7.2d) on day 195 where it largely remains until day 206 (Fig. 7.6d). The plume is then visible mostly in state 1 until day 211 when it briefly disappears, meaning that a plume is consistently visible for 19 consecutive days in late July. While in state 1 the plume appears consistently in the location seen in Fig. 7.2c. While in state 2 the surface expression of the plume occupies

a significant width of the calving front (∼2 km) and there is infrequently a secondary plume on the eastern side of the fjord.

A record of ice velocity at KNS1 (Fig. 7.6c) shows a peak on day 192, and the subsequent decrease of velocity to values below those in the early melt season is suggestive of the formation of efficient subglacial channels in the vicinity of KNS1 (*Sole et al.*, 2011). The establishment of efficient channels would suggest that following peak runoff (day $\gtrsim$ 200), our 'rapid' meltwater transit scenario may be appropriate. We continue however to consider the end member 'rapid' and 'delayed' cases, with runoff from the former peaking at 800 $m^3 s^{-1}$ on day 195 and from the latter at 650 $m^3 s^{-1}$ on day 202.

Runoff is sufficiently high in the mid melt season that modelled plume visiblity reproduces the observed visibility even for the most spatially distributed case considered, consisting of 8 independent point sources or a line source of 800 m width (Fig. 7.6e, P8/L800). We may also compare the plume modelling with our observations of the fjord surface from our time-lapse imagery. On day 200, the plume flows down-fjord at the surface for a number of kilometres (Fig. 7.2d). Our modelling (Fig. 7.4) would suggest this requires upwards of 200 $m^3 s^{-1}$ from a point source or by analogy, upwards of 2 $m^2 s^{-1}$ from a line source. Since we have argued that in the early melt season focussed runoff does not exceed 50 $m^3 s^{-1}$ from a point source or 0.5 $m^2 s^{-1}$ from a line source, there may be a focussing of runoff in the mid melt season relative to the early melt season.

Late melt season (day 211-260)

From day 211 to day 230, surface melting remains high with a peak of 600 $m^3 s^{-1}$ on day 222 in the 'rapid' scenario and 450 $m^3 s^{-1}$ on day 232 in the 'delayed' scenario (Fig. 7.6e). On day 230 there is a marked decrease in melt with subsequent runoff remaining below 350 $m^3 s^{-1}$ before ceasing on day 257. In the late melt season, plume surface expression is sporadic, with frequent switching between state 0 and 1 (Fig. 7.6d). This variability has no diurnal pattern (i.e. plumes do not appear or disappear at the same time of day), which is consistent with observed muted diurnal variability in runoff from large glacial catchments in Greenland (*Cowton et al.*, 2013). The plume does

however appear in a preferred location, similar to or slightly west of the plume seen in Fig. 7.2c. The plume is last seen on day 240, with the last of our images taken on day 250.

The lack of correspondence between variability in runoff and plume visibility means that none of our hydrological scenarios reproduce the observed sporadic plume visibility (Fig. 7.6e). Runoff during the period of plume fluctuation remains high and would certainly be large enough to sustain a plume at the fjord surface continuously if all runoff was emerging from a single narrow subglacial channel. Therefore our inference is that in the late melt season runoff emerges into the fjord in a spatially distributed fashion, with sporadic focussing resulting in a plume visible at the fjord surface. In the late melt season the hydrological system thus appears rather unstable, a point we return to below.

7.4.3 Summary of results

The hydrological scenario which most closely matches the observed plume visibility throughout the season consists of 8 independent point sources or a line source of 800 m width (Fig. 7.6e, P8/L800). This spatially distributed scenario broadly reproduces the lack of plume visibility in the early melt season and the onset of a visible plume in the mid melt season. Of course the hydrological system may also evolve through the season; the observed plume visibility would also be recreated by a system which is more spatially distributed than the P8/L800 scenario in the early melt season and less spatially distributed than the P8/L800 scenario in the mid melt season. The oscillatory nature of plume visibility in the late melt season is not captured by any of our runoff and hydrological scenarios, and is suggestive of a highly dynamic system.

However, our images only rarely show more than one distinct plume, and the plume is often observed in the same location. This may reflect a preferred location for runoff which is the largest of many point sources. In the mid melt season the significant width of calving front in contact with the plume may be indicative of a wide subglacial channel or perhaps a number of closely spaced point sources with plumes merging before the fjord surface. Based on scalings in *Cenedese and Gatto* (2016) and a terminus fjord

depth of 250 m, two point sources at KNS separated by less than ∼70 m will generate plumes which interact, potentially reducing entrainment and helping the plumes to reach the fjord surface.

It is certainly clear that there cannot be a single narrow subglacial channel routing the majority of the runoff throughout the melt season; the models predict that this would result in a plume continuously visible at the fjord surface from day 155 to beyond day 250 (Fig. 7.6e, P1/L100), and this is not observed. Under consistently high runoff (Fig. 7.6b) we instead we see a plume only periodically. The broad conclusion from our results is therefore that for much of the melt season runoff emerges into the fjord at the grounding line in a spatially distributed and diffuse fashion.

7.5 Sensitivities

Of critical importance to the conclusions drawn in this paper are the estimates of catchment runoff and the critical discharge required for a plume to reach the surface. In this section we describe possible sources of error on these estimates. Sensitivies are presented for a point source of 50 $m^3\,s^{-1}$ discharge; results for line source plumes (not shown) are similar.

We first consider catchment runoff. HIRHAM5 has a demonstrated ability to simulate catchment runoff accurately in the Godthåbsfjord region (*Langen et al.*, 2015). The degree day factors for ice (11.9 $mm\,d^{-1}{}^{\circ}C^{-1}$) and for snow (4.5 $mm\,d^{-1}{}^{\circ}C^{-1}$) used in our PDD model are comparable to or slightly higher than values previously reported for Greenland, a fact which may be explained by the high elevations of KNS1-4 (*Braithwaite*, 1995; *Hock*, 2003). The PDD approach is simple but nevertheless compares well with the more sophisticated HIRHAM5 (Fig. 7.6b). The agreement between these two independent approaches gives us confidence in our estimates of catchment runoff. Perhaps the greatest uncertainty in runoff comes from lack of knowledge of the transit time of meltwater from production to when it enters the fjord. We have however shown by considering end members that this complication does not affect our broad conclusions.

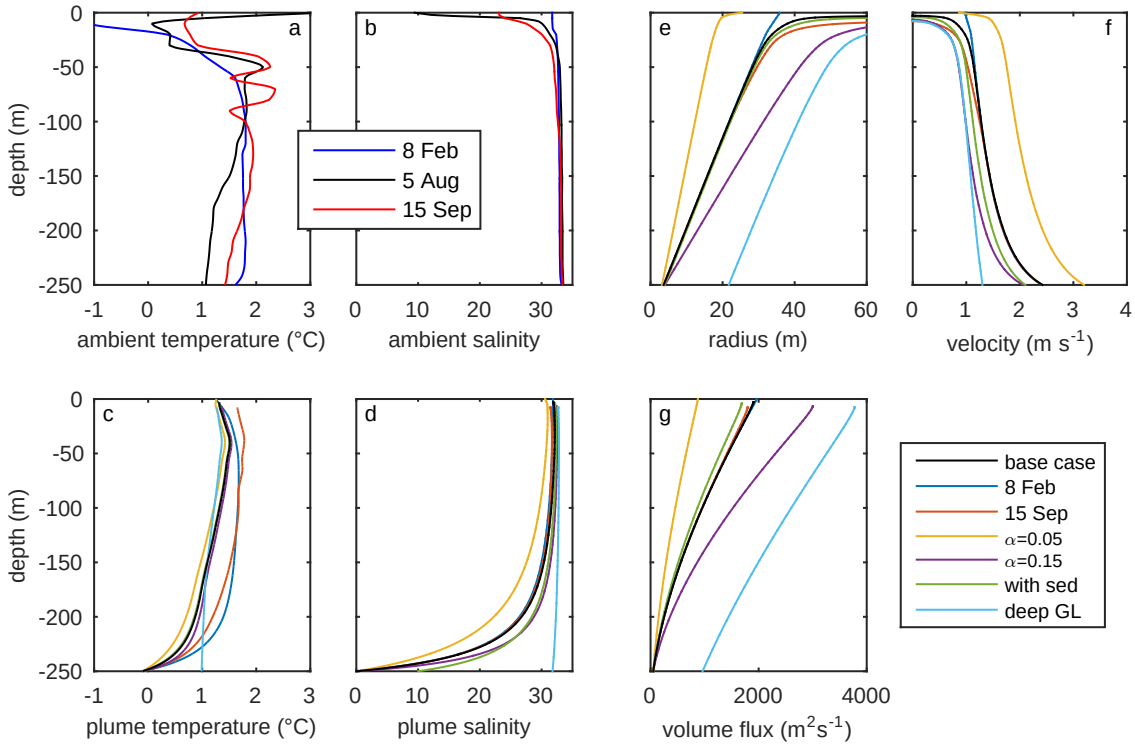

Figure 7.7: (a) temperature and (b) salinity profiles from the proglacial fjord in 2009, digitised from *Mortensen et al.* (2013). The 8 February profile was taken ∼10 km from KNS, while the 5 August and 15 September profiles were taken ∼35 km from KNS. Main plume modelling results shown in Figs. 7.3, 7.5 and 7.4 use the profile from 5 August. (c)-(g) show sensitivity experiments for a point source plume with 50 $m^3\,s^{-1}$ subglacial discharge. Black lines in (c)-(g), labelled 'base case', indicate the default case plotted in Fig. 7.3. Sensitivities considered are '8 Feb': uses 8 February ambient profiles, '15 Sep' uses 15 September ambient profiles, '$\alpha = 0.05$' uses a small entrainment coefficient, '$\alpha = 0.15$' uses a high entrainment coefficient, 'with sed' considers a plume with sediment, as described in the text, and 'deep GL' considers a deeper grounding line at 400 m depth (only the 250 m closest to the fjord surface are plotted).

In our plume modelling we use ambient fjord conditions sampled on 5 August 2009 (Fig. 7.3c and d) approximately 35 km from the terminus of KNS (*Mortensen et al.*, 2013). The significant distance from the terminus means that the stratification at the calving front could differ from the profile we use; dense ice mélange prevented

detailed surveying of the fjord closer to the terminus. The ambient fjord conditions also show a seasonal evolution with a freshening of water close to the surface during the summer months (*Mortensen et al.*, 2013). To test how plume dynamics respond to seasonal changes in fjord stratification we ran BPT with ambient profiles from 8 February and 15 September 2009 (Fig. 7.7a and b). The lack of a fresh surface layer in the February profile means that the plume reaches the surface more easily, while use of the September profile produces only very minor differences relative to the default 5 August profile (Fig. 7.7c-g). Observations by *Mortensen et al.* (2013) suggest that the fresh surface layer is well established by late June and that the August profile is therefore likely representative of the stratification for much of the summer. In May and early June it is possible that the fresh surface layer is absent (*Mortensen et al.*, 2013); however our modelling suggests that this makes it easier for a plume to reach the surface, thus lowering the critical discharge needed for the plume to reach the fjord surface and strengthening our conclusions regarding the distributed nature of subglacial discharge. In summary, our analysis suggests that seasonal changes in stratification do not affect our conclusions.

The rate at which the plume entrains ambient fjord water is parameterised in BPT by assuming that the degree of entrainment is proportional to the vertical velocity of the plume (*Morton et al.*, 1956). The constant of proportionality, α, has here been set to 0.1, and the mixing parameters in our MITgcm modelling have also been tuned to this value (Chapter 4; *Slater et al.*, 2015). However, this turbulence closure has not yet received validation in the specific case of proglacial discharge plumes adjacent to tidewater glaciers, and furthermore some authors advocate slightly different values of α (e.g. *Turner*, 1979). To test the sensitivity of our results to this choice, we considered low ($\alpha = 0.05$) and high ($\alpha = 0.15$) values, which span the range of values in the literature. The value of α strongly affects plume dynamics; a higher value results in a plume with a larger width and volume flux, but lower velocity (Fig. 7.7c-g). However the value of α does not here strongly affect the height reached by the plume; use of $\alpha = 0.15$ results in a plume with maximum height within 4 m of a plume having $\alpha = 0.1$.

Therefore, for these ambient conditions, the critical discharge required for a plume to reach the fjord surface does not depend strongly on the value of α.

Proglacial discharge plumes can contain significant volumes of sediment (*Tedstone and Arnold*, 2012) which may alter the dynamics of the plume. The presence of suspended sediment in the plume would act to increase the density of plume water, thus decreasing plume buoyancy. As the plume rises, mixing with ambient water would decrease the sediment concentration. An assessment of the importance of sediment can be achieved by increasing the density of subglacial discharge by using a non-zero initial salinity. We model a plume with an initial salinity of 10, resulting in a reduction in plume buoyancy equivalent to a sediment load of 8 $\mathrm{kg\,m^{-3}}$, which may be considered high for Greenland subglacial discharge (*Cowton et al.*, 2012). The sediment-laden plume is, as expected, weaker than without sediment yet it still shows good evidence of reaching the fjord surface (Figs. 7.7c and d, 'with sed'). The relatively small effect of this sediment load on plume dynamics may be explained by the sub-linear relationship between plume velocity and initial plume buoyancy (Chapter 5; *Slater et al.*, 2016), meaning that plume dynamics are quite insensitive to initial plume buoyancy.

The bathymetry near the grounding line at KNS is not known in great detail. A grounding line depth of 250 m has been widely assumed (*Mortensen et al.*, 2014; *Lea et al.*, 2014; *Bendtsen et al.*, 2015), however we recognise that the grounding line depth of KNS could conceivably be somewhat greater and display across-fjord variability. To test the sensitivity of our results to a deeper grounding line we ran BPT with a grounding line depth of 400 m. CTD profiles from further down-fjord where the bathymetry is deeper than 250 m indicate that the fjord is very weakly stratified at depth (*Mortensen et al.*, 2014), therefore we use the values of temperature and salinity at 250 m depth to fill the depth range from 250 to 400 m. Under this scenario, the modelled plume (Fig. 7.7c-g, 'deep GL') still reaches the fjord surface due to the weak fjord stratification at depth and relatively thin fresh surface layer. We therefore suggest that our conclusions will hold even if future surveys reveal that KNS has a significantly deeper grounding line than currently believed.

A final important point is that our plume modelling has assumed that the calving front at KNS is flat and vertical. Side-scan sonar has recently shown that the calving fronts of a number of tidewater glaciers in west Greenland can be substantially undercut and deeply incised in the location of plumes (*Rignot et al.*, 2015; *Fried et al.*, 2015). The confinement of a plume within an incision into the ice could potentially modify the rate of mixing between the plume and ambient fjord water, thus affecting its likelihood of reaching the fjord surface. Such feedbacks between the shape of the calving front and the dynamics of the plume are not captured by our modelling.

7.6 Discussion

7.6.1 Near-terminus subglacial hydrology

Our modelling suggests that for most of the 2009 melt season, runoff volumes easily exceed the critical discharge required to produce a plume visible at the fjord surface. Yet particularly in the early and late melt season, plumes are only intermittently visible. Based on these observations, we argue that runoff must often emerge into the fjord in a spatially distributed fashion, either through numerous narrow channels, a single but very wide channel, or through some other complex and diffuse system. Spatially distributed hydrological systems are associated with high basal water pressure (*Fountain and Walder*, 1998); our findings are therefore qualitatively consistent with borehole water pressure records from near the termini of calving glaciers, which have found basal water pressures close to ice overburden (*Meier et al.*, 1994; *Vieli et al.*, 2004; *Sugiyama et al.*, 2011). Furthermore high basal water pressures are associated with low basal drag, and our results are therefore also consistent with recent ice model inversions, which found that the beds beneath fast-flowing glaciers in Greenland provide almost no resistance to flow (*Shapero et al.*, 2016).

Distributed subglacial hydraulic systems may take the form of networks of linked subglacial cavities or saturated subglacial sediments with channels incised into the bed (e.g. *Fountain and Walder*, 1998). Our results do not permit us to differentiate between these morphologies and both may plausibly persist near the terminus of KNS.

The presence of deforming subglacial sediment is thought to be fundamental to the fast flow of Antarctic ice streams (e.g *Alley et al.*, 1986) and there is some evidence for the presence of thick layers of sediment beneath the Greenland ice sheet (*Walter et al.*, 2014). *Walder and Fowler* (1994) developed a theoretical framework for subglacial drainage in saturated, deformable till, suggesting that under conditions of high subglacial discharge, low effective pressure and low surface slope (all of which are likely satisfied at the terminus of KNS), drainage may occur stably through shallow and wide canals incised into the subglacial sediment. It is plausible that such a drainage system exists near the terminus of KNS, with the resulting low effective pressure driving high ice velocity, and the wide and distributed nature of canals spreading runoff across the grounding line and resulting in plumes only intermittently visible at the fjord surface.

Alternatively, distributed drainage make take place in a network of linked subglacial cavities, and there is theoretical support (e.g. *Kamb*, 1987; *Fowler*, 1987; *Schoof*, 2010) for the prevalence of this style of drainage when ice slides rapidly over its bed. Such work was initially motivated by the study of surging glaciers but is equally applicable to the fast flowing termini of calving glaciers. These theoretical studies consider drainage through Röthlisberger channels and linked cavities in the presence of basal sliding. Each suggests a transition between drainage through channels and drainage through cavities which depends on sliding velocity and the magnitude of subglacial discharge. For low sliding velocity and high subglacial discharge, drainage through cavities is unstable and drainage will preferentially take place through channels. For high sliding velocity and low subglacial discharge, drainage through efficient channels is unstable and will instead take place through a network of linked cavities (*Kamb*, 1987; *Fowler*, 1987; *Schoof*, 2010).

We do not attempt quantitative application of these idealised theories to the terminus of KNS as this would require values for a number of poorly constrained parameters. Nevertheless it is plausible that the extremely high sliding velocities near the terminus of KNS ($\sim$20 $\mathrm{m\,d^{-1}}$, Fig. 7.1) might render efficient subglacial channels unstable and promote drainage through an inefficient network of linked subglacial cavities. This

could explain the spatially distributed nature of subglacial runoff inferred from our plume observations.

One may also consider the seasonal evolution of the drainage system near the terminus of KNS. In the early melt season, when we see sustained runoff but no plume, the drainage system might be expected to exist stably as a network of linked cavities. The increase in runoff in the mid melt season could be sufficient to cross the threshold into channelised drainage, while the oscillation of plume visibility in the late melt season might be indicative of a system which is close to the cavity/channel threshold (*Kamb*, 1987). Equally, much of the variability in plume visibility can be captured by a single hydrological scenario (e.g. P8/L800 in Fig. 7.6e), providing evidence for a hydrological system which is fairly static but spatially distributed throughout the melt season.

We acknowledge that much of this discussion is speculative and it will require much further study to elucidate the precise nature of the hydrological system near the terminus of KNS. Consideration of a longer dataset spanning multiple years might be illuminating, particularly if there is significant interannual variability in runoff. It would also be interesting to further evaluate our arguments by investigating - along similar lines to that undertaken in this study - a much slower flowing tidewater glacier. According to the theories of transition between channelised and distributed drainage discussed above, a slower flowing tidewater glacier would more readily form efficient channels near the terminus and should therefore have a plume visible at the fjord surface more frequently (once catchment runoff and fjord stratification have been taken into account).

Three recent studies present results which are consistent with our arguments. At fast flowing Rink Glacier in West Greenland, *Bartholomaus et al.* (2016) suggest that routing all runoff through a single narrow subglacial channel would give a plume visible at the fjord surface far more frequently than is observed. At the same glacier and based on the presence of plumes visible at the fjord surface long after surface melting had ceased, *Schild et al.* (2016) argued for significant subglacial storage of meltwater and therefore a distributed hydrological system. Finally, *Fried et al.* (2015) mapped

the terminus morphology at Kangerlussuup Sermia (KS), west Greenland, finding at least seven distinct submarine cavities in the calving front, only a few of which were associated with plumes visible at the fjord surface. Despite the significantly lower ice velocity at KS, these observations indicate that there are similarities with the drainage system we infer at KNS, with runoff spread between multiple conduits at the grounding line, and the resulting plumes not necessarily visible at the fjord surface.

7.6.2 Implications for ice dynamics

The structure and evolution of the subglacial hydrological system exerts a strong control on ice velocity. We here discuss the possible implications of our findings for ice motion at KNS.

Land-terminating glaciers in Greenland show a hydrologically-induced seasonal cycle in ice motion, often displaying slowest motion in late summer during periods of stable or decreasing runoff when efficient channels reduce basal water pressure over a significant area of the bed (e.g. *Bartholomew et al.*, 2010; *Andrews et al.*, 2014). *Sole et al.* (2011) report that ice velocities at KNS in summer 2009 show this same evolution between 35 km and 48 km from the glacier terminus. Remote sensing of ice velocity (*Moon et al.*, 2014; *Fahnestock et al.*, 2015) extends evidence for this behaviour to within a few kilometres of the KNS terminus. Similarly, *Howat et al.* (2010) showed that a number of tidewater glaciers further north in Greenland display this same seasonal evolution of ice velocity, which they infer is driven by the evolution of subglacial drainage.

However, the extent to which this evolution occurs within the last few kilometres before the glacier terminus remains unclear. Our results suggest that efficient subglacial channels do not persist near the terminus. In the late melt season it may then be the case that efficient channels exist further inland, but that runoff from these channels spreads as it approaches the terminus region. This spreading might be initiated as the channel approaches the terminus where the glacier becomes close to flotation and basal sliding becomes sufficiently high (Fig. 7.1) to render Röthlisberger channels unstable (*Kamb*, 1987; *Fowler*, 1987; *Schoof*, 2010).

In a distributed system which shows resistance to channelisation, as we infer exists near the terminus of KNS, water pressure increases with runoff (*Kamb*, 1987) and therefore ice velocity would be expected to scale with runoff. Such behaviour has been observed at lake-terminating Glacier Perito Moreno in Patagonia (*Sugiyama et al.*, 2011) and *Moon et al.* (2014) have argued for similar behaviour at a number of marine-terminating glaciers around Greenland. Thus under distributed subglacial drainage, increased surface melting may increase basal lubrication and drive tidewater glacier acceleration. Using an idealised model, *Pfeffer* (2007) has suggested that increasing basal lubrication can lead to irreversible tidewater glacier retreat.

Testing these hypotheses requires high temporal resolution records of ice velocity at the terminus, in order to disentangle hydrologically forced changes in ice motion over various timescales from other terminus processes affecting ice velocity such as loss of buttressing and terminus retreat. However, we believe that our results provide motivation for further study of near-terminus subglacial hydrology, and suggest that consideration of only a single point on the glacier surface (e.g. *Howat et al.*, 2010; *Moon et al.*, 2014) may not resolve spatial heterogeneity in glacier dynamics.

7.6.3 Implications for submarine melting

We finally consider the implications of our results for submarine melting of the calving front of KNS. Both MITgcm and BPT include submarine melting, but submarine melting has not been the focus of this paper and we include only a brief discussion here drawing on previous modelling.

Chapter 4; *Slater et al.* (2015) showed that more distributed near-terminus subglacial hydrology leads to more homogeneous submarine melting across the glacier calving front and higher total submarine melt volumes. Based on these results, splitting discharge over 8 channels (hydrological scenario P8, Fig. 7.6e) would elevate total submarine melting by a factor 3.5 over the single channel case. However a completely distributed hydrological scenario considered in Chapter 4; *Slater et al.* (2015), using comparable discharge and warmer water than that recorded at KNS, resulted in an average melt rate of 3.6 $\mathrm{m\,d^{-1}}$. Thus average submarine melt rates at KNS are likely to be substantially

smaller than the ice velocity of $\sim$20 $\mathrm{m\,d^{-1}}$, irrespective of near-terminus subglacial hydrology. Routing the majority of subglacial discharge through a single channel can give very high localised melt rates of $\sim$10 $\mathrm{m\,d^{-1}}$ in the vicinity of the channel (*Xu et al.*, 2013; *Kimura et al.*, 2014), which approaches but is still smaller than the ice velocity at KNS. It is worth noting that even if submarine melting cannot match ice velocity, it may still play a role in terminus stability by undercutting the terminus, potentially influencing calving.

It should of course also be noted that the these melt rates are based on a parameterisation which has yet to receive validation at a tidewater glacier (*Holland and Jenkins*, 1999; *Straneo and Cenedese*, 2015). Nevertheless, under current modelling understanding, submarine melt rates at KNS may not pace ice velocity even in a localised fashion, and when spatially averaged over the terminus are nearly an order of magnitude smaller than ice velocity.

7.7 Conclusion

We have combined modelled catchment runoff and plume dynamics with a record of plume surface expression to investigate near-terminus subglacial hydrology at Kangiata Nunata Sermia, a large tidewater glacier in south-west Greenland. For a large proportion of the summer the catchment runoff greatly exceeds the discharge required to create a plume that would reach the fjord surface, yet there are extended periods when there is no plume visible. This can only be explained by the runoff emerging into the fjord in a spatially distributed fashion. We thus argue that subglacial drainage near the glacier terminus is often spatially distributed, formed either from numerous point sources of subglacial discharge, a single but very wide subglacial channel or possibly a complex combination of the two. We have discussed how these features may be incised into subglacial sediment or ice, and in the latter case how rapid basal sliding might destabilise efficient channels near the terminus.

Our arguments have a number of possible implications. Firstly, distributed subglacial drainage at the terminus will lead to more homogeneous submarine melting of the

calving front and higher total submarine melt volumes. Under current modelling understanding however, spatially averaged submarine melt rates at KNS are at least an order of magnitude smaller than the terminus ice velocity, and even very focussed and high magnitude subglacial discharge cannot induce local melt rates matching the terminus ice velocity. Secondly, the structure and evolution of the subglacial drainage system exerts an important control on ice velocity. Inland from the terminus the formation of efficient subglacial channels leads to a pronounced and sustained decrease in ice velocity in late summer (*Sole et al.*, 2011; *Moon et al.*, 2014; *Fahnestock et al.*, 2015). If pervasive distributed drainage exists near the terminus, ice velocity in the terminus region may respond to meltwater forcing differently to ice further inland. In particular ice velocity in the terminus region may then scale with catchment runoff.

Finally we note that in the absence of a sub-diurnal temporal resolution record of ice velocity, we cannot fully evaluate these arguments in this study. We hope that this work will provide motivation for further study of near-terminus subglacial hydrology at tidewater glaciers. *Joughin et al.* (2008b) have suggested that surface melt induced speed-up of tidewater glaciers is of only small relative magnitude near the terminus and therefore less important than other processes such as terminus retreat. However it remains possible that increased surface melting may be the driver of terminus retreat; increased surface melt entering a pervasive distributed drainage system will lead to increased basal lubrication, and subsequently acceleration and thinning. This mechanism has the potential to drive unstable retreat as described by *Pfeffer* (2007) and could therefore provide an alternative to or amplifier of ocean forcing in explaining tidewater glacier change in Greenland, particularly for glaciers where modelled submarine melt rates are very much smaller than ice velocity.

Chapter 8

Synthesis

The overall aim of this thesis has been to improve understanding of the interaction between the Greenland Ice Sheet and the ocean through modelling of submarine melt rates at tidewater glaciers. This work has been motivated by the recent rapid changes at the marine-terminating margins of the ice sheet, initiated in the mid-1990s (*Rignot and Kanagaratnam*, 2006; *Moon et al.*, 2012) and thought to be at least partly related to oceanic warming (*Straneo and Heimbach*, 2013). Given likely continued warming of the ocean around Greenland (*Yin et al.*, 2011), there is clear potential for significant future mass loss from the ice sheet, yet the details of the interaction between tidewater glaciers and the ocean are uncertain.

The first section of this synthesis chapter summarises the findings of this thesis. The findings are then brought together to offer a simple rule for submarine melting which captures the principal modelled variability in submarine melt rate. Spatial variability in melt rate and links to calving are discussed, and models from this thesis are compared with observational constraints on submarine melting. The significance of submarine melting in the recent past and future evolution of the ice sheet is considered, before discussion of future directions and concluding remarks.

8.1 Summary of findings

The first results section (Chapter 4) explored links between submarine melting and the spatial pattern of emergence of subglacial discharge at the glacier grounding line ('near-terminus subglacial hydrology') using the Massachusetts Institute of Technology general circulation model (MITgcm). Greenland-relevant rates of subglacial discharge (Q = 125, 250 and 500 m^3/s) were input at the glacier grounding line into an idealised fjord with calving front width of 2 km and ambient fjord conditions representative of Store Glacier in west Greenland. These discharges were input through either 1, 2, 3, 5, 10 or 50 individual subglacial channels. Three further simulations had the same subglacial discharges uniformly distributed across the glacier grounding line.

It was found that the near-terminus subglacial hydrology strongly influences both the spatial pattern and the total volume of submarine melting. Discharge through a single channel results in a vigorous plume which induces rapid but localised submarine melting directly above the channel, with distal parts of the calving front melting only very slowly. For example, when 500 m^3/s of subglacial discharge emerges from a single channel, modelled melt rates can exceed 12 m/d within the plume, but drop to less than 0.2 m/d outside the plume. As the number of subglacial channels is increased, the subglacial discharge per channel decreases so that the resulting plumes are weaker and maximum melt rates smaller. Splitting 500 m^3/s discharge over 5 channels decreases the maximum modelled melt rates to 9 m/d. The proportion of the calving front in contact with a plume however increases with the number of channels, so that more of the calving front experiences the high water velocities and temperatures responsible for submarine melting. In consequence, the total submarine melt volume induced (or equivalently the spatial mean submarine melt rate) increases if subglacial runoff is split between numerous channels. For a given subglacial discharge, the greatest submarine melt volume is achieved by spreading the discharge uniformly across the grounding line; under these circumstances, melt volumes exceed by a factor of 5 those generated by inputting the same discharge through a single channel. The amplification factor would likely be even higher if a wider calving front was considered. These

results demonstrate that the near-terminus subglacial hydrology is a key mediator of the interaction of a tidewater glacier with the ocean. Channelised delivery of runoff into the fjord will generate heterogeneity in calving front shape forming incised chimneys, calving bays and isolated headlands. Distributed delivery of runoff promotes flatter but perhaps more uniformly undercut calving fronts with higher total ablation by submarine melting.

In Chapter 5, a much simpler model - buoyant plume theory (BPT) - was used to investigate the dependence of in-plume submarine melting to variation in key physical parameters such as the magnitude of subglacial discharge, fjord temperature, density stratification and the plume geometry. Some of these relationships have been considered previously (e.g *Jenkins*, 2011; *Xu et al.*, 2013; *Sciascia et al.*, 2013; *Cowton et al.*, 2015); the results presented in this thesis build on these valuable studies by (i) focussing on tidewater glaciers rather than ice shelves, the difference being the dominance of subglacial discharge in plume buoyancy; (ii) proceeding analytically rather than numerically, which facilitates greater understanding of why the relationships take the form they do; (iii) offering an explanation for some of the differences between previous studies; and (iv) focussing on idealised rather than particular cases, giving a systematic overview of the factors affecting submarine melt rates.

In common with previous studies (*Jenkins*, 2011; *Xu et al.*, 2012, 2013; *Sciascia et al.*, 2013; *Kimura et al.*, 2014), it is found that local melt rate is proportional to the magnitude of subglacial discharge raised to a power γ, but that the most appropriate value of γ depends on the magnitude of subglacial discharge, the fjord stratification and the plume geometry. For very high discharges and weakly stratified fjords, $\gamma < 1/3$ regardless of plume geometry, while for low discharges and strongly stratified fjords, $\gamma = 3/4$ $(2/3)$ for point (line) source plumes. In intermediate cases γ is often close to $1/3$. This range in γ helps to explain the variation in the value of γ found in the above studies. After arguing for a linear dependence of melt on fjord temperature (see also *Jenkins* (2011); *Xu et al.* (2012); *Sciascia et al.* (2013)) and a non-linear (linear) dependence of total melt on fjord depth for a point (line) source plume, the scalings are combined into a single parameterisation providing a useful first-order estimate of

total submarine melt rate. This parameterisation facilitates a 'back-of-the-envelope' calculation suggesting that due to increased ocean temperature and ice sheet surface melting, submarine melt rates may have increased by ∼50% in recent decades and may further increase by 80-140% by the end of the century.

Chapter 6 tried to go beyond simply estimating submarine melt rate by beginning to think about the effect of submarine melting on glacier dynamics through changing the shape of the calving front, thought to be a key control on calving. This work was motivated by two papers (*Fried et al.*, 2015; *Rignot et al.*, 2015) published during the course of this thesis which imaged the submerged part of a number of calving fronts in west Greenland, revealing undercut and incised chimney features and significant variability in shape across the calving front. The revealed morphologies are very different from the uniformly flat and vertical calving fronts assumed in modelling of melt rates to date. This chapter therefore sought to understand the formation of undercut calving fronts, and the feedback of undercutting on submarine melting. A new framework was developed, building on existing BPT (Chapter 5; *Jenkins* (2011)), but allowing the ice ocean boundary to evolve according to the modelled melt rates. For simplicity, only line source plume models were considered so that the results are strictly appropriate only for wide subglacial channels.

Using this framework, many interesting conclusions can be reached. Firstly, due to a cancellation between reduced plume buoyancy and reduced entrainment into the plume, the degree and details of calving front undercutting have little effect on submarine melt rate at a given depth. All else being equal, submarine melt rate at a given depth will therefore not differ between a vertical and an undercut calving front. There is, however, something of a positive feedback because undercutting increases the surface area of the ice-ocean interface. Given that melt rates at a point are unaffected by undercutting, this has the effect of increasing total ablation by submarine melting. In sum, undercutting has a weak effect on local submarine melt rate but increases total submarine melt rate due to increased ice-ocean surface area. Secondly, steady state calving fronts are possible, in which the shape of the calving front has completely adjusted to the vertical profile of submarine melt rate, so that despite differential

submarine melting, the calving front does not change shape. Whether real glaciers reach this state is unclear, but it is certainly more likely to occur at slower-flowing glaciers with infrequent subsurface calving, giving more time for submarine melting to shape the calving front. Thirdly, submarine melt rates are generally higher at depth due to warm subtropical water, but all models of submarine melting show an area of very low melt rate near the grounding line where the plume retains the cold signature of the emerging subglacial discharge. If beginning from a vertical calving front, this area of low melt rate will result in the formation of a toe, limiting the undercutting experienced by the glacier. Alternatively, assuming a channel-like shape near the grounding line can compensate for low melt rates, driving deep undercutting consistent with observations (*Fried et al.*, 2015; *Rignot et al.*, 2015). As such, it is suggested that the presence of subglacial channels (specifically their shape) plays a fundamental role in the process of undercutting by plume-driven submarine melting. Fourthly, the undercut shapes obtained depend on the subglacial discharge and fjord stratification; in particular, steep undercutting is generated at the maximum height in the fjord reached by the plume, which depends on the two mentioned factors. Lastly, undercutting takes time, which may not be available at Greenland's fastest-flowing glaciers with frequent full-depth calving events. Undercutting may therefore be more prevalent at glaciers where submarine melt rates can compete with the ice velocity.

The final results chapter sought to compare similar plume modelling to that in Chapters 4 and 5 with observations from Kangiata Nunata Sermia (KNS), a large tidewater glacier in south-west Greenland. Based on measured fjord properties (*Mortensen et al.*, 2011, 2013), plumes were modelled with both MITgcm and BPT, suggesting that subglacial discharges of 50 m^3/s (0.5 m^2/s) from a point (line) source are sufficient for the resulting plume to generate an expression at the fjord surface. Despite modelled surface runoff (*Hock*, 2003; *Langen et al.*, 2015) exceeding these thresholds for the majority of the melt season, hourly observations of the fjord surface by time-lapse camera (*Sole et al.*, 2011) reveal plumes only infrequently reach the surface. It is argued that these observations can be reconciled if runoff emerges into the fjord from the glacier grounding line in a spatially distributed fashion; either through numerous narrow

subglacial channels or through a smaller number of very wide subglacial channels. It is certainly clear that a majority of the surface runoff cannot all be routed through a single narrow subglacial channel for most of the melt season; such a situation would result in a plume consistently visible at the fjord surface, which is precluded by the time-lapse imagery.

These results suggest that, in the terminology of Chapter 4, the near-terminus subglacial hydrology at KNS is located towards the distributed end of the spectrum, driving more spatially homogeneous submarine melting and higher total melt volumes (Chapter 4). Despite these higher total melt volumes, under current modelling understanding neither spatially averaged nor local submarine melt rates will pace the ice velocity of ∼20 m/d at the terminus (*Joughin et al.*, 2011).

The inferences on near-terminus subglacial hydrology at KNS were also used to motivate a discussion on subglacial hydrology and links to ice dynamics at fast-moving tidewater glaciers. The suppression of efficient subglacial channels under rapid basal sliding in theoretical models (*Fowler*, 1987; *Kamb*, 1987; *Schoof*, 2010) is highlighted as a potential explanation for the inferred distributed hydrology near the terminus. It is therefore suggested that if sustained, a distributed drainage system near the terminus could induce sustained ice flow acceleration under increased surface melting, contrary to findings at land-terminating glaciers (e.g. *Bartholomew et al.*, 2010) but similar to those at lake-terminating Perito Moreno in Patagonia (*Sugiyama et al.*, 2011). Such hydrology-dynamics coupling could provide an alternative mechanism to the ocean in driving tidewater glacier thinning, acceleration and retreat.

8.2 Synthesis of findings

Having summarised the findings of this thesis, the results are now brought together to provide an overview of key factors influencing spatial and temporal variability in submarine melting. Armed with this overview, the effect of submarine melting on calving front shape and links to calving are discussed, followed by a comparison to observational constraints on submarine melt rate.

8.2.1 Factors affecting submarine melt rate

The findings from Chapters 4-6 of this thesis can be combined and synthesised to provide a comprehensive quantification of the factors affecting in-plume submarine melt rates at tidewater glaciers. Eqs. 5.11 and 5.20 provide first-order estimates for the total submarine melt rate induced by a half-conical and line plume respectively in an unstratified fjord. A few brief extensions may be made to improve the utility of these expressions and to take into account the relationships developed in Chapters 4 and 6.

The spatial average in-plume melt rate (measured in m/d) is perhaps a more intuitive quantity than the total submarine melt rate given by Eqs. 5.11 and 5.20. The former quantity is obtained by dividing the total submarine melt rate by the plume-ice contact area $\frac{3}{5}\alpha h^2$ for the half-conical plume and by the plume height h for the line plume, where a factor of z_0 has been neglected in the half-conical expression. The expressions apply for an unstratified fjord, and the notation is the same as in Chapter 5.

As discussed in Chapter 6, undercutting of the calving front increases the ice-ocean surface area. If the calving front is uniformly undercut (i.e. the ice-ocean boundary is a straight line) and θ, measured from the horizontal, is the slope of the calving front (Fig. 6.1) then the surface area of the ice-ocean boundary scales as $(\sin\theta)^{-1}$. Since (for a line plume) the melt rate at a given depth is little affected by undercutting, the total submarine melt rate has the same scaling. Furthermore the 'horizontal melt rate' (or displacement of the ice-ocean boundary in the along-fjord direction due to submarine melting) also scales as $(\sin\theta)^{-1}$.

These considerations, together with Eqs. 5.11 and 5.20 then suggest that for a line source plume, the mean in-plume melt rate $\dot{m}$ may be well approximated by a relationship of the form

$$\dot{m} = A_l Q_0^{1/3}(T_a - T_l)/\sin\theta \tag{8.1}$$

where A_l and T_l are constants to be determined, Q_0 is the subglacial discharge per unit width, T_a is the (unstratified) fjord temperature and θ is the angle between the uniformly undercut calving front and the horizontal. For a point source plume, the

equivalent relationship is

$$\dot{m} = A_p Q_0^{1/3} (T_a - T_p) h^{-1/3} \tag{8.2}$$

where A_p and T_p are constants, Q_0 is the subglacial discharge, T_a is the (unstratified) fjord temperature and h is the fjord depth. As described in Chapter 6, consideration of the effect of undercutting on point source plumes has not been attempted in this thesis due to the significant difficulties of capturing the interaction between ice geometry, entrainment and plume dynamics in three dimensions. As such, it is not yet clear how θ should be incorporated into Eq. 8.2, and inclusion of θ is not attempted here.

As in Chapter 5, the constants A_l, A_p, T_l, and T_p are obtained by running the full plume model for varying parameters and then minimising the root mean square relative error between full plume model melt rates and simple parameterisation melt rates (Eqs. 8.1 and 8.2). The result of this procedure for the line plume is shown in Fig. 8.1 ('Unstratified'), with best fit constants $A_l = 1.05\ \mathrm{s}^{1/3}(^\circ\mathrm{C})^{-1}\mathrm{d}^{-1}$ and $T_l = -1.48\ ^\circ\mathrm{C}$, giving a root mean square relative error of 12%. The equivalent result for the point source plume is shown in Fig. 8.2 ('Unstratified'), with best fit constants $A_l = 1.63\ \mathrm{m}^{1/3}\mathrm{s}^{1/3}(^\circ\mathrm{C})^{-1}\mathrm{d}^{-1}$ and $T_l = -1.47\ ^\circ\mathrm{C}$, and root mean square relative error of 22%.

A significant limitation of these expressions is that they are strictly appropriate only for unstratified fjords. While some proglacial fjords, particularly in Svalbard and Alaska (e.g. *Bartholomaus et al.*, 2013; *Sundfjord et al.*, 2017) can be close to unstratified, proglacial fjords are generally stratified in both salinity and temperature (e.g. *Straneo and Cenedese*, 2015). It has been shown in Chapter 5 that stratification may modify, for example, the relationship between melt rate and subglacial discharge. Furthermore, Eq. 8.1 is only strictly appropriate when the calving front is uniformly undercut, so that $\sin\theta$ does not vary with depth. For calving fronts which are concave or convex, $\sin\theta$ varies with depth. There are, however, reasons to believe that Eqs. 8.1 and 8.2 may provide a good first-order estimate of submarine melt rate even in stratified fjords with complex calving front shapes, if depth-averaged fjord temperature is used in place of T_a, and depth-averaged calving front angle is used in place of θ. A number of studies using

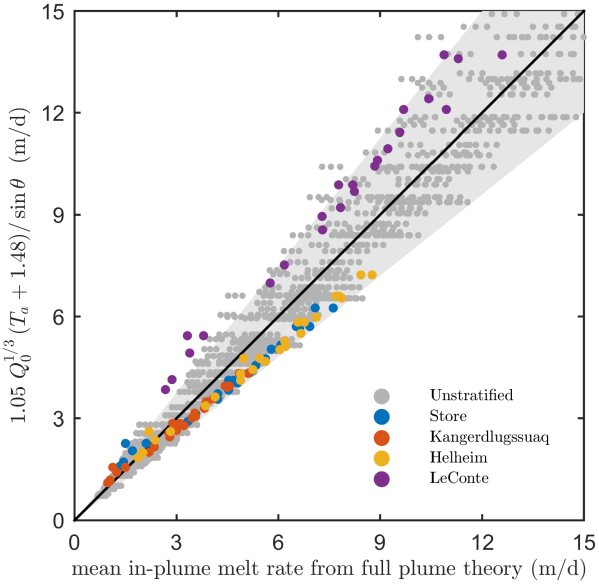

Figure 8.1: Comparison of mean in-plume submarine melt rate as predicted by full buoyant plume theory (x-axis) and the simple scaling Eq. 8.1 for a line plume. Light grey markers show results from unstratified fjords with all combinations of Q_0 = 0.1, 0.6, 1.1, 1.6, 2.1 m^2/s; h = 100, 300, 500, 700 m; T_a = 0, 2, 4, 6, 8 °C; S_a = 30, 32, 34 psu; and calving front slope θ from the five shapes in Fig. 6.2a. Black line is the 1-1 relationship while grey shading shows 20% either side of the 1-1 line. Coloured markers indicate results for the real fjord stratifications described in the text, for the same range of Q_0 and calving front shape.

more realistic, stratified fjord conditions find similar relationships between submarine melt rate and subglacial discharge (*Xu et al.*, 2012; *Sciascia et al.*, 2013; *Cowton et al.*, 2015), and submarine melt rate and depth-averaged water temperature (*Xu et al.*, 2013) to those in Eqs. 8.1 and 8.2. This may be because proglacial fjords are typically weakly stratified at depth so that for a significant height of the calving front, plumes behave as if in an unstratified fjord (Chapter 5). The use of a depth-averaged calving front angle may be a good approximation because for convex or concave calving fronts, the depth-average angle will overestimate the slope in some places and underestimate it in others.

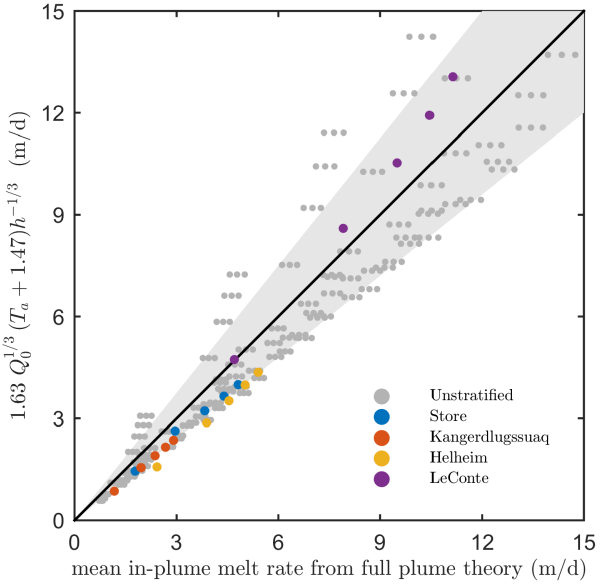

Figure 8.2: Comparison of mean in-plume submarine melt rate as predicted by full buoyant plume theory (x-axis) and the simple scaling Eq. 8.2 for a point plume. Light grey markers show results from unstratified fjords with all combinations of Q_0 = 10, 60, 110, 160, 210 m^3/s; h = 100, 300, 500, 700 m; T_a = 0, 2, 4, 6, 8 °C and S_a = 30, 32, 34 psu. Black line is the 1-1 relationship while grey shading shows 20% either side of the 1-1 line. Coloured markers indicate results for the real fjord stratifications described in the text, for the same range of Q_0.

The utility of Eqs. 8.1 and 8.2 in real fjord stratifications and with more complex calving front shapes can be tested by once more comparing the full plume model melt rate with Eqs. 8.1 and 8.2. Figs. 8.1 and 8.2 show the results for four realistic stratifications from Store (*Chauché et al.*, 2014), Helheim (*Straneo et al.*, 2011), Kangerdlugssuaq (*Christoffersen et al.*, 2011) and LeConte (*Motyka et al.*, 2013) Glaciers, and for the idealised calving front shapes used in Chapter 6 (Fig. 6.2a). The simple parameterisations tend to overestimate melt rate relative to the full plume model at LeConte Glacier, and there is a general underestimation at the other three large Greenland glaciers. Some possible reasons for disagreement have already been touched on in Chapter 5. Rather than embarking on extensive discussion at this late stage of the thesis, analysis of this disagreement is left for future work. The important

Factor	First-order relationship	Second order comments
Subglacial discharge Q_0	$Q_0^{1/3}$	Exponent can be smaller than 1/3 for high Q_0 and up to 2/3 for low Q_0 and a linearly stratified fjord
Fjord temperature T_a	Linear function of depth-averaged temperature $\overline{T}_a$	For very small Q_0, melt rate can become more sensitive to T_a. Deviation from scaling also due to using depth-averaged temperature when temperature varies with depth
Fjord salinity S_a	Independent of S_a	Larger S_a slightly increases plume buoyancy and therefore melt rates. Use of a depth-average salinity is equivalent to assuming an unstratified fjord; plume dynamics will differ in a stratified fjord
Fjord depth h	Independent of h	Melt rates may increase weakly with h due to the dependence of in-situ freezing point on pressure
Calving front undercut shape θ	Reciprocol of depth-average $(\overline{\sin\theta})^{-1}$	Only strictly appropriate for uniformly undercut calving fronts - more complex for curved calving fronts

Table 8.1: Summary of line plume melt rate scalings.

point here is that Eqs. 8.1 and 8.2 do indeed continue to provide useful estimates of melt rate even in realistically stratified fjords and at calving fronts with complex shapes.

Finally, hydrology may be incorporated into these simple estimates of submarine melting following Chapter 4. If $Q_{catchment}$ is the total catchment runoff and is split over n channels, then the runoff per channel is $Q_{catchment}/n$. In Chapter 4, for example, $Q_{catchment}$ takes the value 125, 250 or 500 m^3/s and n is either 1, 2, 3, 5, 10 or 50. Based on the scalings in Eqs. 8.1 and 8.2, the melt rate in each plume then scales with $n^{-1/3}$ while the total melt rate from all n plumes scales with $n^{2/3}$. This is essentially the same relationship described in Chapter 4 (section 4.3.1 and Fig. 4.3), the small discrepancy lying in the Q-exponent, which is here and in Chapter 5 assumed to be 1/3, while in Chapter 4 was assumed to be 0.4. From a practical perspective, the difference between these exponents is minimal. If instead a line plume of width w is assumed, then the discharge per unit width initiating the plume is $Q_{catchment}/w$, so that the melt rate in the plume scales with $w^{-1/3}$ and the total volume of melting due to the plume scales with $w^{2/3}$. This provides something of an extension or restatement of the conclusions from Chapter 4, in which the width of the line plume was fixed at $w = 2$ km. These

Factor	First-order relationship	Second order comments
Subglacial discharge Q_0	$Q_0^{1/3}$	Exponent can be smaller than 1/3 for high Q_0 and up to 3/4 for low Q_0 and a linearly stratified fjord
Fjord temperature T_a	Linear function of depth-averaged temperature $\overline{T}_a$	As for line plume
Fjord salinity S_a	Independent of S_a	As for line plume
Fjord depth h	$h^{-1/3}$	As for line plume
Calving front undercut shape θ	Not studied in this thesis	

Table 8.2: Summary of point plume melt rate scalings.

scalings once more suggest that the total melt volume increases as discharge becomes distributed, in this case as the width of a line plume is increased.

The foregoing discussion on factors affecting submarine melt rate is summarised in Tables 8.1 and 8.2. Across a wide parameter space in subglacial discharge, fjord stratification, calving front height and calving front shape, the in-plume submarine melt rate (or more precisely, the horizontal retreat of the calving front due to in-plume submarine melting) scales with the magnitude of subglacial discharge raised to the power of 1/3 and is linearly related to the thermal forcing (Eqs. 8.1 and 8.2), and for a line plume is inversely proportional to the sine of the calving front slope (Eqs. 8.1). Despite the acknowledged complications regarding neglected factors, real stratifications and complex calving front shapes, it remains the case that Eqs. 8.1 and 8.2 capture these first-order relationships between submarine melt rate and key physical parameters (Figs. 8.1 and 8.2). These results may therefore provide useful first-order estimates of submarine melt rates at tidewater glaciers for inclusion in coarse-scale, depth-integrated ice sheet models, or for estimating variability in submarine melt rate over many glaciers or through time with minimal data requirements. For such purposes it may be sufficient to capture only the leading order variability in melt rate, with the higher order effects (Tables 8.1 and 8.2) of little practical significance. More detailed or precise study of melt rate can always be achieved through recourse to full BPT (Chapters 5-7) or general circulation models such as MITgcm (Chapters 4 and 7).

8.2.2 Spatial variability in submarine melt rate

Of course, the characterisation of submarine melting at a glacier, or even per plume, by a single number is rather simplistic as it neglects vertical variation in melt rate, lateral variation in melt rate within the plume, and lateral variation in melt rate across the wider calving front due to the presence or absence of plumes and due to wider fjord and calving front circulation. As such, this thesis has also focussed on spatial variability in melt rate, and the effect of differential melting on calving front shape.

Vertical variation in melt rate within plumes arises largely due to vertical variation in plume temperature and velocity, arising from plume dynamics and fjord stratification. Considering first plume temperature, within a short distance above the grounding line, plumes have not yet had sufficient time to mix substantially with the ambient fjord water and therefore retain the cold signature of the emerging subglacial discharge (Chapters 4 and 5, Figs. 4.2 and 5.2). This has the effect of producing an area of low submarine melt rate near the grounding line. This effect prevails over a height above the grounding line (z_0 in Chapter 5) which depends on the magnitude of subglacial discharge, so that for example, the plume is 80% as warm as the ambient fjord by ∼50 m above the grounding line for a half-conical plume of discharge 50 m^3/s or for a line plume of discharge 2 m^2/s. As such, for shallow glaciers, the plume may retain the cold signature of subglacial discharge over the full height of the calving front while for deeply grounded glaciers this effect is important only in a small region close to the grounding line. Above this region, the temperature stratification of the fjord becomes more important. Plumes do not however simply track the fjord stratification because the water entrained at a certain depth mixes with all of the water entrained up to that depth. To generalise, fjords in Greenland are warm at depth and cold at the surface (e.g. *Straneo and Cenedese*, 2015). Plumes transport the warm deep water towards the surface and therefore often only cool slightly once reaching the colder surface waters (e.g. Figs. 7.3 and 7.5). Thus if proglacial fjords experience cold surface water, this can slightly decrease melting (e.g. Fig. 6.2b).

For a half-conical plume, plume velocity decreases with height above the grounding line

(Chapter 5, Fig. 5.2), particularly so if the plume encounters fresher, lighter water close to the fjord surface (Chapter 7, Fig. 7.3), as is often found in proglacial fjords. For a line plume, plume velocity is approximately constant with depth in an unstratified fjord, but will again decrease with height above the grounding line in a stratified fjord (Chapters 5 and 7, Fig. 7.5). Since submarine melt rate is proportional to plume velocity (Chapter 3), the result is to decrease submarine melt rates with height. The vertical profile of submarine melting is ultimately determined by both temperature and velocity. In the region where the plume retains the signature of the cold subglacial discharge, vertical variation in melt rate is controlled by plume temperature (Chapter 5) and melt rate increases with height above the grounding line. Above this region, vertical variation in melt rate is controlled by plume velocity (Chapter 5) and melt rate decreases with height above the grounding line. The maximum melt rate is thus located between the two regimes; for deeply grounded glaciers this will be close to the grounding line (Chapters 4 and 6, Figs. 4.2 and 6.2b) while for shallow glaciers entering relatively unstratified fjords, the maximum melt rate could be closer to the fjord surface (e.g. Fig. S3.2c).

Lateral variation of melt rate within a plume is mentioned briefly here but has not been a focus of this thesis; indeed all the results chapters have used 'top-hat' buoyant plume theory in which plume properties are averaged over the width of the plume, clearly removing any lateral variability within the plume. The modelling of plumes in MITgcm in Chapter 4 resolves lateral variability in plume properties (e.g. Fig. 4.2). As might be expected, velocities are highest in the core of the plume and decrease towards the edges. In terms of temperature, the core of the plume is somewhat insulated from the ambient fjord water; thus the core of the plume remains colder for a greater height above the grounding line and is warmer at the fjord surface. The effect on melting appears similar to that discussed above for vertical variation: close to the grounding line, plume temperature controls lateral variability in melting with lower melt rates in the core of the plume relative to the edges (Fig. 4.2i). Closer to the surface, plume velocity dominates, giving highest melt rates in the core of the plume (Fig. 4.2i).

Strong lateral variability in melt rate at a calving front arises from the presence or

absence of plumes, in turn controlled by the locations at which subglacial discharge is discharged at the grounding line (Chapter 4). Parts of a calving front in contact with a plume melt rapidly due to the high water velocities and the transport of warm water from depth, while parts of a calving front distant from a plume melt much more slowly as they lack high water velocities with which to drive the transfer of heat from ocean to ice (Fig. 4.2). While the entrainment of water into plumes does result in elevated across-ice water velocities close to the plume, the magnitude of these velocities is at least an order of magnitude smaller than within the plume, so that the melt rates generated are significantly smaller. The contrast in melt rate can be very significant; for a single plume initiated by a high subglacial discharge, the simulations presented in Chapter 4 suggest a possible ∼12 m/d differential in melt rate over a few hundred metres (Fig. 4.2i). As the number of discharging channels is increased, the proportion of the calving front directly affected by a plume increases and the lateral variability in melt rate decreases. If subglacial discharge emerges uniformly along the grounding line there is no lateral variability in melt rate. As such, the key control on lateral variability in submarine melting is the near-terminus subglacial hydrology. This motivated the work presented in Chapter 7, in which it was suggested that at KNS, drainage into the fjord often occurs in a spatially distributed fashion consisting of numerous narrow channels or perhaps a few very wide channels. The implication is that lateral variation in submarine melt rate at KNS is supressed, though there may still be some large differences in melt rate between locations in contact with a plume and those which are not (e.g. Fig. 4.2j and k).

8.2.3 Effect of spatial variability in melt rate on calving front shape and links to calving

Differential rates of submarine melting across the calving front will, if sustained, change the shape of the calving front. The shape of the calving front influences stresses within the ice and possibly the calving process (*O'Leary and Christoffersen*, 2013; *Wagner et al.*, 2016), and is therefore a key link between the ocean and tidewater glacier dynamics. Chapter 6 sought to understand how vertical variability in submarine melt rate affects calving front shape. Because submarine melt rates broadly decrease

with height above the grounding line (section 8.2.2), submarine melting will generally undercut calving fronts. Particularly marked undercutting can occur if the plume does not reach the fjord surface - in this case, melt rates are high within the plume but low just above, creating a strong differential in melt rate. A similar effect may occur when the plume reaches the fjord surface because ice above the water will melt less rapidly than the submerged ice; in this case the marked undercutting would occur at the waterline.

There are, however, complications to this overall picture of undercutting. As described above, plumes can for some distance retain the signature of the cold subglacial discharge, resulting in a region where melt rates increase with height above the grounding line. If this profile of submarine melting is applied to an initially vertical calving front, it will result in a region which is 'overcut', or 'toes-out' near the grounding line. I would suggest that, in the location of subglacial channels, these features will not form. Firstly, it should be said that the near-grounding line details emerging from the models presented in this thesis should not be over-interpreted for a number of reasons, including (i) that the size of subglacial channels at the glacier grounding line is not known, and the concept of transition from channel to plume is not well-defined, and (ii) neither MITgcm nor BPT as presented are ideally suited for examining these details: the former has insufficient resolution to resolve the details, and the latter omits key processes such as the likely reduction of entrainment due to the proximity of the ocean floor. Despite these caveats, I would suggest that an initially vertical calving front may not be appropriate near the grounding line - it is much more likely that there is a smooth transition into the horizontal ice-water interface characterising the roof of the subglacial channel as you move up-glacier, and that this feature prevails throughout the year. Secondly, supposing a toe did form, the plume may detach a little from the ice (e.g. *Kimura et al.*, 2014) so that the 'lee' side of the toe could experience reduced melt rate while the remainder of the toe might continue to melt rapidly; such a process would tend to melt away such toes. A final point, which is the most persuasive, is that such toes are not seen in side-scan sonar data, which instead shows deep undercutting disappearing underneath the glacier (*Fried et al.*, 2015; *Rignot*

et al., 2015). In Chapter 6 it was shown that the effect of melting on the ice depends not only on the melt rate but also on the shape of the calving front, and that despite low melt rates near the grounding line, toes do not form if a subglacial channel-like shape is imposed in the initial calving front. It may therefore be the case that the subglacial channel itself plays a key role in creating the deeply undercut calving fronts which have been observed by compensating for the region of low melt rates found near the grounding line. Some toe features have however been observed at locations displaced from subglacial channels (*Fried et al.*, 2015; *Rignot et al.*, 2015). These may result from across-ice water motion driven by entrainment into plumes.

A second complication concerns timescales of undercutting. Based on the results in Chapter 6, it takes approximately a melt season (or ∼100 days) for a calving front to transition from approximately vertical into a stationary undercut shape (Fig. 6.4). The largest and fastest-flowing glaciers in Greenland undergo frequent full-depth calving events which may regularly reset the calving front to vertical. In contrast, slower-flowing glaciers with infrequent full-depth calving events may be systems where submarine melting has more time to shape the calving front. Such discussion is at present rather speculative; in particular we do not know whether glaciers are undercut seasonally or perhaps more likely retain some imprint of their late-summer morphology through the winter, when small volumes of subglacial meltwater may still emerge at the grounding line. Thus while vertical profiles of submarine melting may promote undercutting, the actual shape reached by the calving front may vary from glacier to glacier and depend on additional factors such as the ice velocity.

Calving fronts will also be shaped by lateral variability in submarine melt rate. In particular, the contrast between strong melting within a plume and weak melting to the sides of the plume (e.g. Fig. 4.2i) will incise 'chimney' features into a calving front. If there are multiple plumes (e.g. Fig. 4.2j) there may be multiple incisions, with isolated 'headlands' developing between the plumes. Combined with the undercutting discussed in the previous paragraph, calving fronts may develop numerous incised, undercut chimneys. This morphology has now been observed at tidewater glaciers in west Greenland (*Fried et al.*, 2015; *Rignot et al.*, 2015).

Undercutting of the terminus may promote calving by destabilising the ice above (e.g. *Benn et al.*, 2007), with calving occurring when surface crevasses intersect the roof of the undercut cavity (*Fried et al.*, 2015). If there are no additional feedbacks, the calving rate would in this case be equal to the submarine melt rate at depth. *O'Leary and Christoffersen* (2013) however suggest that undercutting of the calving front displaces the stress field up-glacier, promoting larger calving events and leading to a calving rate which exceeds the submarine melt rate forcing. This would provide a mechanism for even low rates of submarine melting to drive rapid calving, potentially lending submarine melting a role at the fastest-flowing glaciers in Greenland, where current understanding suggests the ice velocity is significantly larger than the submarine melt rate. Other authors (*Cook et al.*, 2014; *Todd and Christoffersen*, 2014; *Krug et al.*, 2015) reach the opposite conclusion in finding little effect of undercutting on calving rate, and it has been suggested the discrepancy arises because the model considered in *O'Leary and Christoffersen* (2013) was diagnostic (not time-evolving). In the other models, it appears that the glacier geometry adjusts to the undercutting so that the stress field is not substantially perturbed (*Cook et al.*, 2014); it remains unclear however whether this is true in general or is affected by the details of the glaciers modelled (in particular their velocity and their proximity to flotation). A further factor emerges once across-fjord variability is considered - it may be that if the incised chimney is narrow, the ice either side is able to stabilise the undercut ice through bridging stresses. At present, the effect of undercutting on calving is far from clear.

Calving at Greenland's fastest-flowing glaciers such as Jakobshavn Isbrae is dominated by full-depth buoyancy-driven events. Bottom-out rotational events may be promoted by the presence of toes near the grounding line (*Wagner et al.*, 2016), and arguably the low melt rates near the grounding line which arise from the modelling in this thesis could form these toes (see also *Carroll et al.* (2016)). Conversely, undercutting of these huge calving fronts might reduce the bottom-out buoyancy of these huge icebergs, potentially stabilising the terminus.

Lateral calving front morphology is also likely to be a first-order control on calving, but has been little investigated due to the difficulties in modelling calving in three

dimensions. It has been suggested that at Store Glacier, rapid submarine melting due to plumes promotes undercut-driven calving in some parts of the calving front, and creates isolated headlands which undergo infrequent full-depth buoyancy-driven calving (*Chauché et al.*, 2014; *Todd and Christoffersen*, 2014). Despite these large calving events being driven by buoyancy, it may still be submarine melting which paces the process through determining the rate at which the headlands are isolated. As for the vertical dimension then, the link between lateral calving front shape and calving is also poorly understood and is a significant limitation when trying to assess the impact of submarine melting on tidewater glacier dynamics.

8.3 Comparison to observations

Ideally, the modelling results presented in this thesis could be validated by comparison to field observations. For submarine melting, this is problematic due to the extreme difficulty of making such measurements, and due to the number of factors which can influence melt rates. This thesis identifies subglacial hydrology, subglacial runoff and fjord temperature as the three most important factors influencing submarine melt rate at a tidewater glacier. An ideal dataset would constitute simultaneous knowledge of these three factors and submarine melt rate. At present, only fjord temperature can be directly measured (e.g. *Straneo et al.*, 2010); subglacial runoff can only be estimated by surface melt modelling and assumptions about routing thereafter (Chapter 7), hydrology only inferred from plume surface expression (Chapter 7), fjord hydrography (*Stevens et al.*, 2016) or calving front morphology (*Fried et al.*, 2015; *Rignot et al.*, 2015), and submarine melt rate estimated from indirect methods such as fjord heat fluxes (*Jackson and Straneo*, 2016) or above-water terminus evolution (*Luckman et al.*, 2015). Unsurprisingly, combining uncertainties from these factors obfuscates attempts to make quantitative model to observation comparisons.

Fried et al. (2015) present side-scan sonar observations of marine-terminating Kangerlussuup Sermia in west Greenland, showing multiple undercut chimneys (Fig. 2.11), presumably associated with multiple subglacial channels discharging runoff into the

fjord. These observations strongly support the style of melting modelled in Chapter 4 (Fig. 4.2j), with elevated melt rates within plumes and weaker melting elsewhere. The number of undercut chimneys suggests that, on the scale presented in Chapter 4, Kangerlussuup Sermia is towards the distributed end of the spectrum. As an aside, the terminology which has been used might be considered misleading - 'distributed subglacial hydrology' has conventionally been used to describe subglacial water draining inefficiently through a network of linked cavities or subglacial till (*Fountain and Walder*, 1998), whereas in the recent tidewater literature it has been used to describe a system with multiple channels discharging runoff into a fjord (Chapter 4; *Fried et al.* (2015)). The latter situation is in many senses 'channelised', and perhaps its description should be more explicit.

The system observed rather directly by *Fried et al.* (2015) is similar to that inferred to persist at KNS (Chapter 7). Whether this is a general result applicable across all tidewater glaciers is not clear. *Schild et al.* (2016) have observed four distinct plumes on the fjord surface in front of Rink Glacier (west Greenland), and indeed there may be more plumes which do not reach the surface in this deep and stratified fjord (*Bartholomaus et al.*, 2016). Conversely, *Stevens et al.* (2016) suggest that at Saqqarliup Sermia (also west Greenland), the vast majority of surface melt emerges from a single subglacial channel. Saqqarliup Sermia flows significantly more slowly (∼1 m/d; *Joughin et al.* (2010)) than Kangerlussuup Sermia (∼5 m/d; *Fried et al.* (2015)), KNS (∼20 m/d; *Joughin et al.* (2010)) or Rink (∼12 m/d; *Bartholomaus et al.* (2016)). As discussed in Chapter 7, perhaps the ice velocity exerts a control on near-terminus subglacial hydrology, with multiple discharging channels at fast-flowing glaciers, while slow-flowing (well-grounded) glaciers behave more like land-terminating glaciers with only one or two subglacial channels.

Because subglacial hydrology exerts such a strong influence on submarine melting (Chapter 4), any comparison of front-wide modelled and observed melt rate must consider hydrology. *Xu et al.* (2013) report good agreement between modelled (2±0.3 m/d) and fjord heat flux inferred melt rate (3±1 m/d). By modelling a section of the calving front measuring 150 m in the across-fjord direction, and assuming this was

representative of the full calving front, there is an implicit assumption of numerous subglacial channels spaced at 150 m. As shown in Chapter 4, the presence of numerous channels increases the area-averaged melt rate. While uncertain, there are thought to be two main channels at Store (*Todd et al.*, 2017), so that if all discharge was routed through these two channels, the modelled area-averaged melt rate would likely decrease into disagreement with the observationally inferred value of 3 m/d.

Such considerations pervade comparison of modelled melt rates with observational constraints. Under the modelling undertaken in this thesis, calving front-averaged melt rates >1 m/d, a value significantly exceeded by almost all of the observational estimates of melt rate (section 2.4.3), are only achievable with numerous subglacial channels. Even for an example with high subglacial discharge and warm water, the modelling presented in Chapter 4 suggests that for a single subglacial channel, area-averaged melt rates are just 0.65 m/d, and would be lower if a wider calving front had been modelled. This could be considered evidence for the existence of numerous channels (as observed at Kangerlussuup Sermia; Fig. 2.11; *Fried et al.* (2015)), but such a conclusion may be overly simplistic for many reasons including principally the uncertainty associated with 'observed' melt rates and the neglect of processes which might drive submarine melting outside of plumes. Due to their ability to drive very rapid submarine melting, this thesis has focussed on plumes, but in the absence of numerous subglacial channels, the majority of the area of the calving front may undergo 'non-plume' melting. This could take the form of melting induced by wider fjord circulation, for example water pulled across the calving front for entrainment into plumes, or perhaps melt-driven convection where the buoyancy driving the convection is provided by melting itself rather than subglacial discharge. At present, neither of these is predicted to drive rapid melting; melting from outside of the plume in Fig. 4.2i contributes only ∼25% of the total, and maximum melt rates from melt-driven convection have been estimated at ∼0.2 m/d (*Magorrian and Wells*, 2016). These processes have therefore not received as much attention as plumes and have perhaps even fewer observational constraints. Despite the predicted weaker melt rates, these processes could dominate the front-wide

melting on the glacier but are poorly understood and present another barrier in the comparison of modelled and observed melt rates.

Two datasets in particular illuminate variability in submarine melt rate and facilitate more detailed comparison. The first comes from estimates of toward-glacier fjord heat flux at LeConte Glacier in Alaska (*Motyka et al.* (2013), Fig. 2.13) which describes variability in total submarine meltwater flux under varying subglacial discharge. Application of the parameterisations Eqs. 5.11 and 5.20 (since they are formulated in terms of the total submarine meltwater flux) is shown in Fig. 8.3. As already discussed, the assumption of a single channel giving rise to a single point source plume results in a total submarine meltwater flux significantly lower than suggested by the data (Fig. 8.3). Even increasing to 5 subglacial channels does not significantly improve agreement. By contrast, the assumption of a wide subglacial channel producing a wide line plume gives better agreement with the data, although for the best match a channel width comparable to the width of the calving front ($\sim$1 km, *Motyka et al.* (2013)) must be assumed. More broadly, and as described by *Motyka et al.* (2013), the data in Fig. 8.3 support the functional form of the relationship between melting and subglacial runoff; that is, submarine melt rate being proportional to the magnitude of runoff raised to the power of 1/3.

The second dataset is that in *Luckman et al.* (2015), which presents satellite-derived frontal ablation rates from three tidewater glaciers in Svalbard over slightly longer than one year. There are very strong correlations between frontal ablation rate and ocean temperature, suggesting that calving is being driven by melt undercutting. It is not entirely obvious that the frontal ablation rate (i.e. rate of calving of ice above the water) should be identical to the submarine melt rate (rate of ice removal below the water). If the two are not in balance, the calving front would become steadily more undercut, or develop a toe; and presumably this situation would have to be resolved by infrequent large calving events. However, given the consistency of the relationship between frontal ablation and temperature over more than one year, it seems reasonable to assume that ablation and melting are in balance, so that the frontal ablation rates can be thought of as submarine melt rates.

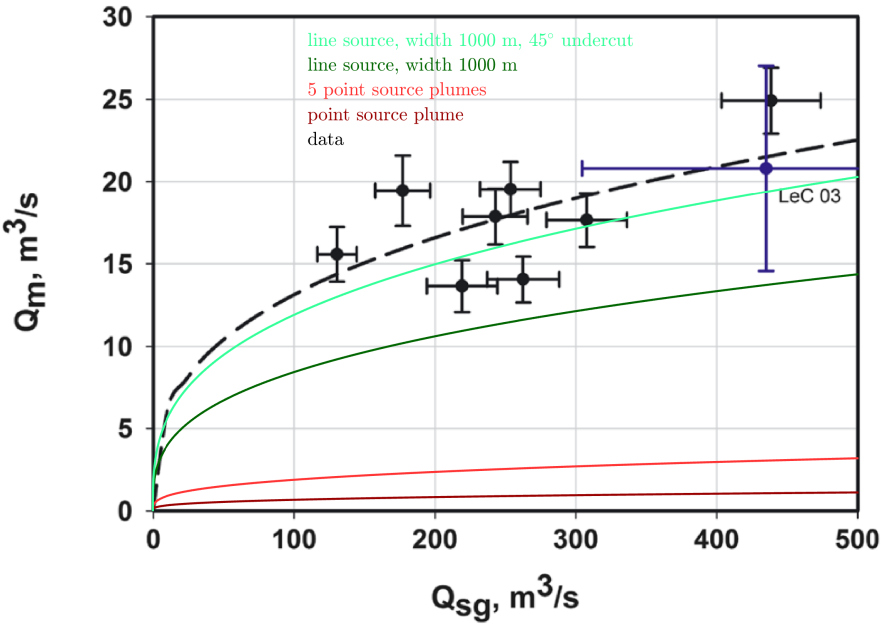

Figure 8.3: Relationship between subglacial discharge Q_{sg} and submarine meltwater flux Q_m at LeConte Glacier. Black and blue markers show observational estimates, based on hydrographic data at a flux gate ∼1.5 km from the terminus (*Motyka et al.*, 2013). Coloured lines show modelled in-plume submarine meltwater fluxes based on Eqs. 5.11 and 5.20. Figure modified from *Motyka et al.* (2013).

Fig. 8.4 shows the result of estimating frontal ablation rate using the simple parameterisations described above (Eqs. 8.1 and 8.2), for various subglacial discharges. Interestingly, no single value of subglacial discharge provides a good fit to the data. In order to match the gradient of melt rate versus ocean temperature suggested by the data requires a high subglacial discharge. But a high subglacial discharge overestimates the melt rate at low ocean temperature. Therefore, a good fit to the data requires variable subglacial discharge, with larger subglacial discharge when ocean temperatures are high. This is eminently reasonable, as the low ocean temperatures occur during winter when runoff is minimal, with high ocean temperatures during summer when runoff is high. Thus, it is interesting to note that while the data presented in *Luckman et al.* (2015) most obviously show that submarine melt rate responds to ocean temperature, application of the simple melt rate parameterisations in Eqs. 8.1 and 8.2 suggests that

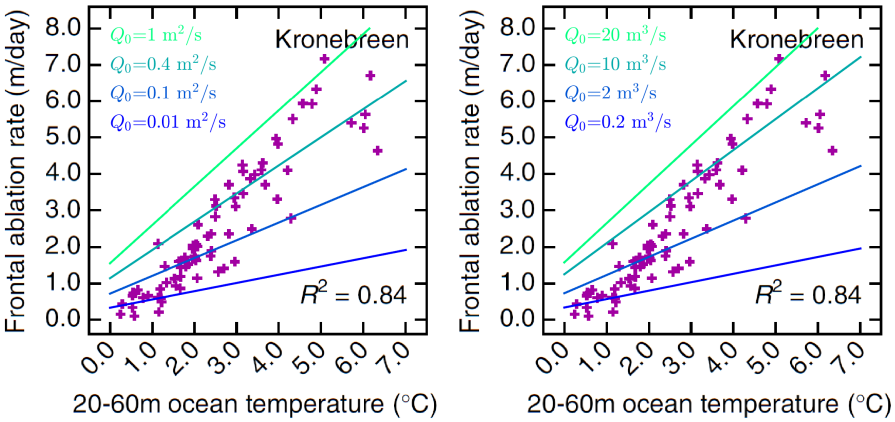

Figure 8.4: Comparison of frontal ablation at Kronebreen, Svalbard (*Luckman et al.*, 2015) with in-plume submarine melt rates from the simple parameterisations developed in section 8.2.1 above. Left: line plume and right: point source plume. Lines are overlain on the figure from *Luckman et al.* (2015) and show the relationship between modelled melt rate and ocean temperature for the indicated subglacial discharges.

the data also support a role for subglacial discharge. Similarly, the data presented in *Luckman et al.* (2015) is not quite evidence that melt rate responds linearly to ocean temperature; this would be the case if all other variables were fixed, but subglacial discharge in particular will have varied through the period of study. Thus, the frontal ablation rates at high ocean temperature are not directly comparable to those at low temperature because it is likely that subglacial discharge will have differed, and we understand subglacial discharge to impact melt rate. According to the modelling presented in this thesis, the observed response of melt rate to temperature is too sensitive to be due to temperature alone, invoking subglacial discharge as an additional driver of melting. Once this is done, a good fit of modelled to 'observed' melt rate can be achieved.

It should however be noted that the frontal ablation rates presented in *Luckman et al.* (2015) are averaged over the width of the calving front, while the parameterisations Eqs. 8.1 and 8.2 apply only where there are plumes. It is conceivable that the entire calving front could be covered by plumes, but this would require an extremely high

catchment discharge, on the order of 3000 m^3/s for the highest melt rates, while melt modelling suggests maximum catchment discharge of $\sim$500 m^3/s for Kronebreen (*Darlington*, 2015). This discrepancy could be interpreted in a number of ways: (i) the heat transfer coefficient in the melt rate parameterisation should be increased, giving higher melt rates for lower discharges, (ii) high rates of submarine melting occur even outside of plumes, so that it is not necessary to cover the calving front in plumes to generate melting over the width of the calving front, or (iii) rapid and concentrated melting occurs inside the plumes, but this concentrated melting induces widespread calving, so that the calving process spreads the effect of submarine melting over the width of the calving front. Based on observations of plumes at the fjord surface, and inferences of focussed subglacial runoff at other tidewater glaciers (*Fried et al.*, 2015; *Stevens et al.*, 2016), it seems unlikely that the whole calving front would be covered by plumes and thus my interpretation is that processes (ii) and (iii) may be important at tidewater glaciers. Of course, the heat transfer coefficient is also poorly constrained so that it is possible that factor (i) is also involved.

In spite of the many difficulties in the comparison of modelled and observed melt rates, an optimist could argue for signs of agreement under the assumption of numerous subglacial channels or a single very wide channel (e.g. *Xu et al.* (2013); Fig. 8.3). Furthermore, the modelled dependencies of submarine melting on water temperature and the magnitude of subglacial runoff are rather roughly supported (*Motyka et al.* (2013); *Luckman et al.* (2015); Figs. 8.3 and 8.4). If anything, front-wide observed melt rates might be considered higher than modelled equivalents, particularly if there are few subglacial channels (e.g. Fig. 8.3). In the latter case, melt rates outside of plumes become important but are currently very poorly understood. As has been seen in the examples presented, there are so many factors at play that the comparisons are not sufficiently strong or quantitative to offer constraints on the heat and salt transfer coefficients in the melt rate parameterisation (Chapter 3), which is the root of much of the model uncertainty. Further observations are therefore imperative to constrain modelled melt rates.

8.4 Importance of submarine melting to Greenland ice sheet dynamics

This thesis was motivated by the recent observations of rapid dynamic changes at the marine-terminating margins of the Greenland Ice Sheet, potentially initiated by increased submarine melting at the calving fronts of tidewater glaciers. This thesis used numerical modelling in an attempt to illuminate the poorly understood process of submarine melting and to assess its importance for the stability of the Greenland Ice Sheet.

A first-order assessment of the importance of submarine melting is to compare submarine melt rate to ice velocity. These comparisons come with the caveat that the heat transfer coefficient in the melt rate parameterisation is not well constrained. Under current modelling understanding then, and for typical Greenland fjord conditions, submarine melt rates may reach very high values at localised points, for example exceeding 12 m/d in Fig. 4.2i. Once a calving front-wide average is considered, the melt rate typically drops considerably (to $\sim$1 m/d) unless the majority of the calving front is covered by plumes, when the average rate may reach $\sim$3 m/d (Chapter 4).

As such, localised submarine melt rates are likely to exceed the ice velocity at the majority of Greenland's tidewater glaciers, while front-wide average rates are likely to exceed the ice velocity only at the slowest-flowing glaciers. At Greenland's fastest-flowing glaciers, such as Jakobshavn Isbrae, Helheim and KNS, even localised melting may not pace the ice velocity. The relevance of such arguments depends on the effect of melting on calving. It could be that in order for melting to have a significant effect, the pace of melting must exceed the ice velocity over a significant fraction of the calving front. This being the case, current modelling of submarine melting does not suggest a particularly important role for submarine melting. Alternatively, it could be that focussed melting exceeding the ice velocity drives localised grounding line retreat which subsequently spreads across the calving front, destabilising the glacier. The observations of *Luckman et al.* (2015) perhaps support this latter conclusion, and one could then conclude that submarine melting is an important factor at the majority of

Greenland's tidewater glaciers. On a final note, the presence of the $\sin\theta$ term in Eq. 8.1 means that glaciers with ice shelves or ice tongues (e.g. Petermann Glacier or 79N) are intrinsically more sensitive to submarine melting - they have such a huge surface area in contact with the ocean that even weak submarine melting can contribute significantly to terminus mass balance.

In general, it is not possible to draw sweeping conclusions on the importance of submarine melting without better knowledge of how melting may influence calving. This thesis has taken steps towards this goal by considering the effect of differential melting on calving front shape (Chapters 4 and 6). In agreement with observations (*Fried et al.*, 2015; *Luckman et al.*, 2015) the results suggest melting will undercut and cut notches into calving fronts, which may define calving style. However, the results also suggest that this process requires time, which may not be afforded at Greenland's fastest-flowing glaciers due to frequent full-depth calving events which presumably reset the calving front to a 'pre-melt' state. This could be taken as further evidence that melting has perhaps a greater role at slower-flowing glaciers, but once more this makes assumptions on the coupling of melting and calving; it could be that even a minor reshaping of the calving front is sufficient to increase full-depth calving rate (*O'Leary and Christoffersen*, 2013). It is certainly clear that ice dynamics play a central role in the recent behaviour of Greenland's tidewater glaciers. The modelled rates of submarine melting are not sufficient to have driven retreat directly, rather melting might be seen as a perturbation which retreats the grounding line into an unstable position at which ice dynamics takes over and drives the glacier towards a new, stable, retreated state.

Even if submarine melting turns out to be less important at faster-flowing glaciers, this does not preclude a role for the ocean. Ice flow modelling of these systems suggests that buttressing by ice mélange has a strong influence on calving rate and glacier stability (*Cook et al.*, 2014; *Todd and Christoffersen*, 2014; *Krug et al.*, 2015). Glaciers such as Jakobshavn Isbrae, Helheim and Kangerdlugssuaq certainly have thick, year-round ice mélange, and it could be that the arrival of warm water thins the ice mélange, reducing the backstress on the glacier and increasing calving rate.

Considering time-evolution of submarine melt rate, a back-of-the-envelope calculation described in Chapter 5 and repeated here based on Eqs. 8.1 and 8.2 suggests that in recent decades, under a 50% increase in subglacial discharge and a fjord temperature increase from 2°C to 3°C, submarine melt rate has increased by ∼50%. This could have a significant impact at a glacier where previously, submarine melt rate and ice velocity were in some sense balanced.

In sum and if pushed, I would argue there is good evidence for the importance of submarine melting in the dynamics of slower-flowing glaciers in Greenland. At the fastest-flowing glaciers, other mechanisms may be more important, such as variability in ice mélange buttressing and surface-melt induced acceleration. Increased submarine melting could, therefore, very well have initiated much of the dynamic change observed at tidewater glaciers around Greenland and may continue to have a significant impact on the ice sheet in the future as the ocean warms. As has already been stated, such conclusions overlook our lack of understanding of the effect of melting on calving, and uncertainty in crucial melt rate parameters. Further work on the coupling of melt to calving, and better observational constraints on submarine melting are much needed to strengthen or refute these conclusions.

8.5 Limitations

There are a number of limitations of the results presented in this thesis which prevent the drawing of clear conclusions on the relevance of submarine melting to the Greenland Ice Sheet. Firstly, the extreme difficulty of gaining observational data on submarine melting means it is currently problematic to validate modelled submarine melt rates. As described above, comparisons between model and observation can be made, but it is currently not possible to draw rigorous or quantitative conclusions. In particular, modelled melt rates are essentially linearly sensitive to the heat exchange parameter γ_T (Chapter 3). It has been acknowledged throughout this thesis that uncertainty in the value of this parameter is a significant limiting factor in our confidence of modelled melt rates.

Secondly, this thesis has focussed on plumes initiated by subglacial discharge. Plumes play an important role in pulling warm water towards the calving front (*Cowton et al.*, 2016), and it is very likely that the highest rates of submarine melting are found where such plumes are in contact with a calving front (Chapter 4). However, plumes may cover only a small fraction of the calving front (e.g. Fig. 4.2i), and in the absence of numerous plumes, the majority of the calving front may undergo melting due to other processes, such as secondary fjord circulation or melt-driven convection. These other processes may dominate the front-wide submarine melt rate. The relative importance of in-plume melting and wider melting for glacier dynamics remains unclear, but it is certainly the case that there are other forms of submarine melting besides the in-plume melting studied in this thesis, and a full understanding of ice-ocean interaction requires further study of wider calving front processes.

Finally, due to poor understanding of calving processes, it might be said that even with a perfect knowledge of submarine melting, we would still be unsure of the effect on glacier dynamics. This thesis has taken important steps towards understanding the coupling of submarine melting and calving through calving front shape (Chapter 6), but the interaction of submarine melting and calving across the many calving styles observed around Greenland remains poorly understood. As such, the results presented in this thesis are one step removed from the glacier dynamics which motivated the research questions, limiting the reach of the conclusions that can be drawn.

8.6 Future directions

As should be clear from the preceding discussion, much further work is needed to gain a good understanding of ice-ocean interaction and the importance of this process for the dynamics of the Greenland Ice Sheet. This work could take a number of directions and philosophies.

First and foremost, we require better observational constraints on submarine melt rates. It is not yet clear how this can be achieved given the difficulty of obtaining such constraints. One method is the fjord heat flux method where detailed oceanographic

measurements at a flux gate allow the calculation of a toward-glacier heat flux which can be converted to a submarine melt rate. In order to reduce the large uncertainties on these estimates, the heat flux gate should be located close to the glacier and should be densely sampled, observations should be made over as long a period as possible, and there would ideally be few icebergs present at the fjord surface (*Jackson and Straneo*, 2016). These factors are easiest to satisfy at small glacier-fjord systems, and by combining with modelling, the results from these smaller systems could then be transferred up to large fast-flowing glaciers.

An alternative method is that taken by *Luckman et al.* (2015), who used high spatial and temporal resolution satellite imagery to calculate frontal ablation rates at a tidewater glacier, which they then compare to fjord temperature. With improving satellite capability, it may now be possible to apply this procedure to glaciers around Greenland. An obvious difficulty is in the monitoring of fjord temperature, but this may be less of a concern in Greenland due to the limited seasonality in deep fjord water temperature compared to Svalbard (*Straneo et al.*, 2011; *Luckman et al.*, 2015). The largest seasonal variability in forcing in Greenland may come from subglacial discharge, which could be estimated from surface melt modelling (e.g. Chapter 7).

A second important direction concerns the coupling of melting to calving. At various points in this thesis the conclusions have been limited by poor understanding of the effect of melting on calving. Work on this process could use time-lapse imagery to study the relationship between calving style and proxies for submarine melting, such as fjord water temperature or the presence of plumes. Another approach could use three-dimensional ice flow modelling to understand the effect of submarine melting on stresses within the glacier (*Todd et al.*, 2017).

Concerning the philosophy of approach, the advantage of studies such as *Luckman et al.* (2015) is in their derivation of the frontal ablation (or calving) rate. Ultimately, ice flow models need calving rate parameterisations. Estimates of submarine melting are one step removed from calving rate, with that step being the coupling of melting to calving. Arguably, working directly with the calving rate, and seeking relationships

between calving rate and forcings motivated by understanding of submarine melting (e.g. Eqs. 8.1 and 8.2 and Figs. 8.3 and 8.4) is a more straightforward and practical approach. These calving rate parameterisations could then be incorporated into ice flow models, and the approach validated by studying the resulting glacier dynamics, on which there is significant data over many years. Such an approach acknowledges the complexity of the ice-ocean interaction process but does not seek to understand every detail, instead aiming to capture and parameterise the first-order relationships and validate the approach indirectly through easily measurable quantities. On the other hand, it is not clear that this approach would lead to improved process understanding, or represent the important processes appropriately. Furthermore, easily measurable quantities such as ice velocity and terminus position respond to many more factors than submarine melting, and separating out the effect of submarine melting would be difficult.

8.7 Concluding remarks

This thesis has undertaken numerical modelling of submarine melt rates at Greenland's tidewater glaciers, thought to be a key process driving their recent thinning, acceleration and retreat. Despite its potential importance, submarine melting is poorly understood, limiting our ability to predict future evolution of the Greenland Ice Sheet.

This thesis identifies near-terminus subglacial hydrology, fjord water temperature and the magnitude of subglacial runoff as the principal controls on the magnitude of submarine melt rate. A model for calving front undercutting by submarine melting was developed, suggesting that the impact of submarine melting increases as a calving front becomes more undercut. These factors have been combined into simple parameterisations capturing leading order variability in modelled submarine melt rate. Of these principal controls, subglacial hydrology is perhaps the least well constrained; the final results chapter suggests that at a large tidewater glacier in south-west Greenland, subglacial hydrology is often distributed in nature.

This thesis has made important progress in understanding variability in melt rate and

the effect of melting on calving through changing calving front shape. Nevertheless, reaching definitive conclusions regarding the importance of submarine melting to Greenland tidewater glaciers is not yet appropriate, due to the lack of observational data with which to constrain modelled melt rates, and the lack of understanding of the effect of submarine melting on calving. At present therefore, it is rather tentatively suggested that there is an important role for submarine melting at slower-flowing glaciers in Greenland, but that unless the calving process is substantially amplified by melting, melt rates are not sufficient to perturb the dynamics of the fastest-flowing glaciers, where other factors such as variability in mélange butressing could dominate. Better observations are essential, and when combined with improved modelling, will drive much-needed progress in this relatively young field of study, ultimately leading to better constraints on Greenland's future contribution to sea level.

Chapter S1

Supporting information for 'Effect of near-terminus subglacial hydrology on tidewater glacier submarine melt rates'

S1.1 Initial and Boundary Conditions

The hydrographic sections of *Chauché et al.* (2014) (their Figure 2), taken from close to Rink and Store Glaciers in West Greenland, were digitized and averaged to obtain initial and boundary conditions for the model. We have excluded their 'Store 2010 plume' data since we initiate the simulations without a plume. We also exclude the 'Store 2010' data due to the existence of a cold layer at ∼125 m depth which is anomalous compared to the other three sections. The average profiles are shown in Fig. 4.1a. They are applied throughout the domain as an initial condition, and also used as a boundary condition at the ocean end of the domain where, as in *Sciascia et al.* (2013), we apply a sponge layer which restores properties towards the initial conditions. Net flow of water

into the domain is maintained at zero by applying small correction velocities to the open ocean boundary.

S1.2 Model diffusivities

As discussed in the main article, the turbulent nature of subglacial discharge plumes leads to the entrainment of surrounding fjord water, and since this turbulence is not fully resolved in the model, some parameterization is required. This is achieved in the model using Laplacian eddy diffusivities. Under the choices described in the main article, we leave one degree of freedom (K) with which to set the magnitude of entrainment into the plume, and calibrate this as follows. We model a cubic domain of side 500 m, with ambient conditions identical to those of the main fjord runs (Fig. 4.1a). From the centre bottom of the domain we issue a discharge q of fresh (0 psu), cold (0°C) water, with q taking values 1, 3, 10, 30, 100 and 500 m^3/s. The result is a buoyant plume rising upwards through the water column. We model this process at 2.5, 5 and 10 m isotropic resolution. We vary the model diffusivity K in increments of 0.01 m^2/s and compare the modeled plume radius, velocity, temperature and salinity to that predicted by buoyant plume theory. The buoyant plume model we use is that presented in *Morton et al.* (1956), which solves equations ensuring conservation of mass, momentum, heat and salt for an axisymmetric plume with top-hat profiles for properties in the plume cross-section.

In order to extract plume radius $B(z)$, and top-hat vertical velocity $W(z)$, temperature $T(z)$ and salinity $S(z)$ from the simulations, we first let the simulations reach a steady state, achieved ∼2000s after model initiation. We then take temporal averages of model outputs over the period between 2000s and 10000s model time, which provides a sufficient time interval to smooth out the turbulence present in the model. We calculate volume Q_V, momentum Q_M, heat Q_T and salt flux Q_S as

$$Q_V(z_0) = \Delta x \Delta y \sum w \tag{S1.1}$$

$$Q_M(z_0) = \Delta x \Delta y \sum w^2 \tag{S1.2}$$

$$Q_T(z_0) = \Delta x \Delta y \sum wt \tag{S1.3}$$

$$Q_S(z_0) = \Delta x \Delta y \sum ws \tag{S1.4}$$

where the sums run over all cells at $z = z_0$ having vertical velocity $w > 0$. $\Delta x = \Delta y$ are the x and y grid resolutions and t/s are the temperature/salinity in each cell. The top-hat plume quantities we are interested in can then be calculated as

$$B(z) = Q_V / \sqrt{\pi Q_M} \tag{S1.5}$$

$$W(z) = Q_M / Q_V \tag{S1.6}$$

$$T(z) = Q_T / Q_V \tag{S1.7}$$

$$S(z) = Q_S / Q_V \tag{S1.8}$$

We quantify the agreement of plume theory and MITgcm by calculating the root mean square difference in radius, velocity, temperature and salinity predicted by the two methods. Buoyant plume theory is not well suited to predicting plume behaviour when plumes reach neutral buoyancy (e.g. *Morton et al.*, 1956), nor does it make any account of the plume reaching the fjord surface. These zones are therefore excluded from comparison, as detailed in the examples below.

For $q = 500$ m^3/s, our highest discharge, there is generally excellent agreement between plume theory and MITgcm, with the simulations capturing both the expected magnitudes and profile shape for radius, velocity, temperature and salinity (Fig. S1.1). Note that the divergence close to the surface is, as mentioned above, due to the fact that plume theory makes no account of the fjord surface. A value of $K = 0.15$ m^2/s provides marginally the lowest root mean square difference between modeled and theoretical plume velocity, but in general underestimates mixing between the plume and ambient water, as is reflected in the poor fit to width, temperature and salinity. Use of $K = 0.14$ m^2/s gives excellent agreement between simulation and theory for width, temperature and salinity, and reasonable agreement for velocity. We therefore take $K = 0.14$ m^2/s as the best value to simulate a plume with initial discharge $q = 500$ m^3/s.

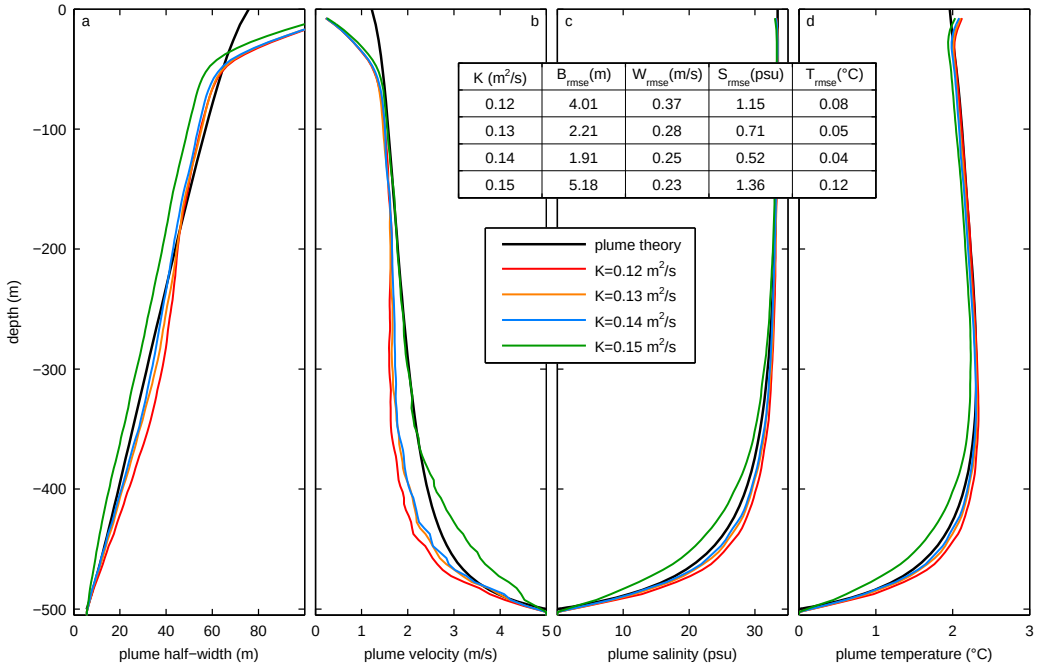

K (m^2/s)	B_{rmse}(m)	W_{rmse}(m/s)	S_{rmse}(psu)	T_{rmse}(°C)
0.12	4.01	0.37	1.15	0.08
0.13	2.21	0.28	0.71	0.05
0.14	1.91	0.25	0.52	0.04
0.15	5.18	0.23	1.36	0.12

Figure S1.1: Comparison of buoyant plume theory (black) and MITgcm simulations of varying K (colors), for a vertically issuing plume of initial flux 500 m^3/s. In (a) we compare plume width, (b) velocity, (c) salinity and (d) temperature. The inset table shows the root mean square difference between plume theory and MITgcm, excluding the top 50 m.

For a lower discharge of $q = 30$ m^3/s (Fig. S1.2), agreement is poor in the lowest 50 m, though this does not prevent good agreement further up the water column. We attribute the poor fit at depth to the fact that the plume is contained within very few cells, and that at 5 m resolution, we are forcing what is a relatively weak plume to occur over an area of at least 25 m^2. We therefore discount the bottom 50 m from the root mean square difference calculation. Plume theory and MITgcm also diverge as plume theory reaches neutral buoyancy. This arises because the MITgcm plume initially overshoots its level of neutral buoyancy before sinking back down to finally reach buoyant equilibrium. The final level reached is illustrated by the dashed horizontal lines in Fig. S1.2a, and shows good agreement with plume theory for the higher values of K considered. We therefore also exclude the 50 m below the plume theory neutral buoyancy level from the root mean square difference calculation. The lowest root mean square difference between MITgcm and theory for velocity, temperature and salinity is then achieved

when $K = 0.07$ m^2/s, which also closely approximates the neutral buoyancy level predicted by plume theory. Using $K = 0.06$ m^2/s provides a marginally better fit to plume width, but a significantly worse fit to velocity, temperature and salinity. We therefore choose $K = 0.07$ m^2/s as the best value to simulate the $q = 30$ m^3/s plume.

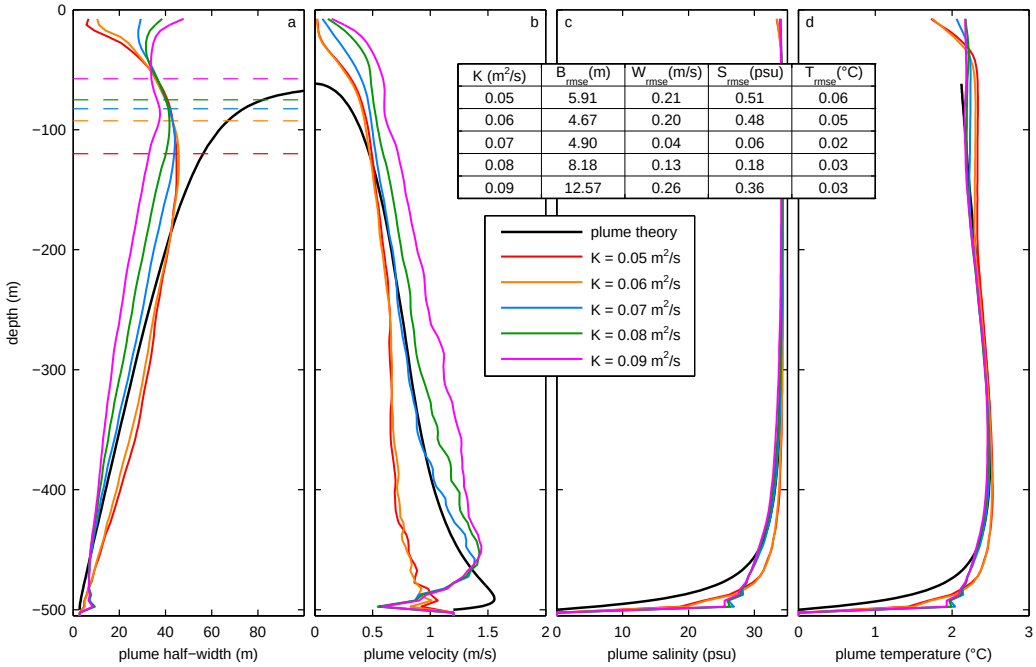

Figure S1.2: Comparison of buoyant plume theory (black) and MITgcm simulations of varying K (colors), for a vertically issuing plume of initial flux 30 m^3/s. In (a) we compare plume width, (b) velocity, (c) salinity and (d) temperature. The inset table shows the root mean square difference between plume theory and MITgcm, excluding the 50 m closest to neutral buoyancy (as defined by plume theory) and the 50 m at the bottom. Dashed horizontal lines in panel (a) indicate the level at which the MITgcm plume finally finds neutral buoyancy.

Similar arguments for $q = 1$, 3, 10 and 100 m^3/s yield best values for diffusivity of $K = 0.03$, 0.05, 0.05 and 0.1 m^2/s respectively. These results are presented in Fig. 4.1b. A power law fit to this data suggests K is approximately proportional to $q^{1/4}$. This might be expected since in a linear stratification, Morton (1956) shows using plume theory that plume velocity scales with initial buoyancy flux (here equivalent to q) raised to the power 1/4. Since in plume theory the rate of entrainment is proportional

to plume velocity, it follows that entrainment is proportional to $q^{1/4}$, which appears to be reflected in our fitted values of K. We use this power law fit (Fig. 4.1b) to set a diffusivity K for each α experiment. Explicitly, for a total discharge Q and $n = 1/\alpha$ channels, we set $K = 0.032\,(Q/n)^{0.237}$. In the $\alpha = 0$ experiments, we set Q/n to be the discharge per cell along the calving front. Thus for example in the $Q_{125}\alpha_0$ simulation we set $K = 0.032\,(125/400)^{0.237} = 0.025$ m^2/s.

For our experiments regarding sensitivity to resolution, we use the same fitting procedure to find appropriate values of K for simulating plumes with $q = 5$ and 250 m^3/s at 2.5 m and 10 m resolution. At 2.5 m resolution we obtain best values of $K = 0.03$ m^2/s for $q = 5$ m^3/s and $K = 0.06$ m^2/s for $q = 250$ m^3/s. The 10 m resolution equivalents are $K = 0.06$ m^2/s for $q = 5$ m^3/s and $K = 0.34$ m^2/s for $q = 250$ m^3/s. As expected therefore, diffusivity should increase with grid size, and as at 5 m resolution, diffusivity increases with plume discharge.

S1.3 Melt rate parameterization

The full equations used to calculate the submarine melt rate on the calving front in the model are

$$\dot{m}\,(c_i\,(T_b - T_i) + L) = c_w C_d^{1/2} \Gamma_T U\,(T - T_b) \tag{S1.9}$$

$$\dot{m} S_b = C_d^{1/2} \Gamma_S U\,(S - S_b) \tag{S1.10}$$

$$T_b = \lambda_1 S_b + \lambda_2 + \lambda_3 z \tag{S1.11}$$

$$U = \max\left(\sqrt{v^2 + w^2}, U_0\right) \tag{S1.12}$$

$\dot{m}$ is the submarine melt rate; (T_b, S_b) are the ice-ocean boundary layer temperature and salinity; T_i is the ice temperature; (L, c_w, c_i) are the latent heat of melting and heat capacities of water and ice; and (λ_1, λ_2, λ_3) describe the variation of freezing point with salinity S_b and depth z. $C_d^{1/2}\Gamma_T$ and $C_d^{1/2}\Gamma_S$ are the thermal and diffusive Stanton numbers. T, S and v/w are the free-stream temperature, salinity and ice-tangential water velocities in the region beyond the ice-ocean boundary layer, and are taken from the grid cells adjacent to the ice. U_0 is a minimum melt velocity which is motivated

as described in the main article. Eqs. S1.9 and S1.10 provide a statement of heat and salt conservation at the ice-ocean boundary, while Eq. S1.11 ensures that the boundary remains at the salinity and pressure dependent melting point.

Symbol	Description	Value	Units
T_i	ice temperature	-25	°C
c_i	ice heat capacity	2000	J / kg °C
c_w	water heat capacity	3994	J / kg °C
L	latent heat of ice melt	3.34×10^5	J/kg
$C_d^{1/2}\Gamma_T$	thermal Stanton number	1.10×10^{-3}	-
$C_d^{1/2}\Gamma_S$	haline Stanton number	3.10×10^{-5}	-
U_0	minimum melt velocity	0.04	m/s
λ_1	freezing point salinity slope	-0.0575	°C/psu
λ_2	freezing point offset	0.0901	°C
λ_3	freezing point depth slope	7.61×10^{-4}	°C/m
ρ_i	ice density	917	kg/m^3
ρ_w	meltwater density	1000	kg/m^3
$\bar{\rho}_w$	average fjord water density	1028.6	kg/m^3
A	Glen's flow law parameter	10^{-24}	1 / Pa^{3}s
p	Glen's flow law parameter	3	-
f	friction factor	0.1	-
η	Darcy-Weisbach exponent	5/4	-
g	gravitational acceleration	9.81	m/s^2
h	terminus ice thickness	600	m
d	fjord depth	500	m

Table S1.1: Values of physical parameters used in this study.

S1.4 Channel sizes

S1.4.1 Theory

In each of our simulations, a fixed total discharge Q is split between a number of channels. In order to relate discharge through each channel to a channel cross-sectional size and channel flow velocity, we balance wall melt and creep closure in a semi-circular Röthlisberger channel (*Röthlisberger*, 1972). The defining equations are from *Schoof* (2010), and the notation is identical with the exception of channel size X, which has been changed from S to avoid a clash with the fjord water salinity, the Glen's Flow Law parameter p, which has been changed from n to avoid a clash with the number of channels, and the Darcy-Weisbach exponent η, which has been changed from α to avoid a clash with the parameter indexing our simulations. The time evolution of the cross-sectional size, X, of a semi-circular subglacial channel is given by

$$\frac{dX}{dt} = c_1 q\Psi - c_2 N^p X \tag{S1.13}$$

where q is the channel discharge, Ψ is the hydraulic gradient, defined below, and $N = p_i - p_w$ is the effective pressure; p_i is the ice pressure and p_w is the water pressure in the channel. p and A are Glen's flow law parameters, while $c_1 = 1/\rho_i L$ and $c_2 = 2Ap^{-p}$ are constants related to wall melt and creep closure; ρ_i is ice density and L is the latent heat of melting ice.

The second defining equation, in common with *Schoof* (2010), is the Darcy-Weisbach law relating discharge, channel size and hydraulic gradient through

$$q = c_3 X^\eta |\Psi|^{-1/2}\Psi \tag{S1.14}$$

where $c_3 = (2^{1/2}(\pi+2)/\pi^{1/2}\rho_w f)^{1/2}$ is a geometric constant; ρ_w is water density and f is a friction factor. $\eta = 5/4$ is constant. The hydraulic gradient Ψ is given by

$$\Psi = -\rho_w g \frac{\partial b}{\partial s} - \frac{\partial p_w}{\partial s} \tag{S1.15}$$

where s is a coordinate along the channel, g is gravity and $b(s)$ is the bed topography.

At first glance, Eq. S1.14 provides the needed relation between discharge and channel size, but Ψ is not independent of q and X, so further manipulation is required. In steady state (which we assume to exist), the channel size does not change in time, so Eq. S1.13 becomes

$$c_1 q \Psi - c_2 N^p X = 0 \tag{S1.16}$$

Eqs. S1.14 and S1.16 are then two equations in the two unknowns p_w (through Ψ) and X. All other variables are pre-defined. Solving Eq. S1.14 for X results in

$$X = c_3^{-1/\eta} \Psi^{-1/2\eta} q^{1/\eta} \tag{S1.17}$$

and substituting into Eq. S1.16 gives a relation

$$\Psi = k N^{2\eta p/(2\eta+1)} q^{(2-2\eta)/(2\eta+1)} \tag{S1.18}$$

where $k = (c_1 c_2^{-1} c_3^{1/\eta})^{-2\eta/(2\eta+1)}$ is constant. Eqs. S1.17 and S1.18 give the final result. Noting $\eta = 5/4$ we obtain $X \propto q^{6/7}$ and using $q = XV$ gives $V \propto q^{1/7}$. For a total discharge Q split evenly between n channels, each channel has $X \propto (Q/n)^{6/7}$ and $V \propto (Q/n)^{1/7}$.

Concerning the stability of this equilibrium channel size, we have here assumed that the through channel discharge q is fixed. This choice results in the equilibrium channel size being stable (e.g. *Nye*, 1976). The other possibility offered by Eq. S1.14 is to hold Ψ constant - in this case the equilibrium channel size is unstable (e.g. *Schoof*, 2010). The above analysis is valid for a channel which is hydraulically isolated from other channels, a situation which may occur even when channels are in close proximity due to pressure gradients set up by bed topography (*Schoof*, 2010). In our most distributed cases however, we do not expect the channels to be hydraulically isolated, and in these cases, many studies (e.g. *Fountain and Walder*, 1998; *Schoof*, 2010) suggest that some channels would grow at the expense of others, eventually leading to a smaller number of larger channels. The more distributed cases we model might therefore not be considered

steady state cases - rather these might approximate a transient state of the subglacial hydrologic system early in the melt season, with a transistion to a more channelized (larger α) system as the summer progresses.

S1.4.2 Implementation

The values of constant parameters in Eqs. S1.17 and S1.18 are listed in Table S1.1. For a discharge q through a given channel it remains to define effective pressure $N = p_i - p_w$ in order to calculate X and thus channel flow velocity V. We are only concerned with the values of these variables at the channel mouth. The channel mouth is situated at the grounding line of the glacier, 500m under the fjord surface in our model, thus $p_w = \bar{\rho}_w g d$ where $d = 500$ m and $\bar{\rho}_w$ is the average density of fjord water through the water column. The ice pressure is related to the thickness h of the glacier at the terminus by $p_i = \rho_i g h$. Many tidewater glaciers in Greenland are close to flotation, so in this idealized model we take $h = 600$ m. The resulting relationship between channel discharge, size and velocity is plotted in Fig. 4.1c. At the model resolution of 5 m at the calving front, the channel size has to be rounded to the nearest 25 m^2, and the velocity readjusted to achieve the required discharge.

S1.5 Further discussion of sensitivity experiments

Results of the sensitivity experiments are displayed in Table 4.1, summarized in the main article and discussed further here.

The melt calculation used in this study has been discussed extensively elsewhere (e.g. *Holland and Jenkins*, 1999). Total melt proves relatively insensitive to change in ice temperature T_i because of the dominance of the latent heat L in Eq. S1.9. Total melt does not quite increase in a 1:1 fashion with $C_d^{1/2}\Gamma_T$ due to the limiting effect of salt diffusion, but this is a secondary effect for the range of conditions encountered in this study.

Regarding sensitivity to a uniform shift in ambient temperature ΔT_a at all depths, spatially averaged submarine melt rate changes by approximately 25% in response to

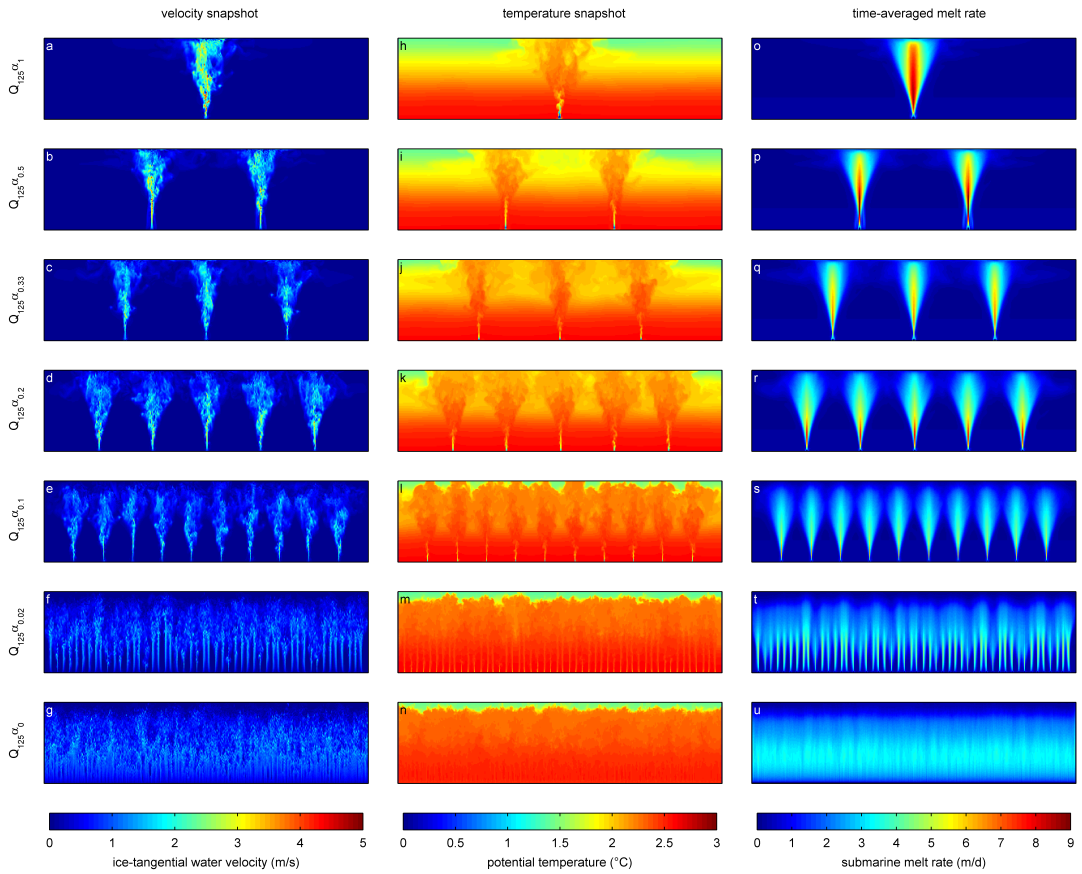

Figure S1.3: Snapshots of ice-tangential water velocity and ice-adjacent temperature, and time averaged melt rates for all the experiments having a total discharge $Q = 125$ m^3/s.

a decrease/increase in ambient temperature of 1°C, consistent with linear relationships between melt rate and water temperature described by *Xu et al.* (2012) and *Sciascia et al.* (2013). A shift in ambient salinity S_a by ±0.5 psu at all depths does not have a great impact on total melt because the magnitude of change in salinity is not sufficient to result in a significant increase in plume buoyancy.

An increase in channel width (with channel size held constant) results in an increase in total melt, because the resulting plume is broader and retains its buoyancy for longer. This leads to higher plume water velocities and thus higher melt rates. Supposing channels preferred a broad and low shape rather than the semi-circular cross-section

assumed in this study, melt would increase in each of our simulations, but the increase would be greater in the more distributed cases. In common with the results of *Kimura et al.* (2014), use of a no-slip condition in our model dramatically reduces melt rates, as it creates a layer of slow moving water in the cells adjacent to the ice. Since the model configuration in this study does not have sufficient resolution to resolve the viscous ice-ocean boundary layer, use of the no-slip condition here is not justified (*Kimura et al.*, 2014).

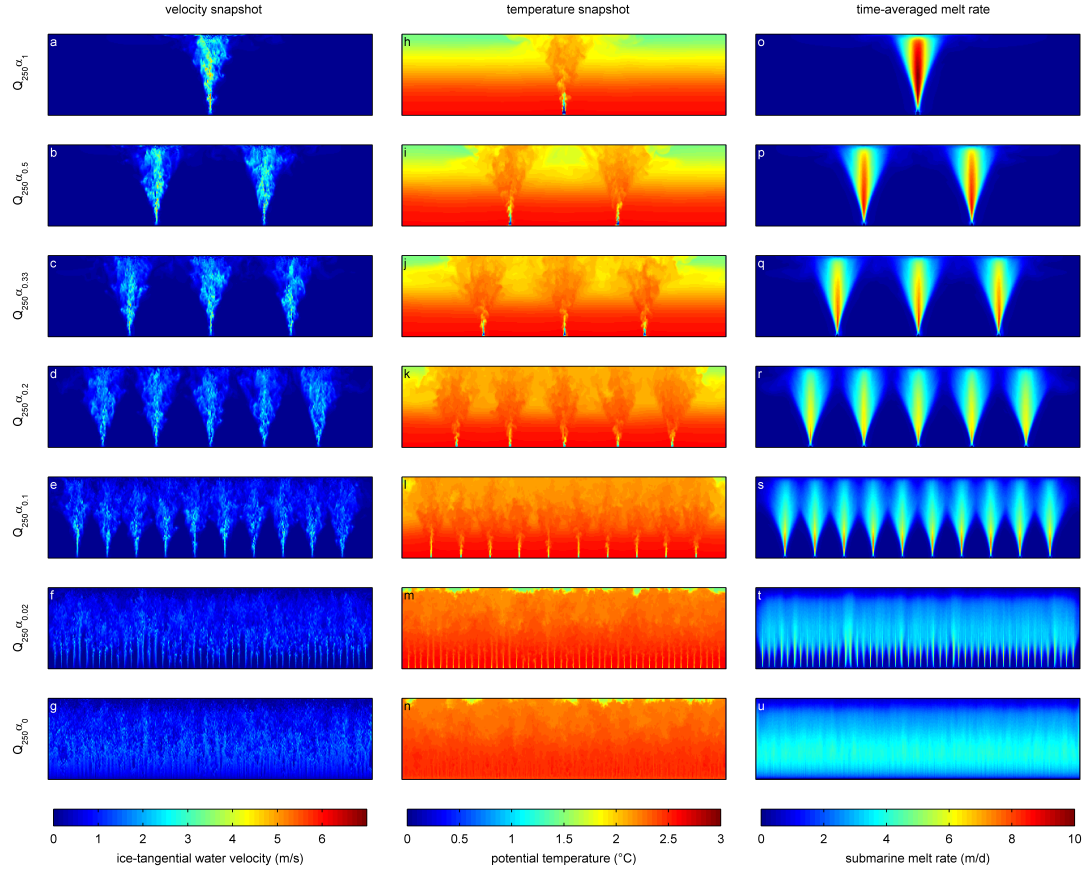

Figure S1.4: Equivalent of Fig. S1.3 for $Q = 250$ m^3/s.

In order to maintain a certain discharge, a reduction in channel flow velocity requires an increase in channel size. The decrease in total melt when channel velocity is increased is therefore consistent with the presence of a narrower channel. In addition, and as in *Kimura et al.* (2014), a high channel velocity results in the core of the plume being more separated from the ice, leading to lower melt rates. The magnitude of change in

total melt resulting from a halving or doubling of channel velocity is not large however, being less than 6%. Note that it was not possible to undertake sensitivity to channel width and velocity for $\alpha = 0.02$, because the channels in this experiment consist of a single cell and thus cannot be made smaller or changed in shape.

We now turn to sensitivity to diffusivity K. For a single plume, a decrease in K increases the turbulence in the model, which results in greater mixing between the plume and the ambient fjord water, and thus a broader and slower plume. A broader plume will melt a larger area of the calving front, while a decrease in water velocity will decrease local melt rates.

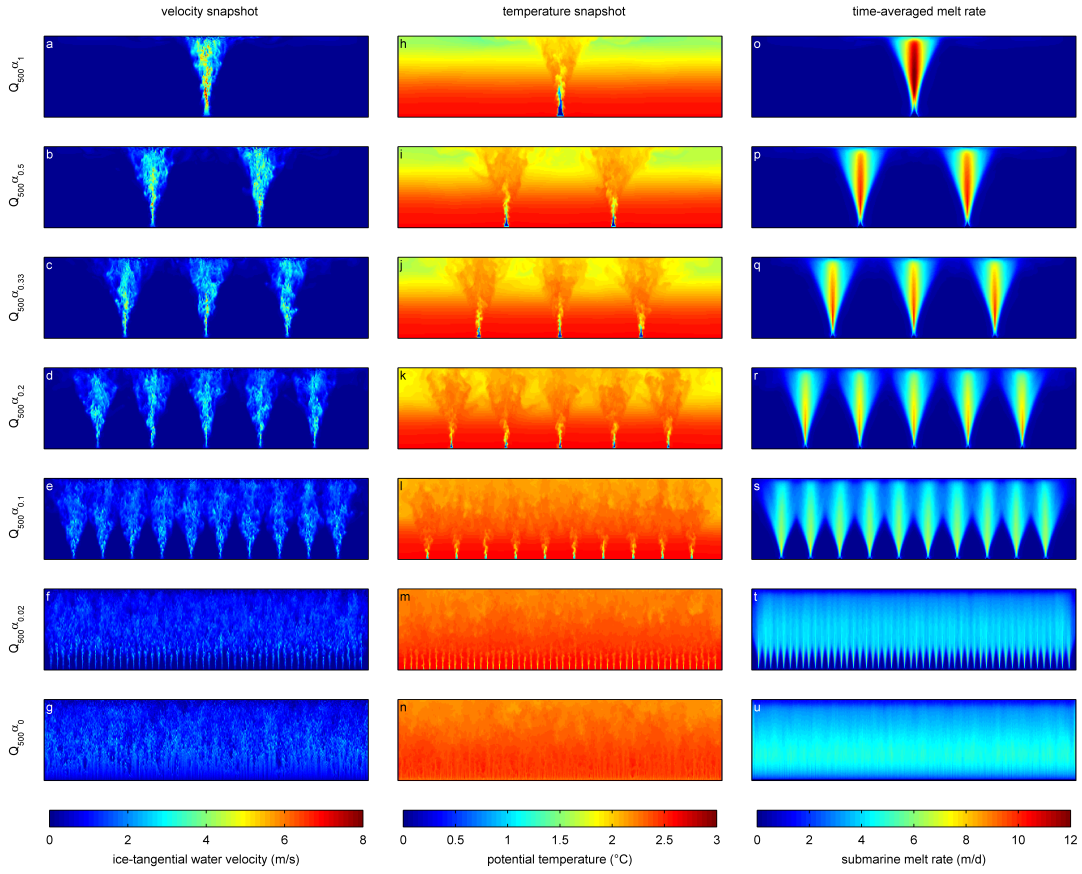

Figure S1.5: Equivalent of Fig. S1.3 for $Q = 500$ m^3/s.

In the $Q_{250}\alpha_1$ case, the change in total melt arising from variation in K is dominated by variation in plume width, such that spatially averaged melt rate increases with

decreasing K. Conversely, for $Q_{250}\alpha_{0.02}$, melt rate decreases with a lower value of K; while the same analysis regarding plume width applies at depth, the plumes soon merge so that they cannot increase their width any further. Thereafter, the increased mixing associated with lower values of K means that the plume is less buoyant and thus less energetic as it rises, resulting in decreased melt rates close to the surface, and driving the decrease in total melt. Using the higher value of K in the $Q_{250}\alpha_{0.02}$ results in no change in total melt; in this case the decrease in melt at depth from narrower plumes balances the increase in melt near the surface from reduced plume mixing.

As described above, we have attempted to choose appropriate values for K at 2.5 m and 10 m resolution. However, these do not provide subgrid-scale mixing entirely equivalent to the 5 m resolution case, since the spatial pattern of difference in melt achieved by change in model resolution is similar to that of the low and high diffusivity experiments at 5 m resolution. In the 2.5 m resolution simulations, melt rates are decreased at depth, but increased near the surface relative to the 5 m resolution equivalents. Ultimately this leads to modest increases in total melt. At 10 m resolution and for $\alpha = 0.02$ or $\alpha = 1$ we obtain melt rates which are decreased by $\sim$15% relative to the 5 m resolution simulations. The patterns of melt change indicate that in our 10 m resolution simulations, the plumes are not mixing with ambient water to the extent they do at 5 m resolution. Therefore agreement might be improved by decreasing K in our 10 m resolution experiments.

Chapter S2

Supporting information for 'Scalings for submarine melting at tidewater glaciers from buoyant plume theory'

S2.1 Dropping melt and drag terms from plume equations

In the main article we quote a scaling for when the melt and drag terms in Eqs. 5.1 become important. These are derived here.

S2.1.1 Melt terms

We first estimate the height on the calving front Z_m at which the volume added to the plume from melting becomes comparable to the initial volume flux Q_{0m}:

$$\int_0^{Z_m} 2b\dot{m}\, dz \approx Q_{0m} \tag{S2.1}$$

Since both submarine melt and the initial volume flux have zero salinity, this provides an estimate of when the buoyancy added to the plume by submarine melt becomes comparable to the initial buoyancy flux.

At a first level of approximation, the integral may be evaluated using the solution to the plume equations excluding melt and drag terms (i.e. using Eqs. 5.6), and by taking the point source limit (i.e. neglecting the finite source correction). We also use

$$\dot{m} = \frac{c_w C_d^{1/2} \Gamma_T u (T - T_b)}{c_i (T_b - T_i) + L} \approx \frac{c_w C_d^{1/2} \Gamma_T u (T - T_b)}{L} \approx \frac{c_w C_d^{1/2} \Gamma_T u (T_a - T_0)}{L} \tag{S2.2}$$

where the first approximation follows as $L \gg c_i(T_b - T_i)$, and the second approximation holds (roughly) for $z \gg z_0$ as in this regime $T \to T_a$. The integral may then be evaluated as

$$\int_0^{Z_m} 2b\dot{m}\, dz = \frac{2c_w C_d^{1/2} \Gamma_T (T_a - T_0)}{L} \left(\frac{9\alpha Q_{0m} g_0'}{5\pi} \right)^{1/3} \int_0^{Z_m} z^{2/3}\, dz \tag{S2.3}$$

By equating to the initial volume flux as in Eq. (S2.1) we obtain a relationship between the height on the calving front Z_m and the subglacial discharge Q_{0m} at which total submarine melt flux is similar to the initial volume flux

$$Q_{0m}^{2/3} = \frac{6}{5} \frac{c_w C_d^{1/2} \Gamma_T}{L} \left(\frac{9\alpha g_0'}{5\pi} \right)^{1/3} (T_a - T_0)\, Z_m^{5/3} \tag{S2.4}$$

S2.1.2 Drag term

The right hand side of Eq. 5.1b may be written

$$\frac{\pi}{2} b^2 g' - 2C_d b u^2 = \frac{\pi}{2} b^2 g' - 2C_d b^2 g' \frac{u^2}{b g'} \approx \frac{\pi}{2} b^2 g' - 2C_d b^2 g' \frac{5}{8\alpha} = \frac{\pi}{2} b^2 g' \left(1 - \frac{5C_d}{2\pi\alpha} \right) \tag{S2.5}$$

Where the second equality follows from the definition of Γ in section 5.2.4. We see that including drag reduces plume buoyancy by a factor $5C_d/2\pi\alpha \approx 0.08$, and the effect is equivalent to reducing g by the same factor. Therefore an approximate analytical solution to the plume equations with a drag term can be obtained simply by replacing g with $(1 - 5C_d/2\pi\alpha)g$ throughout Eqs. 5.6. Considering particularly plume velocity

Symbol	Description	Value	Units
α	entrainment coefficient	0.1	-
g	gravitational acceleration	9.81	$\mathrm{m\,s^{-2}}$
C_d	plume-ice drag coefficient	9.7×10^{-3}	-
Γ_T	heat transfer coefficient	1.1×10^{-2}	-
Γ_S	salt transfer coefficient	3.1×10^{-4}	-
c_w	heat capacity of water	3974	$\mathrm{J\,kg^{-1}\,{}^{\circ}C^{-1}}$
c_i	heat capacity of ice	2009	$\mathrm{J\,kg^{-1}\,{}^{\circ}C^{-1}}$
L	latent heat of ice melt	334000	$\mathrm{J\,kg^{-1}}$
T_i	ice temperature	-10	$^{\circ}$C
λ_1	freezing point salinity slope	-5.73×10^{-2}	$\mathrm{{}^{\circ}C\,psu^{-1}}$
λ_2	freezing point offset	8.32×10^{-2}	$^{\circ}$C
λ_3	freezing point depth slope	-7.53×10^{-4}	$\mathrm{{}^{\circ}C\,m^{-1}}$
β_S	haline contraction coefficient	7.86×10^{-4}	$\mathrm{psu^{-1}}$
β_T	thermal expansion coefficient	3.87×10^{-5}	$\mathrm{{}^{\circ}C^{-1}}$

Table S2.1: Chapter 5 parameter values

in the point source limit, this replacement introduces a factor

$$(1 - 5C_d/2\pi\alpha)^{1/3} \approx 1 - 5C_d/6\pi\alpha \tag{S2.6}$$

Therefore the presence of the drag term reduces plume velocity by $\sim$2.5%. The magnitude of change is such that we can safely neglect the drag term in the plume equations.

S2.2 Mathematical details from the uniform stratification solution

S2.2.1 Properties of T_b

In the main article we state a number of results regarding T_b; these are derived here. Consider the melt rate parameterisation Eqs. 5.2. By eliminating $\dot{m}$ from Eq. 5.2a using Eq. 5.2b and then eliminating T_b in favour of S_b using Eq. 5.2c we can obtain a quadratic for S_b

$$a_1 S_b^2 + a_2 S_b + a_3 = 0 \tag{S2.7}$$

where the coefficients are given by

$$a_1 = \lambda_1(c_i\Gamma_S - c_w\Gamma_T) \tag{S2.8}$$

$$a_2 = c_w\Gamma_T(T - \lambda_2 - \lambda_3(h-z)) + \Gamma_S(c_i(\lambda_2 + \lambda_3(h-z) - \lambda_1 S - T_i) + L) \tag{S2.9}$$

$$a_3 = -\Gamma_S S(c_i(\lambda_2 + \lambda_3(h-z) - T_i) + L) \tag{S2.10}$$

and then S_b is given by the positive branch of the quadratic formula

$$S_b = \frac{1}{2a_1}\left(-a_2 + \sqrt{a_2^2 - 4a_1a_3}\right) \tag{S2.11}$$

Note that u does not appear in any of the coefficients, it cancels when we substitute Eq. 5.2b into Eq. 5.2a. Therefore $dS_b/du = 0$. Further we use Eq. 5.2c to get $dS_b/du = \lambda_1^{-1} dT_b/du$, therefore we also have $dT_b/du = 0$.

By direct differentiation of Eq. (S2.11) we get

$$\frac{dT_b}{dT} = -\frac{\lambda_1 c_w \Gamma_T}{2a_1}\left(1 - \frac{a_2}{\sqrt{a_2^2 - 4a_1a_3}}\right) \tag{S2.12}$$

For parameters within a reasonable range for glacial fjords (and see also Table S2.1) it may be shown that $a_1 > 0$, $a_2 > 0$ and $a_3 < 0$, and so $0 < a_2/\sqrt{a_2^2 - 4a_1a_3} < 1$. The prefactor in Eq. (S2.12) is constant and may be evaluated as $-\lambda_1 c_w \Gamma_T / 2a_1 \approx 1/2$

(note $c_i\Gamma_S \ll c_w\Gamma_T$ and $\lambda_1 < 0$), and therefore it follows that $0 < dT_b/dT < 1$, as is stated in the main article.

Lastly, differentiation with respect to S gives (note we use $c_i(T_b - T_i) \ll L$)

$$\frac{dT_b}{dS} = \frac{\lambda_1 \Gamma_S L}{\sqrt{a_2^2 - 4a_1 a_3}} \tag{S2.13}$$

from which it easily follows (noting $\lambda_1 < 0$) that $dT_b/dS < 0$, which is the final result used in the main article.

S2.3 Mathematical details from the linear stratification section

S2.3.1 Non-dimensionalisation of equations

While this procedure has been extensively studied previously (e.g. *Morton et al.*, 1956; *Morton*, 1959; *Turner*, 1979) we believe it worthwhile to include a sketch of the non-dimensionalisation of the plume equations and characteristic plume heights as our prefactors differ slightly from others in the literature. We first define plume volume flux $Q = \pi b^2 u/2$, momentum flux $M = \pi b^2 u^2/2$, buoyancy flux $B = \pi b^2 u g'/2$. We define equivalent non-dimensional fluxes $\tilde{Q}$, $\tilde{M}$ and $\tilde{B}$, and non-dimensional depth $\tilde{z}$ by

$$Q = (2\pi)^{1/4}\,\alpha^{1/2} B_0^{3/4} (N^2)^{-5/8} \tilde{Q} \tag{S2.14a}$$

$$M = B_0 (N^2)^{-1/2} \tilde{M} \tag{S2.14b}$$

$$B = B_0 \tilde{B} \tag{S2.14c}$$

$$z = (2\pi)^{-1/4}\,\alpha^{-1/2} B_0^{1/4} (N^2)^{-3/8} \tilde{z} \tag{S2.14d}$$

where B_0 is the initial buoyancy flux of the plume. One can then show with these definitions that the analytical model plume equations reduce to

$$\frac{d\tilde{Q}}{d\tilde{z}} = \tilde{M}^{1/2} \qquad \frac{d\tilde{M}}{d\tilde{z}} = \frac{\tilde{Q}\tilde{B}}{\tilde{M}} \qquad \frac{d\tilde{B}}{d\tilde{z}} = -\tilde{Q} \tag{S2.15}$$

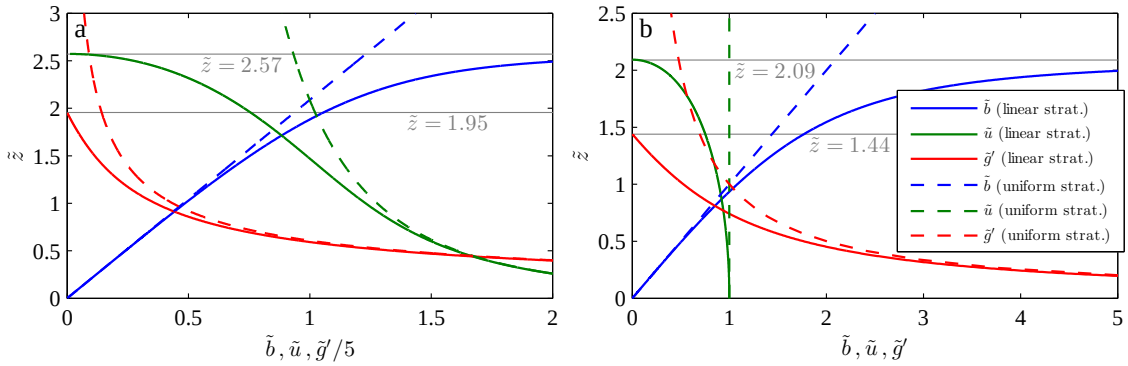

Figure S2.1: Solution to the non-dimensional plume equations for (a) half-conical plume geometry and (b) line plume geometry. Solid lines are the linear stratification solution, dashed lines are the uniform stratification solution. Note that (a) differs from Fig. 1 of *Morton et al.* (1956) and Fig. 6.17 of *Turner* (1979) only in the prefactors of the non-dimensional variables.

For a point source of buoyancy only, the relevant initial conditions are $\tilde{Q} = 0$, $\tilde{M} = 0$, $\tilde{B} = 1$ at $\tilde{z} = 0$, starting from which Eqs. (S2.15) can be solved numerically with solution shown in Fig. S2.1a. To make contact with the main article define non-dimensional radius by $\tilde{b} = \sqrt{2\tilde{Q}^2/\pi\tilde{M}}$, velocity by $\tilde{u} = \tilde{M}/\tilde{Q}$ and reduced gravity by $\tilde{g}' = \tilde{B}/\tilde{Q}$. The expressions for characteristic plume heights presented in Eqs. 5.16 are obtained by combining the solution in Fig. S2.1a with Eq. S2.14d and Eq. 5.6c.

S2.3.2 Total submarine melt rates

In general total submarine melt rates for the plume in a linear stratification are difficult to investigate analytically, but some progress can be made. Following arguments made in the main article, let us take some multiple of plume velocity βu (for constant β) as a proxy for local submarine melt. We can then rewrite total melt in terms of the non-dimensional variables introduced above and in the main article. Consider first the case where the plume does not reach the surface.

$$\dot{M} = 2\beta\,(2\pi)^{-1/4}\,\alpha^{-1/2}\,(Q_0 g_0')^{3/4}\,(N^2)^{-5/8}\int_{\tilde{z}_0}^{2.57}\tilde{b}\tilde{u}\,d\tilde{z} \tag{S2.16}$$

If we were considering a point source, then the lower limit of the integral would be 0, such that the integral would be independent of Q_0 and N^2 and then we'd have $\dot{M} \propto Q_0^{3/4}(N^2)^{-5/8}$. Since we in fact have a finite source of subglacial discharge, we need to retain the lower limit $\tilde{z}_0$ which means the integral is not quite independent of Q_0 and N^2. We can split the integral into the point source contribution and the correction for a finite source

$$\int_{\tilde{z}_0}^{2.57} \tilde{b}\tilde{u}\, d\tilde{z} = \int_{0}^{2.57} \tilde{b}\tilde{u}\, d\tilde{z} - \int_{0}^{\tilde{z}_0} \tilde{b}\tilde{u}\, d\tilde{z} \tag{S2.17}$$

In the main article we noted that for tidewater glacier-relevant parameters we have $z_0 < z_1$ (where z_1 is defined in the main article or using Eq. (S2.14d) with $\tilde{z} = 1$). In non-dimensional terms this is stated as $\tilde{z}_0 < 1$, and means that the uniform stratification solution $\tilde{b} \propto \tilde{z}$ and $\tilde{u} \propto \tilde{z}^{-1/3}$ can be used to evaluate the second integral

$$\int_{0}^{\tilde{z}_0} \tilde{b}\tilde{u}\, d\tilde{z} \propto \tilde{z}_0^{5/3} \tag{S2.18}$$

so that the finite source correction term is proportional to $Q_0^{3/4}(N^2)^{-5/8} \cdot Q_0^{1/4}(N^2)^{5/8} = Q_0$. This is an increasing function of Q_0 and therefore its presence slightly reduces the 3/4 exponent which would be obtained taking into account only the first integral. Numerically we find that the second integral is often small compared to the first, therefore a total melt rate-discharge exponent of 3/4 is a good approximation when the plume does not reach the surface.

When the plume does reach the surface we have instead

$$\dot{M} = 2\beta\,(2\pi)^{-1/4}\,\alpha^{-1/2}\,(Q_0 g_0')^{3/4}\,(N^2)^{-5/8} \int_{\tilde{z}_0}^{\tilde{z}_h} \tilde{b}\tilde{u}\, d\tilde{z} \tag{S2.19}$$

where $\tilde{z}_h = (2\pi)^{1/4}\,\alpha^{1/2}\,(Q_0 g_0')^{-1/4}\,(N^2)^{3/8}(z_0 + h)$ is the non-dimensional height corresponding to the fjord surface. This is best investigated numerically as is discussed in the main article, but we can recover the uniform stratification scaling here. Suppose the fjord stratification is sufficiently weak (N^2 close to 0) that we have $\tilde{z}_h < 1$. Then we

can evaluate the integral with the uniform stratification solution $\tilde{b} \propto \tilde{z}$ and $\tilde{u} \propto \tilde{z}^{-1/3}$

$$\int_{\tilde{z}_0}^{\tilde{z}_h} \tilde{b}\tilde{u}\, d\tilde{z} \propto \tilde{z}_h^{5/3} - \tilde{z}_0^{5/3} \tag{S2.20}$$

such that total melt scales as

$$\dot{M} \propto Q_0^{3/4}(N^2)^{-5/8} Q_0^{-5/12}(N^2)^{5/8}\left[(z_0+h)^{5/3} - z_0^{5/3}\right] = Q_0^{1/3}\left[(z_0+h)^{5/3} - z_0^{5/3}\right] \tag{S2.21}$$

and finally taking the point source limit $h \gg z_0$ we recover the uniform stratification total melt scaling $\dot{M} \propto Q_0^{1/3} h^{5/3}$ as in Eq. 5.11.

S2.3.3 Derivation of plume temperature contrast for stratification in temperature and salinity

We provide here a derivation of Eq. 5.18. By combining Eqs. 5.12 and integrating we obtain

$$\frac{Qg'_T - Q_0 g'_{T0}}{N_T^2} = \frac{Qg'_S - Q_0 g'_{S0}}{N_S^2} \tag{S2.22}$$

Upon rearranging, noting $g' = g'_T + g'_S$ and using Eq. (S2.14c) we get

$$Qg'_T = \frac{Q_0(g'_{T0} + g'_{S0})\tilde{B} - Q_0 g'_{S0} + Q_0 g'_{T0} N_S^2/N_T^2}{1 + N_S^2/N_T^2} \tag{S2.23}$$

At z_{mh} we have $\tilde{B} = -|\lambda|$ where λ is some constant (Fig. S2.1a). Due to the dominance of salinity in the equation of state we have $g'_{S0}/g'_{T0} \sim 250$. By considering the limits of Eq. (S2.23) one can show that for $10 < |N_S^2/N_T^2| < 50$ (which covers glacial applications) we have

$$Qg'_T \approx -(1+|\lambda|)\frac{N_T^2}{N_S^2} Q_0 g'_{S0} \tag{S2.24}$$

giving

$$T_a - T \approx -(1+|\lambda|)\frac{dT_a/dz}{dS_a/dz}\frac{Q_0}{Q}(S_{a,0} - S_0) \tag{S2.25}$$

which is proportional to $Q_0^{1/4}(N_T^2)(N_S^2)^{-3/8}$ using Eqs. (S2.14a)-(S2.14d) and again noting $N^2 \approx N_S^2$.

S2.4 Line plumes

S2.4.1 Uniform stratification

In the line plume case the plume is wedge-shaped (Fig. S2.2) with thickness b. The defining equations which are the equivalent expressions to Eqs. 5.1 can be found in *Jenkins* (2011).

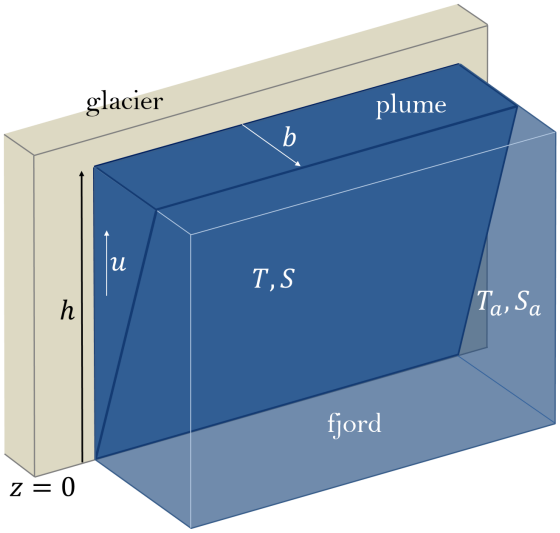

Figure S2.2: Line plume geometry. In this case b refers to the thickness of the plume.

In the line plume case the dimensionless number characterising the balance between buoyancy and momentum of the plume is given by $\Gamma = bg'/\alpha u^2$. As before we fix b_0 and u_0 by setting $Q_0 = b_0 u_0$ and $\Gamma_0 = 1$, giving

$$b_0 = \left(\frac{\alpha Q_0^2}{g_0'}\right)^{1/3} \qquad u_0 = \left(\frac{Q_0 g_0'}{\alpha}\right)^{1/3} \tag{S2.26}$$

Neglecting melt and drag terms as before and specialising to a uniform stratification, the plume solution is given by (e.g. *Linden et al.*, 1990; *Kaye*, 2008; *Straneo and Cenedese*, 2015)

$$b = \alpha\,[z + z_0] \qquad u = \left(\frac{Q_0 g_0'}{\alpha}\right)^{1/3} \tag{S2.27a}$$

$$T = T_0 + (T_a - T_0)\left(1 - \frac{z_0}{z + z_0}\right) \qquad S = S_a\left(1 - \frac{z_0}{z + z_0}\right) \tag{S2.27b}$$

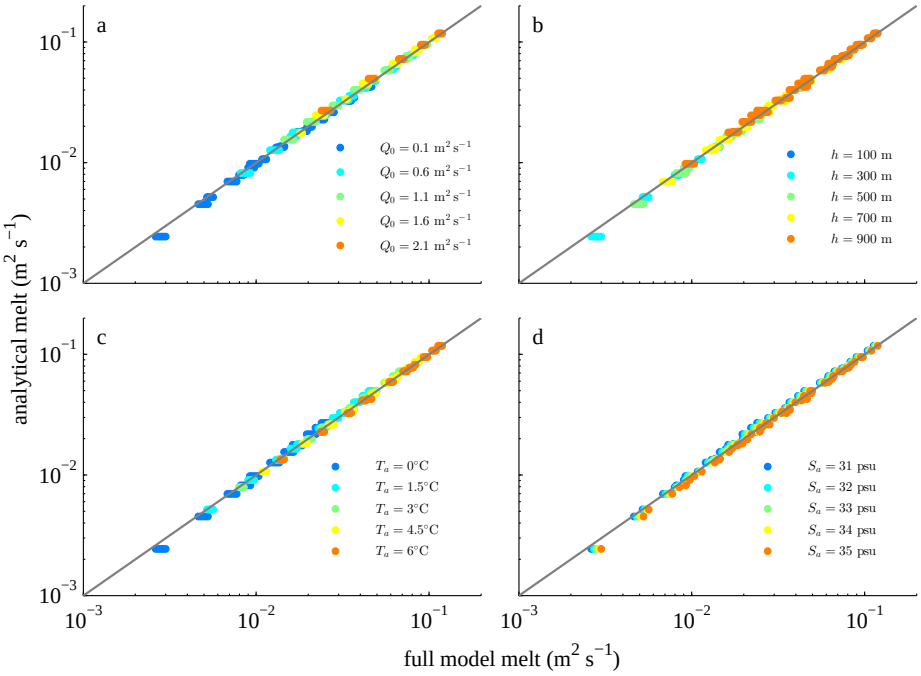

Figure S2.3: Equivalent of Fig. 5.4 for the line plume. Comparison of total submarine melt per unit width as predicted by the full model and by Eq. 5.20. Points with $h \lesssim 70z_0$ (e.g. $Q_0 = 2.1$ m^3 s^{-1}, $h = 100$ m) have been excluded as the total melt rate-discharge exponent is not well approximated by $1/3$ for these points.

The finite source correction $z_0 = (Q_0^2/\alpha^2 g_0')^{1/3}$ may be obtained by ensuring $Q(z = 0) = Q_0$. Regarding submarine melting, Fig. S2.3 is the equivalent of Fig. 5.4, and shows the result of using Eq. 5.20 to predict total submarine melt rates. Points with $h \lesssim 70z_0$ (e.g. $Q_0 = 2.1$ m^3 s^{-1}, $h = 100$ m) have been excluded as the total melt rate-discharge exponent is not well approximated by $1/3$ for these points.

S2.4.2 Linear stratification

Again while this procedure has been discussed extensively in the literature (e.g. *Wright and Wallace*, 1979; *Bush and Woods*, 1999) we believe it worth providing an outline here. Define flux quantities for volume $Q = bu$, momentum $M = bu^2$ and buoyancy

$B = bug'$. Define non-dimensional equivalents by

$$Q = \alpha^{1/3} B_0^{2/3} (N^2)^{-1/2} \tilde{Q} \tag{S2.28a}$$

$$M = B_0 (N^2)^{-1/2} \tilde{M} \tag{S2.28b}$$

$$B = B_0 \tilde{B} \tag{S2.28c}$$

$$z = \alpha^{-1/3} B_0^{1/3} (N^2)^{-1/2} \tilde{z} \tag{S2.28d}$$

where $B_0 \approx Q_0 g_0'$ is the initial buoyancy flux per unit width. The plume equations then reduce to

$$\frac{d\tilde{Q}}{d\tilde{z}} = \frac{\tilde{M}}{\tilde{Q}} \qquad \frac{d\tilde{M}}{d\tilde{z}} = \frac{\tilde{Q}\tilde{B}}{\tilde{M}} \qquad \frac{d\tilde{B}}{d\tilde{z}} = -\tilde{Q} \tag{S2.29}$$

For an infinitessimal line source of buoyancy only, the relevant initial conditions are $\tilde{Q} = 0$, $\tilde{M} = 0$, $\tilde{B} = 1$ at $\tilde{z} = 0$, starting from which Eqs. (S2.29) can be solved numerically with solution shown in Fig. S2.1b. To make contact with the main article define non-dimensional width by $\tilde{b} = \tilde{Q}^2/\tilde{M}$, velocity by $\tilde{u} = \tilde{M}/\tilde{Q}$ and reduced gravity by $\tilde{g}' = \tilde{B}/\tilde{Q}$. Expressions for characteristic line plume heights in a linear stratification are (e.g. *Wright and Wallace* (1979); *Bush and Woods* (1999), see also Fig. S2.1b)

$$z_{mh} = 2.09\,(N^2)^{-1/2} \left(\frac{Q_0 g_0'}{\alpha}\right)^{1/3} - \left(\frac{Q_0^2}{\alpha^2 g_0'}\right)^{1/3} \tag{S2.30a}$$

$$z_{br} = 1.44\,(N^2)^{-1/2} \left(\frac{Q_0 g_0'}{\alpha}\right)^{1/3} - \left(\frac{Q_0^2}{\alpha^2 g_0'}\right)^{1/3} \tag{S2.30b}$$

Chapter S3

Supporting information for 'A model for tidewater glacier undercutting by submarine melting'

S3.1 Derivation of evolution equation

We here provide a derivation of Eq. 6.3 as it may seem counterintuitive for the $\sin\theta$ term to appear in the denominator. Ignoring ice velocity, which simply translates the calving front to the right, a schematic of calving front evolution under submarine melting is shown in Fig. S3.1. We consider a section of calving front at time t with slope θ. At time $t+\delta t$, submarine melting at rate $\dot{m}$ has retreated the calving front by a perpendicular distance $\dot{m}\,\delta t$. Assuming that the calving front slope is still θ then simple trigonometry gives the horizontal displacement of the calving front as $\delta x = \dot{m}\,\delta t/\sin\theta$. Therefore, including ice velocity, the displacement of the calving front at fixed z is given by $\partial x/\partial t = v - \dot{m}/\sin\theta$, as in Eq. 6.3. We may additionally express $\sin\theta$ as

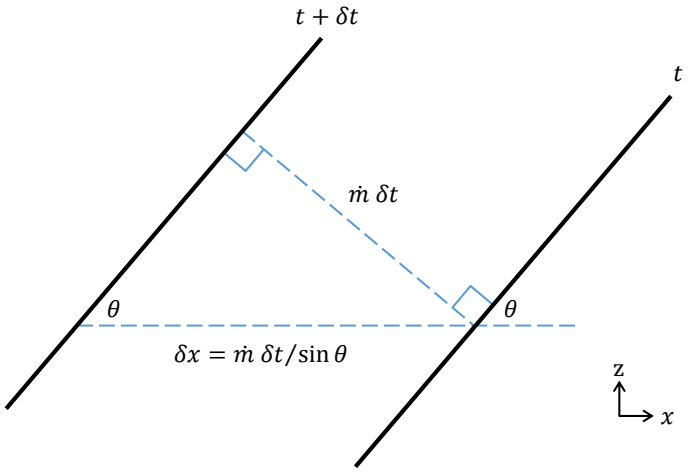

Figure S3.1: Schematic of calving front evolution.

$(1 + (\partial x/\partial z)^2)^{-1/2}$. Note that the possibility that the calving front slope at $t + \delta t$ might differ slightly from θ is a higher-order consideration.

S3.2 Definition of 'broad' subglacial channels

In the main article we note that use of a line plume model is only strictly appropriate for 'broad' subglacial channels generating 'broad' plumes, as the line plume model neglects entrainment at the sides of the plume. At a vertical calving front, a line plume of across-fjord breadth W which reaches the fjord surface will have a frontal entraining area hW, where h is the fjord depth. This area will increase if the calving front becomes undercut. In an unstratified fjord, the *along*-fjord width of the plume at the fjord surface will be approximately $b = \alpha h$ (Chapter 5; *Slater et al.*, 2016), where b has the same definition as in Fig. 6.1. Thus the surface area of the two triangular sides of the plume is approximately $2 \times \frac{1}{2} \times \alpha h \times h = \alpha h^2$. Use of a line plume model neglects entrainment at these sides. This might be considered a good approximation provided the surface area of the sides is small relative to the frontal surface area, say when $\alpha h^2/(hW) < 0.2$. For $\alpha = 0.1$ we obtain $W > h/2$. Thus when $h = 500$ m, we obtain $W > 250$ m. At a smaller calving front, say with $h = 250$ m, we'd need $W > 125$ m.

S3.3 Numerical details

Eqs. 6.1-6.3 are solved numerically in MATLAB. As outlined in the main article, we may for sufficient subglacial discharge neglect the feedback of calving front shape on plume dynamics. Thus Eqs. 6.1-6.2 decouple from Eq. 6.3; that is, we may solve Eqs. 6.1-6.2 assuming a vertical calving front, and use the obtained profile of submarine melt rate to solve Eq. 6.3.

Eqs. 6.1-6.2 of the main article are solved using an explicit Runge-Kutta 4th/5th order method (MATLAB function *ode45*), which gives a profile of submarine melting at arbitrary vertical resolution Δz. Eq. 6.3 of the main article is integrated using a first-order upwind method, in which the calving front position x_i^{n+1} at depth z and timestep $t + \Delta t$, is given in terms of the calving front position x_i^n at depth z and timestep t and the calving front position x_{i-1}^n at depth $z - \Delta z$ and timestep t by

$$x_i^{n+1} = x_i^n + \Delta t \left\{ v - \dot{m}_i \left[1 + \left(\frac{x_i^n - x_{i-1}^n}{\Delta z} \right)^2 \right]^{1/2} \right\} \tag{S3.1}$$

where $\dot{m}_i = \dot{m}(z)$. The near-grounding line slope boundary condition $\left(\frac{\partial x}{\partial z}\right)_{gl}$ referred to in the main article is enforced at the grid point closest to the grounding line ($i = 1$).

Note that while it is neglected in this paper, the feedback of calving front morphology on plume dynamics could be included by solving Eqs. 6.1-6.2 at each timestep, using the updated calving front shape from Eq. S3.1, which appears in Eqs. 6.1-6.2 through the $\sin\theta$ term.

We apply Eq. S3.1 on a uniformly spaced grid with $\Delta z = 1$ m and with a timestep $\Delta t = 0.1$ days. The grid begins at a height of 1 m above the grounding line. Sensitivity tests show that our results are insensitive to grid resolution and proximity to the grounding line. Note that for stability, the grid spacing and timestep must satisfy the Courant-Friedrichs-Lewy (CFL) condition $\dot{m} \cos\theta \Delta t / \Delta z < 1$, where $\dot{m} \cos\theta$ is the vertical component of ice-ocean boundary motion due to melting. Since $\cos\theta < 1$, the CFL condition will be satisfied when $\dot{m} \Delta t / \Delta z < 1$.

The steady state solutions shown in Fig. 6.3 of the main article are also obtained numerically. Eq. 6.5 may be written

$$\frac{\partial x}{\partial z} = \sqrt{\left(\frac{v}{\dot{m}}\right)^2 - 1} \tag{S3.2}$$

which is integrated using the same explicit Runge-Kutta 4th/5th order method (MATLAB function *ode45*) and with initial condition $x = 0$ m at $z = 1$ m.

As described in the main article, for the examples in which we include a 'subglacial channel' the initial calving front shape is taken from one of the steady state examples up until the depth of maximum melt rate, and thereafter merged into a vertical calving front. Exactly how this merging is done is not critical, but we include details of our choice here. We denote the height of maximum melting by z_{mm}, the calving front position at this depth as x_{mm}, and the slope of the calving front at this depth, as defined by the steady state calving front, as s_{mm}.

For $z < z_{mm}$, the initial calving front shape is therefore defined by Eq. 6.5. Above, we merge to vertical over a smoothing height h_s in which the calving front position is given by

$$x(z) = x_{mm} + \int_{z_{mm}}^{z} s_{mm}\left(1 - \frac{z' - z_{mm}}{h_s}\right) dz' \qquad z_{mm} < z < z_{mm} + h_s \tag{S3.3}$$

which is essentially the simplest smooth function with the properties $\partial x/\partial z = s_{mm}$ at z_{mm} and $\partial x/\partial z = 0$ (i.e. vertical) at $z_{mm} + h_s$. For the examples described in the main paper we choose a smoothing height $h_s = 200$ m. Finally for $z_{mm} + h_s < z < h$ the initial calving front is vertical.

S3.4 Stationary calving fronts with alternative fjord stratification

Stationary calving fronts are described by Eq. 6.5. Their shape therefore depends on the profile of submarine melting. In turn, this depends on the assumed fjord stratification.

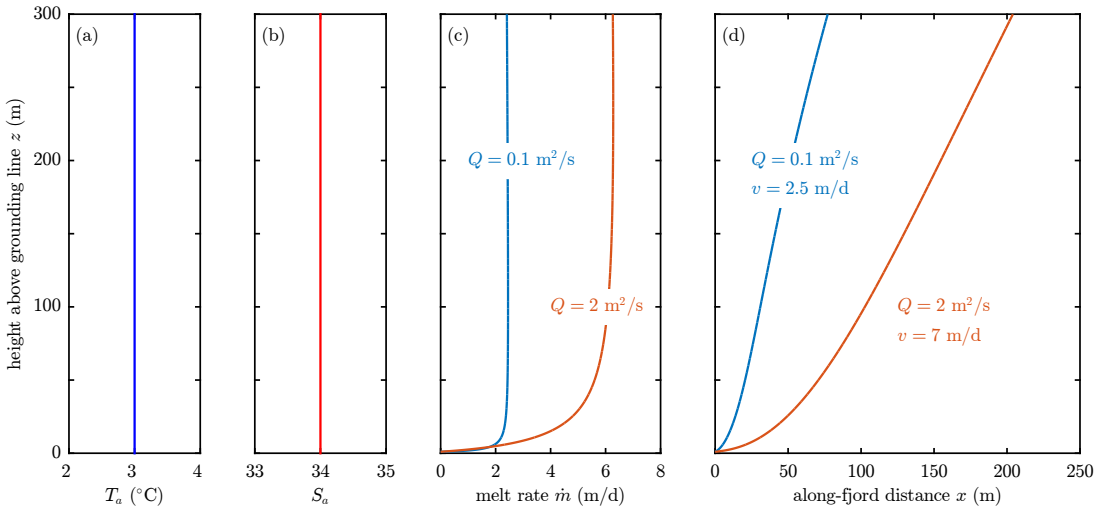

Figure S3.2: Effect on stationary calving front of having an unstratified fjord: (a) ambient temperature, (b) ambient salinity, (c) melt rate and (d) stationary calving front shape.

In the main article we use an idealised stratification which is generally representative of deep fjords in Greenland (*Straneo and Cenedese*, 2015). Some (generally shallower) glacial fjords are however very weakly stratified for much of the water column (e.g. *Bartholomaus et al.*, 2013).

Fig. S3.2 shows the effect on stationary calving front shape of assuming unstratified fjord conditions in a shallower fjord ($h = 300$ m). The unstratified conditions lead to a melt rate profile which is nearly constant with height, except for a region close to the grounding line where plume temperature and thus melt rate are increasing (Fig. S3.2c). As a result, the stationary calving fronts have a fairly constant slope, except near the grounding line where they are convex (Fig. S3.2d).

S3.5 Sensitivity of results to initial subglacial channel shape

In the main article we motivate the inclusion of a subglacial channel at the base of the initial calving front shape and show some examples of calving front evolution (Fig. 6.4). At the end of section S3.3 above we described how the shapes of the initial subglacial

channel in the main article are defined. Here we show that the steady state shape reached by the calving front is not sensitive to the choice of initial channel shape (for a given grounding line boundary condition).

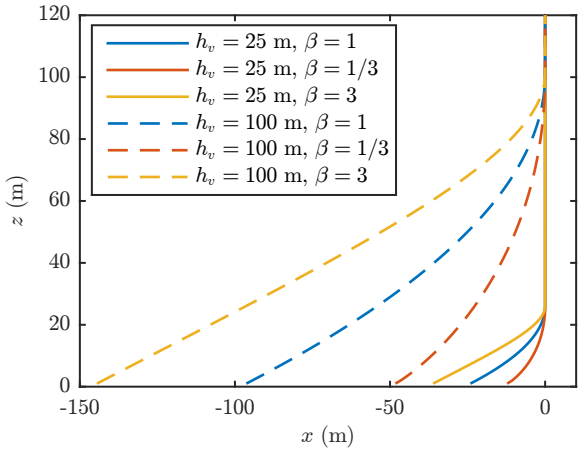

Figure S3.3: Various possible initial channel geometries given by Eq. S3.4 for the example shown in Fig. 6.4a.

A rather general expression for the shape of a subglacial channel having grounding line slope s_{gl} at a height z_0, and merging to vertical over a height h_v is given by

$$x(z) = \int_{z_0}^{z} s_{gl} \left[1 - \left(\frac{z' - z_0}{h_v} \right)^{\beta} \right] dz' \qquad z_0 < z < z_0 + h_v \tag{S3.4}$$

There are two free parameters: h_v controls the height of the channel and β controls how quickly the roof of the channel merges into the vertical. For the slope boundary condition used in Fig. 6.4a-c ($s_{gl} = 1.9$) a number of possible channel shapes are plotted in Fig. S3.3. Evolution of the calving front using these shapes is shown in Fig. S3.4. If the channel shape imposed is rather different to the steady state shape (e.g. Fig. S3.4g), it can take some time for the front to adjust to the imposed subglacial channel. In each case however, the calving front tends towards the same shape shown in Fig. 6.4a, suggesting that the shape of calving front reached is insensitive to the details of the subglacial channel imposed.

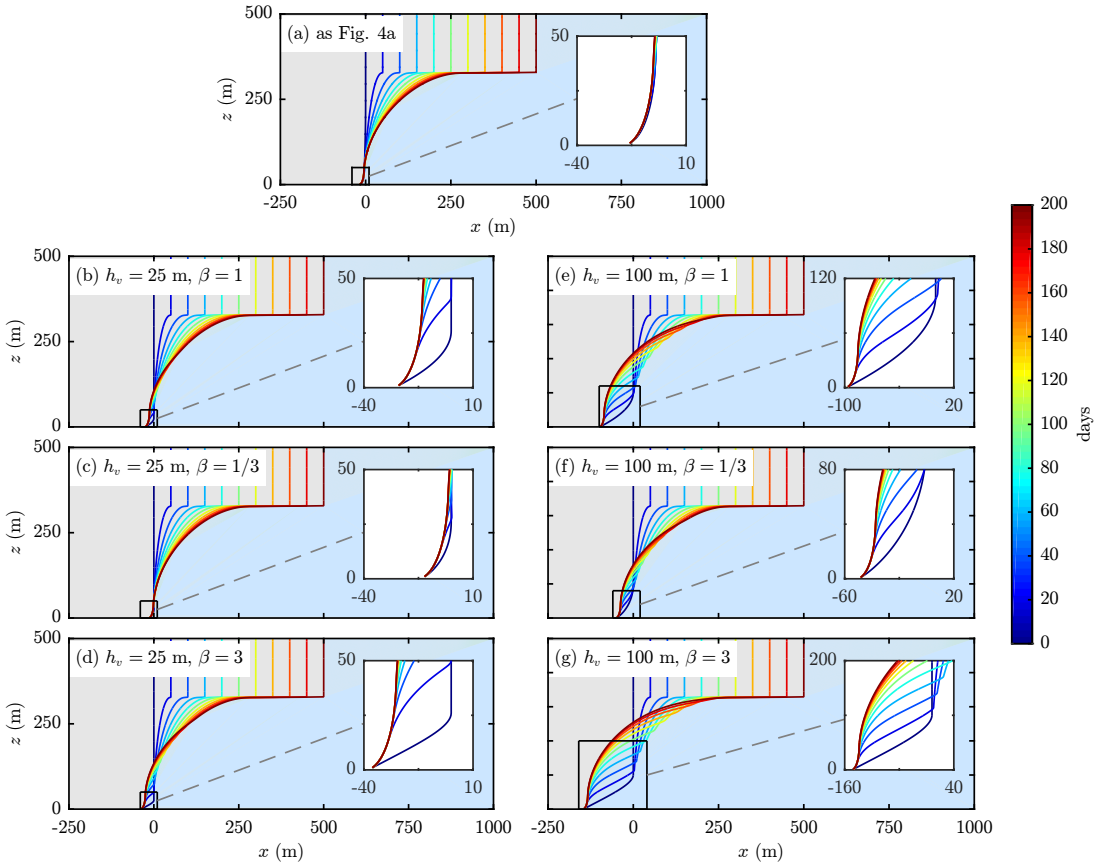

Figure S3.4: Sensitivity of calving front evolution to the imposed initial subglacial channel shape. (a) shows the same simulation as Fig. 6.4a, but run for an additional 100 days. (b)-(g) show evolution, over 200 days, for the different initial channel shapes plotted in Fig. S3.3.

.

S3.6 Discharge threshold for neglecting the feedback of submarine melting, drag and morphology

In the main article we state that provided there is sufficient subglacial discharge, the feedback of submarine melting and drag on plume dynamics may be neglected, and since these are the only terms in which the calving front shape appears, calving front shape may also be neglected. A detailed analysis for a point source plume at a vertical

calving front was made in Chapter 5; *Slater et al.* (2016), here we adapt the result therein to a line source plume at a undercut calving front.

The volume flux of submarine meltwater will be roughly equal to the volume flux of subglacial discharge Q when (details in Chapter 5; *Slater et al.* (2016))

$$Q^{2/3} \approx \frac{c_w C_d^{1/2} \Gamma_T \left(T_a - T_0\right)}{L} \left(\frac{g_0'}{\alpha}\right)^{1/3} l \tag{S3.5}$$

where parameter values are given in Table S3.1. A subscript '0' denotes values at the grounding line, and l is the length of the calving front, measured from the grounding line to the fjord surface. For a given fjord temperature T_a and calving front length l, if subglacial discharge Q exceeds that given by Eq. S3.5 then we may neglect the aforementioned feedbacks on plume dynamics. For the examples considered in the main paper we have $T_a - T_0 \approx 3°\text{C}$ and $l \approx 1000$ m at most, giving a threshold discharge of $Q = 0.01$ m^2/s, above which the feedback of shape may be neglected. The two examples considered in the main paper, $Q = 0.1$ and 2 m^2/s, lie above this threshold.

S3.7 Richardson number-dependent entrainment parameterisation

Throughout the main paper we use a slope-dependent entrainment parameterisation (*Pedersen*, 1980)

$$\dot{e} = \alpha \sin\theta \, u \tag{S3.6}$$

with $\alpha = 0.1$ (*Turner*, 1979). This parameterisation has seen common use in models of glacial plumes (e.g. *Jenkins*, 2011; *Magorrian and Wells*, 2016) and has field support (*Pedersen*, 1980). A more general Richardson number-dependent parameterisation (*Kochergin*, 1987) has however also been used in a glacial setting (e.g. *Holland and Feltham*, 2006), so we here test the sensitivity of our results to use of this alternative entrainment parameterisation. The *Kochergin* (1987) parameterisation is defined by

$$\dot{e} = \frac{C_L^2}{\text{Sc}_t} \sqrt{1 + \frac{\text{Ri}}{\text{Sc}_t}} \, u \tag{S3.7}$$

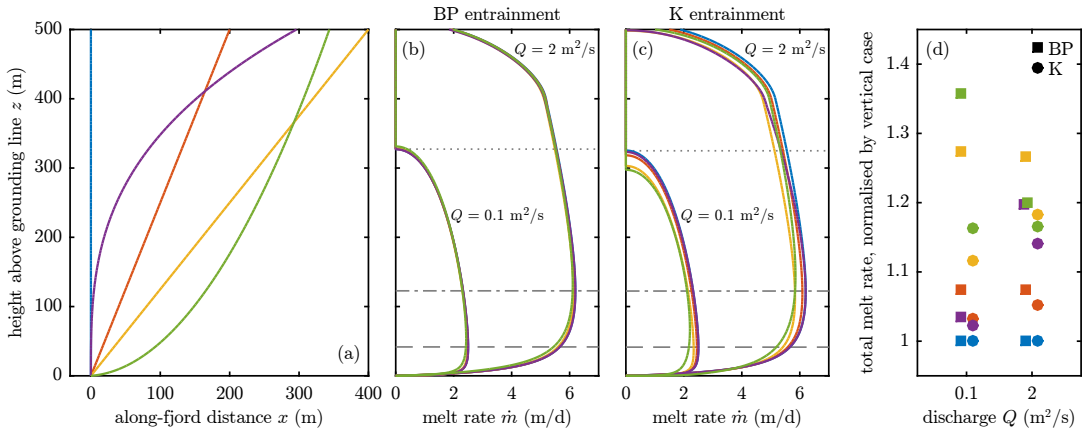

Figure S3.5: As Fig. 6.2, but additionally comparing the *Pedersen* (1980) entrainment parameterisation (BP) used throughout the main paper with the alternative *Kochergin* (1987) entrainment parameteristion (K).

where $\mathrm{Ri} = bg'/u^2$ is the Richardson number, Sc_t is the turbulent Schmidt number, given by

$$\mathrm{Sc}_t = \frac{\mathrm{Ri}}{0.0725\left(\mathrm{Ri} + 0.189 - \sqrt{\mathrm{Ri}^2 - 0.316\mathrm{Ri} + 0.189^2}\right)} \tag{S3.8}$$

and we take $C_L = 0.9$ so that Eq. S3.7 agrees with Eq. S3.6 when the parameterisations are applied at a vertical calving front in an unstratified ambient. Note that this entrainment parameterisation is not well defined when Ri becomes negative so we additionally impose $\mathrm{Ri} = \max\left[0, bg'/u^2\right]$.

Fig. S3.5c shows the results of using the *Kochergin* (1987) entrainment parameterisation at the various calving front shapes considered in Fig. 6.2. For comparison we also duplicate the results for the *Pedersen* (1980) entrainment parameterisation used throughout the main paper (Fig. S3.5b). Use of the *Kochergin* (1987) parameterisation lends submarine melt rate a slightly higher dependence on calving front shape, with more undercut calving fronts having slightly lower local submarine melt rate (Fig. S3.5c). As a result, total melt rate is less elevated at undercut calving fronts relative to vertical calving fronts when using the *Kochergin* (1987) parameterisation (Fig. S3.5d). Nevertheless, with the *Kochergin* (1987) parameterisation, it remains a good approximation to neglect the feedback of calving front shape on submarine

Symbol	Description	Value	Units
α	entrainment coefficient	0.1	-
g	gravitational acceleration	9.81	$\mathrm{m\,s^{-2}}$
C_d	plume-ice drag coefficient	9.7×10^{-3}	-
Γ_T	heat transfer coefficient	1.1×10^{-2}	-
Γ_S	salt transfer coefficient	3.1×10^{-4}	-
c_w	heat capacity of water	3974	$\mathrm{J\,kg^{-1}\,{}^{\circ}C^{-1}}$
L	latent heat of ice melt	334000	$\mathrm{J\,kg^{-1}}$

Table S3.1: Chapter 6 parameter values

melting, as is done in sections 6.3.2 and 6.3.3 of the main paper based on the *Pedersen* (1980) parameterisation.

Bibliography

Ahlstrom, A. P., et al. (2008), A new programme for monitoring the mass loss of the Greenland ice sheet, *Geological Survey of Denmark and Greenland Bulletin*, *15*, 61–64.

Ahlstrom, A. P., et al. (2013), Seasonal velocities of eight major marine-terminating outlet glaciers of the Greenland ice sheet from continuous in situ gps instruments, *Earth System Science Data*, *5*(2), 277–287, doi: 10.5194/essd-5-277-2013.

Alley, R. B., D. D. Blankenship, C. R. Bentley, and S. T. Rooney (1986), Deformation of till beneath ice stream B, West Antarctica, *Nature*, *322*(6074), 57–59, doi: 10.1038/322057a0.

Andresen, C. S., et al. (2012), Rapid response of Helheim Glacier in Greenland to climate variability over the past century, *Nature Geoscience*, *5*, 37–41, doi: 10.1038/ngeo1349.

Andrews, L. C., G. A. Catania, M. J. Hoffman, J. D. Gulley, M. P. Luthi, C. Rsyer, R. L. Hawley, and T. A. Neumann (2014), Direct observations of evolving subglacial drainage beneath the Greenland ice sheet, *Nature*, *7520*(514), 80–83, doi: 10.1038/nature13796.

Baines, P. G., and R. S. J. Sparks (2005), Dynamics of giant volcanic ash clouds from supervolcanic eruptions, *Geophysical Research Letters*, *32*(24), doi: 10.1029/2005GL024597.

Bamber, J. L., et al. (2013), A new bed elevation dataset for Greenland, *The Cryosphere*, *7*(2), 499–510, doi: 10.5194/tc-7-499-2013.

Bartholomaus, T. C., C. F. Larsen, and S. O'Neel (2013), Does calving matter? Evidence for significant submarine melt, *Earth and Planetary Science Letters*, *380*, 21–30, doi: 10.1016/j.epsl.2013.08.014.

Bartholomaus, T. C., et al. (2016), Contrasts in the response of adjacent fjords and glaciers to ice-sheet surface melt in West Greenland, *Annals of Glaciology*, *57*, 25–38, doi: 10.1017/aog.2016.19.

Bartholomew, I., P. Nienow, D. Mair, A. Hubbard, M. A. King, and A. Sole (2010), Seasonal evolution of subglacial drainage and acceleration in a Greenland outlet glacier, *Nature Geoscience*, *3*, 408–411, doi: 10.1038/ngeo863.

Batchelor, G. K. (1954), Heat convection and buoyancy effects in fluids, *Quarterly Journal of the Royal Meteorological Society*, *80*(345), 339–358, doi: 10.1002/qj.49708034504.

Bendtsen, J., J. Mortensen, K. Lennert, and S. Rysgaard (2015), Heat sources for glacial ice melt in a West Greenland tidewater outlet glacier fjord: The role of subglacial freshwater discharge, *Geophysical Research Letters*, *42*(10), 4089–4095, doi: 10.1002/2015GL063846.

Benn, D. I., C. R. Warren, and R. H. Mottram (2007), Calving processes and the dynamics of calving glaciers, *Earth-Science Reviews*, *82*(3-4), 143–179, doi: 10.1016/j.earscirev.2007.02.002.

Bevan, S. L., A. Luckman, S. A. Khan, and T. Murray (2015), Seasonal dynamic thinning at Helheim Glacier, *Earth and Planetary Science Letters*, *415*, 47–53, doi: 10.1016/j.epsl.2015.01.031.

Bjork, A. A., K. H. Kjaer, N. J. Korsgaard, S. A. Khan, K. K. Kjeldsen, C. S. Andresen, J. E. Box, N. K. Larsen, and S. Funder (2012), An aerial view of 80 years of climate-related glacier fluctuations in southeast Greenland, *Nature Geoscience*, *5*, 427–432, doi: 10.1038/ngeo1481.

Bondzio, J. H., H. Seroussi, M. Morlighem, T. Kleiner, M. Rückamp, A. Humbert, and E. Y. Larour (2016), Modelling calving front dynamics using a level-set method: application to Jakobshavn Isbræ, West Greenland, *The Cryosphere*, *10*(2), 497–510, doi: 10.5194/tc-10-497-2016.

Box, J. E., L. Yang, D. H. Bromwich, and L. Bai (2009), Greenland ice sheet surface air temperature variability: 1840-2007, *Journal of Climate*, *22*(14), 4029–4049, doi: 10.1175/2009JCLI2816.1.

Braithwaite, R. J. (1995), Positive degree-day factors for ablation on the Greenland ice sheet studied by energy-balance modelling, *Journal of Glaciology*, *41*(137), 153–160, doi: 10.3198/1995JoG41-137-153-160.

Bush, J. W. M., and A. W. Woods (1999), Vortex generation by line plumes in a rotating stratified fluid, *Journal of Fluid Mechanics*, *388*, 289–313.

Campbell, F. M., P. W. Nienow, and R. S. Purves (2006), Role of the supraglacial snowpack in mediating meltwater delivery to the glacier system as inferred from dye tracer investigations, *Hydrological Processes*, *20*(4), 969–985, doi: 10.1002/hyp.6115.

Carr, J. R., A. Vieli, and C. Stokes (2013), Influence of sea ice decline, atmospheric warming, and glacier width on marine-terminating outlet glacier behavior in northwest Greenland at seasonal to interannual timescales, *Journal of Geophysical Research: Earth Surface*, *118*(3), 1210–1226, doi: 10.1002/jgrf.20088.

Carroll, D., D. A. Sutherland, E. L. Shroyer, J. D. Nash, G. A. Catania, and L. A. Stearns (2015), Modeling turbulent subglacial meltwater plumes: implications for fjord-scale buoyancy-driven circulation, *Journal of Physical Oceanography*, *45*(8), 2169–2185, doi: 10.1175/JPO-D-15-0033.1.

Carroll, D., et al. (2016), The impact of glacier geometry on meltwater plume structure and submarine melt in Greenland fjords, *Geophysical Research Letters*, *43*(18), 9739–9748, doi: 10.1002/2016GL070170.

Cenedese, C., and V. M. Gatto (2016), Impact of two plumes' interaction on submarine melting of tidewater glaciers: A laboratory study, *Journal of Physical Oceanography*, *46*(1), 361–367, doi: 10.1175/JPO-D-15-0171.1.

Cenedese, C., and P. F. Linden (2014), Entrainment in two coalescing axisymmetric turbulent plumes, *Journal of Fluid Mechanics*, *752*(R2), doi: 10.1017/jfm.2014.389.

Chauché, N., A. Hubbard, J. C. Gascard, J. E. Box, R. Bates, M. Koppes, A. Sole, P. Christoffersen, and H. Patton (2014), Ice-ocean interaction and calving front morphology at two West Greenland tidewater outlet glaciers, *Cryosphere*, *8*, 1457–1468, doi: 10.5194/tc-8-1457-2014.

Christoffersen, P., R. I. Mugford, K. J. Heywood, I. Joughin, J. A. Dowdeswell, J. P. M. Syvitski, A. Luckman, and T. J. Benham (2011), Warming of waters in an East Greenland fjord prior to glacier retreat: mechanisms and connection to large-scale atmospheric conditions, *The Cryosphere*, *5*(3), 701–714, doi: 10.5194/tc-5-701-2011.

Christoffersen, P., M. O'Leary, J. H. Van Angelen, and M. Van Den Broeke (2012), Partitioning effects from ocean and atmosphere on the calving stability of Kangerdlugssuaq Glacier, East Greenland, *Annals of Glaciology*, *53*(60), 249–256, doi: 10.3189/2012AoG60A087.

Cook, S., I. C. Rutt, T. Murray, A. Luckman, T. Zwinger, N. Selmes, A. Goldsack, and T. D. James (2014), Modelling environmental influences on calving at Helheim Glacier in eastern Greenland, *The Cryosphere*, *8*(3), 827–841, doi: 10.5194/tc-8-827-2014.

Cowton, T., P. Nienow, I. Bartholomew, A. Sole, and D. Mair (2012), Rapid erosion beneath the Greenland ice sheet, *Geology*, *40*(4), 343–346, doi: 10.1130/G32687.1.

Cowton, T., P. Nienow, A. Sole, J. Wadham, G. Lis, I. Bartholomew, D. Mair, and D. Chandler (2013), Evolution of drainage system morphology at a land-terminating Greenlandic outlet glacier, *Journal of Geophysical Research: Earth Surface*, *118*(1), 29–41, doi: 10.1029/2012JF002540.

Cowton, T., D. Slater, A. Sole, D. Goldberg, and P. Nienow (2015), Modeling the impact of glacial runoff on fjord circulation and submarine melt rate using a new subgrid-scale parameterization for glacial plumes, *Journal of Geophysical Research: Oceans*, *120*(2), 796–812, doi: 10.1002/2014JC010324.

Cowton, T., A. Sole, P. Nienow, D. Slater, D. Wilton, and E. Hanna (2016), Controls on the transport of oceanic heat to Kangerdlugssuaq Glacier, East Greenland, *Journal of Glaciology*, *62*(236), 1167–1180, doi: 10.1017/jog.2016.117.

Cuffey, K., and W. S. B. Paterson (2010), *The Physics of Glaciers*, Academic Press.

Darlington, E. (2015), Meltwater delivery from the tidewater glacier Kronebreen to Kongsfjorden, Svalbard; insights from in-situ and remote-sensing analyses of sediment plumes, Ph.D. thesis, University of Loughborough.

Enderlin, E. M., and I. M. Howat (2013), Submarine melt rate estimates for floating termini of Greenland outlet glaciers (2000–2010), *Journal of Glaciology*, *59*(213), 67–75, doi: doi:10.3189/2013JoG12J049.

Enderlin, E. M., I. M. Howat, and A. Vieli (2013), High sensitivity of tidewater outlet glacier dynamics to shape, *The Cryosphere*, *7*, 1007–1015, doi: 10.5194/tc-7-1007-2013.

Enderlin, E. M., I. M. Howat, S. Jeong, M.-J. Noh, J. H. van Angelen, and M. R. van den Broeke (2014), An improved mass budget for the Greenland ice sheet, *Geophysical Research Letters*, *41*(3), 866–872, doi: 10.1002/2013GL059010.

Enderlin, E. M., G. S. Hamilton, F. Straneo, and D. A. Sutherland (2016), Iceberg meltwater fluxes dominate the freshwater budget in Greenland's iceberg-congested glacial fjords, *Geophysical Research Letters*, *43*(21), 11,287–11,294, doi: 10.1002/2016GL070718.

Eorola, K. (2006), About the performance of HIRLAM version 7.0, *HIRLAM Newsletter, No. 51, HIRLAM-A Programme, De Bilt, Netherlands*, pp. 93–102.

Fahnestock, M., T. Scambos, T. Moon, A. Gardner, T. Haran, and M. Klinger (2015), Rapid large-area mapping of ice flow using Landsat 8, *Remote Sensing of Environment*, *185*, 84–94, doi: 10.1016/j.rse.2015.11.023.

Fettweis, X., G. Mabille, M. Erpicum, S. Nicolay, and M. V. d. Broeke (2011), The 1958-2009 Greenland ice sheet surface melt and the mid-tropospheric atmospheric circulation, *Climate Dynamics*, *36*(1), 139–159, doi: 10.1007/s00382-010-0772-8.

Fettweis, X., B. Franco, M. Tedesco, J. H. van Angelen, J. T. M. Lenaerts, M. R. van den Broeke, and H. Gallee (2013), Estimating the Greenland ice sheet surface mass balance contribution to future sea level rise using the regional atmospheric climate model MAR, *The Cryosphere*, *7*, 469–489, doi: 10.5194/tc-7-469-2013.

Fofonoff, P., and R. C. Millard (1983), Algorithms for computation of fundamental properties of seawater, *Unesco Technical Papers in Marine Science*, *44*.

Forget, G., J.-M. Campin, P. Heimbach, C. N. Hill, R. M. Ponte, and C. Wunsch (2015), ECCO version 4: an integrated framework for non-linear inverse modeling and global ocean state estimation, *Geoscientific Model Development*, *8*(10), 3071–3104, doi: 10.5194/gmd-8-3071-2015.

Fountain, A. G., and J. S. Walder (1998), Water flow through temperate glaciers, *Reviews of Geophysics*, *36*(3), 299–328, doi: 10.1029/97RG03579.

Fowler, A. C. (1987), Sliding with cavity formation, *Journal of Glaciology*, *33*(115), 255–267, doi: 10.3198/1987JoG33-115-255-267.

Fretwell, P., et al. (2013), Bedmap2: improved ice bed, surface and thickness datasets for Antarctica, *The Cryosphere*, *7*(1), 375–393, doi: 10.5194/tc-7-375-2013.

Fried, M. J., G. A. Catania, T. C. Bartholomaus, D. Duncan, M. Davis, L. A. Stearns, J. Nash, S. E., and D. Sutherland (2015), Distributed subglacial discharge drives significant submarine melt at a Greenland tidewater glacier, *Geophysical Research Letters*, *42*(21), 9328–9336, doi: 10.1002/2015GL065806.

Gladish, C. V., D. M. Holland, A. Rosing-Asvid, J. W. Behrens, and J. Boje (2015), Oceanic boundary conditions for Jakobshavn Glacier. Part I: Variability and renewal of Ilulissat Icefjord waters, 2001-14, *Journal of Physical Oceanography*, *45*(1), 3–32, doi: 10.1175/JPO-D-14-0044.1.

Hanna, E., et al. (2011), Greenland ice sheet surface mass balance 1870 to 2010 based on twentieth century reanalysis, and links with global climate forcing, *Journal of Geophysical Research: Atmospheres*, *116*(D24), doi: 10.1029/2011JD016387.

Hansen, J., M. Sato, and R. Ruedy (1997), Radiative forcing and climate response, *Journal of Geophysical Research: Atmospheres*, *102*(D6), 6831–6864, doi: 10.1029/96JD03436.

Hewitt, I. J. (2013), Seasonal changes in ice sheet motion due to melt water lubrication, *Earth and Planetary Science Letters*, *371-372*, 16–25, doi: 10.1016/j.epsl.2013.04.022.

Hock, R. (2003), Temperature index modelling in mountain areas, *Journal of Hydrology*, *282*, 104–115, doi: 10.1016/S0022-1694(03)00257-9.

Holland, D. M., and A. Jenkins (1999), Modeling thermodynamic ice-ocean interactions at the base of an ice shelf, *Journal of Physical Oceanography*, *29*(8), 1787–1800, doi: 10.1175/1520-0485(1999)029<1787:MTIOIA>2.0.CO;2.

Holland, D. M., R. H. Thomas, B. de Young, M. H. Ribergaard, and B. Lyberth (2008a), Acceleration of Jakobshavn Isbrae triggered by warm subsurface ocean waters, *Nature Geoscience*, *1*(10), 659–664, doi: 10.1038/ngeo316.

Holland, P. R., and D. L. Feltham (2006), The effects of rotation and ice shelf topography on frazil-laden ice shelf water plumes, *Journal of Physical Oceanography*, *36*(12), 2312–2327, doi: 10.1175/JPO2970.1.

Holland, P. R., A. Jenkins, and D. M. Holland (2008b), The response of ice shelf basal melting to variations in ocean temperature, *Journal of Climate*, *21*(11), 2558–2572, doi: 10.1175/2007JCLI1909.1.

Howat, I. M. (2017), MEaSUREs Greenland ice mapping project (GIMP) 2000 image mosaic, version 1, *NASA National Snow and Ice Data Center Distributed Active Archive Center*, doi: 10.5067/4RNTRRE4JCYD.

Howat, I. M., J. E. Box, Y. Ahn, A. Herrington, and E. M. McFadden (2010), Seasonal variability in the dynamics of marine-terminating outlet glaciers in Greenland, *Journal of Glaciology*, *56*(198), 601–613, doi: 10.3189/002214310793146232.

Howat, I. M., A. Negrete, and B. E. Smith (2014), The Greenland ice mapping project (GIMP) land classification and surface elevation data sets, *The Cryosphere*, *8*(4), 1509–1518, doi: 10.5194/tc-8-1509-2014.

Hunt, G. R., and N. B. Kaye (2001), Virtual origin correction for lazy turbulent plumes, *Journal of Fluid Mechanics*, *435*, 377–396.

Hunt, G. R., and N. B. Kaye (2005), Lazy plumes, *Journal of Fluid Mechanics*, *533*, 329–338, doi: 10.1017/S002211200500457X.

Huppert, H. E., and J. S. Turner (1980), Ice blocks melting into a salinity gradient, *Journal of Fluid Mechanics*, *100*(2), 367–384, doi: 10.1017/S0022112080001206.

Hurrell, J. W. (1995), Decadal trends in the North Atlantic oscillation: Regional temperatures and precipitation, *Science*, *269*(5224), 676–679, doi: 10.1126/science.269.5224.676.

Iken, A., and R. A. Bindschadler (1986), Combined measurements of subglacial water pressure and surface velocity of Findelengletscher, Switzerland: conclusions about drainage system and sliding mechanism, *Journal of Glaciology*, *32*(110), 101–119, doi: 10.3198/1986JoG32-110-101-119.

Inall, M. E., T. Murray, F. R. Cottier, K. Scharrer, T. J. Boyd, K. J. Heywood, and S. L. Bevan (2014), Oceanic heat delivery via Kangerdlugssuaq Fjord to the south-east Greenland ice sheet, *Journal of Geophysical Research: Oceans*, *119*(2), 631–645, doi: 10.1002/2013JC009295.

IPCC (2013), *Summary for Policymakers*, book section SPM, pp. 1–30, Cambridge University Press, Cambridge, United Kingdom and New York, NY, USA, doi: 10.1017/CBO9781107415324.004.

Jackson, R. H., and F. Straneo (2016), Heat, salt, and freshwater budgets for a glacial fjord in Greenland, *Journal of Physical Oceanography*, *46*(9), 2735–2768, doi: 10.1175/JPO-D-15-0134.1.

Jackson, R. H., F. Straneo, and D. A. Sutherland (2014), Externally forced fluctuations in ocean temperature at Greenland glaciers in non-summer months, *Nature Geoscience*, *7*(7), 503–508, doi: 10.1038/ngeo2186.

James, T. D., T. Murray, N. Selmes, K. Scharrer, and M. O'Leary (2014), Buoyant flexure and basal crevassing in dynamic mass loss at Helheim Glacier, *Nature Geoscience*, *7*, 593–596, doi: 10.1038/ngeo2204.

Jenkins, A. (1991), A one-dimensional model of ice shelf-ocean interaction, *Journal of Geophysical Research: Oceans*, *96*(C11), 20,671–20,677, doi: 10.1029/91JC01842.

Jenkins, A. (1999), The impact of melting ice on ocean waters, *Journal of Physical Oceanography*, *29*(9), 2370–2381, doi: 10.1175/1520-0485(1999)029¡2370:TIOMIO¿2.0.CO;2.

Jenkins, A. (2011), Convection-driven melting near the grounding lines of ice shelves and tidewater glaciers, *Journal of Physical Oceanography*, *41*(12), 2279–2294, doi: 10.1175/JPO-D-11-03.1.

Jenkins, A., K. W. Nicholls, and H. F. J. Corr (2010), Observation and parameterization of ablation at the base of Ronne Ice Shelf, Antarctica, *Journal of Physical Oceanography*, *40*(10), 2298–2312, doi: 10.1175/2010JPO4317.1.

Jensen, T. S., J. E. Box, and C. S. Hvidberg (2016), A sensitivity study of annual area change for Greenland ice sheet marine terminating outlet glaciers: 1999-2013, *Journal of Glaciology*, *62*(231), 72–81, doi: 10.1017/jog.2016.12.

Jiskoot, H., D. Juhlin, H. St Pierre, and M. Citterio (2012), Tidewater glacier fluctuations in central East Greenland coastal and fjord regions (1980s-2005), *Annals of Glaciology*, *53*(60), 35–44, doi: 10.3189/2012AoG60A030.

Johnson, H. L., A. Münchow, K. K. Falkner, and H. Melling (2011), Ocean circulation and properties in Petermann Fjord, Greenland, *Journal of Geophysical Research: Oceans*, *116*(C1), doi: 10.1029/2010JC006519.

Joughin, I., and B. E. Smith (2013), Further summer speedup of Jakobshavn Isbrae, *Cryosphere Discussions*, *7*(6), 5461–5473, doi: 10.5194/tcd-7-5461-2013.

Joughin, I., I. Howat, R. B. Alley, G. Ekstrom, M. Fahnestock, T. Moon, M. Nettles, M. Truffer, and V. C. Tsai (2008a), Ice-front variation and tidewater behavior on Helheim and Kangerdlugssuaq Glaciers, Greenland, *Journal of Geophysical Research: Earth Surface*, *113*(F1), doi: 10.1029/2007JF000837.

Joughin, I., S. B. Das, M. A. King, B. E. Smith, I. M. Howat, and T. Moon (2008b), Seasonal speedup along the western flank of the Greenland ice sheet, *Science*, *320*(5877), 781–783, doi: 10.1126/science.1153288.

Joughin, I., B. E. Smith, I. M. Howat, T. Scambos, and T. Moon (2010), Greenland flow variability from ice-sheet-wide velocity mapping, *Journal of Glaciology*, *56*(197), 415–430, doi: 10.3189/002214310792447734.

Joughin, I., I. M. Howat, B. E. Smith, and T. Scambos (2011), MEaSUREs Greenland ice velocity: Selected glacier site velocity maps from InSAR, *Boulder, Colorado, USA: NASA DAAC at the National Snow and Ice Data Center*, doi: 10.5067/MEASURES/CRYOSPHERE/nsidc-0481.001.

Kamb, B. (1987), Glacier surge mechanism based on linked cavity configuration of the basal water conduit system, *Journal of Geophysical Research*, *92*(B9), 9083–9100, doi: 10.1029/JB092iB09p09083.

Kämpf, J. (2010), *Advanced Ocean Modelling*, Springer-Verlag Berlin Heidelberg, doi: 10.1007/978-3-642-10610-1.

Kaye, N. B. (2008), Turbulent plumes in stratified environments: A review of recent work, *Atmosphere-Ocean*, *46*(4), 433–441, doi: 10.3137/ao.460404.

Khan, S. A., et al. (2014), Glacier dynamics at Helheim and Kangerdlugssuaq glaciers, southeast Greenland, since the little ice age, *The Cryosphere*, *8*(4), 1497–1507, doi: 10.5194/tc-8-1497-2014.

Kimura, S., P. R. Holland, A. Jenkins, and M. Piggot (2014), The effect of meltwater plumes on the melting of a vertical glacier face, *Journal of Physical Oceanography*, *44*(12), 3099–3117, doi: 10.1175/JPO-D-13-0219.1.

Kjeldsen, K., et al. (2015), Spatial and temporal distribution of mass loss from the Greenland ice sheet since AD 1900, *Nature*, *528*, 396–400, doi: 10.1038/nature16183.

Kjeldsen, K. K., J. Mortensen, J. Bendtsen, D. Petersen, K. Lennert, and S. Rysgaard (2014), Ice-dammed lake drainage cools and raises surface salinities in a tidewater outlet glacier fjord, West Greenland, *Journal of Geophysical Research: Earth Surface*, *119*(6), 1310–1321, doi: 10.1002/2013JF003034.

Kochergin, V. P. (1987), *Three-Dimensional Prognostic Models*, pp. 201–208, American Geophysical Union, doi: 10.1029/CO004p0201.

Krug, J., G. Durand, O. Gagliardini, and J. Weiss (2015), Modelling the impact of submarine frontal melting and ice mélange on glacier dynamics, *The Cryosphere*, *9*, 989–1003, doi: 10.5194/tc-9-989-2015.

Langen, P. L., et al. (2015), Quantifying energy and mass fluxes controlling Godthabsfjord freshwater input in a 5-km simulation (1991-2012), *Journal of Climate*, *28*(9), 3694–3713, doi: 10.1175/JCLI-D-14-00271.1.

Lea, J. M., D. W. F. Mair, F. M. Nick, B. R. Rea, D. van As, M. Morlighem, P. W. Nienow, and A. Weidick (2014), Fluctuations of a Greenlandic tidewater glacier driven by changes in atmospheric forcing: observations and modelling of Kangiata Nunaata Sermia, 1859-present, *The Cryosphere*, *8*(6), 2031–2045, doi: 10.5194/tc-8-2031-2014.

Lefebre, F., H. Gallee, J.-P. van Ypersele, and W. Greuell (2003), Modeling of snow and ice melt at ETH camp (West Greenland): A study of surface albedo, *Journal of Geophysical Research*, *108*(D8), doi: 10.1029/2001JD001160.

Lenaerts, J. T. M., M. R. van den Broeke, W. J. van de Berg, E. van Meijgaard, and P. Kuipers Munneke (2012), A new, high-resolution surface mass balance map of Antarctica (1979-2010) based on regional atmospheric climate modeling, *Geophysical Research Letters*, *39*(4), doi: 10.1029/2011GL050713.

Linden, P. F., G. F. Lane-Serff, and D. A. Smeed (1990), Emptying filling boxes: the fluid mechanics of natural ventilation, *Journal of Fluid Mechanics*, *212*, 309–335, doi: 10.1017/S0022112090001987.

Losch, M. (2008), Modeling ice shelf cavities in a z coordinate ocean general circulation model, *Journal of Geophysical Research: Oceans*, *113*(C8), doi: 10.1029/2007JC004368.

Losch, M., D. Menemenlis, J. M. Campin, P. Heimbach, and C. Hill (2010), On the formulation of sea-ice models. Part 1: Effects of different solver implementations and parameterizations, *Ocean Modelling*, *33*(1–2), 129–144, doi: 10.1016/j.ocemod.2009.12.008.

Luckman, A., T. Murray, R. de Lange, and E. Hanna (2006), Rapid and synchronous ice-dynamic changes in East Greenland, *Geophysical Research Letters*, *33*(3), doi: 10.1029/2005GL025428.

Luckman, A., D. I. Benn, F. Cottier, S. Bevan, F. Nilsen, and M. Inall (2015), Calving rates at tidewater glaciers vary strongly with ocean temperature, *Nature Communications*, *6*, doi: 10.1038/ncomms9566.

MacAyeal, D. R. (1984), Thermohaline circulation below the Ross Ice Shelf: A consequence of tidally induced vertical mixing and basal melting, *Journal of Geophysical Research: Oceans*, *89*(C1), 597–606, doi: 10.1029/JC089iC01p00597.

MacAyeal, D. R. (1985), Evolution of tidally triggered meltwater plumes below ice shelves, in *Antarctic Research Series*, vol. 43, pp. 133–143, doi: n/a.

Magorrian, S. J., and A. J. Wells (2016), Turbulent plumes from a glacier terminus melting in a stratified ocean, *Journal of Geophysical Research: Oceans*, *121*(7), 4670–4696, doi: 10.1002/2015JC011160.

Mankoff, K. D., F. Straneo, C. Cenedese, S. B. Das, C. G. Richards, and H. Singh (2016), Structure and dynamics of a subglacial discharge plume in a Greenlandic fjord, *Journal of Geophysical Research: Oceans*, *121*(12), 8670–8688, doi: 10.1002/2016JC011764.

Marshall, J., C. Hill, L. Perelman, and A. Adcroft (1997a), Hydrostatic, quasi-hydrostatic, and nonhydrostatic ocean modeling, *Journal of Geophysical Research: Oceans*, *102*(C3), 5733–5752, doi: 10.1029/96JC02776.

Marshall, J., A. Adcroft, C. Hill, L. Perelman, and C. Heisey (1997b), A finite-volume, incompressible Navier Stokes model for studies of the ocean on parallel computers, *Journal of Geophysical Research: Oceans*, *102*(C3), 5753–5766, doi: 10.1029/96JC02775.

McFadden, E. M., I. M. Howat, I. Joughin, B. E. Smith, and Y. Ahn (2011), Changes in the dynamics of marine terminating outlet glaciers in West Greenland (2000–2009), *Journal of Geophysical Research: Earth Surface*, *116*(F2), doi: 10.1029/2010JF001757.

McPhee, M. G. (1992), Turbulent heat flux in the upper ocean under sea ice, *Journal of Geophysical Research: Oceans*, *97*(C4), 5365–5379, doi: 10.1029/92JC00239.

McPhee, M. G., J. H. Morison, and F. Nilsen (2008), Revisiting heat and salt exchange at the ice-ocean interface: Ocean flux and modeling considerations, *Journal of Geophysical Research: Oceans*, *113*(C6), doi: 10.1029/2007JC004383.

Meier, M., et al. (1994), Mechanical and hydrological basis for the rapid motion of a large tidewater glacier 1. Observations, *Journal of Geophysical Research*, *99*(B8), 15,219–15,229, doi: 10.1029/94JB00237.

Meier, M. F., and A. Post (1987), Fast tidewater glaciers, *Journal of Geophysical Research*, *92*(B9), 9051–9058, doi: 10.1029/JB092iB09p09051.

Mernild, S. H., E. Hanna, J. C. Yde, J. Cappelen, and J. K. Malmros (2014), Coastal Greenland air temperature extremes and trends 1890-2010: annual and monthly analysis, *International Journal of Climatology*, *34*(5), 1472–1487, doi: 10.1002/joc.3777.

Moin, P., and K. Mahesh (1998), Direct numerical simulation: A tool in turbulence research, *Annual Reviews of Fluid Mechanics*, *30*, 539–578, doi: 10.1146/annurev.fluid.30.1.539.

Moon, T., I. Joughin, B. Smith, and I. Howat (2012), 21st-century evolution of Greenland outlet glacier velocities, *Science*, *336*(6081), 576–578, doi: 10.1126/science.1219985.

Moon, T., I. Joughin, B. Smith, M. R. van den Broeke, W. J. van de Berg, B. Noel, and M. Usher (2014), Distinct patterns of seasonal Greenland glacier velocity, *Geophysical Research Letters*, *41*(20), 7209–7216, doi: 10.1002/2014GL061836.

Moon, T., I. Joughin, and B. Smith (2015), Seasonal to multi-year variability of glacier surface velocity, terminus position, and sea ice/ice melange in northwest Greenland, *Journal of Geophysical Research: Earth Surface*, doi: 10.1002/2015JF003494.

Morlighem, M., E. Rignot, J. Mouginot, H. Seroussi, and E. Larour (2014), Deeply incised submarine glacial valleys beneath the Greenland ice sheet, *Nature Geoscience*, *7*, 418–422, doi: 10.1038/ngeo2167.

Morlighem, M., E. Rignot, J. Mouginot, H. Seroussi, and E. Larour (2015), IceBridge BedMachine Greenland, version 2, *Boulder, Colorado, USA: NASA DAAC at the National Snow and Ice Data Center*, doi: 10.5067/AD7B0HQNSJ29.

Morlighem, M., J. Bondzio, H. Seroussi, E. Rignot, E. Larour, A. Humbert, and S. Rebuffi (2016), Modeling of Store Gletscher's calving dynamics, West Greenland, in response to ocean thermal forcing, *Geophysical Research Letters*, *43*(6), 2659–2666, doi: 10.1002/2016GL067695.

Mortensen, J., K. Lennert, J. Bendtsen, and S. Rysgaard (2011), Heat sources for glacial melt in a sub-arctic fjord (Godthabsfjord) in contact with the Greenland ice sheet, *Journal of Geophysical Research: Oceans*, *116*(C1), doi: 10.1029/2010JC006528.

Mortensen, J., J. Bendtsen, M. R. J., K. Lennert, M. Truffer, F. M., and R. S. (2013), On the seasonal freshwater stratification in the proximity of fast-flowing tidewater outlet glaciers in a sub-arctic sill fjord, *Journal of Geophysical Research: Oceans*, *118*(3), 1382–1395, doi: 10.1002/jgrc.20134.

Mortensen, J., J. Bendtsen, K. Lennert, and R. S. (2014), Seasonal variability of the circulation system in a West Greenland tidewater outlet glacier fjord, Godthabsfjord (64N), *Journal of Geophysical Research: Earth Surface*, *119*(12), 2591–2603, doi: 10.1002/2014JF003267.

Morton, B., G. Taylor, and J. Turner (1956), Turbulent gravitational convection from maintained and instantaneous sources, *Proceedings of the Royal Society of London Series a-Mathematical and Physical Sciences*, *234*(1196), 1–23, doi: 10.1098/rspa.1956.0011.

Morton, B. R. (1959), Forced plumes, *Journal of Fluid Mechanics*, *5*(1), 151–163, doi: 10.1017/S002211205900012X.

Motyka, R. J., L. Hunter, K. A. Echelmeyer, and C. Connor (2003), Submarine melting at the terminus of a temperate tidewater glacier, LeConte Glacier, Alaska, U.S.A., *Annals of Glaciology*, *36*(1), 57–65, doi: 10.3189/172756403781816374.

Motyka, R. J., M. Truffer, M. Fahnestock, J. Mortensen, S. Rysgaard, and I. Howat (2011), Submarine melting of the 1985 Jakobshavn Isbrae floating tongue and the triggering of the current retreat, *Journal of Geophysical Research: Earth Surface*, *116*(F1), doi: 10.1029/2009JF001632.

Motyka, R. J., W. P. Dryer, J. Amundson, M. Truffer, and M. Fahnestock (2013), Rapid submarine melting driven by subglacial discharge, LeConte Glacier, Alaska, *Geophysical Research Letters*, *40*(19), 5153–5158, doi: 10.1002/grl.51011.

Mugford, R. I., and J. A. Dowdeswell (2011), Modeling glacial meltwater plume dynamics and sedimentation in high-latitude fjords, *Journal of Geophysical Research: Earth Surface*, *116*(F1), doi: 10.1029/2010JF001735.

Murray, T., et al. (2015), Extensive retreat of Greenland tidewater glaciers, 2000-2010, *Arctic, Antarctica, and Alpine Research*, *47*(3), 427–447, doi: 10.1657/AAAR0014-049.

Myers, P. G., N. Kulan, and M. H. Ribergaard (2007), Irminger Water variability in the West Greenland Current, *Geophysical Research Letters*, *34*(17), doi: 10.1029/2007GL030419.

Ng, F. S. L. (1998), Mathematical modelling of subglacial drainage and erosion, Ph.D. thesis, University of Oxford.

Nick, F., C. van der Veen, A. Vieli, and D. Benn (2010), A physically based calving model applied to marine outlet glaciers and implications for the glacier dynamics, *Journal of Glaciology*, *56*(199), 781–794, doi: 10.3189/002214310794457344.

Nick, F. M., A. Vieli, I. M. Howat, and I. Joughin (2009), Large-scale changes in Greenland outlet glacier dynamics triggered at the terminus, *Nature Geoscience*, *2*(2), 110–114, doi: 10.1038/ngeo394.

Nick, F. M., A. Vieli, M. L. Andersen, I. Joughin, A. Payne, T. L. Edwards, F. Pattyn, and R. S. W. van de Wal (2013), Future sea-level rise from Greenland's main outlet glaciers in a warming climate, *Nature*, *497*, 235–238, doi: 10.1038/nature12068.

Nye, J. F. (1976), Water flow in glaciers: Jokulhlaups, tunnels and veins, *Journal of Glaciology*, *17*(76), 181–207.

O'Leary, M. (2011), Frontal processes on tidewater glaciers, Ph.D. thesis, University of Cambridge.

O'Leary, M., and P. Christoffersen (2013), Calving on tidewater glaciers amplified by submarine frontal melting, *The Cryosphere*, *7*(1), 119–128, doi: 10.5194/tc-7-119-2013.

Payne, A. J., P. R. Holland, A. P. Shepherd, I. C. Rutt, A. Jenkins, and I. Joughin (2007), Numerical modeling of ocean-ice interactions under Pine Island Bay's ice shelf, *Journal of Geophysical Research: Oceans*, *112*(C10), doi: 10.1029/2006JC003733.

Pedersen, F. B. (1980), Dense bottom currents in rotating ocean, *Journal of the Hydraulics Division*, *106*, 1291–1308.

Pfeffer, W. T. (2007), A simple mechanism for irreversible tidewater glacier retreat, *Journal of Geophysical Research*, *112*(F3), doi: 10.1029/2006JF000590.

Polyakov, I. V., U. S. Bhatt, H. L. Simmons, D. Walsh, J. E. Walsh, and X. Zhang (2005), Multidecadal variability of North Atlantic temperature and salinity during the twentieth century, *Journal of Climate*, *18*(21), 4562–4581, doi: 10.1175/JCLI3548.1.

Pritchard, H. D., R. J. Arthern, D. G. Vaughan, and L. A. Edwards (2009), Extensive dynamic thinning on the margins of the Greenland and Antarctic ice sheets, *Nature*, *461*(7266), 971–975, doi: 10.1038/nature08471.

Reeh, N. (1968), On the calving of ice from floating glaciers and ice shelves, *Journal of Glaciology*, *7*(50), 215–232, doi: 10.3198/1968JoG7-50-215-232.

Rignot, E., and P. Kanagaratnam (2006), Changes in the velocity structure of the Greenland ice sheet, *Science*, *311*(5763), 986–990, doi: 10.1126/science.1121381.

Rignot, E., and K. Steffen (2008), Channelized bottom melting and stability of floating ice shelves, *Geophysical Research Letters*, *35*(2), doi: 10.1029/2007GL031765.

Rignot, E., J. L. Bamber, M. R. van den Broeke, C. Davis, Y. Li, W. J. ven de Berg, and E. ven Meijgaard (2008), Recent Antarctic ice mass loss from radar interferometry and regional climate modelling, *Nature Geoscience*, *1*, 106–110, doi: 10.1038/ngeo102.

Rignot, E., M. Koppes, and I. Velicogna (2010), Rapid submarine melting of the calving faces of West Greenland glaciers, *Nature Geoscience*, *3*(3), 187–191, doi: 10.1038/ngeo765.

Rignot, E., I. Velicogna, M. R. van den Broeke, A. Monaghan, and J. T. M. Lenaerts (2011), Acceleration of the contribution of the Greenland and Antarctic ice sheets to sea level rise, *Geophysical Research Letters*, *38*, doi: 10.1029/2011GL046583.

Rignot, E., I. Fenty, D. Menemenlis, and Y. Xu (2012), Spreading of warm ocean waters around Greenland as a possible cause for glacier acceleration, *Annals of Glaciology*, *53*(60), 257–266, doi: 10.3189/2012AoG60A136.

Rignot, E., S. Jacobs, J. Mouginot, and B. Scheuchl (2013), Ice-shelf melting around Antarctica, *Science*, *341*(6143), 266–270, doi: 10.1126/science.1235798.

Rignot, E., I. Fenty, Y. Xu, C. Cai, and C. Kemp (2015), Undercutting of marine-terminating glaciers in West Greenland, *Geophysical Research Letters*, *42*(14), 5909–5917, doi: 10.1002/2015GL064236.

Roeckner, E., et al. (2003), The atmospheric general circulation model ECHAM5. Part 1: Model description., *Max Planck Institute for Meteorology Rep. 349*.

Röthlisberger, H. (1972), Water pressure in intra- and subglacial channels, *Journal of Glaciology*, *11*(62), 177–203, doi: 10.3198/1972JoG11-62-177-203.

Ryan, J. C., A. L. Hubbard, J. E. Box, J. Todd, P. Christoffersen, J. R. Carr, T. O. Holt, and N. Snooke (2015), UAV photogrammetry and structure from motion to assess calving dynamics at Store Glacier, a large outlet draining the Greenland ice sheet, *The Cryosphere*, *9*(1), 1–11, doi: 10.5194/tc-9-1-2015.

Schild, K. M., R. L. Hawley, and B. F. Morriss (2016), Subglacial hydrology at Rink Isbrae, West Greenland inferred from sediment plume appearance, *Annals of Glaciology*, *57*, 118–127, doi: 10.1017/aog.2016.1.

Schoof, C. (2007), Ice sheet grounding line dynamics: Steady states, stability, and hysteresis, *Journal of Geophysical Research: Earth Surface*, *112*(F3), doi: 10.1029/2006JF000664.

Schoof, C. (2010), Ice-sheet acceleration driven by melt supply variability, *Nature*, *468*(7325), 803–806, doi: 10.1038/nature09618.

Sciascia, R., F. Straneo, C. Cenedese, and P. Heimbach (2013), Seasonal variability of submarine melt rate and circulation in an East Greenland fjord, *Journal of Geophysical Research: Oceans*, *118*(5), 2492–2506, doi: 10.1002/jgrc.20142.

Sciascia, R., C. Cenedese, D. Nicoli, P. Heimbach, and S. F. (2014), Impact of periodic intermediary flows on submarine melting of a Greenland glacier, *Journal of Geophysical Research: Oceans*, *199*(10), 7078–7098, doi: 10.1002/2014JC009953.

Seale, A., P. Christoffersen, R. I. Mugford, and M. O'Leary (2011), Ocean forcing of the Greenland ice sheet: Calving fronts and patterns of retreat identified by automatic satellite monitoring of eastern outlet glaciers, *Journal of Geophysical Research: Earth Surface*, *116*(F3), doi: 10.1029/2010JF001847.

Shapero, D. N., I. R. Joughin, K. Poinar, M. Morlighem, and F. Gillet-Chaulet (2016), Basal resistance for three of the largest Greenland outlet glaciers, *Journal of Geophysical Research: Earth Surface*, *121*(1), 168–180.

Shepherd, A., et al. (2012), A reconciled estimate of ice-sheet mass balance, *Science*, *338*(6111), 1183–1189, doi: 10.1126/science.1228102.

Shreve, R. L. (1972), Movement of water in glaciers, *Journal of Glaciology*, *11*(62), 205–214, doi: 10.3198/1972JoG11-62-205-214.

Slater, D. A., P. W. Nienow, T. R. Cowton, D. N. Goldberg, and A. J. Sole (2015), Effect of near-terminus subglacial hydrology on tidewater glacier submarine melt rates, *Geophysical Research Letters*, *42*(8), 2861–2868, doi: 10.1002/2014GL062494.

Slater, D. A., D. N. Goldberg, P. W. Nienow, and T. R. Cowton (2016), Scalings for submarine melting at tidewater glaciers from buoyant plume theory, *Journal of Physical Oceanography*, *46*(6), 1839–1855, doi: 10.1175/JPO-D-15-0132.1.

Sole, A., P. Nienow, I. Bartholomew, D. Mair, T. Cowton, A. Tedstone, and M. A. King (2013), Winter motion mediates dynamic response of the Greenland ice sheet to warmer summers, *Geophysical Research Letters*, *40*(15), 3940–3944, doi: 10.1002/grl.50764.

Sole, A. J., D. W. F. Mair, P. W. Nienow, I. D. Bartholomew, M. A. King, M. J. Burke, and I. Joughin (2011), Seasonal speedup of a Greenland marine-terminating outlet glacier forced by surface melt induced changes in subglacial hydrology, *Journal of Geophysical Research: Earth Surface*, *116*(F3), doi: 10.1029/2010JF001948.

Spender, M. (1933), Mapmaking during the expedition, *Meddelelser om Gronland*, *104*(2).

Stevens, L. A., F. Straneo, S. B. Das, A. J. Plueddemann, A. L. Kukulya, and M. Morlighem (2016), Linking glacially modified waters to catchment-scale subglacial discharge using autonomous underwater vehicle observations, *The Cryosphere*, *10*(1), 417–432, doi: 10.5194/tc-10-417-2016.

Straneo, F., and C. Cenedese (2015), The dynamics of Greenland's glacial fjords and their role in climate, *Annual Reviews of Marine Science*, *7*(1), 89–112, doi: 10.1146/annurev-marine-010213-135133.

Straneo, F., and P. Heimbach (2013), North Atlantic warming and the retreat of Greenland's outlet glaciers, *Nature*, *504*, 36–43, doi: 10.1038/nature12854.

Straneo, F., G. S. Hamilton, D. A. Sutherland, L. A. Stearns, F. Davidson, M. O. Hammill, G. B. Stenson, and A. Rosing-Asvid (2010), Rapid circulation of warm subtropical waters in a major glacial fjord in East Greenland, *Nature Geoscience*, *3*(3), 182–186, doi: 10.1038/ngeo764.

Straneo, F., R. G. Curry, D. A. Sutherland, G. S. Hamilton, C. Cenedese, K. Vage, and L. A. Stearns (2011), Impact of fjord dynamics and glacial runoff on the circulation near Helheim Glacier, *Nature Geoscience*, *4*(5), 322–327, doi: 10.1038/ngeo1109.

Straneo, F., D. A. Sutherland, D. Holland, C. Gladish, G. S. Hamilton, H. L. Johnson, E. Rignot, Y. Xu, and M. Koppes (2012a), Characteristics of ocean waters reaching Greenland's glaciers, *Annals of Glaciology*, *53*(60), 202–210, doi: 10.3189/2012AoG60A059.

Straneo, F., O. Sergienko, and P. Heimbach (2012b), Understanding the dynamic response of Greenland's marine terminating glaciers to oceanic and atmopsheric forcing: A whitepaper by the U.S. CLIVAR working group on Greenland ice sheet-ocean interactions (GRISO), report 2012-2, U.S. CLIVAR project office, Washington, DC 20006, 22 pp.

Sugiyama, S., P. Skvarca, N. Naito, Nozomu, H. Enomoto, S. Tsutaki, K. Tone, S. Marinsek, and M. Aniya (2011), Ice speed of a calving glacier modulated by small fluctuations in basal water pressure, *Nature Geoscience*, *5*, 597–600, doi: 10.1038/ngeo1218.

Sundfjord, A., et al. (2017), Effects of glacier runoff and wind on surface layer dynamics and Atlantic Water exchange in Kongsfjorden, Svalbard; a model study, *Estuarine, Coastal and Shelf Science*, *187*, 260–272, doi: 10.1016/j.ecss.2017.01.015.

Sutherland, D. A., and R. S. Pickart (2008), The East Greenland Coastal Current: Structure, variability, and forcing, *Progress in Oceanography*, *78*(1), 58–77, doi: 10.1016/j.pocean.2007.09.006.

Sutherland, D. A., and F. Straneo (2012), Estimating ocean heat transports and submarine melt rates in Sermilik Fjord, Greenland, using lowered acoustic Doppler current profiler (LADCP) velocity profiles, *Annals of Glaciology*, *53*(60), 50–58, doi: 10.3189/2012AoG60A050.

Sutherland, D. A., F. Straneo, and R. S. Pickart (2014), Characteristics and dynamics of two major Greenland glacial fjords, *Journal of Geophysical Research: Oceans*, *119*(6), 3767–3791, doi: 10.1002/2013JC009786.

Tedesco, M., X. Fettweis, T. Mote, J. Wahr, P. Alexander, J. E. Box, and B. Wouters (2013), Evidence and analysis of 2012 Greenland records from spaceborne observations, a regional climate model and reanalysis data, *The Cryosphere*, *7*(2), 615–630, doi: 10.5194/tc-7-615-2013.

Tedstone, A. J. (2015), Hydrological controls on Greenland ice sheet motion, Ph.D. thesis, University of Edinburgh.

Tedstone, A. J., and N. S. Arnold (2012), Automated remote sensing of sediment plumes for identification of runoff from the Greenland ice sheet, *Journal of Glaciology*, *58*(210), 699–712, doi: 10.3189/2012JoG11J204.

Tedstone, A. J., P. W. Nienow, A. J. Sole, D. W. F. Mair, T. R. Cowton, I. D. Bartholomew, and M. A. King (2013), Greenland ice sheet motion insensitive to exceptional meltwater forcing, *Proceedings of the National Academy of Sciences*, doi: 10.1073/pnas.1315843110.

Tedstone, A. J., P. W. Nienow, N. Gourmelen, A. Dehecq, D. Goldberg, and E. Hanna (2015), Decadal slowdown of a land-terminating sector of the Greenland ice sheet despite warming, *Nature*, *526*(7575), 692–695, doi: 10.1038/nature15722.

Thomas, R., E. Frederick, W. Krabill, S. Manizade, and C. Martin (2009), Recent changes on Greenland outlet glaciers, *Journal of Glaciology*, *55*(189), 147–162, doi: 10.3189/002214309788608958.

Thomas, R. H. (2004), Force-perturbation analysis of recent thinning and acceleration of Jakobshavn Isbrae, Greenland, *Journal of Glaciology*, *50*(168), 57–66, doi: 10.3189/172756504781830321.

Todd, J., and P. Christoffersen (2014), Are seasonal calving dynamics forced by buttressing from ice melange or undercutting by melting? Outcomes from full-stokes simulations of Store glacier, West Greenland, *The Cryosphere*, *8*(6), 2353–2365, doi: 10.5194/tc-8-2353-2014.

Todd, J., et al. (2017), A full-stokes 3D calving model applied to a large Greenland glacier, *Journal of Geophysical Research: Earth Surface*, submitted.

Turner, J. S. (1979), *Buoyancy Effects in Fluids*, Cambridge University Press.

Van As, D., et al. (2014), Increasing meltwater discharge from the Nuuk region of the Greenland ice sheet and implications for mass balance (1960-2012), *Journal of Glaciology*, *60*(220), 314–322, doi: 10.3189/2014JoG13J065.

van den Broeke, M., J. Bamber, J. Ettema, E. Rignot, E. Schrama, W. J. van de Berg, E. van Meijgaard, I. Velicogna, and B. Wouters (2009), Partitioning recent Greenland mass loss, *Science*, *326*(5955), 984–986, doi: 10.1126/science.1178176.

van den Broeke, M. R., E. M. Enderlin, I. M. Howat, P. Kuipers Munneke, B. P. Y. Noël, W. J. van de Berg, E. van Meijgaard, and B. Wouters (2016), On the recent contribution of the Greenland ice sheet to sea level change, *The Cryosphere*, *10*(5), 1933–1946, doi: 10.5194/tc-10-1933-2016.

Vaughan, D., et al. (2013), *Observations: Cryosphere*, book section 4, pp. 317–382, Cambridge University Press, Cambridge, United Kingdom and New York, NY, USA, doi: 10.1017/CBO9781107415324.012.

Vieli, A., J. Jania, H. Blatter, and M. Funk (2004), Short-term velocity variations on Hansbreen, a tidewater glacier in Spitsbergen, *Journal of Glaciology*, *50*(170), 389–398, doi: 10.3189/172756504781829963.

Våge, K., et al. (2011), The Irminger Gyre: Circulation, convection, and interannual variability, *Deep Sea Research Part I: Oceanographic Research Papers*, *58*(5), 590–614, doi: 10.1016/j.dsr.2011.03.001.

Wagner, T. J. W., T. D. James, T. Murray, and D. Vella (2016), On the role of buoyant flexure in glacier calving, *Geophysical Research Letters*, *43*(1), 232–240, doi: 10.1002/2015GL067247.

Walder, J. S., and A. Fowler (1994), Channelized subglacial drainage over a deformable bed, *Journal of Glaciology*, *40*(134), 3–15, doi: 10.3198/1994JoG40-134-3-15.

Walter, F., J. Chaput, and M. P. Luthi (2014), Thick sediments beneath Greenland's ablation zone and their potential role in future ice sheet dynamics, *Geology*, *42*(6), 487–490, doi: 10.1130/G35492.1.

Weertman, J. (1974), Stability of the junction of an ice sheet and an ice shelf, *Journal of Glaciology*, *13*(67).

Wells, A. J., and M. G. Worster (2008), A geophysical-scale model of vertical natural convection boundary layers, *Journal of Fluid Mechanics*, *609*, 111–137, doi: 10.1017/S002211200800234.

Wells, M. G., and J. S. Wettlaufer (2007), The long-term circulation driven by density currents in a two-layer stratified basin, *Journal of Fluid Mechanics*, *572*, 37–58, doi: 10.1017/S0022112006003478.

Wright, S. J., and R. B. Wallace (1979), Two-dimensional buoyant jets in a stratified fluid, *Proc. ASCE, J. Hydraul. Div.*, *105*, 1393–1406.

Xie, S., T. H. Dixon, D. Voytenko, D. M. Holland, D. Holland, and T. Zheng (2016), Precursor motion to iceberg calving at Jakobshavn Isbrae, Greenland, observed with terrestrial radar interferometry, *Journal of Glaciology*, *62*(236), 1134–1142, doi: 10.1017/jog.2016.104.

Xu, Y., E. Rignot, D. Menemenlis, and M. Koppes (2012), Numerical experiments on subaqueous melting of Greenland tidewater glaciers in response to ocean warming and enhanced subglacial discharge, *Annals of Glaciology*, *53*(60), 229–234, doi: 10.3189/2012AoG60A139.

Xu, Y., E. Rignot, I. Fenty, D. Menemenlis, and M. M. Flexas (2013), Subaqueous melting of Store glacier, West Greenland from three-dimensional, high-resolution numerical modeling and ocean observations, *Geophysical Research Letters*, *40*(17), 4648–4653, doi: 10.1002/grl.50825.

Yin, J., J. T. Overpeck, S. M. Griffies, A. Hu, J. L. Russell, and R. J. Stouffer (2011), Different magnitudes of projected subsurface ocean warming around Greenland and Antarctica, *Nature Geoscience*, *4*(8), 524–528, doi: 10.1038/ngeo1189.

Zuo, Z., and J. Oerlemans (1996), Modelling albedo and specific mass balance of the Greenland ice sheet: calculations for the Sondre Stromfjord transect, *Journal of Glaciology*, *42*(141), 305–317, doi: 10.3198/1996JoG42-141-305-317.

Zwally, H. J., W. Abdalati, T. Herring, K. Larson, J. Saba, and K. Steffen (2002), Surface melt-induced acceleration of Greenland ice-sheet flow, *Science*, *297*(5579), 218–222, doi: 10.1126/science.1072708.